Modeling the Non-Linear Rheology of Linear Polymers and Associating Telechelic Polymers

Gun Woo Park

Thesis Submitted in Partial Fulfillment of the
Requirements for the Degree of
Doctor of Philosophy
in
Industrial Product and Processing Engineering

Cycle 29
2014 ∼ 2017

University of Naples Federico II
Department of Chemical, Materials and Production Engineering (DICMaPI)

Modeling the Non-Linear Rheology of Linear Polymers and Associating Telechelic Polymers

by

Gun Woo Park

Tutor: Prof. Giovanni Ianniruberto

Coordinator: Prof. Giuseppe Mensitieri

Abstract

The non-linear rheology of ordinary linear polymers and linear polymers with associable end-group has been examined by means of modeling. This work is motivated by discrepancies between experiments and existing theoretical expectations in the non-linear regime. In the case of associating polymers, we aim at understanding the break-down of Cox-Merz rule, shear thickening, and strain hardening of shear startup, while for conventional linear polymers we focus on the discrepancies typically encountered in the fast uniaxial extensional flows. It is appropriate to mention that most efforts are related to developing a stochastic simulation of associating telechelic polymers (part 1) while the studies of linear polymers in the fast flows (part 2) is rather limited in the persepectives of nematic interactions of oligomer-type solvent.

For reference sample of associating telechelic polymers, the hydrophobically modified ethoxylated urethane (HEUR) is selected because of plenty of experimental data have been reported in the past. This information is collected into chapter 1 considering both morphology and dynamical aspects. HEUR is made up by poly(ethylene oxide) (PEO) end-capped with short hydrophobic groups. Above the so-called critical micelle concentration, HEUR in aqueous solutions forms flower-like micelles where the core is composed of aggregated hydrophobic end-groups. Since the aggregation is physically reversible, chain ends can detach from the core, and attach to neighboring micelles (thus forming bridges). The probability of bridge formation increases with increasing HEUR concentration, and a transient network eventually builds up. The linear viscoelastic behavior of HEUR systems is somehow simple since they exhibit a single-mode Maxwell-like response with a dominant relaxation time (related to the association/dissociation dynamics), exhibiting a power-law dependence on HEUR concentration and molar mass. On the contrary, HEUR solutions exhibit a complex nonlinear rheological behavior. The Cox-Merz rule is often violated since the steady shear viscosity can reveal shear thickening while the dynamic viscosity only shows shear thinning. In the shear rate range of the viscosity thickening, the first normal stress coefficient remains at its LVE value.

As regards the shear startup response at high shear rates, strain hardening is often observed both for the viscosity and for the first normal stress coefficient. Remarkably, the overshoot of stress growth function is well beyond linear viscoelastic envelope. Motivated by these experimental observations, new stochastic simulation is proposed where its coarse-graining level is the consequence of trade off between computation time (within few days for non-equilibrium simulation) and availability to capture detailed mechanism behind rheological observations, especially for number of elastically active chains. This newly developed stochastic simulation is based on Langevin dynamics coupled with an additional stochastic step for topological renewal. Parameters of the simulations are size of micelles and chains, stiffness of micelle structure, micelle aggregation number, length being related to micelle core, and time ratio between micelle diffusion time and loop-dissociation time. After detailing the algorithm in chapter 2, chapter 3 explores the effect of various parameters on static and dynamical observables. Selected samples are examined in chapter 4 both under equilibrium and non-equilibrium conditions. Results show scaling exponents consistent with experimental data, understanding strain hardening of shear startup in the way of finite extensibility of chains, confirm break-down of Cox-Merz rule due to persistence of bridges, and capture shear-thickening. Details of simulations are reported in the appendix together with the theoretical background and strategy of code development.

In part 2, we examined entangled linear polymers in the extensional flows at flow rates higher than the reciprocal Rouse time. In the classical molecular models, the steady-state extensional viscosity is characterized by four regimes: (i) the linear regime with Trouton ratio equal to 3, (ii) viscosity thinning with exponent -1, (iii) upturn due to chain stretch, and (iv) approach to an asymptotic value due to finite extensibility. The advent of data from extensional rheology, however, reveals that the theoretical expectation is not strictly true, and the tendency depends on the details of chemistry. To be specific, polystyrene (PS) melt shows the spontaneous decrease even beyond the reciprocal Rouse time with an exponent of -1/2, while polyisoprene (PI) and poly(n-butyl acrylate) (PnBA) shows the upturn around reciprocal Rouse time. These differences are believed to be due

to the sensitivity of the monomeric friction coefficient to alignment in the statistical segments of polymer chain when the flow rate is larger than reciprocal Rouse time. This is confirmed by measuring components for friction tensor and order parameter of oligomer-type molecular simulations in the simple shear where shear rate is higher than reciprocal self-diffusion time (chapter 6). In this context, we also analyze PS solutions in its oligomeric solvents, all having the same linear-viscoelasticity (chapter 7). The suggested model uses the frictional change due to the change of order parameter that accounts for the nematic interactions. The results quantitatively predict the experimental data from extensional flow.

Acknowledgement

Foremost, I would like to thank my advisor Prof. Giovanni Ianniruberto for guiding me the non-linear rheology of polymers and transient networks. Without his support, it might be very difficult to reach the final goal of my research activities in Naples. I am also very grateful to Prof. Giuseppe Marrucci who actively involved in my research activities and suggest many possible (but more promising) pathway to reach research objectives of mine. Thanks to Dr. Antonio Brasiello who guide me practical aspects of molecular dynamics simulation at the beginning of my life in Naples.

Thanks to all of my colleagues and professors of SUPOLEN for widening of my eyes on variety complex soft matters from chemical structures to dynamical behaviors. Especially for Prof. Daniel Read and Prof. Dimitris Vlassopoulos who strengthen this study with important comments as member of international committees of my thesis. Thanks to kind assistance from the personnel of the SCoPE Computing Center of University of Federico II.

I will forever be thankful to my formal supervisor Prof. Kwang Soo Cho who have been supporting plenty of theoretical background and sharing personal opinions to me. I am also grateful for my formal colleagues in Korea who are pulling for me about my scientific career path.

Finally, my deep and sincere gratitude to my family for their continuous and unparalleled love. I am grateful to my wife Ae Gyeong being here for me. Thank you for my daughter Da Som born in Naples with healthy and beauty. I especially thank my parents and sister who take care about me since I was born.

This studies cannot be done without financial supporting from EU through the ITN SUPOLEN project (grant no. 607937).

Dedicated to my family with love

Contents

List of Figures

List of Tables

A Stochastic Simulation of Telechelic Associating Polymers

Chapter 1

Associating Telechelic Polymers

1.1 Introduction

Associating telechelic polymers are made up with a long linear chain where the both chain ends produce association point with other chain ends. One of the representative samples of associating telechelic polymer is hydrophobically ethoxylated urethane (HEUR) in aqueous solution. The main chain of HEUR is Poly(Ethylene Oxide) (PEO), and the both of the chain ends are capped with small hydrophobic groups. When polymer concentration higher than the critical micelle concentration (CMC), the morphology of this system is believed by flower-like micelle where the core is aggregation between hydrophobic chain ends surrounded by PEO chains with solvent (François et al. 1996; Winnik and Yekta 1997; Xu et al. 1996; Yekta et al. 1995).

When the distance between micelle is comparable with single chain size, the chain ends are allowed to from bridge. With the increasing concentration, the system becomes a network-like structure, but the strand between network junction is temporal, called transient network. There are many interesting phenomena happens on this transient network in both of linear and non-linear viscoelasticity. First of all, the linear viscoelasticity (LVE) shows that the system is an approximately single-Maxwellian behavior where the time scale is following Arrhenius type time-temperature superposition (TTS). The activation energy is related to dissociate a chain end from its core (Annable et al. 1993;

Tanaka and Edwards 1992b). It is evidently shown by Annable et al. (1993) where the viscosity and relaxation time directly proportional to the length of end-groups. Unlike the simple LVE, the steady-state viscosity in simple shear flow deviates from the complex viscosity, unlike the conventional polymers. The details to deviate from Cox-Merz rule depend on the concentration. It is already shown in Xu et al. (1996), but more clearly reported in Suzuki et al. (2013), where the onset shear rate for shear thinning will decreases in steady-state viscosity due to concentration while the relation between the complex viscosity and concentration is relatively minor. In addition, the lower concentration of HEUR polymer (1wt%) exhibit shear thickening before thinning about a factor of 1.4 while the higher concentration (above 4wt%) does not show such a thickening. The detailed mechanism of shear thickening is still in controversial, but the main postulates are listed as finite extensibility (Marrucci et al. 1993; Yekta et al. 1995), shear-induced bridge formation (Tam et al. 1998), and the repulsive micelle interaction (Ianniruberto and Marrucci 2015).

There are many simulation methods to analysis the non-linear response of the subjected system (Hernández Cifre et al. 2003, 2007; Koga and Tanaka 2005; Sprakel et al. 2009; Van den Brule and Hoogerbrugge 1995). The classical one is Van den Brule and Hoogerbrugge (1995) to use Brownian motion, but the topological update is not rigorous enough for the research objectives of this study. Hernández Cifre et al. (2003) accounts for details of individual parameters while the simulation is based on dumbbell model. Hernández Cifre et al. (2007) suggest the bead-and-spring chain model based on Hernández Cifre et al. (2003) and Van den Brule and Hoogerbrugge (1995), but the topological information is not enough to account network information. One of the most satisfactory method for this study is Sprakel et al. (2009) where the both of the position of micelles and bridge formation are evolved as realization. However, the realization of network rearrangement is through pre-determined bridge distribution function which means the aggregation number (or number of chain ends in the system) cannot be control variable. Hence, the newly developed stochastic simulation in this study takes account both of time evolution for the position of micelle and dissociation/association kinetics

individually.

1.2 Network Theories

1.2.1 Ideal Networks

Starting with theories for ideal networks, the constitutive models on here is assumed materials as hyperelastic body. It means the strain energy function is a scalar function on an appropriate strain measures (details are described in sections 7.1.2 and 7.1.3). The original theories especially for rubber elasticity are based on the assumption (and observation) of internal energy changes during deformation is negligible (Anthony et al. 1942):

$$f = \left(\frac{\partial E}{\partial L}\right)_T - T\left(\frac{\partial S}{\partial L}\right)_T \approx -T\left(\frac{\partial S}{\partial L}\right)_T, \tag{1.1}$$

where f is the force exerted in the specimen at a fixed temperature, E is the internal energy, S is the entropy, T is the temperature, and L is the length of the specimen. Therefore, the only entropic part become important to understand stress-strain relation.

Affine Gaussian Network Theory

The detail construction of constitutive equations for ideal networks are described in section 7.1, but here we describe some sequence of derivation of affine Gaussian network theory that will be used for transient network as well. With the formalism of Eq. (7.19), it is of importance to define strain energy function, W, using free energy of the system, F.

Let start with Gaussian network theory. The probability for Gaussian end-to-end vector, $\mathbf{r}$, is given by

$$P^G(\mathbf{r}) = \left(\frac{3}{2\pi R_c^2}\right)^{3/2} \exp\left(-\frac{3}{2R_c^2}\mathbf{r}\cdot\mathbf{r}\right), \tag{1.2}$$

where $R_c^2 = \langle \mathbf{r}\cdot\mathbf{r}\rangle$. Using Boltzmann entropy theory, we have individual chain entropy as

$$s = k_B \log P^G(\mathbf{r}) + s^{(0)}, \tag{1.3}$$

where s is the entropy of a single chain and $s^{(0)}$ is the term independent of $\mathbf{r}$. For generalization of chain statistics, the single chain entropy can be expressed as

$$s_k = -k_B tr\left(\mathbf{F}\cdot\boldsymbol{\xi}_k\cdot\mathbf{F}^T\right) + s_k^{(0)}, \tag{1.4}$$

where $\boldsymbol{\xi}_k = \xi_k^2\mathbf{r}_k\mathbf{r}_k$ indicate a tensoral representation of unstrained state of k-chain ($\xi_k^2 = \frac{3}{2R_c^2}$. If the chain statistics are independent of another chain, the system entropy is the sum of all the individual chain entropy:

$$\frac{S}{V_s} = \frac{1}{V_s}\sum_{k=1}^{N} s_k = -\frac{k_B}{V_s}\sum_{k=1}^{N} tr\left(\mathbf{F}\cdot\boldsymbol{\xi}_k\cdot\mathbf{F}^T\right) + S^{(0)}/V_s \tag{1.5}$$

$$= -k_B\nu tr\left(\mathbf{F}\cdot\bar{\boldsymbol{\xi}}\cdot\mathbf{F}^T\right) + S^{(0)}/V_s \quad \text{with} \quad \nu = \frac{N}{V_s}, \tag{1.6}$$

where $\bar{\boldsymbol{\xi}}$ is number average of $\boldsymbol{\xi}_k$:

$$\bar{\boldsymbol{\xi}} = \frac{1}{N}\sum_{k=1}^{N}\boldsymbol{\xi}_k, \tag{1.7}$$

which leads $\bar{\boldsymbol{\xi}} = \frac{1}{2}\mathbf{I}$ for isotropic Gaussian chain.

Finally, the strain energy function is given by free energy per unit volume:

$$W = \frac{F}{V_s} = \frac{\nu}{2}k_B T tr\mathbf{B}, \tag{1.8}$$

where $\mathbf{B}$ is called left Cauchy-Green tensor (section 7.1.2). It deduce the stress tensor as

$$\boldsymbol{\tau} = \nu k_B T\mathbf{B} + p\mathbf{I}, \tag{1.9}$$

and the hydrostatic pressure, p, is easily determined for incompressible body.

Note that the final form is fully consist with constitutive equation for isotropic incompressible hyperelastic body (section 7.1.4). There are many advanced models from molecular to phenomenological ones (Treloar 1975) based on hyperelasticity.

1.2.2 Transient Networks

Green-Tobolsky's transient network theory

So far, the network theory for the permernent Gaussian network has been addressed. For the transient networks, however, this is not the same since the stress of material

depends on the history of deformation and rate of deformation. Once all the chains dot not have the same statistics before deformation, the collected unstrained chain property tensor is similar to Eq. described as its original form:

$$\bar{\boldsymbol{\xi}} = \frac{1}{3N}\sum_{l} N_l \xi_l^2 \mathbf{r}_l^2 \mathbf{I}, \tag{1.10}$$

which is the number average for categorized chain property. Unlike rubber elasticity, however, here the numbers of strains are related with elastically active chains, which is non-constant due to the time. Green and Tobolsky (1946) detour this problem by using the same formula as network theory described in above but using $\boldsymbol{\xi}$ as described in (1.10). The static strain energy function without dependency of deformation history becomes

$$W = \frac{\bar{\nu}}{2} k_B T tr\mathbf{B} + W^{(0)} \quad \text{with} \quad \bar{\nu} = \frac{1}{3}\sum_{l} \nu_l \xi_l^2 \mathbf{r}_l^2, \tag{1.11}$$

where the prefactor $\bar{\nu}$ is differ from ν in the theory for ideal network.

Green and Tobolsky (1946) assumed that for given time step, δt, chains are instantaneously deformed with the given deforation fields, then the reforming chains will follows istoropic state. The deformation field following the time t from its unstrained state, but the chain will deformed after forming bridge $tT\prime$. The relative deformation field for the chain can be determined through the multiplicative decomposition:

$$\mathbf{F}(t) = \mathbf{F}_{(r)}(t,t') \cdot \mathbf{F}_{(h)}(t') \quad \Rightarrow \quad \mathbf{F}_{(r)}(t,t') = \mathbf{F}(t) \cdot \mathbf{F}_{(h)}^{-1}(t'), \tag{1.12}$$

where subscript (h) indicate its historical part and (r) indicate relative part for the subject chain. The strain energy function is given by relative part:

$$W = \frac{\bar{\nu}}{2} k_B T tr\left(\sum_{i=1}^{N} \mathbf{F}_{(p),i} \cdot \mathbf{F}_{(p),i}^T\right) \tag{1.13}$$

$$= \frac{\bar{\nu}}{2} k_B T tr\left(\mathbf{F} \cdot \boldsymbol{\phi} \cdot \mathbf{F}^T\right), \tag{1.14}$$

where the elastic deformation tensor due to the elastically active chains are given by

$$\boldsymbol{\phi} = \sum_{i=1}^{N} \boldsymbol{\phi}_i = \sum_{i=1}^{N} \mathbf{F}_{(el),i}^{-1} \cdot \left(\mathbf{F}_{(el),i}^{-1}\right)^T, \tag{1.15}$$

where N is the number of the elastically active chain at initial stage. Unlike the individual strain measures, the number of elastically active chain depends on the history of deformation. One of the simplest way to describe the rate of break chain is using the first order kinetic equation:

$$\frac{1}{N}\frac{dN}{dt} = -\beta, \tag{1.16}$$

where β is a rate of breaking bonds, and N can be replaced by the density of elastically active chain, ν_C, because of incompressibility. It implies the historical dependence to $\boldsymbol{\phi}$ as

$$\boldsymbol{\phi}(t) = \exp(-\beta t)\boldsymbol{\phi}(0) + \int_0^t \exp\left(-\beta(t-t')\right) \mathbf{F}_{(el)}^{-1}(t') \cdot \left(\mathbf{F}_{(el)}^{-1}(t')\right)^T \beta dt', \tag{1.17}$$

where the first term in RHS is destroy of chains from its initial time and the second term in RHS is contribution of elastically activated chains during the time between 0 and t. In this context, the strain energy function and stress-strain relation hold the forms with the ideal network:

$$W = \bar{\nu} k_B T tr\mathbf{F} \cdot \boldsymbol{\phi} \cdot \mathbf{F}^T + W^{(0)}; \tag{1.18}$$

$$\boldsymbol{\tau} = \bar{\nu} k_B T \mathbf{F} \cdot \boldsymbol{\phi} \cdot \mathbf{F}^T + p\mathbf{I}, \tag{1.19}$$

but the details form of $\boldsymbol{\phi}$ must be solved with further approximation of increment of strain energy function, δW. Following this suggestion, the stress-strain relation for shear is given by Green and Tobolsky (1946):

$$\frac{d\dot{\gamma}}{dt} = \frac{1}{G}\frac{d\sigma}{dt} + \frac{\beta}{G}\sigma, \tag{1.20}$$

with the shear modulus

$$G = \bar{\nu} k_B T = \frac{k_B T}{3} \sum_l \nu_l \xi_l^2 \mathbf{r}_l^2. \tag{1.21}$$

The final remakrs are related to the averaged unstrained chain property tensor, $\bar{\boldsymbol{\xi}}$. If we assumed that the individual statistics for chains are the same to each other, $\xi_l = \xi$, the isotropic assumptions work as $\bar{\nu} \approx \nu_C^+$, where ν_C^+ is number density for elastically active bridges. With the suggesting model, Eq. (1.20), the plateau modulus follows

$$G^\circ = G = \bar{\nu} k_B T \approx \nu_C^+ k_B T. \tag{1.22}$$

Tanaka-Edwards' Detachment Frequency

The main approach of Green-Tobolsky is to adapt the theory of rubber elasticity into the viscoelastic material using multiplicative decomposition and the first order kinetics of elastically active chains. The important conclusions are described on Eq. (1.22). The details of kinetics are omitted and described the simplified historical influence into the constitutive equation, and derive Maxwell-like stress-strain relation. Since the material considered on here is physically associable networks, the details on kinetics are of importance. One of the popular approaches is Tanaka and Edwards (1992a,b) where the model address non-entangled regime where the morphology is described in figure 1.1 that account for a well-formed network with an existence of dangling chains. Tanaka and Edwards (1992a) simplify the time evolution for number density of elastically active chain by linearization with memory function, $\mu(t;t')$:

$$\nu^{+}(t) = \nu_{in}(t) + p\int_0^t \mu(t;t')\nu^{\dagger}(t')dt' \quad \text{with } \nu^{\dagger}(t') = \left[n - \nu(t')\right], \tag{1.23}$$

where $\nu^{\dagger}(t')$ represent number density of dangling chains. The memory function is connected with the detachment frequency through the form of so-called chain survival probability, $\Theta(\mathbf{r},t;\mathbf{r}',t')$:

$$\mu(t;t') = \int \Theta(\mathbf{r},t;\mathbf{r}',t')P^{G}(\mathbf{r}')d\mathbf{r}', \tag{1.24}$$

which in principle the form of averaging the chain survival probabilty gave us the time-correlated memory function. Note that $t-t' \to 0$ indicate the suggesting time-correlated memory function becomes the probability of an elementary configurations.

Tanaka and Edwards (1992b) uses detachment frequency as the similar form with Bell (1978) and Evans and Ritchie (1997) based on the transition-state-theory:

$$\beta(r) = \Omega \exp\left(-\frac{1}{k_B T}\left(W - fl^{*}\right)\right) \equiv \beta_0 \exp\left(\frac{fl^{*}}{k_B T}\right), \tag{1.25}$$

where f is the force exerted on the subjected group (here is the end groups), Ω is thermal frequency acting on the subject group, W is energy wall to overcome the reaction, and l^{*} is the landscape to free from interaction. Note that Tanaka and Edwards (1992b)

uses l^* as a statistical length scale while the later studies uses it as size being related with the aggregates (Ianniruberto and Marrucci 2015; Tripathi et al. 2006). The bond lifetime for the subjected group is its reciprocal value:

$$\tau(r) \equiv \beta(r)^{-1} = \tau_0 \exp\left(-\frac{fl^*}{k_B T}\right). \tag{1.26}$$

With the suggested detachment frequency, the memory function becomes simpler forms as

$$\Theta(\mathbf{r}, t; \mathbf{r}', t') = \exp\left(-\int_{t'}^{t''} \beta(\mathbf{r}_{t'',t'}) dt''\right). \tag{1.27}$$

For solution of stationary state, it is appropriate to show

$$\lim_{t\to\infty} \nu = \frac{np\tilde{\mu}(0)}{1 + p\tilde{\mu}(0)}, \tag{1.28}$$

where tilde indicate its Laplace transform.

Tanaka and Edwards (1992c) shows that the breakdown of the Cox-Merz rule. As remarked in Annable et al. (1993), the non-linear response sensitively depends on the function of the detachment frequency where TE model uses a quadratic form for analytical treatment.

1.3 Morphology of the System

In this study, The experimental data mainly refers to Annable et al. (1993), Suzuki et al. (2012), Uneyama et al. (2012), and Xu et al. (1996) where the samples have the similar molecular structure and rheological properties. The exact molecular structure slightly different between the system with different molecular weight is from 10k to 50k. Despite the different molecular information, the system consistently shows the single-Maxwellian behavior about cross-over frequency of dynamic moduli, then start to deviate after cross-over frequency Suzuki et al. (2012). This cross-over time is about second order although the details will depend on the concentration of polymers and molecular weight (Annable et al. 1993).

1.3.1 Describing Sample System

In the 1990s, many publications report about the possible the structure of HEUR in an aqueous solution about rheological properties Annable et al. (1993), Tam et al. (1998), and Xu et al. (1996) morphological using fluorescence and scattering studies Alami et al. (1996), François et al. (1996), and Yekta et al. (1995), and theoretical development to understand micelle interactions Semenov et al. (1995). The morphology will change with HEUR concentration, but the topic on here is especially focused on the concentration where the system strongly deviates from Cox-Merz rule, and shear thickening is observed before thinning. Tripathi et al. (2006) categorized the different sample system used in various papers into dilute, semi-dilute, semi-dilute entangled, and concentrated entangled system using the approach on Graessley (1980). It is of importance to aware that the reference sample in Annable et al. (1993) that shows strong deviation from Cox-Merz rule account dilute regime, and the concentration is about five times small from the semi-dilute regime. In this regards, the study in this thesis is mainly focused on the dilute regime but still higher than critical micelle concentration, c^*, where the micelle structure are represented as 1.1 (down).

1.3.2 Structure of Micelle

Aggregation Number

The core of micelle is composed of the physically aggregated part where the core size is around 2nm (Yekta et al. 1995). The aggregation number p is an expected value of chain ends per micelle where the chain ends belong to loop or bridge is not distinguishable. Xu et al. (1996) expected about 22 ± 2 where the concentration is range of 1 - 10 g/L. Elliott et al. (2003) measures the dependence of p to the molecular weight and concentration. For 25k in M_n and almost 100% of chain ends are capped material, p is range between 5 and 10. According to the Elliott et al. (2003), p depends both of molecular weight and concentration of HEUR, reproduced figure 1.2. In the figure, the number of units in the main chain adjusted from 190 to 670, and the slope of p with concentration becomes

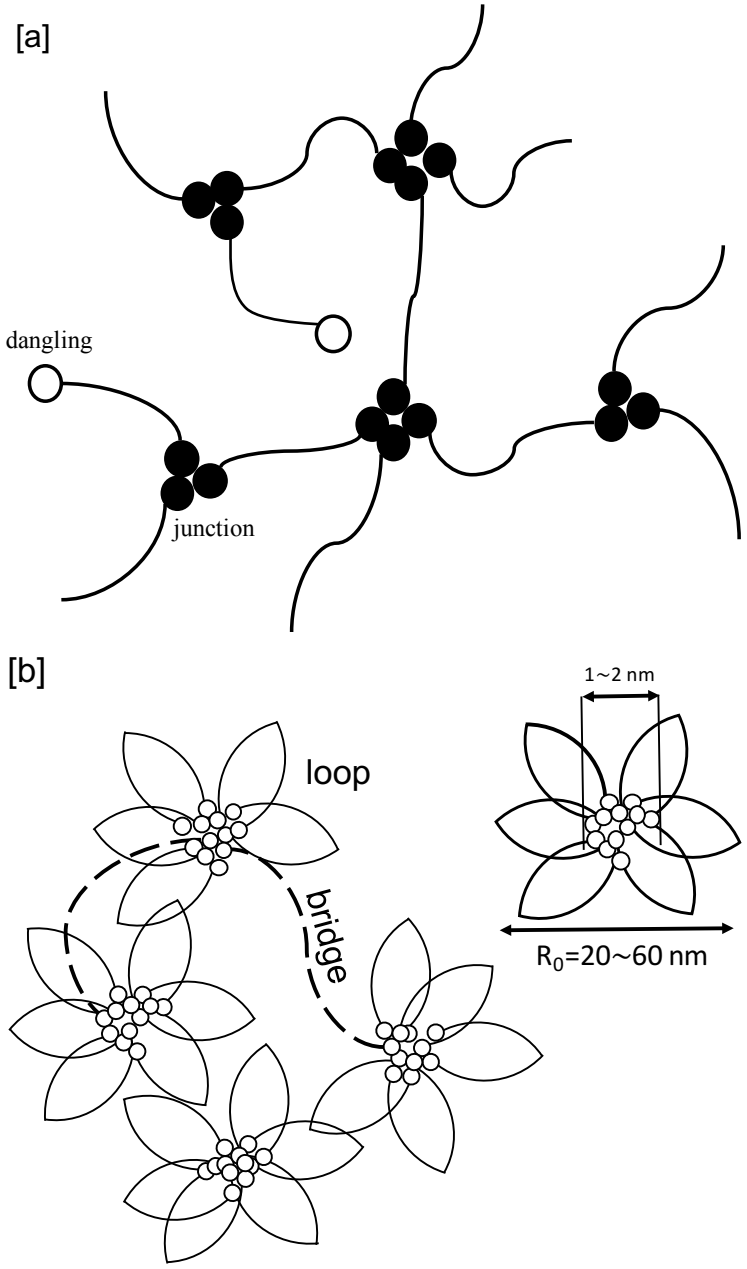

Figure 1.1: Schematic diagram for network-like structure depicted in Tanaka and Edwards (1992a) [a] and expected micelle structure in dilute and semi-dilute without entanglement regime [b].

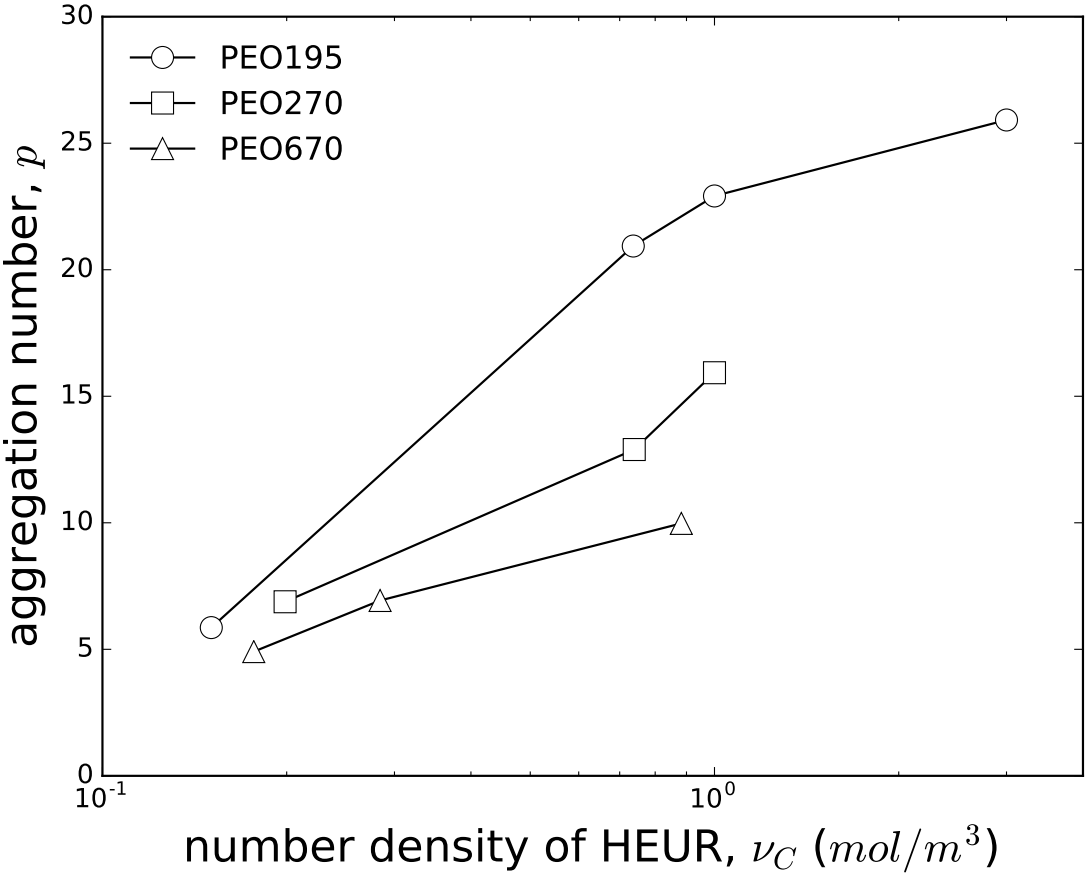

Figure 1.2: Expected aggregation numbers at each concentration of HEUR. Data is reproduced from Elliott et al. (2003).

smaller. In consequence, the 670 ethylene oxide (EO) shows between 5 and 10 in p. Note that the material used in Suzuki et al. (2012) have 430 EO units, which make reasonable about 10 aggregations per micelle. The number of aggregation also affects the size of the core through the exponent of 1/3 that consist with the dimensionality of volume (Meng and Russel 2005):

$$R_{core} = \left(\frac{3pN_{Kp}}{2\pi}\right)^{1/3} l_K, \tag{1.29}$$

where N_{Kp} is length of statistical segment for hydrophobe. With this interpretation, change of p from 10 to 20 will increases 26% of the core size.

Hydrodynamic Radius and Excluded Volume of Micelle

Li and Witten (1994) derive the exclusion of polymer grafted in sphere using the free energy form of

$$\mathscr{F} = \sum_i \int_0^N dt \, \frac{1}{2a^2} \left(\frac{d\mathbf{r}_i(t)}{dt} \right)^2 + \frac{\nu}{2} \int d\mathbf{r} \, n^2(\mathbf{r}), \tag{1.30}$$

where the N is the total number of monomers per chain, a is a microscopic length, ν is excluded-volume parameter, and $n(\mathbf{r})$ is a monomer number density given by $n(\mathbf{r}) = \sum_i \int dt \, \delta(\mathbf{r} - \mathbf{r}_i(t))$ where δ is Dirac-delta function. The basic idea on here is to decompose the elastic energy of stretched chains (the first term in RHS) and the excluded volume interaction part (the second term in RHS) where the monomer density is used as typical Dirac-delta form (Doi and Edwards 1988). This application is used for flower-like micelle where the grafted arms are regarded as half-chain (Semenov et al. 1995) under the assumption of sufficiently large number of arms per micelle, aggregation number p. It is fair to note that the expected p is not that large unlike the previous approach, which allows using similar form especially only accounts the second term in the RHS of Eq. (1.30). The description on here mainly refers to Meng and Russel (2005) where the paper mainly account the size and micelle. The hydrodynamic radius of micelle will depend on p, length and number of statistical segments of chain, l_s and N_s, respectively, excluded-volume parameter ν, through the form of

$$R_M = 0.914 \left(2pN_s^3 \nu \right)^{1/5} l_s, \tag{1.31}$$

where the exclusion size of the micelle is expected by

$$r_c = 0.938R \tag{1.32}$$

based on the theory of grafted polymer on convex surface (Li and Witten 1994). Note that the assumption on the stretched chain used in Li and Witten (1994) and Meng and Russel (2005) valids on higher aggregation numbers which derived two different isotropic segment fraction profiles:

$$n(r) = \begin{cases} 0.198(2p)^{2/5} N^{-4/5} v^{-3/5} (r/r_c)^{-4/3} & r < r_c \\ 1.98 N^{-2} v^{-1} l^{-2} \left(R_M^2 - r^2 \right) & r_c < r < R_M \end{cases}, \tag{1.33}$$

where the first stiff exclusion correspondence the stretched chain described in above and the second part is typical form of excluded volume effect.

Yekta et al. (1995) expected the hydrodynamic radius of the micelle for 34k M_n is about 20nm by intrinsic viscosity with hard-sphere model which is not far from 25nm from dynamic light scattering in the concentration of 1 g/L. With exponent 1/5 in (1.31), the hydrodynamic radius of the micelle is not significantly changed from 20 - 25nm. Collected information about hydrodynamic radius is reported in Meng and Russel (2005), where the radius of the micelle is expected from 10 to 20 which will depend on the molecular weight of polymer and concentration through p. Recall Eq. (1.29), the size ratio between core and micelle with respect to aggregation number becomes

$$\frac{R_M}{R_{core}} \propto p^{-2/15}, \tag{1.34}$$

which suggest that the size change is less than 10% when aggregation number changes factor of 2.

Single Chain Properties

From reported data in Oesterhelt et al. (1999), the Kuhn segment length, l_K, for PEO is about $0.7nm$ where each segment have 1.96 monomers. For the sample used in Suzuki et al. (2012), the expected Kuhn segment number, N_K, is 395, which implies about $14nm$ in the end-to-end distance of chain. This length scale is somehow similar with micelle radius.

1.3.3 Expected System Concentration

Number Density of Micelle and Chains

There are no direct way to measure number density of micelle, ν_m, but the fluoresence studies suggesting expectated value for aggregation number, p, which leads ν_m indirectly (Xu et al. 1996). Note that the p is not accurate and also it is reported only for selected samples. For instance, the sample used in Suzuki et al. (2012) suggest very clean and rich rheological data that will be reported the following sections, without details about

aggregation number. Applying expectated range, the number density of the sample can expected as following way. The number density of chains, ν_c, reported in Suzuki et al. (2012) is $1.8 \times 10^{23}/m^3$. Using previously expected micelle diameter, 20 - 40nm, the expected number density of micelle becomes

$$\nu_m = \frac{\nu_c}{p} = \frac{1}{p}\frac{1.8 \times 10^{-4}}{nm^{-3}} = \frac{1.44}{p}(20nm)^{-3} = \frac{11.52}{p}(40nm)^{-3}. \tag{1.35}$$

With expected value of p from 5 to 20, the processing window for ν_m is between 0.1 and 2.0 per cubic of micelle diameter at the concentration of 1wt% reported in Suzuki et al. (2012).

1.4 Rheological Observations

1.4.1 Linear Viscoelasticity

Dynamic Moduli

It is well-known that the HEUR solution exhibit single-Maxwellian behavior (Annable et al. 1993; Suzuki et al. 2012; Xu et al. 1996) especially when the concentration of HEUR in the solution is dilute regime. From the data of Annable et al. (1993), the dynamic moduli is well fitted with single-Maxwell model:

$$G(t) = G_0 \exp\left(-\frac{t}{\tau}\right), \tag{1.36}$$

where G_0 is the initial and plateau modulus of the model and τ is the dominant relaxation time of the system. More importantly, the time-temperature superposition (TTS) follows Arrhenius type which is one of the sign that the time is kinetically controlled. In detail studies about concentration effect, the accuracy of single Maxwell model is decreased due to concentration Uneyama et al. (2012) and Xu et al. (1996).

Figure 1.3 is dynamic moduli data reproduced from Uneyama et al. (2012) about 40k HEUR polymer in difference concentration where the reference temperature is set with $25C^\circ$. There are fast mode in all the concentration which is believed by chain segment relaxation according to the Uneyama et al. (2012). The measured relaxation time

spectrum (RTS) from the given dynamic moduli, figure 1.3, shows details of time scale contribution into LVE. The dilution of fast relaxation time has been observed especially for the higher concentrations, 5wt% and 10wt%. Note that the RTS is quite sensitive with the given dynamic moduli, for instance, the 2wt% has good separability between fast and slow modes compared with 1wt%. This is due to the dynamic moduli data follows better single-Maxwellian behavior around cross-over frequency. The dominant and slow relaxation time is also diluted due to concentration, but minor.

Uneyama et al. (2012) reports the dependency of platea modulus with respect to polymer concentration:

$$G^{\circ} \propto c^{q} \tag{1.37}$$

where the scaling exponents, q, is about 2.3 in a sparse network where the system exhibit shear thickening, and about 1.8 in higher concentration. This indicates that there are different ways to increasing plateau modulus by added polymer concentration which indirectly suggesting the network structure might be changed.

Time Scales

In the dynamic moduli reported in Suzuki et al. (2012), the frequency higher than cross-over frequency is started to deviate from the single-Maxwellian model. Figure 1.3 (down) is the measured relaxation time spectrum using dynamic moduli data in Uneyama et al. (2012). If the system deserves the only one relaxation time, the spectrum is following Dirac-Delta peak, which is not the case and there are distinguishable two major peaks and the second peak in longer time scale corresponds reciprocal cross-over frequency. The cross-over time peak is following Arrhenius-type time-temperature superposition where the reference temperature set with 25 degree Celsius. In the case of short time scale, however, at least the activation energy has been changed which in consequence three different range of the first peak for 1wt%.

Regarding time scaling exponents reported in Uneyama et al. (2012):

$$\tau_{x} \propto c^{s}, \tag{1.38}$$

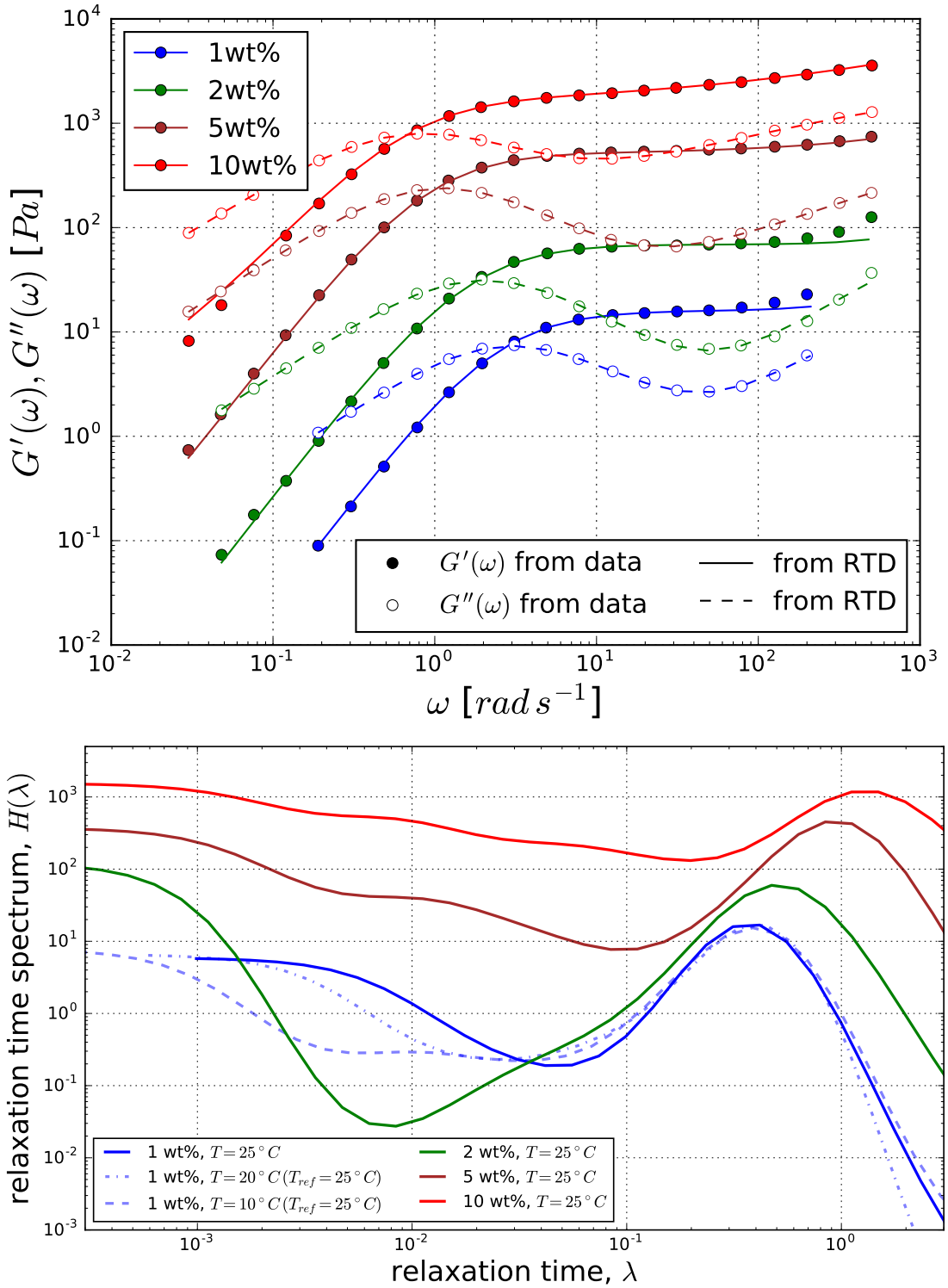

Figure 1.3: Dynamic moduli of HEUR in aqeuous solution reproduced from Uneyama et al. (2012) (up) and calculated relaxation time spectrum (RTS) from dynamic moduli in Uneyama et al. (2012) using fixed-point iteration method Cho and Park (2013) (down).

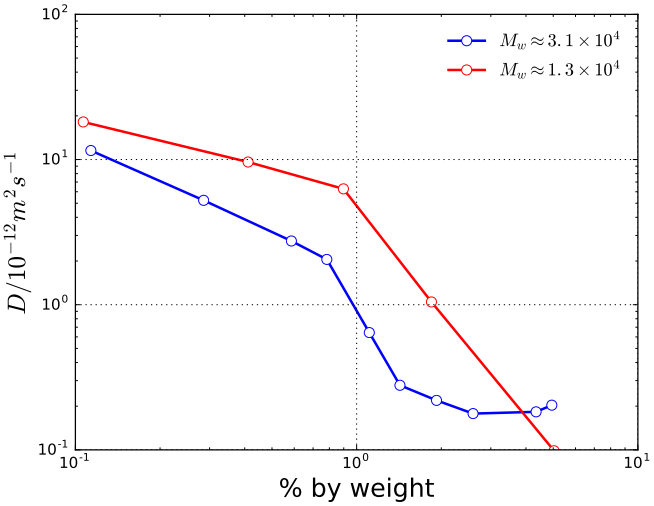

Figure 1.4: The concentration (weight % polymer in D_2O) dependence of the self-diffusion for two different molecular weights. The data is reproduced from Persson et al. (1992).

where s is about 0.63 for sparse network and 0.32 in dense network.

It might be useful to look the different time scales in terms of chain diffusions. Persson et al. (1992) reports self-diffusion coefficient of HEUR molecules using nuclear magnetic resonance (NMR) studies, which is reproduced in figure 1.4. The molecular weight is about 2×10^4 (red) and 3.1×10^4 (blue) which are smaller than the other reference samples (figure 1.5). It is of important to aware that such a diffusion coefficient is molecular point of view, not for center-of-mass diffusion of micelle.

Zero Shear Viscosity

Figure 1.5 reports zero-shear viscosity with the different samples in dilute regime. The polymer structure slightly varied but molecular weight is in similar range except Xu et al. (1996). Note that the sample in Xu et al. (1996) is not perfectly end-capped, and it is about 30% of chains have only one end-capping. Combined with expectation of Uneyama et al. (2012) for G° and τ_x, if the system is not far from single Maxwell, the

zero-shear viscosity have following scaling exponents:

$$\eta_0 \propto c^m, \tag{1.39}$$

where the exponents, $m = s + q$, depends on the concentration and samples, but range around 2.9. It is noteworthy that the all three samples show the similar exponents when ν_C is less than 1 mol/m^3. The details of the change of exponents are reported in Uneyama et al. (2012) where the mechanism is postulated from sparse to a dense network. It is noteworthy that the $\nu_C \approx 0.03$ case, the approximately 2% of chains are active according to the Suzuki et al. (2012). Xu et al. (1996) also reported expected fraction of elastically active bridge is from 1% to 5% in all the range of concentration reported in the figure 1.5. Those expectation is based on the approxiated network theory, Eq. (1.22), which however, is based on the expectation of prefactor as unity with unpublished reference Xu et al. (1996).

1.4.2 Non-Linear Viscoelasticity

Steady-State in Simple Shear

Let x and y be shear and shear gradient directions, and let τ_{xy} be steady-state shear stress. The steady-state viscosity, $\eta(\dot{\gamma})$ in simple shear, and complex viscosity, $\eta^*(\omega)$, in LVE are given by

$$\eta(\dot{\gamma}) = \frac{\tau_{xy}}{\dot{\gamma}} \tag{1.40}$$

$$\eta^*(\omega) = \frac{1}{i\omega} G^*(\omega), \tag{1.41}$$

where τ_{xy} and $\dot{\gamma}$ are steady-state stress and strain rate in simple shear, and $G^*(\omega)$ is the complex modulus in the given frequency, ω. For typical polymers, it is well known that those viscosities are very similar to each other:

$$\eta(\dot{\gamma} = \omega) \approx |\eta^*(\omega)|, \tag{1.42}$$

in the unit of ω in $[rad\, s^{-1}]$ and $\dot{\gamma}$ in $[s^{-1}]$, called Cox-Merz rule (Cox and Merz 1958)

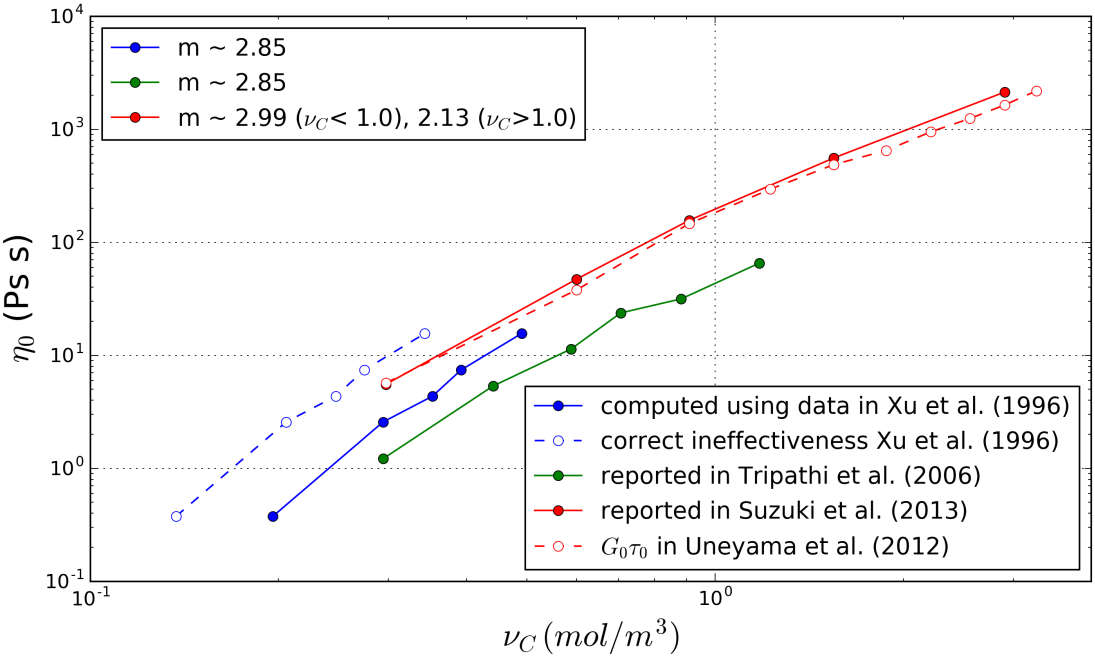

Figure 1.5: Comparison of measured zero-shear viscosity in different samples with $M_n \approx 5.1 \times 10^4$ (Xu et al. 1996) and $M_n \approx 3.4 \times 10^4$ (Tripathi et al. 2006; Uneyama et al. 2012). The reference temperature for samples is 25°C except Xu et al. (1996) in 20°. The inefficiency of end-capping of Xu et al. (1996) is about 0.3.

Interestingly, this is not the case for HEUR solution with the following way. 1.6 is reproduced figure from Xu et al. (1996) where the complex viscosity is calculated by the reported dynamic moduli. First of all, the Cox-Merz rule is not obeyed in the way that an onset of shear thinning is different between viscosity from linear and non-linear responses. Secondly, the shear rate gap of the onset is gradually decreasing with increasing concentration. The dominant relaxation time in LVE has minor dependence with concentration, which is reproduced in the figure with cross-over frequency. The onset of shear thinning in non-linear response and it is not just due to the final slope chain since even the maximum peak shear rate is decreased. Thirdly, the slope of shear thinning is stiffer than -1 in higher concentration regime. The slope in lower concentration is around -1 which is quite stable and the same with the complex viscosity in LVE. Last but not least, the amount of thickening in non-linear response will decrease with concentration. According to the Suzuki et al. (2013), with increasing concentration, the thickening will be disappeared or negligible and eventually the gap between linear and non-linear viscosity becomes minor.

Normal stress difference is also useful to identify anisotropy of stress with the given flow, especially for the first normal stress difference, $N_1 = \tau_{xx} - \tau_{yy}$, is useful to account the difference of normal stress in the shear and the shear gradient directions. Because the normal stress differences commonly depend on the shear rate in a quadratic rule in low shear rate region, the normal stress difference coefficients are frequently used (Larson 1999):

$$\Psi_1(\dot{\gamma}) = \frac{N_1(\dot{\gamma})}{\dot{\gamma}^2}, \qquad \Psi_2(\dot{\gamma}) = \frac{N_2(\dot{\gamma})}{\dot{\gamma}^2}. \tag{1.43}$$

Measuring of the $\Psi_1(\dot{\gamma})$ is quite sensitive depends on the system, but Suzuki et al. (2012) successfully shows with two different apparatus. Unlike the shear thickening in $\eta(\dot{\gamma})$, the Ψ_1 is quite linear up to onset of shear thinning and this onset shear rate is similar to that of $\eta(\dot{\gamma})$. Compiling this results with cessation flow (will cover later), the authors argues about the finite extensible non-lienar elasticity (FENE) might not be the main reason of shear thickening on $\eta(\dot{\gamma})$.

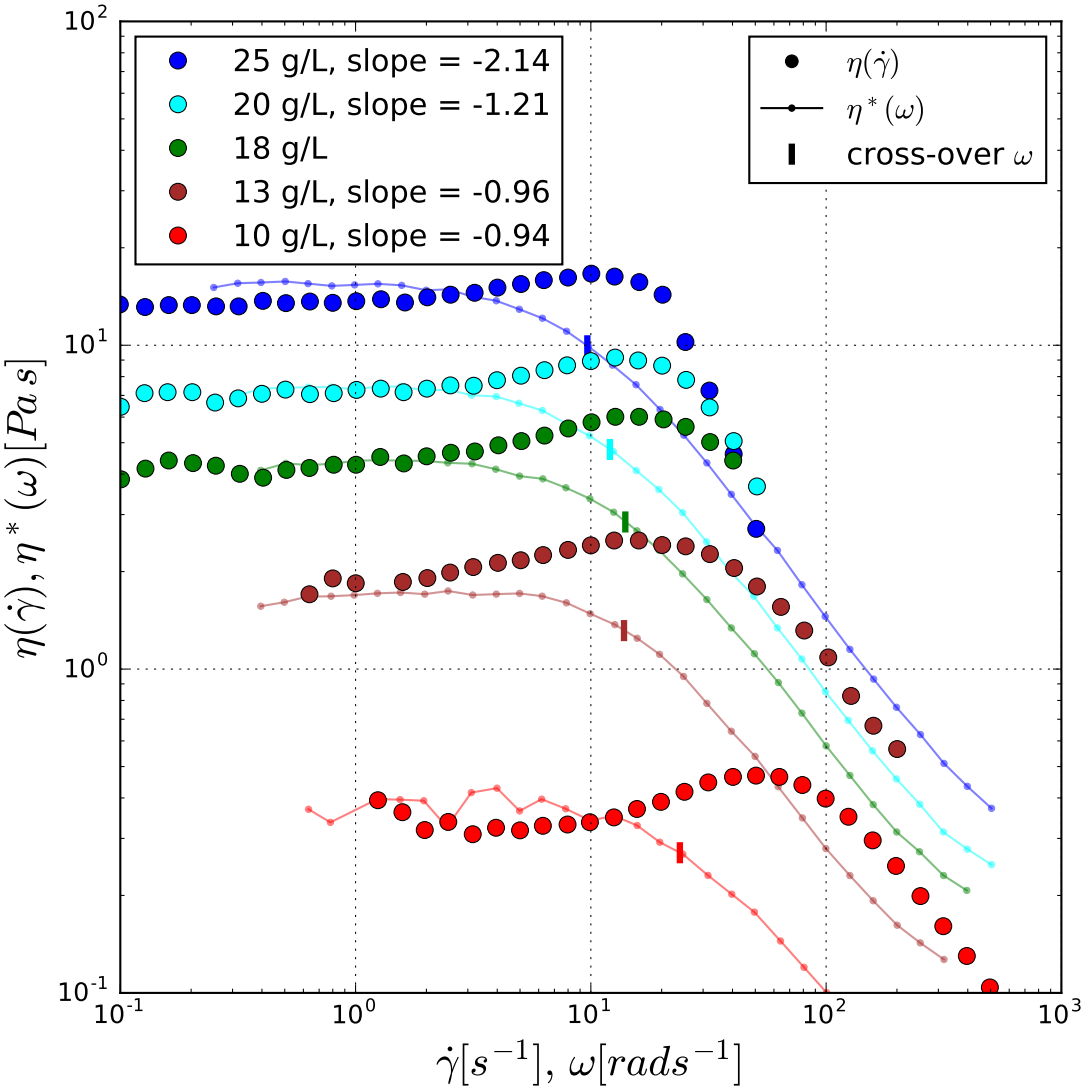

Figure 1.6: Comparison between steady-state viscosity in simple shear and complex viscosity in LVE. Data is reproduced from Xu et al. (1996).

Transient Response

The other interesting phenomena is the strain hardening behaviour observed in transient response in stress growth function, $\eta^+(t;\dot{\gamma})$, and the first normal stress growth function, $\Psi_1^+(t;\dot{\gamma})$:

$$\eta^+(t;\dot{\gamma}) = \frac{1}{\dot{\gamma}}\tau_{xy}^+(t;\dot{\gamma}); \tag{1.44}$$

$$\Psi_1^+(t;\dot{\gamma}) = \frac{1}{\dot{\gamma}^2}N_1^+(t;\dot{\gamma}), \tag{1.45}$$

where the superscript + represent shear rate is increased from time zero, and $\dot{\gamma}$ is the steady-state shear rate. On the same way, we can define stress and normal stress decay functions for cessation of flow as $\eta^-(t;\dot{\gamma})$ and $\Psi_1^-(t;\dot{\gamma})$.

Suzuki et al. (2012) report a rich information about the transient response both of the start-up and after cessation of shear on the different shear rate. The important message on here is that (i) $\dot{\gamma}$ in the linear response regime is following LVE enveloped, and (ii) $\dot{\gamma}$ in the shear thickening regime is following something different LVE envelope with higher $\eta(\dot{\gamma})$ value. Then, (iii) the response starts to experience over-shoot beyond LVE envelope before relax to steady-state when $\dot{\gamma}$ is higher than the onset of shear thinning. The $\Psi_1^+(t;\dot{\gamma})$ only shows the regime (i) and (iii) since $\Psi_1(\dot{\gamma})$ does not show any thickening. It is noteworthy that the stress decay function on the regime (ii) is not distinguishable with the regime (i) except the initial level, $\eta(\dot{\gamma})$. It is questionable why the fast relaxation in the stress decay is not observed if the shear thickening is due to the single-chain stretching. Such a fast relaxation observed in the shear rate in the regime (iii), which is the sign that chain stretching plays a role.

Chapter 2

Methodology

2.1 Model for Simulation

2.1.1 Coarse Grained Micelles and Transient Networks

First of all, the target system is related to lower concentrations in Annable et al. (1993), Suzuki et al. (2012), and Xu et al. (1996) which is classified dilute and (unentangled) semi-dilute regimes (Tripathi et al. 2006). Expected fraction of elastically active bridges are about 2% using Green-Tobolsky theory, Eq. (1.22). Initial scratch for such a system can be started with coarse graining micelles into spherical beads as reported in figure 2.1 where the micelles and core sizes are based on Meng and Russel (2005) and Xu et al. (1996) (see section 1.3). The system in our imagination is schematically reported in figure 2.2 that briefly shows the interactions between micelles in terms of repulsive (using excluded volume effect) and bridge interactions. We decompose evolution equation into micelle diffusion and topological rearrangement, which will be described in later.

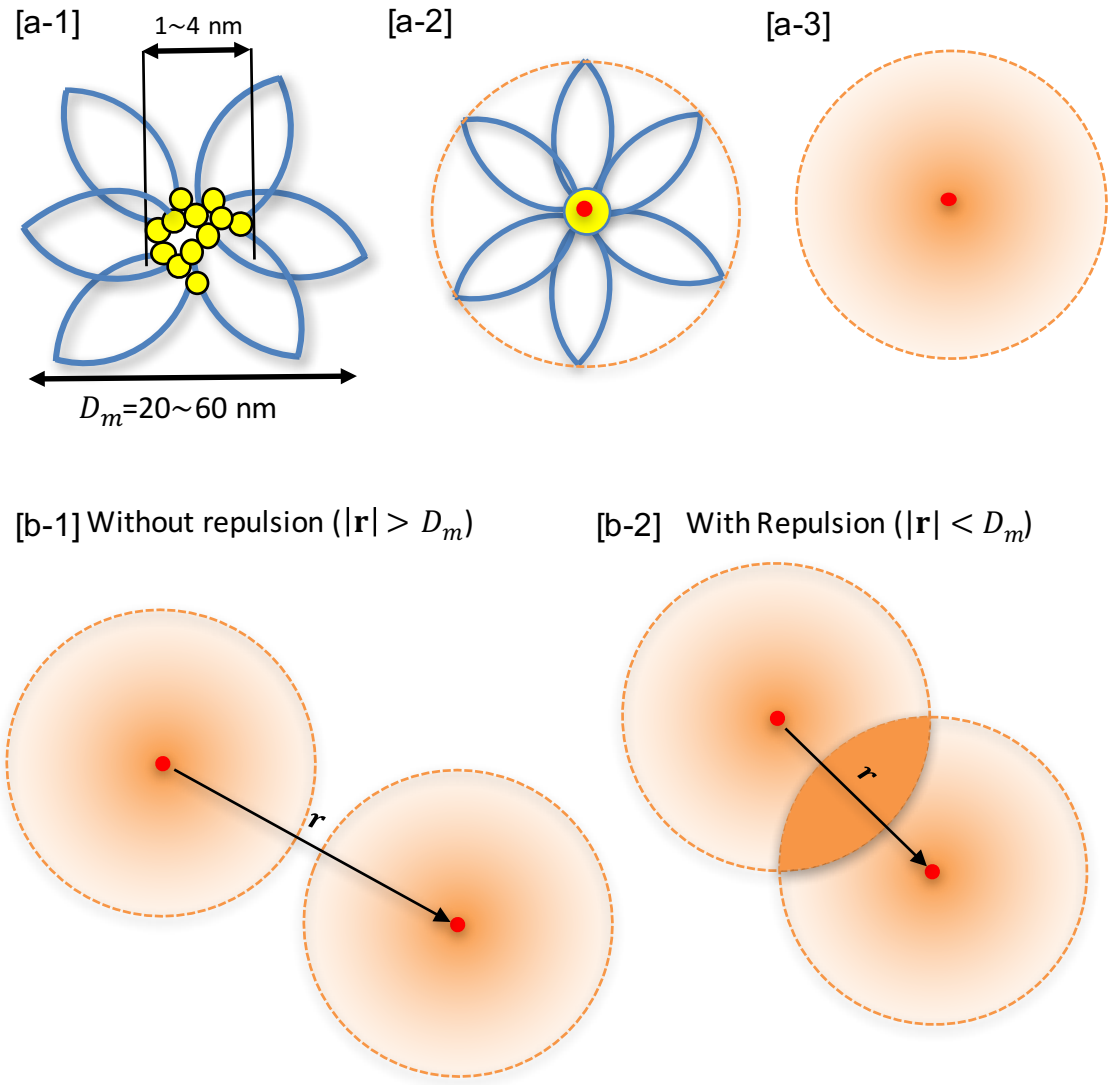

Figure 2.1: Schematic diagram of coarse grained micelle [a] and its repulsive interaction between micelles [b]. Red dots represent a center-of-mass of the given micelle. The simplified micelle version is shown in [a-1] where hydrophobic chain ends are represented by yellow spheres and blue lines for PEO chains. The basic coarse grained micelle used in this simulation is represented in [a-2] using spherical shape for both micelle and its core with diameter of R_0 and l_{cap}, respectively. Note that center-of-mass for micelle (red dot) and that of core are the same. Further simplified micelle is shown in [a-3] with schematic monomer density profile as color gradient.

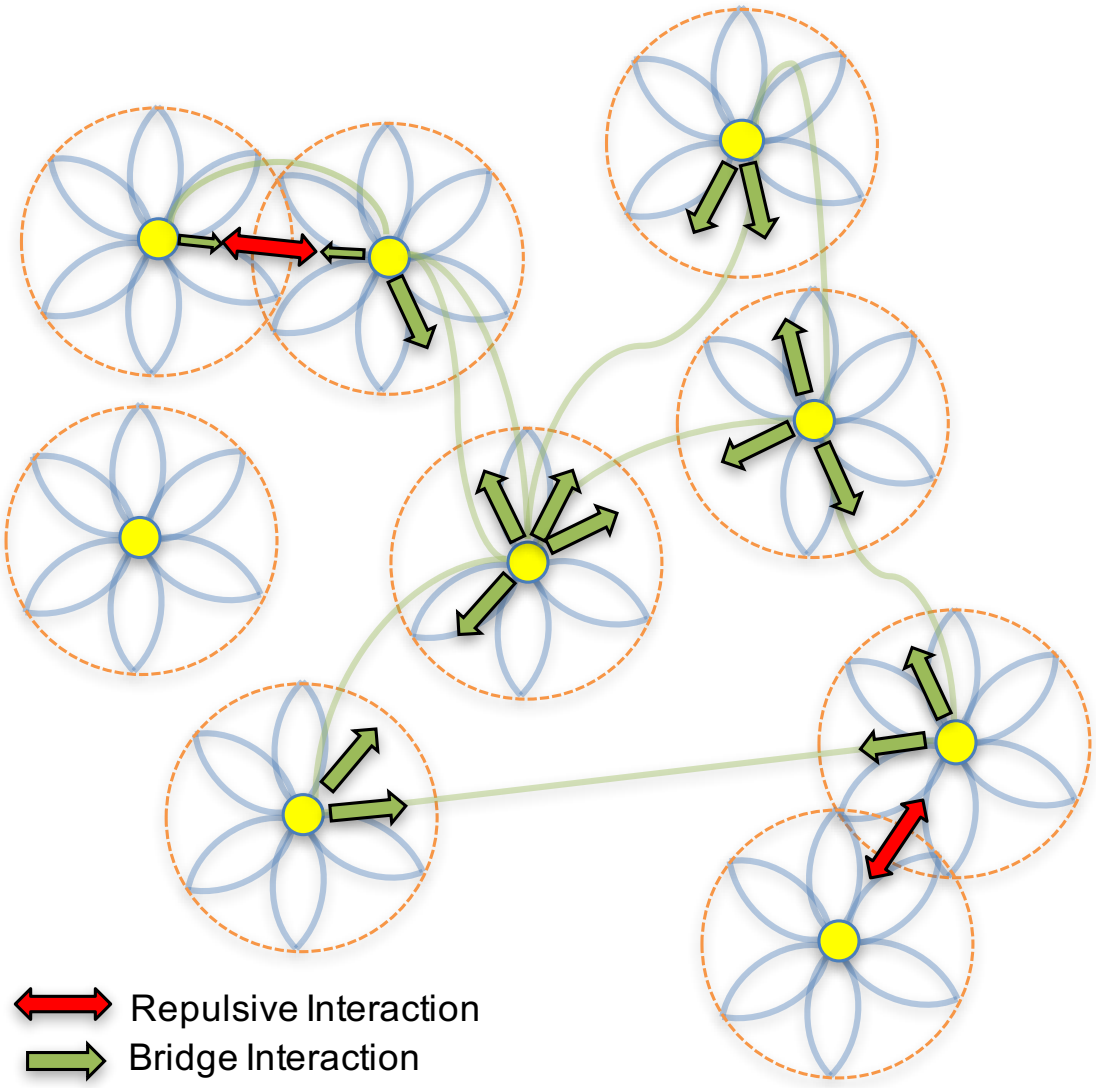

Figure 2.2: Schematic diagram of expected morphology using coarse-grained micelles figure 1.1[b]. The individual micelles are represented in the similar way with figure 2.1[a-2]. Blue and green lines are schematic representation for loop and bridge chains, respectively. Red arrows represent the repulsive interactions, and green arrows represent the bridge interactions.

2.1.2 Time Evolution of Micelle Positions

Brownian Motion

Neglecting interntial effects for Brownian particles, the evolution equation is working on the configurational space:

$$\frac{\partial \mathbf{r}_k}{\partial t} = \frac{1}{\zeta_k}\mathbf{F}^{(ran)}, \tag{2.1}$$

where ζ_k is friction coefficient for k-th particle and $\mathbf{F}^{(ran)}$ is the random force contribution from medium. This stochastic differential equation can be expressed in the way similar with Euler integrator (Greiner et al. 1988), where the time evolutation takes a form of

$$\frac{1}{\zeta}\int_t^{t+dt} \mathbf{F}^{(ran)}(t')dt' \equiv C(t)\left(\mathbf{W}(t+dt) - \mathbf{W}(t)\right) \equiv C(t)\Delta\mathbf{W}(dt), \tag{2.2}$$

where $\mathbf{W}(t)$ denote Wiener process. With Euler-type integrator, each component of the increment for Wiener process follows (Greiner et al. 1988)

$$\Delta W_k(dt) = (12dt)^{1/2}\left(R - 0.5\right), \tag{2.3}$$

where R is random numbers uniformly distributed on the interval (0, 1) and h is the prefactor. Note that the prefactor $\sqrt{12}$ is correction term for variance of R because of $\sigma^2(R) = 12$. The coefficient $C(t)$ is determine through the fluctuation-dissipation theorem (Ermak and McCammon 1978):

$$\langle C(t_p)\Delta W_i(dt)C(t_q)\Delta W_j(dt)\rangle = \delta_{i,j}\delta(t_p - t_q)2\frac{k_B T}{\zeta}dt, \tag{2.4}$$

where $\delta_{i,j}$ is Kroneker-delta and $\delta(t_p - t_q)$ is Dirac-delta functions. Therefore, the coefficient factor becomes constant as

$$C^{(ran)} \equiv C(t) = \sqrt{2\frac{k_B T}{\zeta}}. \tag{2.5}$$

In consequence, the Euler-type integrator leads

$$\mathbf{r}(t+dt) - \mathbf{r}(t) = \sqrt{\frac{2k_B T}{\zeta}}\Delta\mathbf{W}(dt), \tag{2.6}$$

where $\Delta\mathbf{W} = (\Delta W_1, \Delta W_2, \Delta W_3)$.

Configurational Langevin Dynamics

As described in simple Brownian motion, we are neglecting inertial affect which leads the form of configurational Langevin equation. The moment relaxation is much faster than the configurational one while our considerable time scale is even slower than the configurational relaxation time, which makes valid this assumption. Following the suggestion of Ermak and McCammon (1978), we use time step sufficiently small to assume that the configuration of the system does not change during time integration. Note again that we will develop individual stochastic evolution for a topology where the time scale for the topological renewal is at least 10 times larger than the time scale for repulsive Brownian motion. The configurational time evolution given by

$$\frac{\partial \mathbf{r}_i(t)}{\partial t} = \sum_j \frac{\mathbf{D}_{ij}}{k_B T} \cdot \mathbf{F}_j^{nh}(t) + \sum_j \mathbf{C}_{ij} \cdot \mathbf{R}_j, \tag{2.7}$$

where subscript i denote index of micelle where total number of micelles N_p is given by the number density of particles ($\nu_m = N_p/(L_D R_0)^3$ for given box dimension $L_D R_0$), superscript nh means the force only account for non-hydrodynamic interaction part, $\mathbf{D}_{ij}$ is diffusion tensor, and $\mathbf{R}_i$ is random vector that hold the autocorrelation as identity tensor:

$$\langle \mathbf{R}_i(t)\mathbf{R}_j(t')\rangle = \delta_{ij}\delta(t-t')\mathbf{I}. \tag{2.8}$$

Here, the coefficient tensor, $\mathbf{C}_j$ satisfactory

$$\mathbf{D}_{ij} = \sum_{p=1}^{N} \mathbf{C}_{ip}(\{\mathbf{r}\}) \cdot \mathbf{C}_{jq}^T(\{\mathbf{r}\}), \tag{2.9}$$

which can be computed by Cholesky decomposition or iterative way through Chebyshev polynominal approximation (Fixman 1986). Note that Eq. (2.7) valid without hydrodynamic interactions and with hydrodynamic interactions that approximatedly Oseen tensor. The general derivation and details are described in Öttinger (1996).

Diffusion Tensor without Hydrodynamic Interactions

Without hydrodynamic interactions, the suggested configurational Langevin equation have much simpler form because

$$\mathbf{D}_{ij} = D_0\mathbf{I} \Rightarrow \mathbf{C}_{ij} = C^{(ran)}\mathbf{I}, \tag{2.10}$$

where D_0 is self-diffusion coefficient and replaced by k_BT/ζ through Stokes-Einstein limit and $C^{(ran)}$ is the random coefficient described in Eq. (2.5). With these assumptions, the time evolution of position of micelle is described as

$$\frac{\partial \mathbf{r}_k}{\partial t} = \frac{1}{\zeta_k}\left(\sum_{i\in\mathscr{C}_k}\mathbf{F}^{(el)}(\mathbf{r}_i,\mathbf{r}_k) + \sum_i \mathbf{F}^{(rep)}(\mathbf{r}_i,\mathbf{r}_k) + \mathbf{F}^{(ran)}(\mathbf{r}_k)\right), \tag{2.11}$$

where ζ_k is friction coefficient for k-th micelle, $\mathbf{F}^{(el)}$ is force exerted on the chains where the topological information for k-th micelle is given by $\mathscr{C}_k$ which is fixed iduring Langevin time evolution, and $\mathbf{F}^{(rep)}$ is a repulsive force due to micelle exclusion, and $\mathbf{F}^{(ran)}$ is. The frictionc coefficient, ζ_k, will depends on the details of micelle. However, with the assumptions of this studies that will be described in following sections, the individual changes will be ignored with pre-averaged values, and will be replaced by single friction coefficient, ζ, for every micelles.

Throughout this study, the hydrodynamic interaction (HI) is ignored. There are several approximations to implement HI effect in the Langevin equation through the form of Eq. (2.7), and Oseen tensor (Ermak and McCammon 1978) is one of them. The definition and expected effect for a simplified case are accounted in section .

Repulsive Contribution

The repulsive potential on here is not accounted the different exclusion radius reported in Eq. (1.32) based on the segment fraction profile (1.33), where the original theory is derived with the assumption of the highly stretched chain due to higher aggregation number. However, on this study, the only soft-repulsion part is accounted because

of the aggregation number is not that high (from 10 to 20) and because of computational since this part only related with fast dynamics on the system.

Here the construction of repulsive potential rather simplified with the form of:

$$U^{(rep)}(\mathbf{r}_i, \mathbf{r}_k) = k_B T \frac{C_{rep}}{3} \left(1 - \frac{r_{ik}}{R_0}\right)^2 \left(2 + \frac{r_{ik}}{R_0}\right) \tag{2.12}$$

$$\mathbf{F}^{(rep)}(\mathbf{r}_i, \mathbf{r}_k) = -C_{rep} \frac{k_B T}{R_0} \left(1 - \frac{r_{ik}^2}{R_0^2}\right) \hat{\mathbf{r}}_{ik} \quad \text{when } r_{ik} < R_0, \tag{2.13}$$

where $C_{rep} = \langle C_{rep}(\mathbf{r}_k) \rangle_k$ is pre-averaged repulsive coefficient and R_0 is diameter of micelle because the hydrodynamic radius and exclusion size are almost same as (1.32). It must be note that the C_{rep} depends on the p:

$$C_{rep} = C_0 p^k, \tag{2.14}$$

where C_0 is molecular parameters related with chain statistics and the exponent k depends on the interpretation of deformation mechanism. The C_0 depends on the single chain statistics with exponents of 1/5 (Ianniruberto and Marrucci 2015; Meng and Russel 2005), the changes of C_0 due to chains and structure of micelle is ignored throughout the study. In the case of exponent, k, however, there are many suggestion depending on the way of define deformation free energy. Ianniruberto and Marrucci (2015) uses p^2 with simplified uniform monomer density in interaction volume, Sprakel et al. (2009) used $p^{3/2}$ which is related to the free energy of highly deformed case of highly stretched chain (Semenov et al. 1995). In the moderate range, the deformation free energy reported in Semenov et al. (1995) is $1/2 - \nu/3$ where ν is Flory exponents.

Elastic Contribution

The elastic contribution from bridge chains is described by either Gaussian or FENE connector. The Gaussian potential is following the typical forms:

$$U_G(\mathbf{r}_i, \mathbf{r}_k) = \frac{3}{2} k_B T \left(\frac{r_{ik}}{R_c}\right), \tag{2.15}$$

$$\mathbf{F}_G(\mathbf{r}_i, \mathbf{r}_k) = 3 k_B T \frac{\mathbf{r}_{ik}}{R_c^2}. \tag{2.16}$$

The original form of FENE using inverse Langevin function as

$$f = \frac{k_B T}{b} \mathscr{L}^{-1}\left(\frac{r_{ik}}{R_{max}}\right) \tag{2.17}$$

where R_{max} is maximally extendable chain length and the Langevin function is given by

$$\mathscr{L}(x) = \coth(x) - \frac{1}{x}. \tag{2.18}$$

This original form indicate more complicate potential as well (Treloar 1975):

$$U_{FENE}(\mathbf{r}_i, \mathbf{r}_k) = -k_B T N_K \left\{ \log\left[4\pi \sinh\left(\frac{fb}{k_B T}\right)\right] - \log\left(\frac{fb}{k_B T}\right)\right\}. \tag{2.19}$$

Instead of the inverse Langevin function, Warner's approximation is widely used (Warner Jr 1972) which indicates that

$$U_W(\mathbf{r}_i, \mathbf{r}_k) = -\frac{3}{2}\log\left(1 - \frac{r_{ik}^2}{R_{max}^2}\right) \tag{2.20}$$

$$\mathbf{F}_W(\mathbf{r}_i, \mathbf{r}_k) = \left(1 - \frac{r_{ik}^2}{R_{max}^2}\right)^{-1} \mathbf{F}_G(\mathbf{r}_i, \mathbf{r}_k). \tag{2.21}$$

Dimensionality: Micelle Dynamics

The characteristic length scale is set with micelle diameter, R_0. Because of the stiffest potential is repulsive one, the characteristic time scale is set with

$$\tau_R = \frac{\tau_B}{C_{rep}} = \frac{\zeta R_0^2}{k_B T C_{rep}}, \tag{2.22}$$

where τ_R and τ_B indicate repulsive and Brownian time scales. With this approaches, the Euler-type integrator for time evolution becomes

$$\tilde{\mathbf{r}}_k(\tilde{t} + d\tilde{t}) = \tilde{\mathbf{r}}_k(\tilde{t}) + \frac{d\tilde{t}}{C_{rep}} \sum_{i \in \mathscr{C}_k} \tilde{F}^{(el)}(\mathbf{r}_i, \mathbf{r}_k) + \frac{d\tilde{t}}{C_{rep}} \sum_i \tilde{\mathbf{F}}^{(rep)}(\mathbf{r}_i, \mathbf{r}_k) + \sqrt{\frac{2dt}{C_{rep}}} \Delta\mathbf{W}(d\tilde{t}), \tag{2.23}$$

where $t = \tau_R \tilde{t}$ and $\mathbf{F} = \frac{k_B T}{R_0}\tilde{\mathbf{F}}$. It is noteworthy that there are three important length scales: micelle diameter, R_0, to define the effective radius for repulsive potential, chain end-to-end distance, R_c, to define the effect of elasticity due to chain stretching in real unit, and maximally extendable chain length, R_{max}, for FENE connector. Because

repulsive time scale, τ_R, is set with characteristic time, it is natural to set R_0 as the characteristic length. In this sense, the length scales in the system described through the dimensionless (or size ratio) value as

$$R_c = R_0 \tilde{R}_c \tag{2.24}$$

$$R_{max} = R_0 \tilde{R}_{max}. \tag{2.25}$$

Because of $\tilde{R}_c$ is one of the key parameter for the simulation (details will be discussed in chapter 3) for both of micelle dynamics and topological rearrangement. In this regards, here we define new size ratio parameter

$$\alpha = \frac{R_0}{R_c} (= \tilde{R}_c^{-1}), \tag{2.26}$$

where its meaning is simple: the ratio between micelle diameter and chain end-to-end distance. Throughout this study, α, will be used instead of $\tilde{R}_c^{-1}$.

2.1.3 Topological Rearrangement

Probability for Dissociation

Let define the detachment frequency for the chain that attached between i- and j-th micelles:

$$\beta_{ij} = \beta(\mathbf{r}_{ij}) \equiv \beta_0 \exp\left(\frac{F(\mathbf{r}_{ij}) l_{cap}}{k_B T}\right), \tag{2.27}$$

where β_0 is detachment frequency for loop chain: $\Omega \exp(-E/k_B T)$. For the given aggregation number, p, the system have number of chains

$$N_{tot} = \frac{p}{2} N_p \left(\equiv \frac{p}{2} \nu_m \left(L_D R_0\right)^3\right), \tag{2.28}$$

where N_p is a number of micelles in the system. Let the system has N_{tot} chains. For given topological update time step, δt, the expected value for number of detachment becomes

$$N^{\dagger} = N_{tot} \bar{\beta} \delta t, \tag{2.29}$$

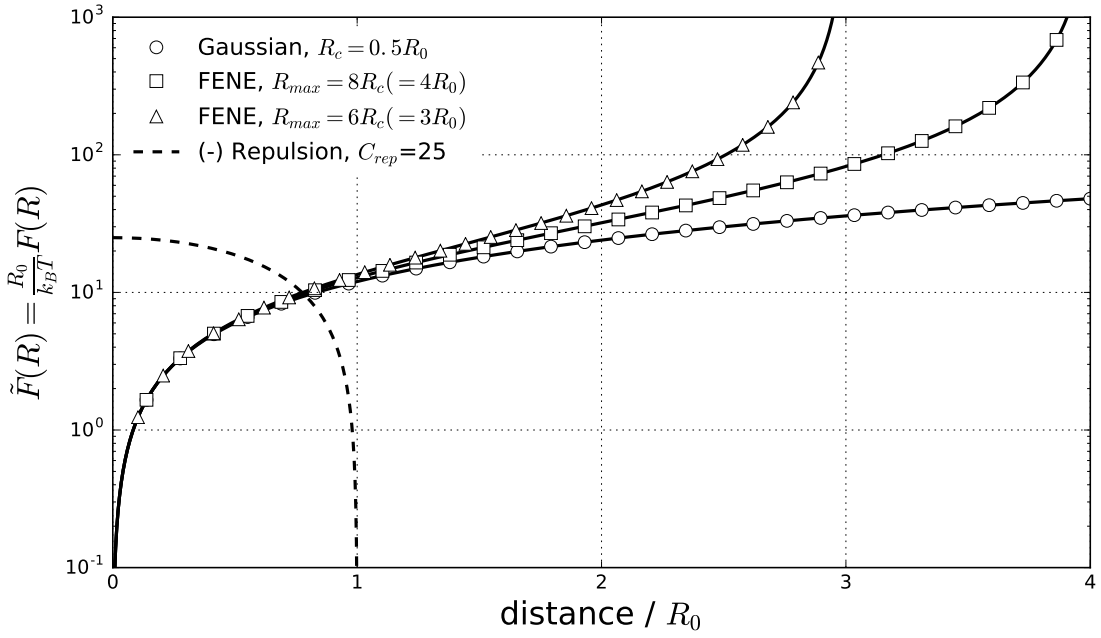

Figure 2.3: Force contributions from repulsive (dashed line) and bridge interactions (symbols) with Gaussian (circle), FENE of $R_{max} = 8R_c$ (square), and FENE of $R_{max} = 6R_c$ (triangle) in the case of α=2.

where $\bar{\beta}$ is number average for the detachment frequency:

$$\bar{\beta} = \frac{1}{N_{tot}} \sum_{i=1}^{N_{tot}} \beta_i. \tag{2.30}$$

Because of $N^{\dagger} \leq N_{tot}$, we have inequality

$$\bar{\beta}\delta t \leq 1. \tag{2.31}$$

Hence, it is appropriate criterion for time increment for topological update by

$$\delta t < \beta_{max}^{-1}, \tag{2.32}$$

where β_{max} is the maximum detachment frequency. If we have cut-off radius for association, r_c, however, the β_{max} can be given by $\beta(r_c)$. Therefore, we have time step criterion

$$dt \leq \delta t < \beta_{max}^{-1} \leq \tau_D. \tag{2.33}$$

On each δt, we select random chain ends in N_{tot} times. The dissociation probability for the selected chain end is given by

$$P_{ij}^{dissoc} = \frac{N^{\dagger}}{N_{tot}} \frac{\beta_{ij}}{\bar{\beta}} = \beta_{ij}\delta t, \tag{2.34}$$

Dissociation Time and Brownian Time

The different between time scale for Langevin dynamic, τ_R, and topological renewal, τ_D, is not clear. Therefore, the two time different is left for aritificial value. One important aspect is with the working hypothesis of simplified Langevin equation and also rheological observations, we interprete τ_D is larger than τ_B, and the gap is at least about 1 decade:

$$\tau_D = R_t \tau_B = R_t C_{rep} \tau_R, \tag{2.35}$$

where the time ratio parameter, $R_t C_{rep}$, is larger than 1.

Dimensionality: Kinetics

Here, we define additional time scale called *loop dissociation time*:

$$\tau_D = \beta_0^{-1} = \Omega^{-1} \exp\left(\frac{E}{k_B T}\right), \tag{2.36}$$

which implies

$$\beta = \frac{1}{\tau_D} \exp(\tilde{F}\tilde{l}_{cap}) \equiv \frac{1}{\tau_D}\tilde{\beta}. \tag{2.37}$$

Therefore, we have

$$P_{ij}^{dissoc} = \beta_{ij}\delta t = \tilde{\beta}_{ij}\delta\tilde{t}\frac{\tau_R}{\tau_D}. \tag{2.38}$$

The criterion for increment of dimensionless time still hold in dimensionless way:

$$d\tilde{t} \leq \delta\tilde{t} \leq \delta\tilde{t}_c \equiv \min\left\{1, \tilde{\beta}(\tilde{r}_c)^{-1}\right\}. \tag{2.39}$$

Note that the minimum time step is given by time step for Langevin equation while the maximum time step is given by topological time or maximum criterion.

Probability map for Association

Once the subjected chain end is detached, it immediately attaches to another micelle. Let say the other chain end is attached to j-th particle, the attachment probability for a micelle is based on the Boltzmann distribution:

$$P_{ij}^{B} = \exp\left(-\frac{U_{ij}}{k_B T}\right), \tag{2.40}$$

where index i denote possible target of micelle that originated from j-th particle. Let cumulative Boltzmann distribution as

$$F'_j(n) = \sum_{i=1}^{n} P_{ij}^{B}, \tag{2.41}$$

where n is up to number of particles, N_p. Obviously, the $F'_j(N_p)$ is sum of all the probability that possibly connect with j-th particle. Then, we have normalized cumulative Boltzmann distribution:

$$F_j(n) = \frac{F'_j(n)}{F'_j(N_p)}. \tag{2.42}$$

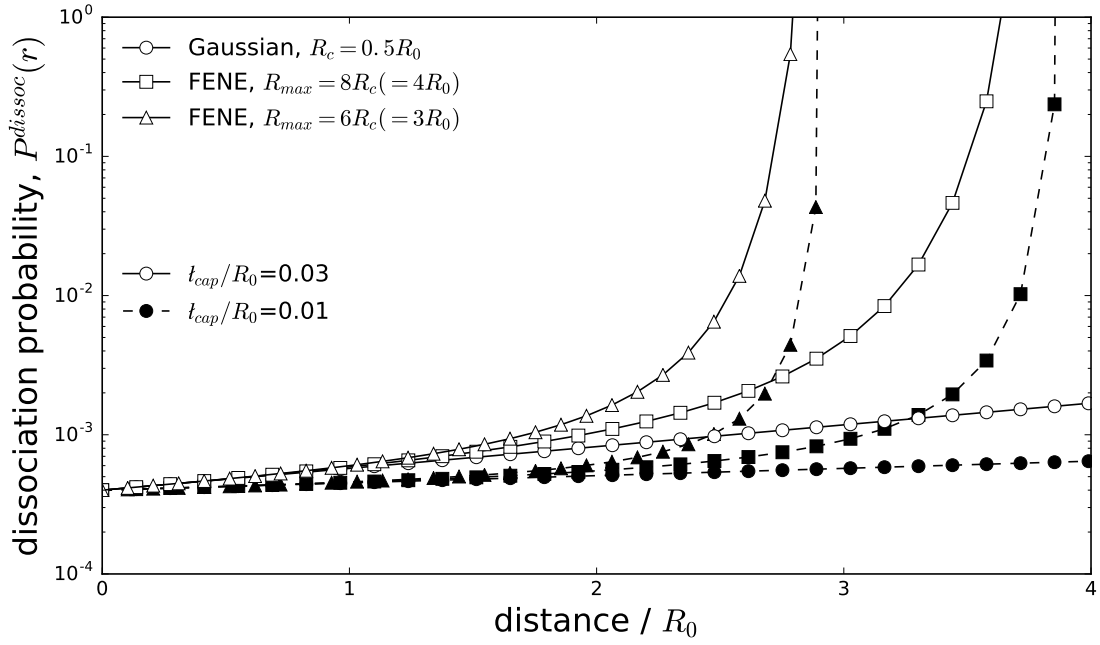

Figure 2.4: Dissociation probability, $P^{dissoc}(r)$, in comparison with the different elastic forces where $l_{cap} = 0.03$ (open symbols) and $l_{cap} = 0.01$ (closed symbols). The other parameters are the same with figure 2.3.

For a given random number, $p \in [0, 1)$, the index function, $\mathscr{I}$, is defined

$$\mathscr{I}(p) = \begin{cases} 1 & \text{if } p < F_j(1) \\ 2 & \text{if } F_j(1) \le p < F_j(2) \\ \vdots & \vdots \\ N_p & \text{if } F_j(N_p - 1) \le p. \end{cases} \tag{2.43}$$

Therefore, for given random number, p, the index of target micelle is given by $\mathscr{I}(p)$. For performance, the cumulating order is sorted by the probability. In addition, the cut-off scheme will be implemented through cell-list method, which will be described on section 8.3.4.

2.2 Technological Report for Simulation

2.2.1 Periodic Boundary Condition

The core of package mainly related with the previously reported information: micellar and topological information. All the individual core package are well separated and verified step-by-step. Section 8 will cover important message for the source code where the whole package becomes larger with its ability to handle SCoPE GRID server, intranode parallelism, multi-layer architecture, input condition parsing system, and supporting sustainability of coding style combined with version control system. The context on here only notes about the practical connection to simulate the suggested time evolutions, so it will lead better understanding for following non-equilibrium simulation section.

The periodic boundary condition (PBC) is popular in the field of simulation when the specific geometrical constraint is not necessary. The PBC keeps the number of particles as its initial values. Basic idea is that the subject box is surrounded by its imaginary boxes, where all the particles in the subjected box are addressed its imaginary box as well. Each time steps, particles travel beyond a boundary of the PBC box will be replaced by its imaginary particle into the main box, called *minimum image convention.*

Minimum Image Convention

Before going further, it is better to mention that the minimum distance between particles in periodic boundary condition (PBC) is using component-wise minimization:

$$r_k^{(m)}(\mathbf{r}_i, \mathbf{r}_j) = \min\left\{x_k(\mathbf{r}_j) - (L_D\mathscr{S} + x_k(\mathbf{r}_i))\right\}, \tag{2.44}$$

where k denote the k-th spatial dimension and L_D is box dimension and the shift set is given by $\mathscr{S} = \{-1, 0, +1\}$, which implies the relative vector of minimum distance from $\mathbf{r}_j$ to $\mathbf{r}_i$ is

$$Crd_\varepsilon\left(\mathbf{r}^{(m)}(\mathbf{r}_i, \mathbf{r}_j)\right) = [r_1(\mathbf{r}_i, \mathbf{r}_j), \cdots, r_{N_D}(\mathbf{r}_i, \mathbf{r}_j)]^T, \tag{2.45}$$

where ε is given basis set. Minimum distance is simply given by Euclidean norm of this relative vector of minimum distance.

Figure 2.5: Schematic diagram for component-wise minimum distance of relative vector.

Let assume that we have 3 particles and the subject particle is labeled as zero, which depicted in figure 2.5. If we started with 0th particle and try to find its the minimum distance with 2nd particle, we have to count its the images of 2nd particle which can be in left or right side. The meaning of real left and right is not important because the axis independence. This is exactly the same meaning with equation 2.44 since

$$d_{ij}^{(m)} = \left|\mathbf{r}^{(m)}(\mathbf{r}_i, \mathbf{r}_j)\right|_2 = \sqrt{\sum_{k=1}^{N_d} (r_k^{(m)}(\mathbf{r}_i, \mathbf{r}_j))^2} \tag{2.46}$$

becomes minimum when each $r_k^{(m)}$ is minimum. Notice that this happens because of the orthonormal basis. *For general basis set, it is of importance that we have to measure component based on reciprocal base vector*, which will not be addressed here since both of equilibrium and non-equilibrium preserve the main box with orthogonality. It is noteworthy that this brute-force algorithm to measure minimum distance is too time consumming that is replaced by RBDIST information where the class definition following in section 8.4.5.

2.2.2 Cell List in Equilibrium Simulation

Cell list is one of popular trick to implement neighbor list with appropriate cut-off distance for a certain interactions between particles. The idea is simple: to divide the PBC box into cells where the size of cells are restricted by effective cut-off length for a given interactions of the system as reported in figure 2.6. It is noteworthy that both of repulsive and bridge interactions are pair-wise potential, Eqs. (2.12) and (2.20), which means the potentials account for relative vectors between micelles. In this sense, we need to compute relative vectors for all the possible pairs of the system which leads the time complexity for Langevin equation, Eq. (2.23), follow $\mathcal{O}(N_p^2)$. With cell-list,

however, the number of necessary pairs for relative vectors are reduced because all the neighbor-cells are counted for measuring, which is represented by blue area in figure 2.6. To be specific, when a micelle is selected for any reason, and need to check relative vector from the selected micelle, we search all the micelles belong to the same cell as the selected micelle (yellow filled cell) and its neighbor cells (blue filled cells), which suggested smaller number of target index compare with whole PBC box. If particles are homogeneously distributed in the all the cell-list, which is true because the size of cells are given by effective cut-off distance of interactions, the time complexit follows $\mathcal{O}(N_{pc}^2)$ where N_{pc} indicates average number of particles inside cells. In this case, the efficiency factor is related to how many cell-division in the system:

$$\varepsilon_C = \left(\frac{N_{sf}}{N_{div}}\right)^{N_{dim}}, \tag{2.47}$$

where N_{sf} is shift factor to find neighbor cell, 3 in this case, and N_{div} is number of cells in one axis. Because we are applying symmetric orthogonal PBC box, simple power of N_{dim} suggest us the efficiency factor. One of simplest case is to use effective cut-off distance as $2R_0$ while box dimension is given by $10R_0$ for each direction that leads the efficiency factor as

$$\varepsilon_C = \left(\frac{3}{5}\right)^3 = 0.216, \tag{2.48}$$

i.e., the computation time becomes 0.216 times of its full computation, roughly.

Figure 2.7 reports about the changes of time efficiency for the different dynamical systems with and without cell-list. The slope of figure 2.7 (in double log plot) indicate the time complexity of the real computational cases. It is easily understood that the repulsive Brownian dynamics (RBD) using Langevin equation without any topological rearrangement. In this sense, the time complexity for RBD without cell-list shows 1.98 which is the same with the asymptotic expectation, $\mathcal{O}(N_p^2)$. Once the cell-list is applied, the exponents changes to 1.08 from 1.98 which is quite dramatic and very ideal examples since RBD uses cutoff distance as R_0 because of repulsive interaction reaches up to R_0, Eq. (2.13). In the case of ATP, however, the slope without cell-list is 1.7 which is even smaller than RBD case. It does not indicate speed of computation, but it indicate the

sensitivity of computation time with respect to N_p. Because topological rearrangement, time complexity of ATP differ from that of RBD. Langevin equation has time complexity of 2, but the topological rearrangement has time complexity of 1 for total number of chains in the PBC box N_{tot}, Eq. (2.28). Since the aggregation number p is set with 5 for in figure 2.7, the topological time complexity only depends on N_p which makes unity. In this sense, the time complexity of 1.7 in figure 2.7 roughly shows that 70% of computational time is used solving Langevin equation. The time analysis record in the code shows that 35% of computational time have been spend for topological rearrangement for the given example, which is consistent with the measured exponent. In this context, about 65% of computational time is affected by cell-list. In this sense, the time complex for ATP with cell-list is 1.46 which is smaller than 1.70 (ATP without cell-list), but much larger than 1.08 (RBD with cell-list).

2.2.3 Simple Shear Flow

So far, the only equilibrium simulation have been addressed. In order to study non-linear response in terms of viscosity and normal stresses, we have to perform non-equilibrium simulation which apply mechanical perturbation of the system, especially for the simple shear. In this study, Lee-Edwards boundary condition has been used Evans and Morriss (2008).

Mechanical Perturbation for Langevin Equation

Consider PBC box as the whole geometry for simplification. The coordination function through deformation of geometry can be described by

$$\mathbf{x}'(\mathbf{x}, t) = \mathbf{x} + \mathbf{u}(\mathbf{x}, t), \tag{2.49}$$

where $\mathbf{u}$ is called displacement vector. For shear flow, the displacement vector becomes $\mathbf{u}(\mathbf{x}, t) = \gamma(t) y \hat{\mathbf{x}}$ where $\gamma = \frac{\partial u_x}{\partial y}$, which means the shear direction is x-axis while the gradient direction is y-axis. For simple shear flow, we have

$$\gamma(t) = \dot{\gamma}_0 t, \tag{2.50}$$

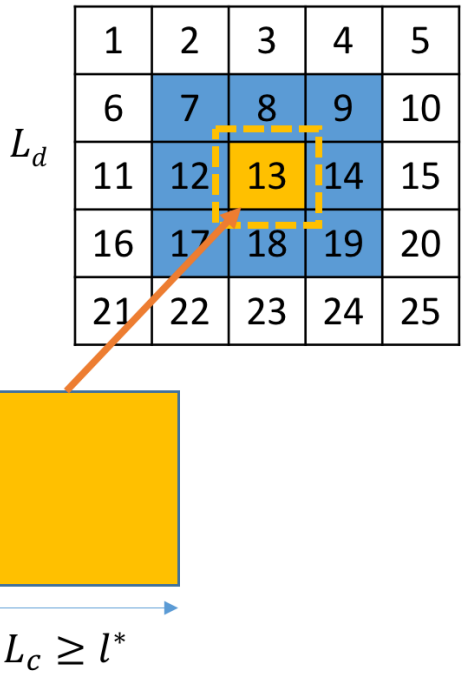

Figure 2.6: Schematic diagram for cell list projected into 2-dimensional plane. L_D represent length of PBC box in one-side (here we use the same length for all the directions) and L_C is length of cells. l^* is the effective distance of the system where it is affected by type of interactions and its parameters. For visualization, yellow cell is the selected cell, and the blue cells are its 2-dimensional neighbor cells.

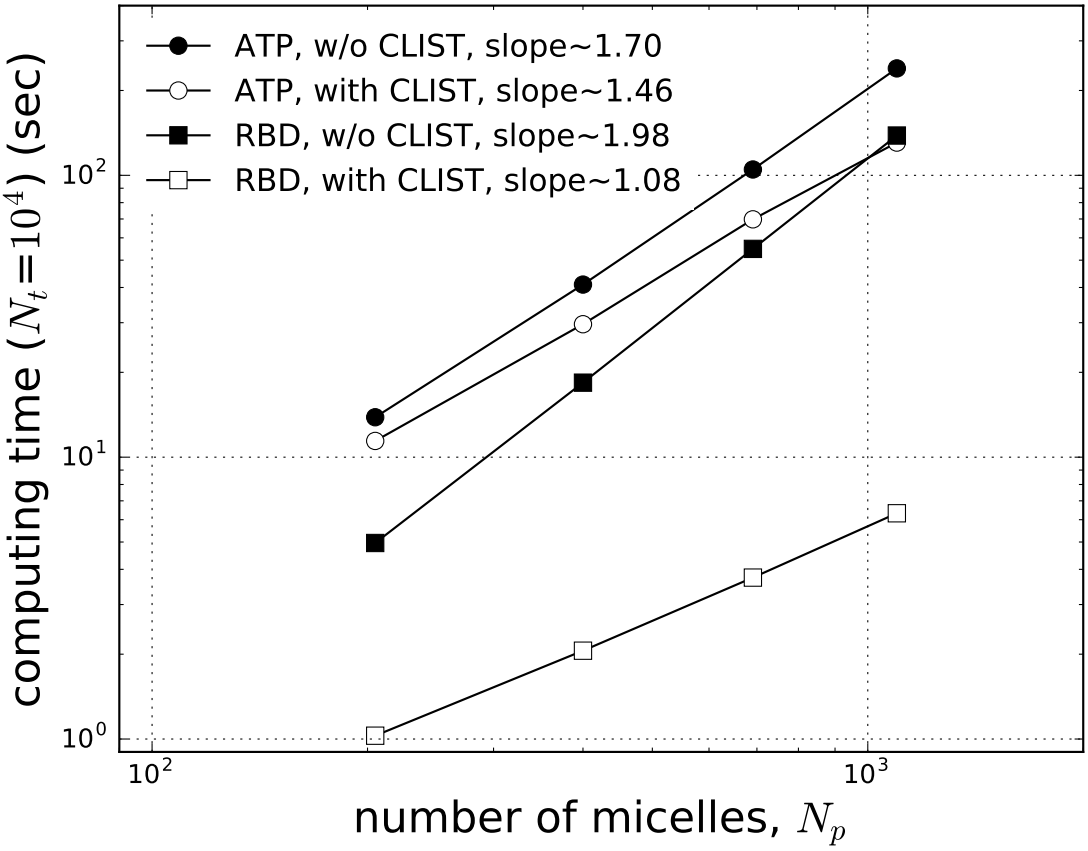

Figure 2.7: Computation time up to 10^4 time steps N_t *vs.* number of micelles in PBC box. Open and closed symbols are with and without cell-list (CLIST), respectively. Blue color represent associating telechelic polymers (ATP) and red color represent repulsive Brownian dynamics (RBD). Note that the number density of micelle ν_m is given by 0.4 in the unit volume (R_0^3). Number of threads keeps a constant as 4.

where $\dot{\gamma}_0$ is given shear rate. Therefore the velocity gradient tensor becomes,

$$\boldsymbol{\kappa} = \nabla \mathbf{v}(\mathbf{x}, t) = \nabla \frac{\partial \mathbf{u}(\mathbf{x}, t)}{\partial t} = \nabla \dot{\gamma}_0 y \hat{\mathbf{x}} = \dot{\gamma}_0 \hat{\mathbf{x}} \hat{\mathbf{y}}. \tag{2.51}$$

Note that rate of strain tensor and rigid body rotation tensor are symmetric and anti-symmetric parts for the velocity gradient tensor, respectively:

$$\boldsymbol{\kappa} = \mathbf{L} + \boldsymbol{\Omega} = \frac{1}{2}\dot{\gamma}_0(\hat{\mathbf{x}}\hat{\mathbf{y}} + \hat{\mathbf{y}}\hat{\mathbf{x}}) + \frac{1}{2}\dot{\gamma}_0(\hat{\mathbf{x}}\hat{\mathbf{y}} - \hat{\mathbf{y}}\hat{\mathbf{x}}). \tag{2.52}$$

With the given $\boldsymbol{\kappa}$, the contribution to the time evolution equation is through

$$dt\boldsymbol{\kappa} \cdot \mathbf{r} = dt\dot{\gamma}_0 y[\mathbf{r}_k]\hat{\mathbf{x}} = d\tilde{t}\tau_R\dot{\gamma}_0 y[\mathbf{r}_k]\hat{\mathbf{x}}, \tag{2.53}$$

which leads the non-dimensional form of time evolution equation as

$$\tilde{\mathbf{r}}_k(\tilde{t} + d\tilde{t}) = \tilde{\mathbf{r}}_k(\tilde{t}) + d\tilde{t}\, Wi_R\, y[\mathbf{r}_k]\hat{\mathbf{x}} + \sqrt{\frac{2dt}{C_{rep}}}\Delta\mathbf{W}(d\tilde{t}) \tag{2.54}$$

$$+ \frac{d\tilde{t}}{C_{rep}} \sum_{i \in \mathscr{C}_k} \tilde{F}^{(el)}(\mathbf{r}_i, \mathbf{r}_k) + \frac{d\tilde{t}}{C_{rep}} \sum_i \tilde{\mathbf{F}}^{(rep)}(\mathbf{r}_i, \mathbf{r}_k), \tag{2.55}$$

with Wiessenberg number based on τ_R: $Wi_R = \dot{\gamma}_0\tau_R$.

2.2.4 Lee-Edwards Boundary Condition

Lee-Edwards sliding bricks representation is one of popular implementation of shear flow into the PBC box (Evans and Morriss 2008).

Coordination Shift through Sliding Bricks Representation

Because of sliding bricks representation, the PBC boundary condition have been changed from directly superposed by $\mathbf{r} = \mathbf{r} \mod L_D$, where L_D is box dimension, to

$$\mathbf{r}' = \mathbf{r} + \dot{\gamma}_0 y \hat{\mathbf{x}} t \mod L_D, \tag{2.56}$$

where plus and minus sign is related with left and right wing on the direction of gradient direction. In dimensionless mannaer, we have

$$\tilde{\mathbf{r}}' = \tilde{\mathbf{r}} + \dot{\gamma}_0\tau_R\tilde{y}\tilde{t}\hat{\mathbf{x}} \mod \tilde{L}_D = \tilde{\mathbf{r}} + \frac{Wi}{CR_t}\tilde{y}\tilde{t}\hat{\mathbf{x}} \left(\equiv \tilde{\mathbf{r}} + Wi_R\tilde{y}\tilde{t}\hat{\mathbf{x}}\right) \mod \tilde{L}_D. \tag{2.57}$$

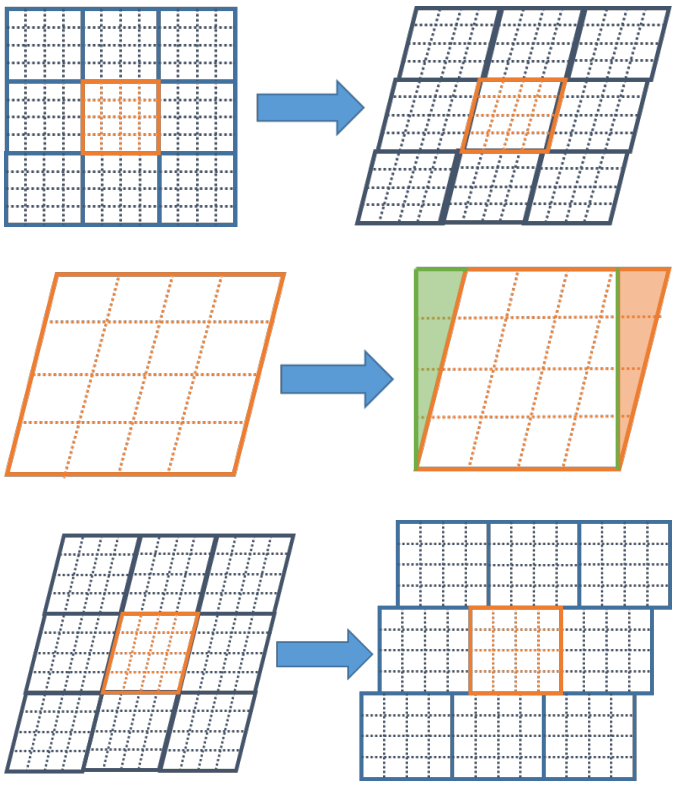

Figure 2.8: Deforming PBC box due to the applied shear flow (top), Remapping to make bricks (middle), and Lee-Edwards sliding bricks representation (bottom).

For simplification, let $Wi_R = \tau_R \dot{\gamma}_0 = \frac{Wi}{CR_t}$ for further approaches. This coordination shift is related with re-mapping from deformed box into bricks (figure 2). In consequence, the overall PBC box with its boundary follows the Lee-Edward sliding bricks representation as figure 3.

Coordination Shift beyond PBC Box

Note that the box shift through the boundary condition (images of PBC box) is given by

$$\tilde{\mathbf{r}}^{\pm\prime} = \tilde{\mathbf{r}}' \pm Wi_R \tilde{L}_D \tilde{t} \hat{\mathbf{x}}, \tag{2.58}$$

where the sign $\pm$ denote the left and right through the direction for gradient of shear. Here, we have to think about the case for shifted factor zero (center). It is of importance

to aware how many PBC box are inter-connected. In the original PBC box scheme, we are using left-right PBC box for each axis, which in consequence, 3^{N_D}, N_D is spatical dimensionality, PBC boxes are subjected to take minimum image convention. With sliding bricks, it still hold since box dimension larger than effective cut-off distance between pair of micelle. Note that the default box dimension is 10 in dimensionless distance while the effective cut-off with $\alpha = 1.5$ is around 2. In consequence, we do not have to adjust shift factor scheme for left-right boxes. The only matter to define the re-mapped box sliding length, $Wi_R\tilde{L}_D\tilde{t} \mod \tilde{L}_D$, is one of the shift factor $\{-1, 0, +1\}$. For instance, if the sliding factor is 2100 while box dimension is 1000, we get re-mapped starting coordinate as 100 (2100%1000), but we cannot assure this starting coordinate is the center of shift factor, 0, because if it beyond half length of box, 500, the appropriate count for shift factor should be +1 instead of 0, so we have replace one right PBC box to one left PBC box. The starting coordination map without consideration of shift factor becomes

$$\tilde{S}_0^{\pm} = \pm Wi_R\tilde{L}_D\tilde{t} \mod \tilde{L}_D. \tag{2.59}$$

Let Z be integer mapping from real number, we can define central mapping function from slide zero to PBC zero:

$$\mathscr{M}_0^{\pm} = \tilde{S}_0^{\pm} + \tilde{L}_D\, Z\left(\frac{2\tilde{S}_0^{\pm}}{\tilde{L}_D}\right). \tag{2.60}$$

Therefore, we have mapping function from slide image to central image:

$$\tilde{\mathbf{r}}^{\pm} = \tilde{\mathbf{r}}' + \mathscr{M}_0^{\pm}\hat{\mathbf{x}} \equiv \mathbf{r}' + \left(\tilde{S}_0^{\pm} + \tilde{L}_D\, Z\left(\frac{2\tilde{S}_0^{\pm}}{\tilde{L}_D}\right)\right)\hat{\mathbf{x}}. \tag{2.61}$$

Minimum Distance between a Pair of Micelles

Underline this aspect, recall the definition for minimum distance in PBC box from the documentation:

$$d_{ij}^{(m)} = \left|\mathbf{r}^{(m)}(\mathbf{r}_i, \mathbf{r}_j)\right|_2 = \sqrt{\sum_{k=1}^{N_d}(r_k^{(m)}(\mathbf{r}_i, \mathbf{r}_j))^2} \tag{2.62}$$

with

$$r_k(\mathbf{r}_i, \mathbf{r}_j) = \min\left\{x_k(\mathbf{r}_j) - (L_D\mathscr{S} + x_k(\mathbf{r}_i))\right\}. \tag{2.63}$$

We can directly replace from old one to one as

$$d_{ij}^{(m)} = |\mathbf{r}^{(m)}(\mathbf{r}_i^{\pm}, \mathbf{r}_j)|_2 \tag{2.64}$$

which is just replace the subjected position vector to shifted image of PBC box.

Constraints by Topological Interactions in Simple Shear Flow

Cell list is powerful to reduce the computation time as described in section 8.3.4. For general cases where potentials are given by secondary interactions without direct connection, cell list can be easily implemented into simple shear flow using increased cell-diameter that account for change of effective distance due to shear flow or using dynamic-offset that allow further index travels of neighbor cells in the PBC boundary (Dobson et al. 2016). In this simulation, however, the bridge chains can be stretched easily and it can be even reach more than half dimension of PBC box (details about chain stretching with respect to applied shear will be reported in later chapters). Since the index sets between micelles (with and without cell list) are used both of neighbor-list identification and relative vector (or distance) information to reduce time and space complexity, such a highly stretched chains increases the effective distance dramatically. For this reason, the cell list functionality is turned off for non-equilibrium simulation, which will be soon updated using decoupled and hierarchical approaches for cell list with index information for interactions and the current connectivity information. Here, the term *decouple* means the index set are separately defined for adjacency list, append 8.1.2, that produce connectivity of the system, which is a key to implement cell list in non-equilibrium simulation. The term *hierarchical approach* means that to decouple two neighbor cells between repulsive potential (the cutoff is naturally given by R_0) and association map (the effective cutoff for α=1.5 case is about $2R_0$), so we have additional efficiency to boost up simulations. In principle, such a hierarchical approach is not related to implement cell list in simple shear, but it will produce additional functionality

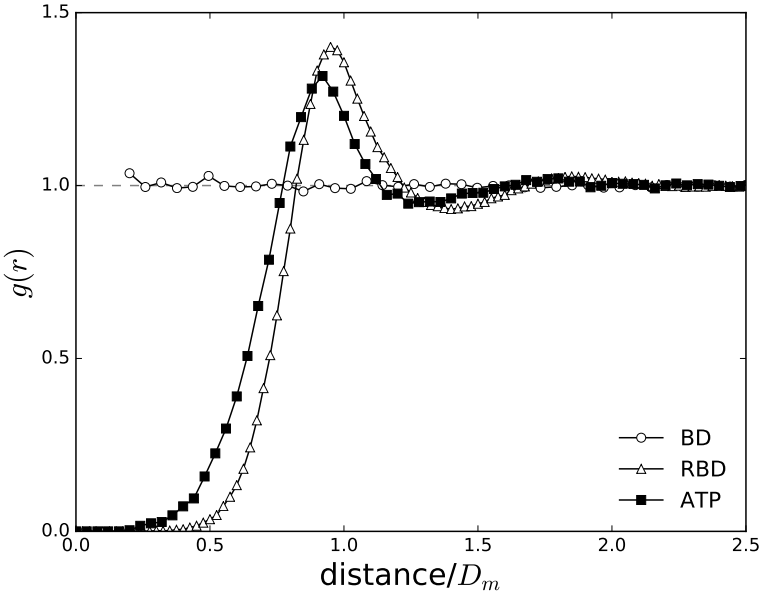

Figure 2.9: Pair-correlation function in the case of pure Brownian dynamics (BD), repulsive Brownian dynamics (RBD), and associating telechelic polymers (ATP). Both RBD and ATP use $C_{rep} = 25$ and $\nu_m R_0^3 = 1$. ATP also uses p=10, τ_D=τ_B, and FENE connectors with $R_c = 2/3R_0$ and $R_{max} = 4.5R_c$.

when we implement dynamic-offset (Dobson et al. 2016) that will increase efficiency factor.

2.3 Effect of Interactions to Static and Dynamical Observables

2.3.1 Micelle Distribution

For quantitative understand of micelle distribution, isotropic pair-correlation function, $g(r)$, is used which is frequently called radial distribution function. Figure 2.9 reports $g(r)$ for the system without any interaction (pure Brownian dynamics; BD), the system with soft repulsion only (repulsive Brownian dynamics; RBD) with $C_{rep} = 25$ and a dimensionless micelle number density $\tilde{\nu}_m = 1$, and the system with both repulsive

and bridge interactions (associating telechelic polymers; ATP) with the other parameters set to $R_c = 2/3R_0$, $l_{cap} = 0.01R_0$, $R_{max} = 4.5R_c$, and $\tau_D = \tau_B$.

The pair-correlation function in the pure BD case is uniform and equal to unity because all the micelles are spatially uncorrelated. In the RBD case, repulsive interactions lower the spatial correlation in the micelle overlap region. At this concentration (comparable to the overlap concentration), the first peak of $g(r)$ is located at distances comparable to the micelle size. In the case of the ATP system, bridge chains introduce a short-range attractive interaction that decreases both the distance and the intensity of the first peak. Since both the repulsive and the bridge-induced elastic interactions acts on distances of the order of the micelle size (in the case of bridges of length comparable to the micelle size), the micelles become spatially uncorrelated at distances larger than a few micelle sizes. This is the reason why the RBD and ATP pair correlation functions in figure 2.9 approach unity at distance less than $2R_0$.

It is noteworthy when we increasing τ_D from τ_B, $g(r)$ is the same as figure 2.9 (no data shown). This indicate that there are no static changes in terms of micelle distribution when $\tau_D \geq \tau_B$.

2.3.2 Diffusivity

Diffusion coefficient can be measured using averaged mean-square-displacement (MSD) of center-of-mass of micelles as

$$\lim_{t\to\infty} \langle (\mathbf{r}_k(t) - \mathbf{r}(0)^2 \rangle_k = 2N_D D t, \tag{2.65}$$

where N_D is spatial dimensionality (3 in this case).

Figure 2.10 report MSD (divided by time) for BD, RBD, and ATP systems. In the purely BD case, diffusion is Fickian at all times, with a dimensionless self-diffusion coefficient equal to unity, as expected. In both the RBD and ATP systems, the curves have a sigmoidal shape, with a purely Brownian behavior at short time ($t \ll \tau_{rep}$). In the RBD case, there is a sub-diffusive behavior in the range of $\tau_{rep} < t < \tau_B$, and then

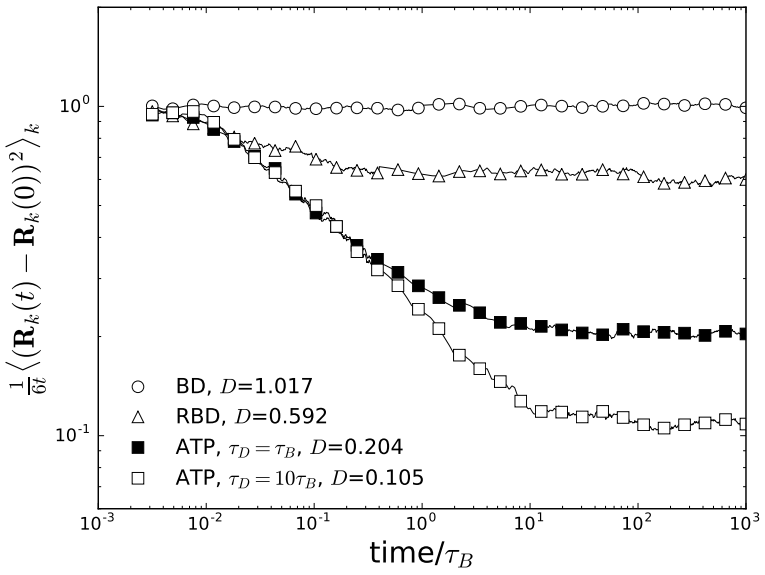

Figure 2.10: Mean-square-displacement of micelles divided by $6t$ in the case of pure Brownian dynamics (BD), repulsive Brownian dynamics (RBD), and associating telechelic polymers (ATP). For ATP, τ_D are set with τ_B or $10\tau_B$. All the other parameters are the same with figure 2.9.

a slower, Fickian diffusion at $t > \tau_B$. Note that

$$\tau_B = \frac{\zeta R_0^2}{k_B T} = \frac{R_0^2}{D}, \tag{2.66}$$

where R_0 is characteristic length scale of the system.

Such a slowing down with respect to the pure BD case is due to the repulsive interactions hindering the displacement of the micelle in the direction where other micelles are already positioned. Note that the slowing down is isotropic since the micelles are homogeneously distributed in space, and it is expected to be stronger with increasing ν_m. In the case of ATP, the bridge-induced attractive interaction introduces additional constraints to the micelle dynamics, thus inducing a further slowing down of the micelle diffusion. The latter phenomenon obviously depends on the strength of the associating interactions. There are two caes of τ_D is given: τ_B and $10\tau_B$. Unlike static properties, the dynamics is affected by loop-dissociation time. The diffusion coefficient becomes half when τ_D becomes 10 times larger, which inversely, the time scale of micelle diffusion for $\tau_D = 10\tau_B$ is twice larger than that of $\tau_D = \tau_B$ case.

2.3.3 Stress Tensor

The stress on the simulation is defined in the way of virial stress where the original derivation following some thermodynamic treatment in the section. There are controversial aspect about the definition for virial stress (Zhou 2003), but here we only account for the configurational space, which makes simple as the following form:

$$\boldsymbol{\tau} = \frac{1}{V} \sum_i \sum_{j>i} \mathbf{R}_{ij} \mathbf{F}_{ij}, \tag{2.67}$$

where the i and j indicate the index for micelles. Indeed, the virial stress itself is collected variable, so it is computed during simulation time rather than post-processing. Note that such a virial stress tensor is identical Kramer expression of polymer solution (Bird et al. 1987) where the solvent contribution is simply described by random force contributions.

2.3.4 Relaxation Modulus

Green-Kubo Relation and Viscosity

With Green-Kubo relation, the relaxation modulus and zero-shear viscosity are given by

$$G(t) = \frac{V}{k_B T}\langle \tau_{xy}(t)\tau_{xy}(0)\rangle; \tag{2.68}$$

$$\eta_0 = \lim_{t\to\infty}\int_0^t G(t)dt, \tag{2.69}$$

where τ_{xy} is shear components of virial stress tensor, $\boldsymbol{\tau}$. Note that there are no preferable direction in the equilibrium simulation, which makes all the pair xy, xz, and yz valids for the definition of shear stress.

Calculation of relaxation modulus from equilibrium simulation, however, is not an easy task because of time complexity and system noisy. Hence, we apply following sequences to solve the problems.First of all, Fast Fourier-Transform (FFT) is used in order to archive time complexity $\mathscr{O}(N_t)$ (section 9.1.1). Note that the time complexity of calculating cross-correlation in direct way is $\mathscr{O}(N_t^2)$ where N_t is number of time series in record. Second, we take not only directional average (say xy, xz, and yz components for stress tensor), but also autocorrelation of normal stress differences (section 9.1.2) following the properties of isotropic fluid (Daivis and Evans 1994). Third, we take time average underline ergodic hypothesis (the effective way to averaging blocks is described in section 9.1.3). Last, we runs multiple samples in the same condition using different random numbers (section 9.1.3). Basically, it is the same procedure of time average, but the GRID server allows to reduce computational time in this way. Details are described in section 9.1.

Through this technical approach, we can improve statistics of stress autocorrelation which makes a lot of advantages to measure rheological observable, especially for zero-shear viscosity, η_0. The reduced noisy still affect when normalized relaxation modulus $G(t)/G(0)$ is about 10^{-2}. Hence, we are using viscosity function

$$\eta(t) = \int_0^t G(t')dt',, \tag{2.70}$$

which is identical to η_0 when $t \to \infty$. We decide cut-off time scale based on change of variables as reported in section 9.1.4, then ignore the noisy $G(t)$ when time is beyond it.

Once $G(t)$ is determined, the complex modulus and viscosity are given by:

$$G^*(\omega) = i\omega \int_0^\infty G(t) \exp(-i\omega t) dt \tag{2.71}$$

$$\eta^*(\omega) = \frac{G^*(\omega)}{i\omega}. \tag{2.72}$$

The direction conversion through Fourier transform, however, suffers from the noise of relaxation modulus. Note again that the used $G(t)$ must be cut-out in noisy part; otherwise, linear regime will drift up due to the noisy.

Dimensions

Using the basic length scale in section 7.2.2, the virial stress can be non-dimensionalized thorugh the form of

$$\boldsymbol{\tau} = \frac{k_B T}{R_0^3} \frac{1}{\tilde{V}} \tilde{R}\tilde{F}. \tag{2.73}$$

Combined with Eq. (2.68), the dimensionality of $\boldsymbol{\tau}$ implies

$$G(t) = \frac{k_B T}{R_0^3} \langle \tilde{\tau}_{xy}(t) \tilde{\tau}_{xy}(0) \rangle_t \equiv \frac{k_B T}{R_0^3} \tilde{G}(0), \tag{2.74}$$

where the dimensional factor strongly depends on the diameter of micelle, R_0. In this context, the dimensionality for the viscosity function, Eq. (2.70) becomes

$$\eta(t) = \frac{k_B T}{R_0^3} \tau_R \int_0^t \tilde{G}(\tilde{t}) d\tilde{t}, \tag{2.75}$$

where $t = \tau_R \tilde{t}$.

Contribution of Random Force

The shear stress can be decoupled into each force contributions, but the correlation with random shear stress is always uncorrelated because of the definition of random:

$$Corr[\tau_{xy}^{(ran)}, \tau_{xy}^{(*)}](t) = Corr[\tau_{xy}^{(*)}, \tau_{xy}^{(ran)}](t) = 0, \tag{2.76}$$

which suggesting that the random contribution can be ignored for relxation modulus.

Contributions of Repulsive and Bridge Interactions

If the system have more than two force contributions betweem particles, the stress autocorrelation suggests the components-wise cross-correlations. Let think about the suggested model for associating telechelic polymers, the repulsive and elastic potential acts individually:

$$Corr[\tau_{xy}, \tau_{xy}](t) = Corr[\tau_{xy}^{(rep)}, \tau_{xy}^{(rep)}](t) + Corr[\tau_{xy}^{(rep)}, \tau_{xy}^{(el)}](t) \tag{2.77}$$

$$+ Corr[\tau_{xy}^{(el)}, \tau_{xy}^{(el)}](t) + Corr[\tau_{xy}^{(el)}, \tau_{xy}^{(rep)}](t), \tag{2.78}$$

simply

$$Corr[\tau_{xy}, \tau_{xy}](t) = Corr[\tau_{xy}^{(rep)}, \tau_{xy}](t) + Corr[\tau_{xy}^{(el)}, \tau_{xy}](t) \tag{2.79}$$

$$= Corr[\tau_{xy}, \tau_{xy}^{(rep)}](t) + Corr[\tau_{xy}, \tau_{xy}^{(el)}](t). \tag{2.80}$$

Unlike convolution, the correlation is not commutative in general (Borsellino and Poggio 1973):

$$Corr[A, B] \neq Corr[B, A], \tag{2.81}$$

except A and B are Hermitan (even function for real valued function). Without lose of generality, we can define the repulsive and elastic contribution as its parts:

$$G^{(el)}(t) = \frac{V}{k_B} Corr[\tau_{xy}^{(el)}, \tau_{xy}](t) \tag{2.82}$$

$$G^{(rep)}(t) = \frac{V}{k_B} Corr[\tau_{xy}^{(rep)}, \tau_{xy}](t), \tag{2.83}$$

which leads the zero-shear viscosity into the component-wise contributions:

$$\eta_0 = \int_0^\infty G(t)dt = \int_0^\infty G^{(el)}(t) + G^{(rep)}\, dt = \eta_0^{(el)} + \eta_0^{(rep)}. \tag{2.84}$$

Dummbell Model

Before going further, it will be useful to report a simulation results for dumbbell. Dumbbell model accounts the permanent connector between a pair of micelles, where all the micelles have one such a connector.Typical description for Dumbbell model is based

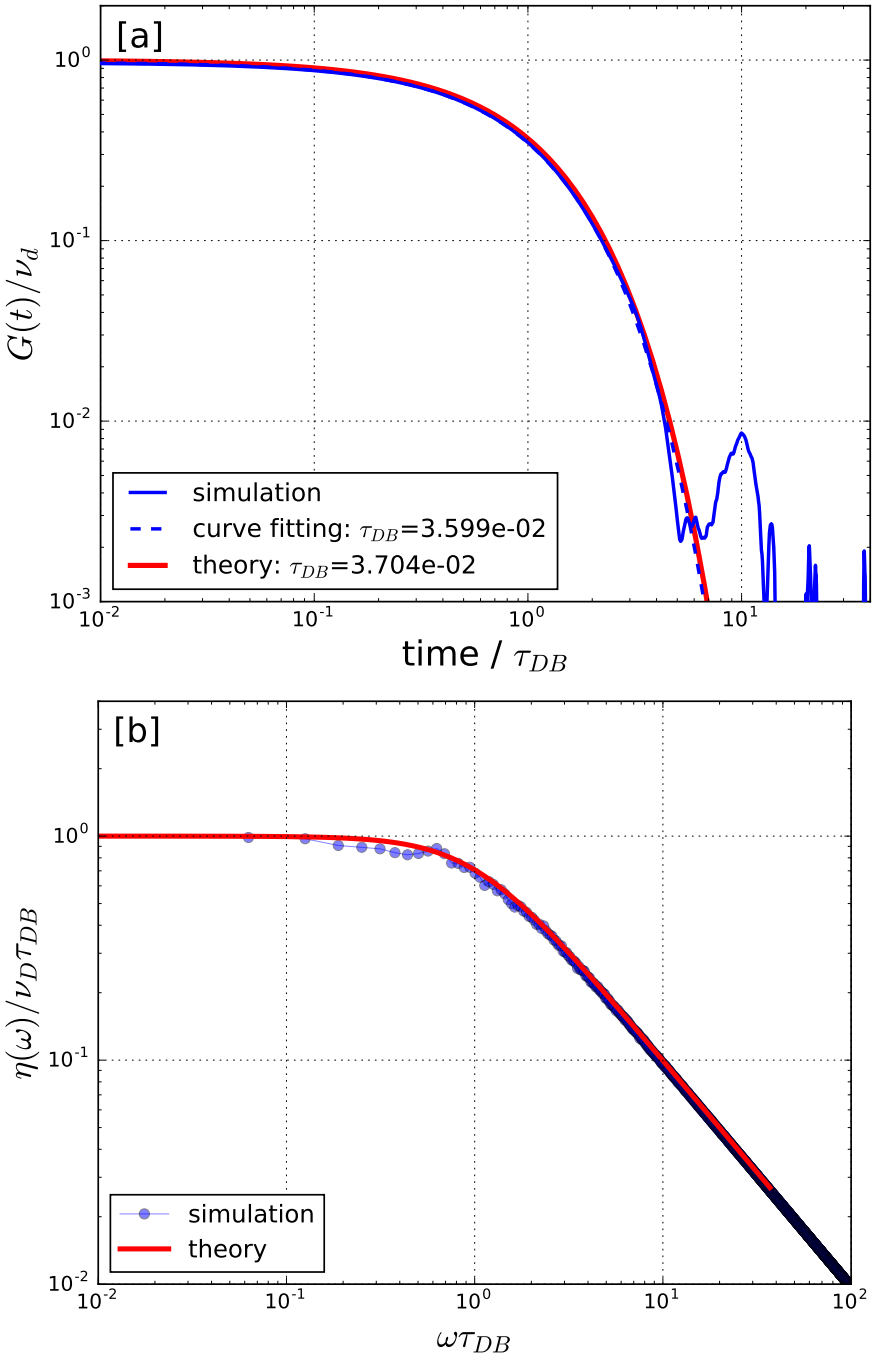

Figure 2.11: Normalized relaxation modulus [a] and normalized complex viscosity [b] in comparison with theoretical expectation of dumbbell model.

on the stochastic time evolution for connector vector where the detailed for positions of micelle is not necessary to specify through the form of

$$d\mathbf{Q} = \langle \boldsymbol{\kappa} \cdot \mathbf{Q} \rangle \, dt - \frac{2}{\zeta} F(\mathbf{Q}) dt + \sqrt{\frac{4k_B T}{\zeta}} \Delta \mathbf{W}(dt), \tag{2.85}$$

where $\mathbf{Q}$ is connector vector and the F is connector force. The remains are identical for the Langevin equation described in Eq. (2.23). The minus sign on the force contribution is due to the fact that the direction of force exerted on dumbbell is opposite to the relative vector, $\mathbf{Q}$. Note that the given stochastic equation is collected variable, so the results are given by distribution function. Hence, it is appropriate to decouple individual contribution from the particle where each particle have one connector with other particle. Let $\mathbf{Q}_{ij} = \mathbf{r}_j - \mathbf{r}_i$, the individual time evolutions can easily described as following:

$$d\mathbf{r}_i = \boldsymbol{\kappa} \cdot \mathbf{r}_i dt + \frac{1}{\zeta} F(\mathbf{r}_i) + \sqrt{\frac{2k_B T}{\zeta}} \Delta \mathbf{W}_i(dt). \tag{2.86}$$

Therefore, the evolution equation for connector vector becomes

$$d\mathbf{Q}_{ij} = d\mathbf{r}_j - d\mathbf{r}_i. \tag{2.87}$$

Note that

$$\Delta \mathbf{W}_j(dt) - \Delta \mathbf{W}_i(dt) = \sqrt{12dt} R'_{ij} = \sqrt{2 \times 12dt} \left(R_{ij} - 0.5 \right), \tag{2.88}$$

where R'_{ij} is uniform distribution from -1 to 1, which indicate the prefactor $\sqrt{2}$ of the same uniform distribution used in Eq. (2.23), R, from -0.5 to 0.5. Because force can be expressed by

$$\mathbf{F}(\mathbf{r}_j) - \mathbf{F}(\mathbf{r}_i) = F_j \hat{\mathbf{r}}_j - F_i \hat{\mathbf{r}}_i = (F_j + F_i) \left(\hat{\mathbf{r}}_j - \hat{\mathbf{r}}_i \right) = 2F_{ij} \hat{\mathbf{Q}}_{ij}, \tag{2.89}$$

the final form is exactly the same with the time evolution equation for connector vector, Eq. (2.85). In this approach, it is easily understood the characteristic time of the system is given by

$$\tau_{DB} = \frac{\tau_B}{12\alpha^2}, \tag{2.90}$$

where $3\alpha^2$ is a spring constant ($\alpha = 1.5$ for this test).

Figure 2.11 (top) shows that the normalized relaxation modulus with its theoretical expectation. Because dumbbell model follows single element Maxwell, the plateau modulus, G°, which is the same with $G(0)$ in this case, is directly related to the number density of dumbbell. The measured characteristic time is the same with theoretical expectation, Eq. (2.90), which leads the possible connection with complex viscosity reported in figure 2.11 (down). In dumbbell model, the zero-shear viscosity is analytically expressed as $\eta_0 = \nu_{DB}\tau_{DB}$ and the complex modulus is easily given by

$$G^*(\omega) = \nu_{DB}\frac{i\omega\tau_{DB}}{1+i\omega\tau_{DB}}, \tag{2.91}$$

which directly gave us the complex viscosity. The simulation results are very consistent with the theoretical expectation, but the noise is observed when $G(t)/G(0)$ is lesser than 0.01 even though the relaxation modulus is in result of average over 100 time blocks.

Repulsive Brownian Motion

The relaxation modulus of repulsive brownian follows stretched exponent:

$$G(t) = G_0 \exp\left(-(t/\tau)^\beta\right), \tag{2.92}$$

where τ is characteristic time and β is related to the dilution exponents from unity. Figure 2.12 shows that $G(t)$ of RBD is well fitted with stretched-exponential form where $\tau \approx 0.3\tau_{rep}$ and $\beta \approx 0.8$.

Associating Telechelic Polymers

Finally, we are accounting for both of repulsive and bridge interactions with individual topological rearrangement. In figure 2.12, ATP systems do not show neither a single-mode relaxation (DUB) nor stretched-exponential (RBD), mostly because of the competition among dynamics of repulsion, connectors, and topological rearrangement. The relaxation occurs more slowly due to the association dynamics, the more so the larger is τ_D.

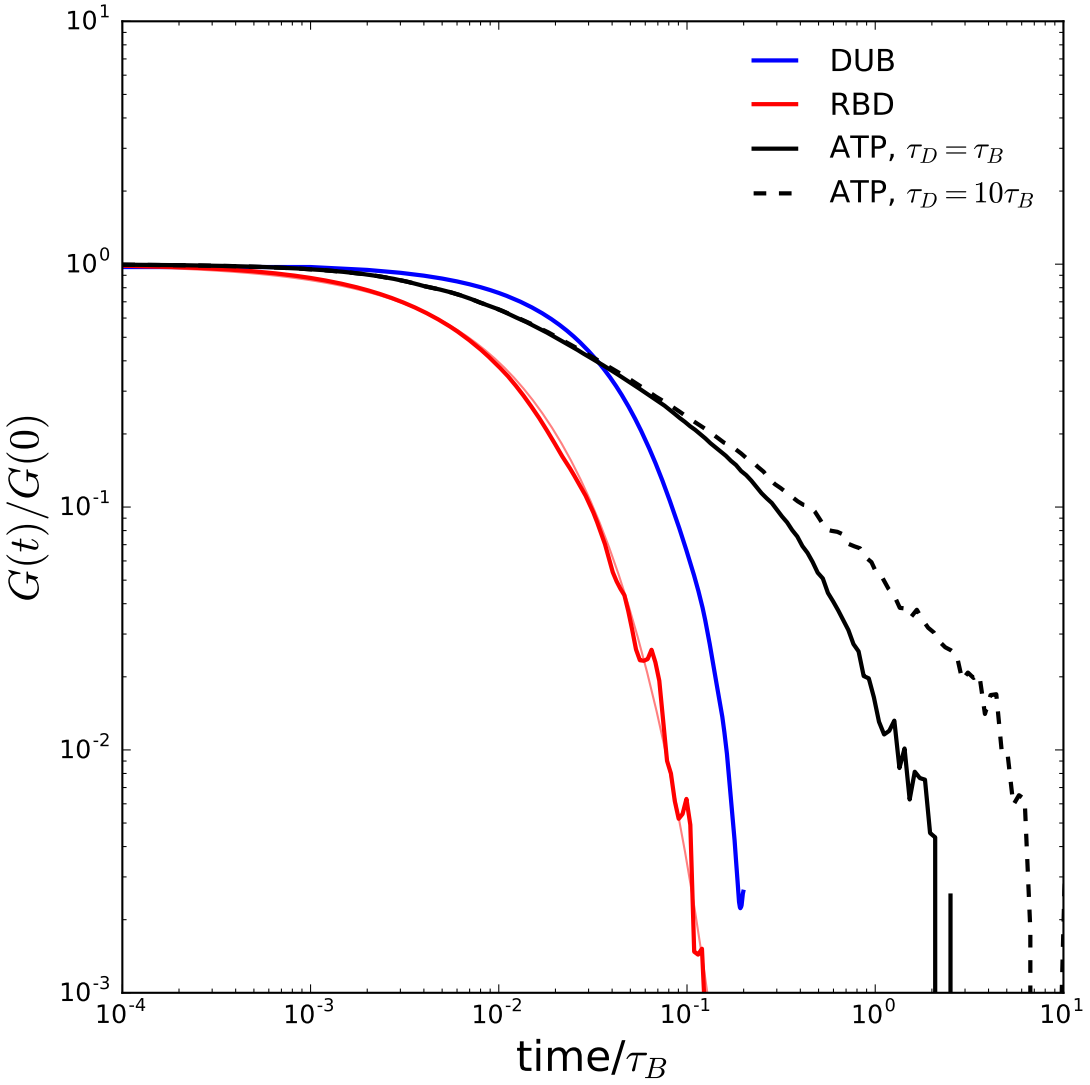

Figure 2.12: Normalized relaxation modulus $G(t)/G(0)$ in the case of dumbbell (DUB), repulsive Brownian dynamics (RBD), and associating telechelic polymers (ATP). For DUB, α is set with 1.5 (Eq. (2.90)) to make consistent with spring constant of ATP. For ATP, τ_D are set with τ_B or $10\tau_B$. All the other parameters are the same with figure 2.9.

Chapter 3

Understanding Parameter Space and Morphology

This chapter gives the effort of understanding parameter space that compatible with reality. The main parameters will remark on the following sections. Also, the equilibrium and non-equilibrium simulation for reference systems will be addressed. The details about scaling exponents on the variety of parameters will be traveled to select the system that will be used for the main results.

3.1 Remarks on the Parameter Space

In this section, the meaning and simulation range of parameters will be examined. The key parameters for the simulation are summarized in table 3.1 with the cross-reference of related equations in the simulation.

3.1.1 Chain and Micelle Dimension

It is already described in Eq. (2.26) where the size ratio parameter, α dominantly use on here. If the chain dimension is increased (so the α is decreased), the associable range becomes larger, then the system produces more active bridges. The expected α is in the range between 1.0 to 2.5, depends on the molecular weight of polymers. In the

Table 3.1: Summary of key parameters and its base unit variables with definition and related equations.

symbols	unit variable	definition
α	-	R_c/R_0, Eq. (2.26)
C_{rep}	-	repulsion coefficient, Eqs. (2.12) (2.13)
p	-	aggregation number, Eq. (2.28)
l_{cap}	R_0 (m)	length related to core, Eq. (2.27)
τ_D	τ_B (sec)	loop-dissociation time, Eq. (2.36)
R_{max}	R_0 (m)	maximally extendable chain length, Eqs. (2.20) (2.21)
ν_m	R_0^{-3} (m^{-3})	number density of micelles, Eq. (2.28)

case of FENE connector, the R_{max} can be given by the statistical segment that is around 10 times of R_c (Ianniruberto and Marrucci 2015). In this study, however, the R_{max} is left as an adjustable parameter in the way to have the same equilibrium statistics since the effective cutoff-radius for Gaussian chain is around $4R_c$. When $R_{max} \geq 6R_c$, no changes happened in the equilibrium both of static and dynamical quantities. However, in this study, this length scale is left for arbitrary value to make reasonable box scale because of the FENE connector have a minor role (when it is sufficiently larger than R_0) for both of statistics and relaxation modulus.

3.1.2 Finite Extensibility of Chains

So far, the only Gaussian chain has been addressed. The main reason is that there are no real changes in the equilibrium simulation when the maximally extendable chain length, R_{max}, is sufficiently larger, say $R_{max} \geq 6R_c$. The individual force contribution to the Langevin integrator is already reported in the figure 2.3 with $R_{max} = 6R_c$ and $R_{max} = 8R_c$. The distinguishable force contribution is almost started with R_0; then the FENE effect is significant after $2R_0$. However, it is worth to mention that the bridge chain distribution is typically concentration around the distance R_0 because

the long-time persist the connector make closer between the pair of micelle that leads to equilibrium distance to balancing between elastic and repulsive forces. Since the repulsion only works when the distance is shorter than R_0, the balanced distance slightly smaller than R_0. In conclusion, FENE does not change the equilibrium structure.

3.1.3 Repulsive Coefficient

Because of repulsion is fast dynamics, the increasing repulsive coefficient reduced the time scale for τ_R. Repulsion has restricted with the distance of R_0, which means the effect of repulsion varies on the average distance between micelle, especially for the bridge distance profile. If average bridge distance is much smaller than R_0, the repulsion makes a significant role in controlling for overall statistics including elastically active bridges. The decision of C_{rep} is not straight-forward, but the prefactor for the Eq. (2.14) is not clear for most of the case. In this context, the choice of C_{rep} is arbitrary but mainly considered two factors. First of all, the repulsive potential is enough to prevent amplifying-multiplicity between bridge formed micelles that leads the aggregation pattern. Once the first bridge formed between a pair of micelles, it introduces long-time correlation the pair with slightly shorter distance than the mean distance with other micelles. If the repulsive potential is soft compare with its counter part, bridge interaction in this case, the perturbed distance is much shorter than others, lead higher probability to make an association. Because we use pre-averaged C_{rep}, which means the internal variable does not affect to the micelle repulsion, this phenomenon leads long-time aggregation patterns. The second consideration is the repulsion should not overwhelm the elastic contribution in the concentration to reach semi-dilute regime. It means, the repulsive contribution is too high to produce the network properties and the system hard to capture the physically meaning status. In this sense, we found that $C_0 = 0.25$ is reasonable choice in Eq (2.14). Note that we are not strictly using C_0 throughout the study the selection procedure includes an artificial point that makes a broad range of selection. In this sense with exponent 2 (or 1.5), the basic structural information report in the later section especially for figures 3.1 and 3.2.

3.1.4 Number density of Micelles and Chains

Because of the range of R_0, however, the dimensionless number density becomes

$$\nu_C = \frac{N_C}{V} = \frac{N_C}{\tilde{V} R_0^3} = \frac{1}{R_0^3}\tilde{\nu}_m, \tag{3.1}$$

which make difficult to predict the real number density. Suzuki et al. (2012) reports the number density of chains with the value of

$$\nu_C = 1.8 \times 10^{23} m^{-3}. \tag{3.2}$$

In order to simulate this specific system, we have to have number density of chains in the range of

$$\tilde{\nu}_C \in [1.44, 11.5], \tag{3.3}$$

which is about 1 decade different. Because of number of chains per micelle is expected from 5 to 10, the expected number density of micelle varied in dimensionless space

$$\tilde{\nu}_m \in [0.144, 2.3]. \tag{3.4}$$

The upper limit for the range of $\tilde{\nu}_m$ also can be narrowed by the overlap concentration. The definition of overlap concentration, ϕ^*, in the simulation without the detail micelle dimension is not easy, but here we simply define the volumetric concentration, ϕ, is unity:

$$\phi^*(\nu_m) \equiv \frac{1}{6}\pi\nu_m^* = 1 \quad \Rightarrow \quad \nu_m^* \approx 1.9. \tag{3.5}$$

It is already well known that the random close packing and hexagonal close packing for the hard sphere are ϕ=0.64 and 0.74 that consist number density of micelle as 1.22 and 1.41, respectively. As described in Vlassopoulos and Cloitre (2014), the fluidity is related to the stiffness of repulsion, and here we use soft repulsion since the expected aggregation number, p, is from 5 to 20. In this sense, the fluidity almost consists with the ϕ^*, so the maximum of $\tilde{\nu}_m$ is set with 2. Combined with the expected p, the simulation range for $\tilde{\nu}_c$ is in between 0.3 and 20. However, the detail change of p is out of the boundary of this simulation. The comparison is mainly done with the change of $\tilde{\nu}_m$ while the p is the given constant.

3.2 Bridge Chain Statistics

3.2.1 Elastically Active Chains

$$f_C^+ = \frac{N_C^+}{N_C} \quad \text{and} \quad f_{DC}^+ = \frac{N_{DC}^+}{N_C}, \tag{3.6}$$

where N_C is number of chains in the system and N_C^+ is number of elastically active chains in the system, and N_{CD}^+ is number of distingushable active chains which means it is not count the multiplicity for the same pair of micelle.

3.2.2 Equilibration

Initially, the micelles are randomly displayed in the space with the same aggregation number without any bridges, and the equilibration of the box initially started with repulsive Brownian dynamics where the topological interactions are ignored. After few times of τ_B, the topological renewal is allowed, and it is monitored by the potential energy, stress components, and the fraction of active bridges, f_C^+. Once the f_C^+ is equilibrated, all the other observable reported above are equilibrate and isotropy. In this context, f_C^+, is selected the main observable to identify the equilibrium. The necessary equilibration time typically accounts the order of 10 based on τ_D when there is no major structure formation, which is the slowest time scale for the system. Figures 3.1 and 3.2 shows f_C^+ and its average multiplicity, w, with respect to time based on τ_R for α in the range of 1 and 2. The equilibration time changes when there is structure forming, such as aggregation that reported in below section.

3.2.3 Aggregation Patterns

The terminology *aggregation* or *clustering* in this study mainly related to the micelle distribution. It is clear that figures 3.1[c1] and 3.2[c1] shows the micelles are collected in one or two bulk state that suggest the system is aggregated through the bridge interaction. It is clear if we compare it with the system without aggregation, figures 3.4[b, c,

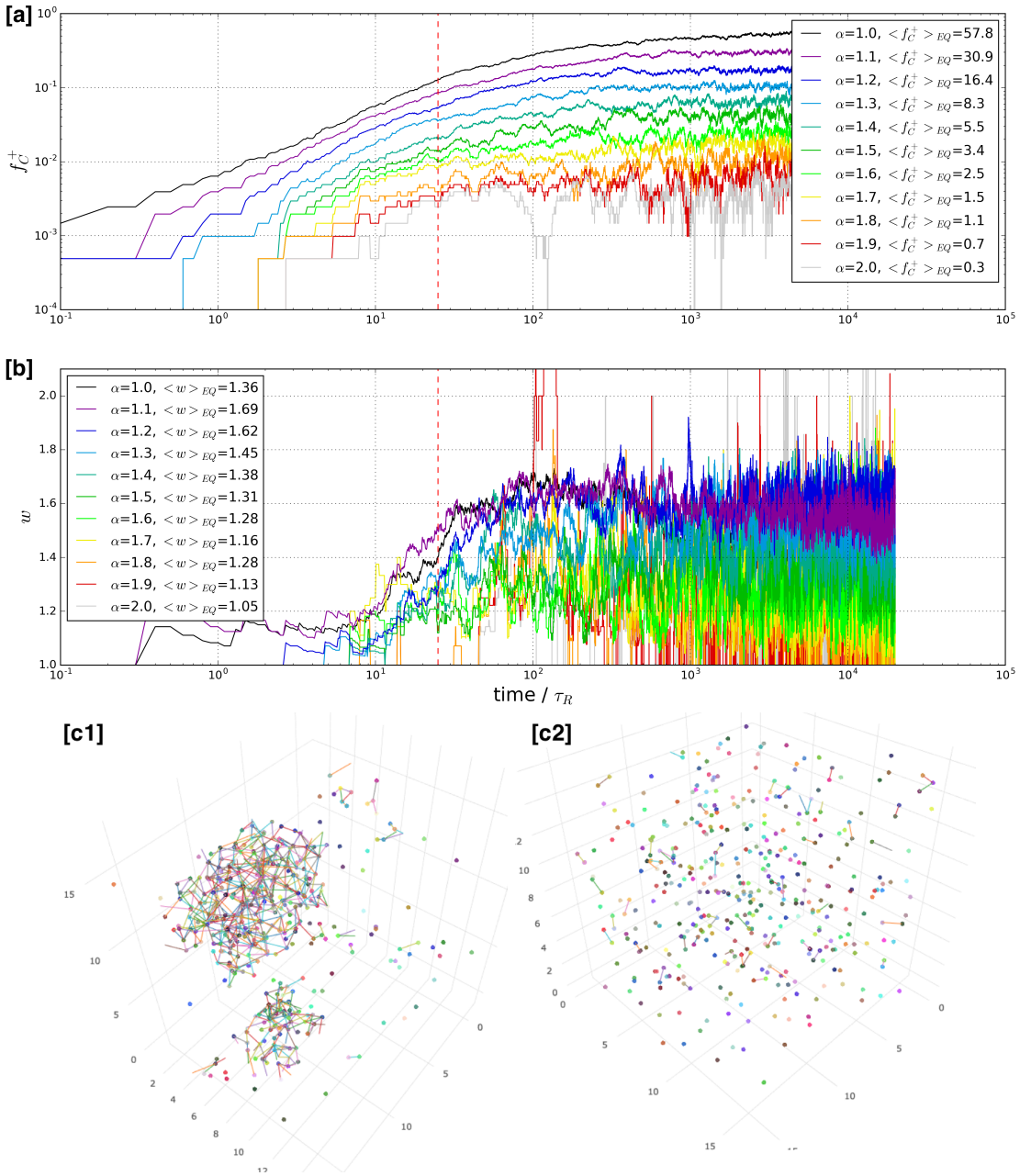

Figure 3.1: Changes of fraction of elastically active chains f_C^+ [a] and average multiplicity w [b] after onset of topological rearrangement at $\tilde{\nu}_m$=0.1. The structure of system are directly visualized in the case of α=1 [c1] and α=1.5 [c2]. Other conditions are the same with figure 2.9.

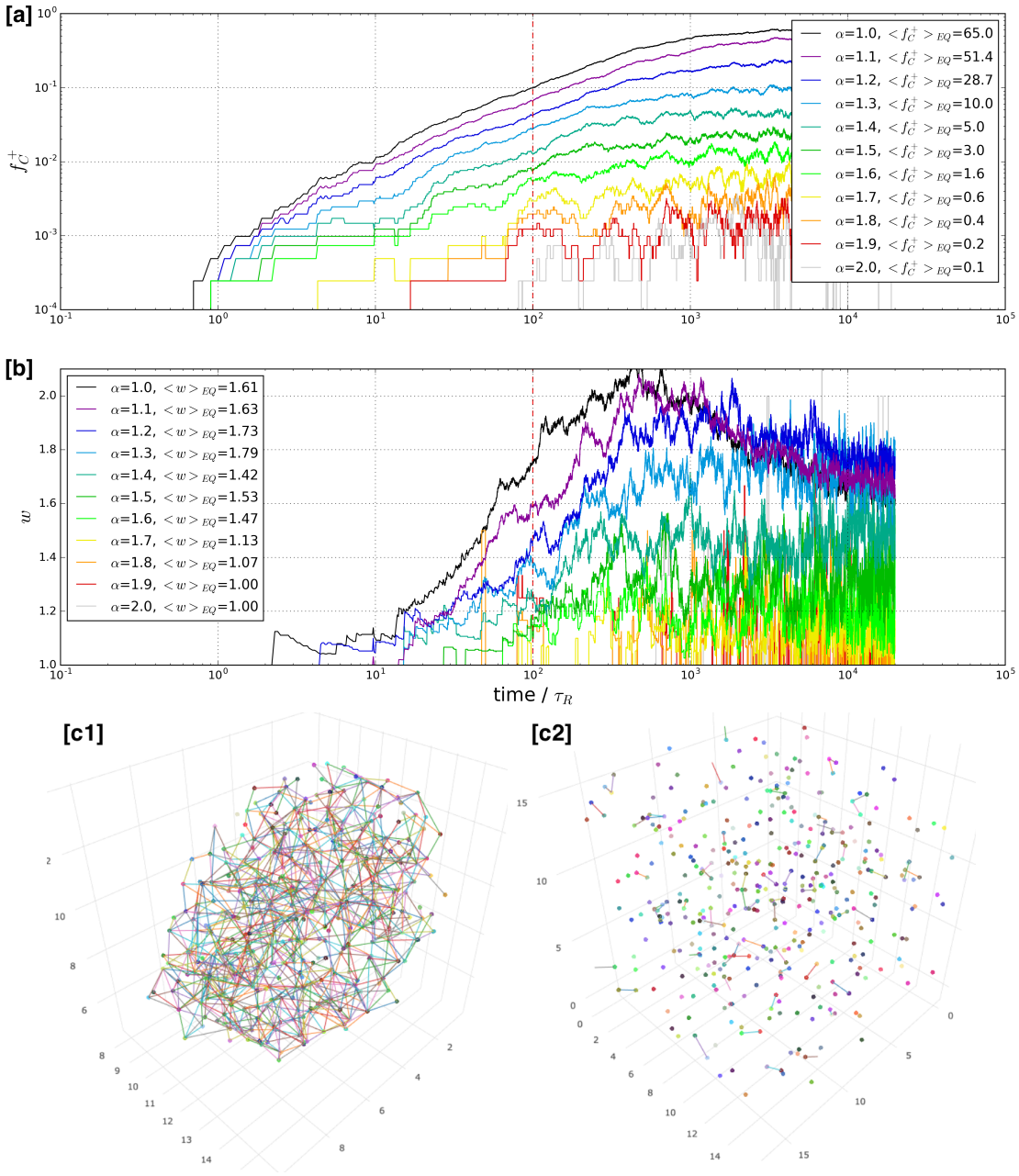

Figure 3.2: Changes of fraction of elastically active chains f_C^+ [a] and average multiplicity w [b] after onset of topological rearrangement at $\tilde{\nu}_m$=0.1. The structure of system are directly visualized in the case of α=1 [c1] and α=1.5 [c2] in the case of $p = 20$ and $C_{rep} = 100$. Other conditions are the same with figure 3.1.

d], 3.1[c2], and 3.2[c2]. Especially figure 3.4[b] suggesting the system highly connected (say percolation) without aggregation that is also shown in the $g(r)$ in figure 3.5.

The driving force of aggregation in this simulation mainly due to the bridge interaction where the effective range for the association is much higher than effective repulsion range (even if chain end-to-end distance is half of micelle diameter, α=2), micelle diameter in this case. When one chain end 'hook' the other micelle in the distance, they pull each other due to the bridge interaction. The 'hooking' distance can be longer when R_c is increases, which means the lower α suggesting higher probability for the association. Because the dissociation time is the slowest dynamic in the system, this 'hook' will persist enough time to start overlap where the repulsion is started to act. In this mechanism, not only the internal balance between repulsion and bridge interaction, the probability to make additional association play a role where the higher p means higher suggestion probability for random selection. If this association kinetics becomes dominant to compare with dissociation of the bridge, the additional bridge will forms on the same pair of micelle: increasing multiplicity, w. The amplifying multiplicity leads stronger bridge interactions that make dissociation time longer. If this procedure is profound, the system going to aggregated direction as the results of w in figures 3.1 and 3.2. As describe above, α=1 for p=10 and p=20 are aggregating in equilibrium where the w show the peak around equilibration time when there are no aggregation, then w is going to decrease because many micelles are already in short distance with the subjected micelle that makes distribute the higher multiplicity of one pair of micelle into lower multiplicity of large pairs of micelle.

3.2.4 Fraction of Elastically Active Chains

The fraction of elastically active chain, f_C^+, is one of key observation that show the bridge forming of the system compared with the fraction of elastically distinguishable active chain, f_{DC}^+. Some points of these values are already reported in figures 3.1 and 3.2 with notation of $\langle \cdots \rangle_{EQ}$. For convenience, the f_C^+ and f_{CD}^+ in equilibrium simulation are reported without average bracket. Figure 3.3 shows the changes of f_C^+ and f_{DC}^+ based

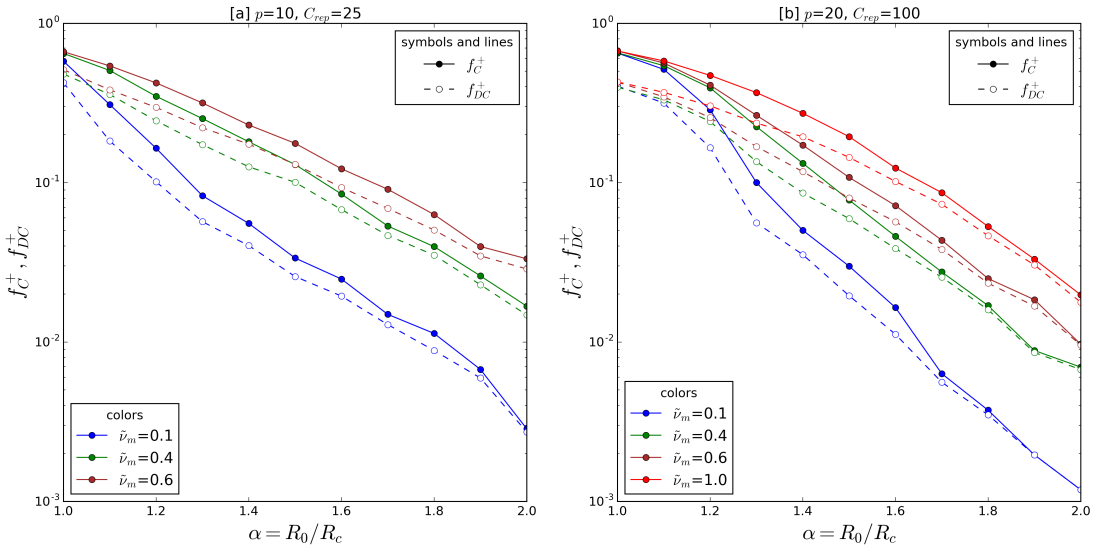

Figure 3.3: Changes of fraction of elastically active chains, f_C^+, and fraction of elastically distinguishable active chains, f_{DC}^+ with different $\tilde{\nu}_m$ due to α. The aggregation numbers are set with p=10 [a] and p=20 [b] that leads C_{rep}=25 and 100, respectively.

on the selected $\tilde{\nu}_m$ as 0.1, 0.4, 0.6, and 1.0 with respect to α. The changes of f_C^+ in non-aggregating system following somehow exponential decay. This is not surprising since association distribution given by Boltzmann distribution, Eq. (2.40), and the average bridge distribution is not critically changed in such a system.

3.3 Micelle Distribution of ATP System

3.3.1 Visualization of PBC Box

Direct visualization of the PBC box is of important to understand the real structural information of the system and network properties. Figure 3.4 is one of the representative systems that shows strongly aggregated system [a], percolated network without aggregation [b], sparse network ($f_C^+ \approx 2\%$)[c], and poorly connected system [d]. The main considerable system in this study is a sparse network where the f_C^+ is around 2%. In this range, it is hard to mention that such a system is network-like structure. Recall

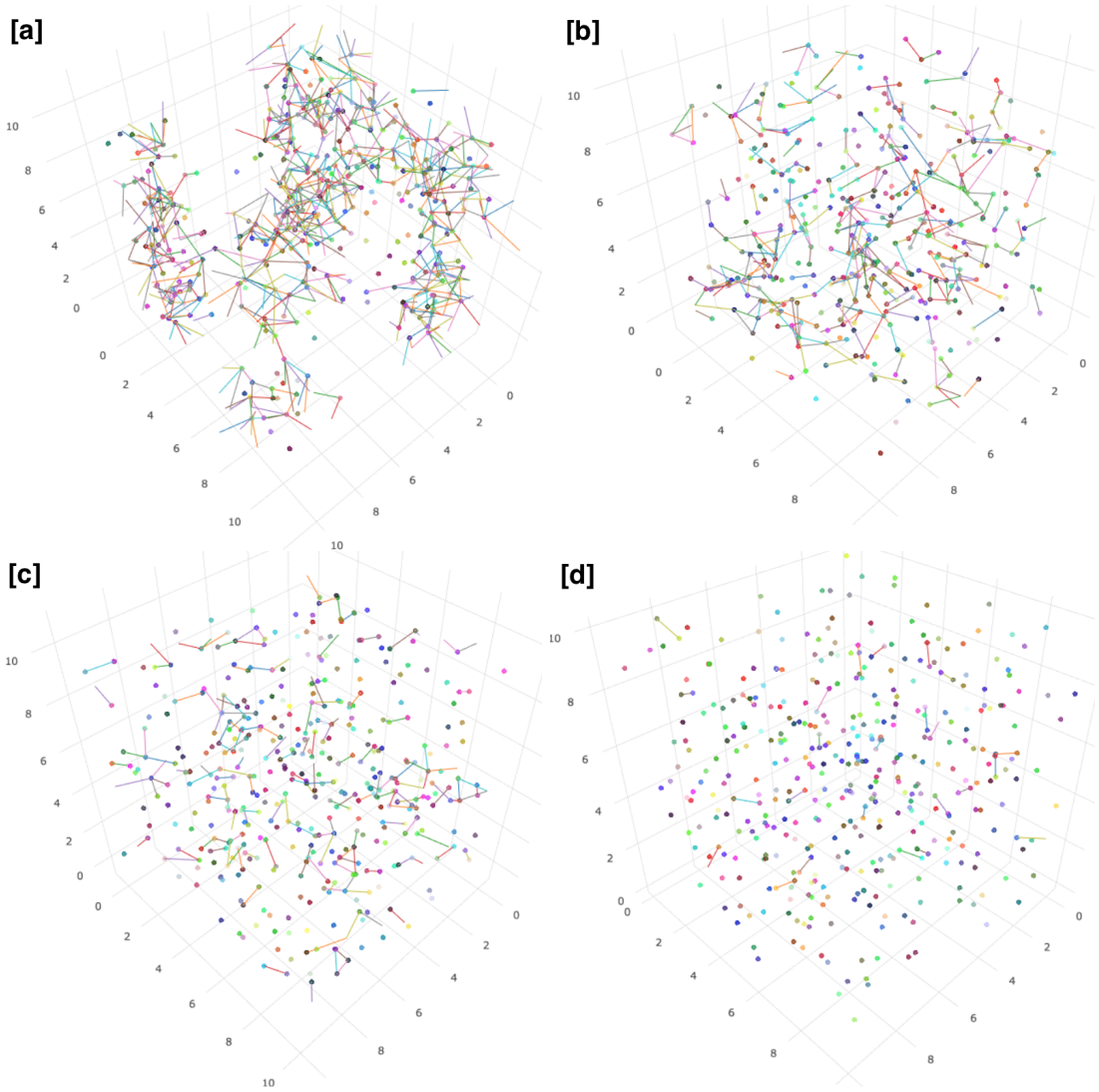

Figure 3.4: Direct visualization of PBC box including position of micelles (dots) and bridges (lines). For visualization purpose, the size of dot are very small compare with R_0, since the average bridge length is around R_0. Three representative samples are selected to visualize aggregated system [a], percolated network without aggregation [b], sparsely connected system [c], and poorly connected system [d].

the experimental data in Suzuki et al. (2013) and Xu et al. (1996), the strong difference between linear and nonlinear viscoelasticity is observed in the dilute regime where the expected f_C^+ is around 2%. As Xu et al. (1996) already mention that the expected functionality of such a system about 0.7, the sparse network consistence with our objectives. Note again that this system is NOT percolated.

3.3.2 Isotropic Pair-Correlation Function

Figure 3.5 shows the changes of $g(r)$ for ATP with the given parameters when α and p are changed. Figure 3.5 (left) shows the different of $g(r)$ due to the structure of the system reported in figure 3.4. In the aggregated system shows the weird broad first shell is observed that consist about the aggregating pattern in the PBC box. Note that the sequence of legend in figure 3.5 is the same sequence of [a], [b], [c], and [d] in figure 3.4 where the only [a] is aggregated system.

3.4 Plateau Modulus and Initial Relaxation Modulus

3.4.1 Linearity between Plateau Modulus and Initial Relaxation Modulus

Because the simulation results do not follow single Maxwell model, the initial relaxation modulus, $G(0)$, is not the same with G°. If $G(0)$ and G° are linearly depended on each other, the measured exponents are the same for both of $G(0)$ and G°. Figure 3.6 reports the computed G° through the storage modulus converted from $G(t)$, where the data is broadly scattered along the plateau region. Taking an average of the scattered data gave us the expected G°, that shows the linearity with $G(0)$. For this reason, $G(0)$ will be used instead of G° throughout the study. The slope, however, is a function of the parameters where the exact relaxation is obscure on here.

In order to measure G°, we use Fourier transform $G(t)$ into $G^*(\omega)$, then we measure $G'(\omega)$ in averaging over plateau regime. Let define $G^\circ = gG(0)$ where the prefactor g indicate the deviation from single Maxwell model. Figure 3.6 show the g is not depended

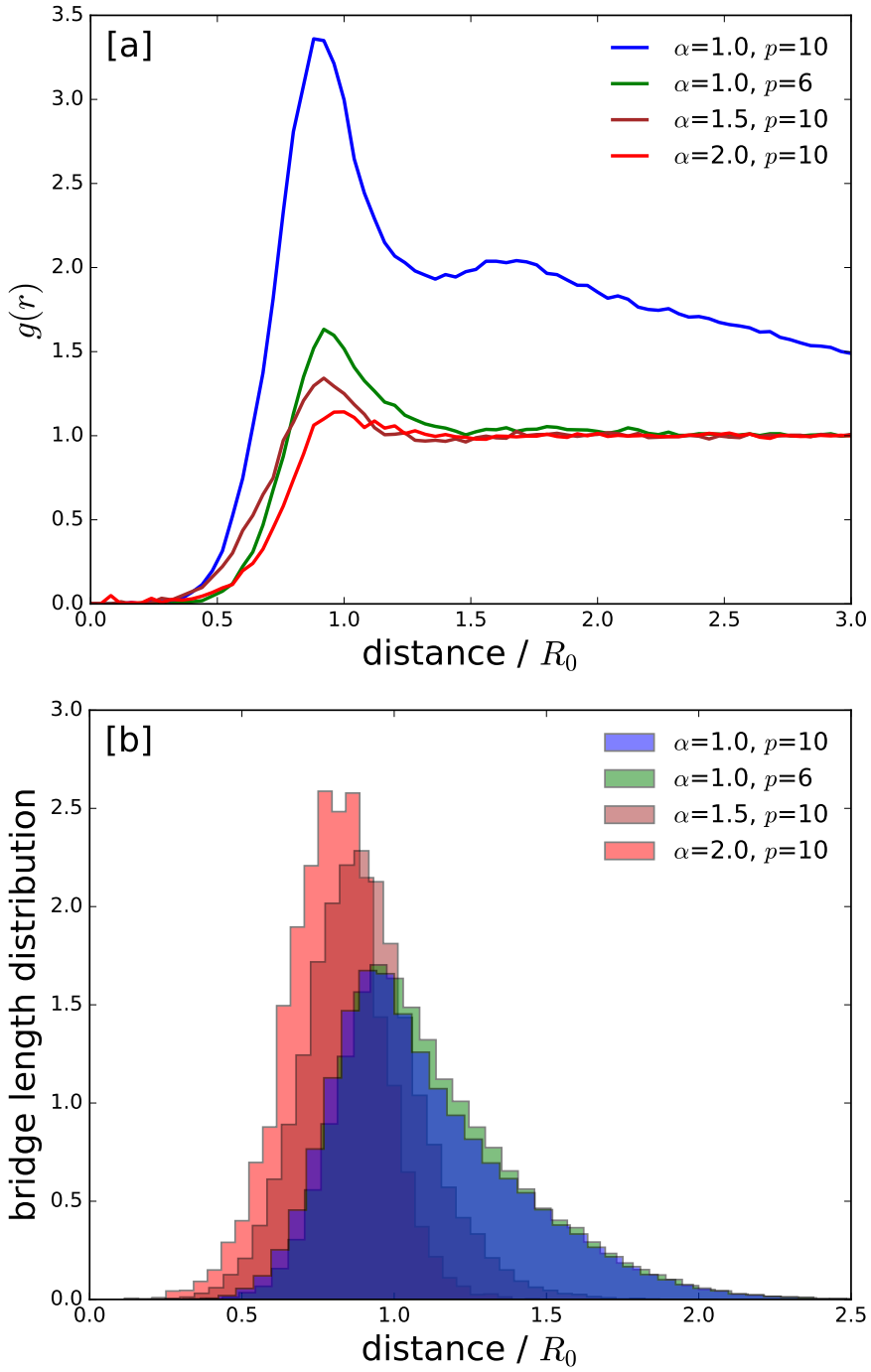

Figure 3.5: Pair-correlation function $g(r)$ [a] and bridge length distribution [b] in the case of associating telechelic polymers (ATP) with different α and p following legend orders. The other parameters are the same with ATP condition in figure 2.9.

on the number density of micelle for the given parameters. For visualization purpose, the x-axis shifted by 0, 1, and 2 with α=1.0, 1.5, and 2.0, respectively. The increasing α, means decreasing R_c, shows the g becomes larger which is not surprise because the repulsive contribution makes different from single Maxwell model. Increasing C_{rep}, however, the g value will increased. Notice that there are no C_{rep} effects for the α=1.0 case since the system has much higher elastically active bridge that makes the repulsive contribution relatively small. Because of linearity between G° and $G(0)$, the scaling relation in below mainly used for $\tilde{G}(0)$ since the value is easily measurable for variance factor for stress autocorrelation in accurate while $\tilde{G}^{\circ}$ needs some treatment to decide.

3.4.2 Initial Relaxation Modulus and Scaling Exponent

To have systematically measurable quantities are of importance when the parameter space is huge. Initial relaxation modulus, $G(0)$, is one of the recommendable observable because it does not suffer from system noise, and possibly represented by the components-wise manner. The changes of α and p (that leads change of C_{rep}) can be understood through the $G(0)$. Many of parameter reported in section 3 is not free from other parameters, but the study excluding the minor changes that reported in chapter 1 will be ignored. In the case of p, the difference is significant for the interesting range of concentration while the detailed form to increase is not clear. Hence, the structural study on here basically used two lower and larger values but not the extremum that suggests possible range of p due to the $\tilde{\nu}_m$.

Effect of Size Ratio Parameter

The range of alpha is expected in between 1 and 2 following the description in section 3.1.1. The inaccuracy for R_0 makes the range of α where the changes of R_c from PEO to HEUR is also related to making broad range. It is of importance to aware that the morphology of the system sensitively depends on α with an increment of 0.1. Hence, 3.7 reports how $\tilde{G}(0)$ changes with respect to α where the connected lines represent the same molecular parameters but different concentration. The distinguishable slopes in lower α

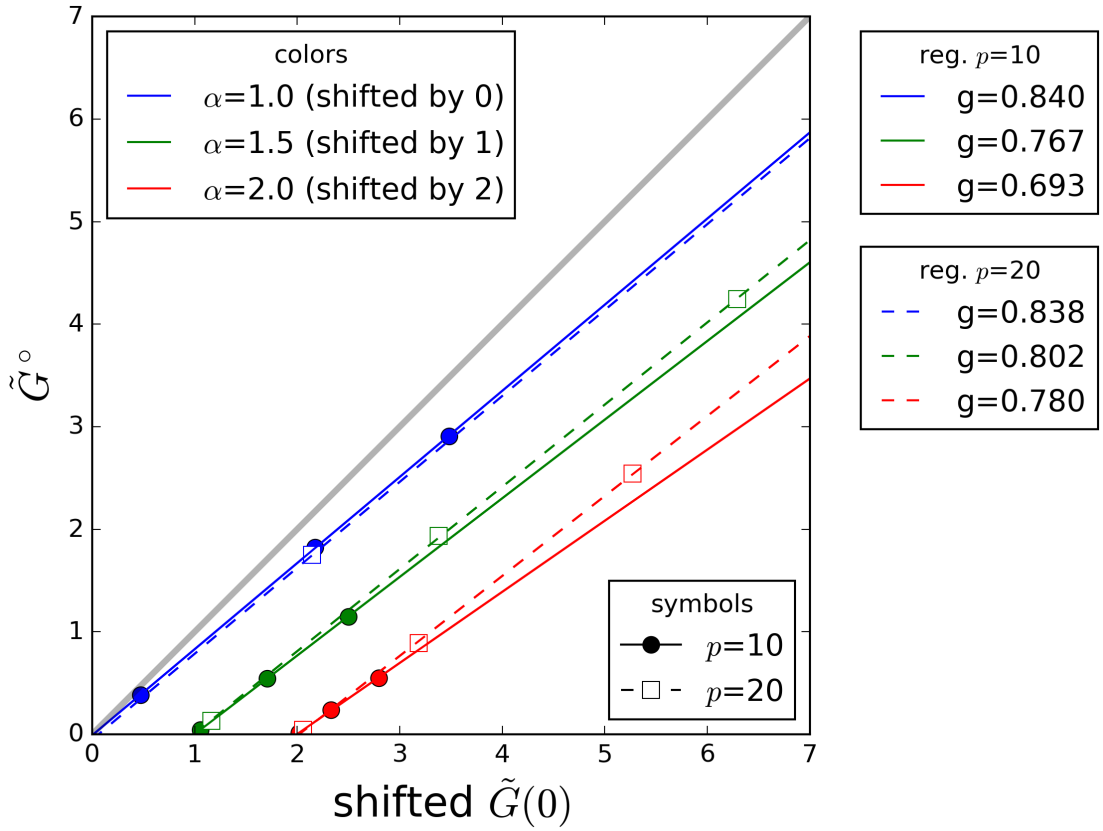

Figure 3.6: Linear relation between initial relaxation modulus, $G(0)$, and plateau modulus, G°. For visualization, $\tilde{G}(0)$ is shifted by unity for each samples. The measured slopes g through linear regressions in the order of $\{\alpha\} = \{1, 1.5, 2\}$ are $\{0.840, 0.767, 0.698\}$ for p=10 and $\{0.838, 0.802, 0.780\}$ for p=20. The black diagonal line represent when $G^\circ = G(0)$.

conditions are related to aggregation that makes different dynamics. In the case of p=10, the changes of $\tilde{G}^{(el)}(0)$ is not distinguishable from α=1.3 where all the points are merged into the same line where the level of modulus between repulsive and elastic contributions are changing due to the α. It consists with the physical insight since the decreasing α means increasing the relative size of R_c that makes longer associations. Most of the data are reported $\tilde{\nu}_m$ in 0.1, 0.4, and 0.6 where that range the initial modulus follows a certain scaling law. When p is given by 20 with $C_{rep} = 100(= 0.25p^2)$, the modulus level of repulsive contribution significantly higher that of p=10. The main reason is due to the high repulsive coefficient, and also elastic contribution becomes larger due to the higher number of chains in the system. The change of scaling exponents around $\tilde{\nu}_m$=0.6 is observed that is not sure in the p=10 case because the most of the data for p=10 is reported up to $\tilde{\nu}_m$=0.6. The slope changes in non-aggregating range ($\alpha \geq 1.4$) becomes larger that mostly due to the higher aggregation number.

Scaling Exponents for Initial Relaxation Modulus

From figure 3.7, we can measure scaling exponents for $\tilde{G}(0)$. Recall Eq. (1.37), the scaling exponent for the initial relaxation modulus q is already observed experimentally (Uneyama et al. 2012) where it shows around 2.3 in lower concentration regime that we are interested in and 1.8 in higher concentration regime. The comparison on here ignore the changes of aggregation number, p, due to polymer concentration, ν_c. In this regards, q values are very similar with the range between 1.8 and 2.3 as reported in 3.8. There is tendency in the change of q on α except the aggregating system (lower α values). First of all, the change of $q^{(el)}$ is increasing all the system that either p is 10 or 20 and also either $\tilde{\nu}_m$ is lower or higher than 0.6. The meaning of exponents represent the sensitivity to $\tilde{\nu}_m$ for the given parameters, and increasing of exponents means the system more sensitive to $\tilde{\nu}_m$ when α is higher. The repulsive contribution, $q^{(el)}$, however, the tendency highly depends on the given parameters. The sort of plateau of $q^{(el)}$ in the $p = 10$ case means the repulsive contribution to the modulus is not change due to α in the range between 1.3 and 2. Recall figure 3.3, it is confirm that the f_C^+ changes with the given $\tilde{\nu}_m$ that

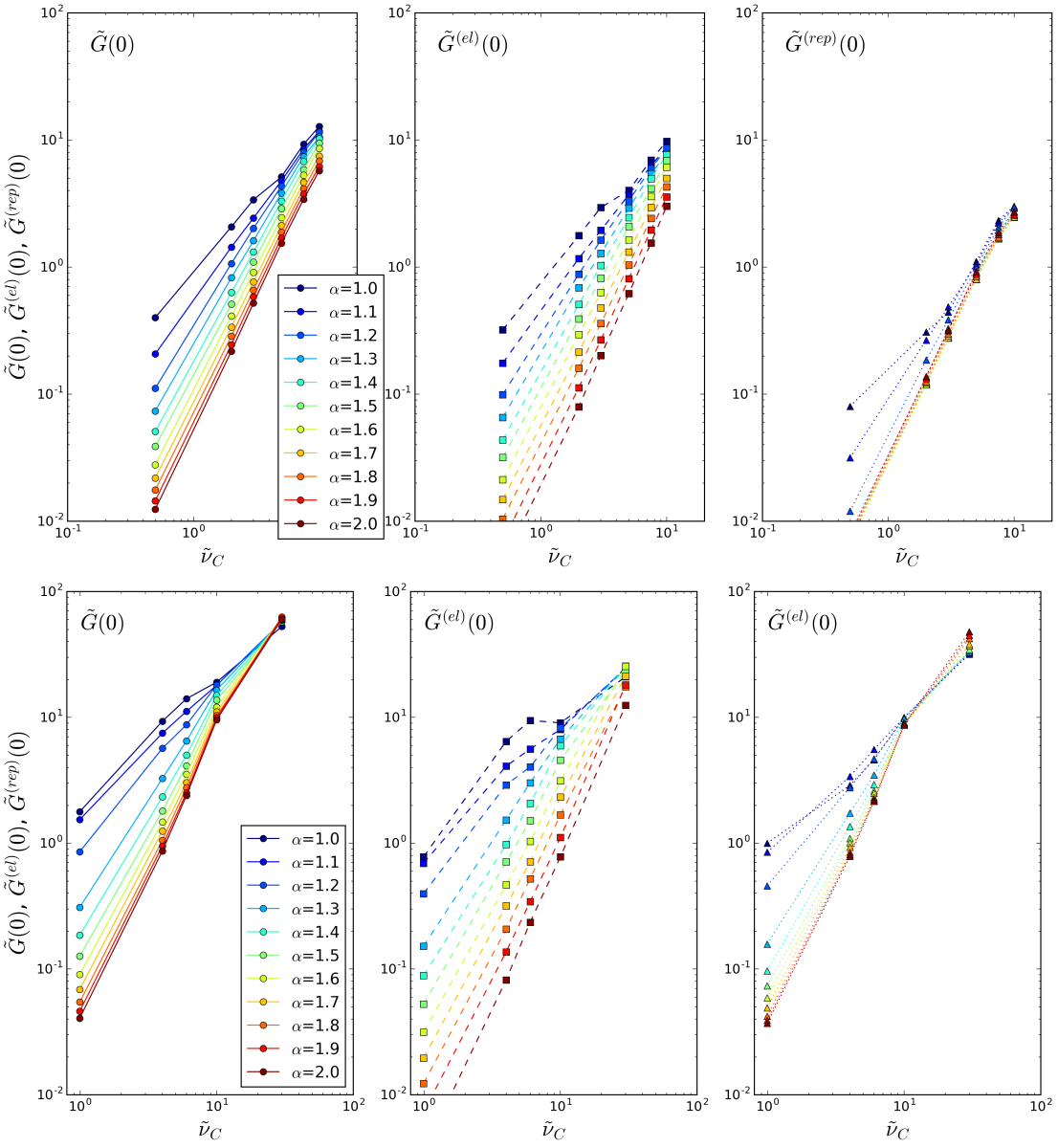

Figure 3.7: Measured $\tilde{G}(0)$ with respect to $\tilde{\nu}_C$ for p=10 (top) and p=20 (bottom) where $C_{rep} = 0.25p^2$. The remain conditions are identical with figure 3.1.

consist with the elastic contribution in figure 3.8.

In the case of p=20, all of the q, $q^{(el)}$, and $q^{(rep)}$ are increasing with respect to α. The strange tendency in its initial is due to aggregation pattern as p=10. The out of trend at α=2 is expected that the repulsive dynamics overwhelm the overall dynamics where the elastic contribution only have a minor role. After transition concentration, $\tilde{\nu}_m = 0.6$, the exponents shows the smaller number compare with its lower concentration regime. The overall exponents changes before and after transition concentration are about 0.4 that consist with Uneyama et al. (2012) although the paper is mostly focused on the elastic contribution from a bridge. The sensitivity of $q^{(el)}$ in higher α reaches around 2.5 but the modulus level for elastic contribution is small in this regime, figure 3.7.

3.4.3 Effect of Elastically Active Chains into Plateau Modulus

From theory of Green-Tobolsky, Eq. (1.22), the plateau modulus proportional to the $\bar{\nu}_C^+$ which is not the same for ν_C^+. Let assumed that

$$G^\circ = gG(0) = h\nu_C^+, \tag{3.7}$$

where g in selected samples are reported in figure 3.6. Figure 3.9 shows the $G(0)$ and G° with respect to f_C^+ (top) and ν_C^+ (bottom) for two reference cases: p=10 and 20. The changes due to the f_C^+ is not clear, but all the test condition shows the linearity between $\tilde{G}(0)$ (or $\tilde{G}^\circ$) and $\tilde{\nu}_C^+$. The g or h are related with the α and C_{rep} in a complicate manner, but one important is that such a high number for $C_{rep} = 100$ in α=2 case is not favorable.

3.5 Relaxation Modulus

3.5.1 Relaxation Mechanism and Time Scales

Similar to dumbbell model, the bridge chains are relaxed through the Brownian motion of micelles. One of the simplest cases for this time scale is dumbbell where the one connector exist between a pair of micelle that suggests the time scale for the such

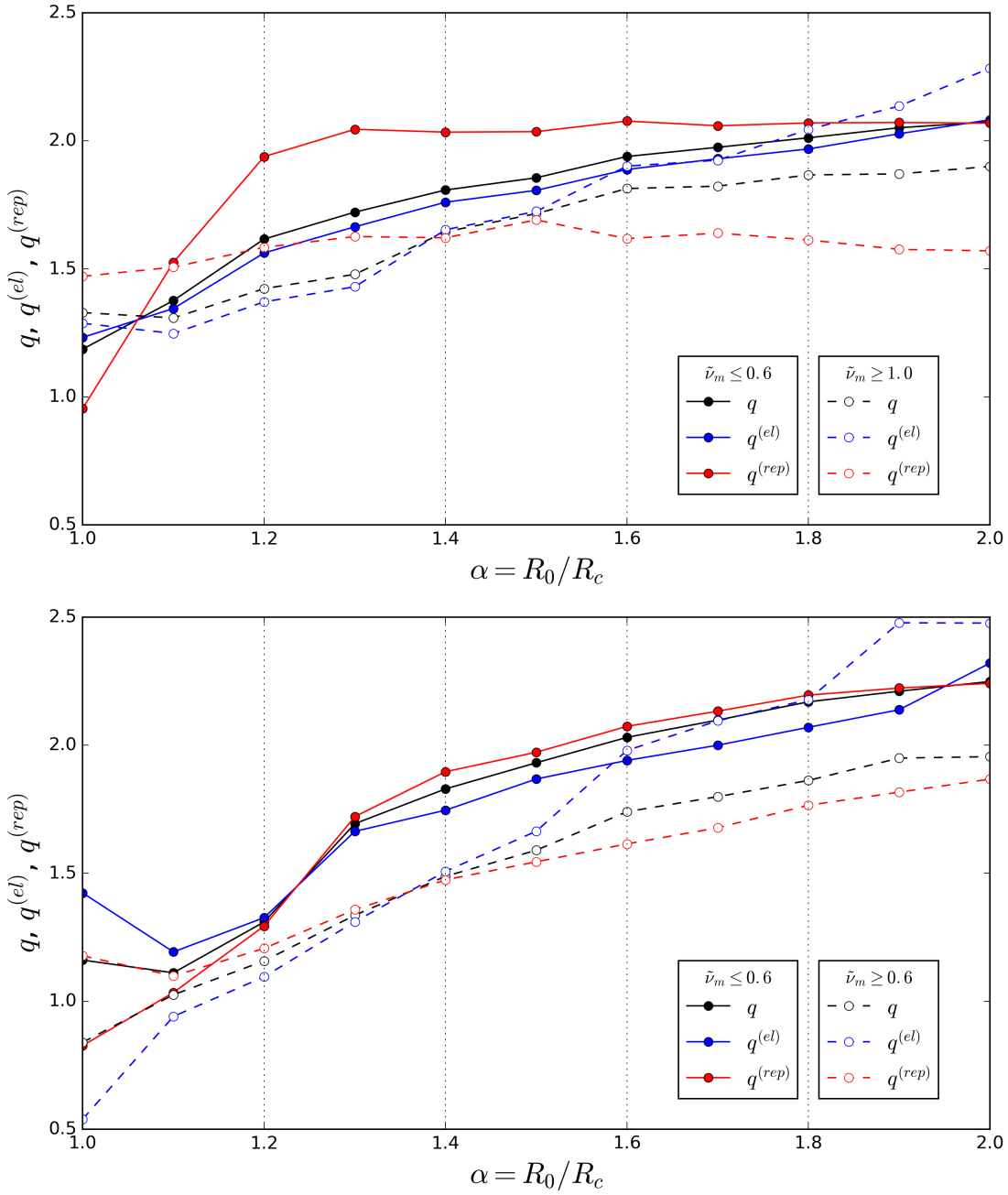

Figure 3.8: The effect of α to the measured scaling exponents of $\tilde{G}(0)$, q. The given aggregation number is p=10 (top) and p=20 (bottom) and with the same condition in figure 3.7.

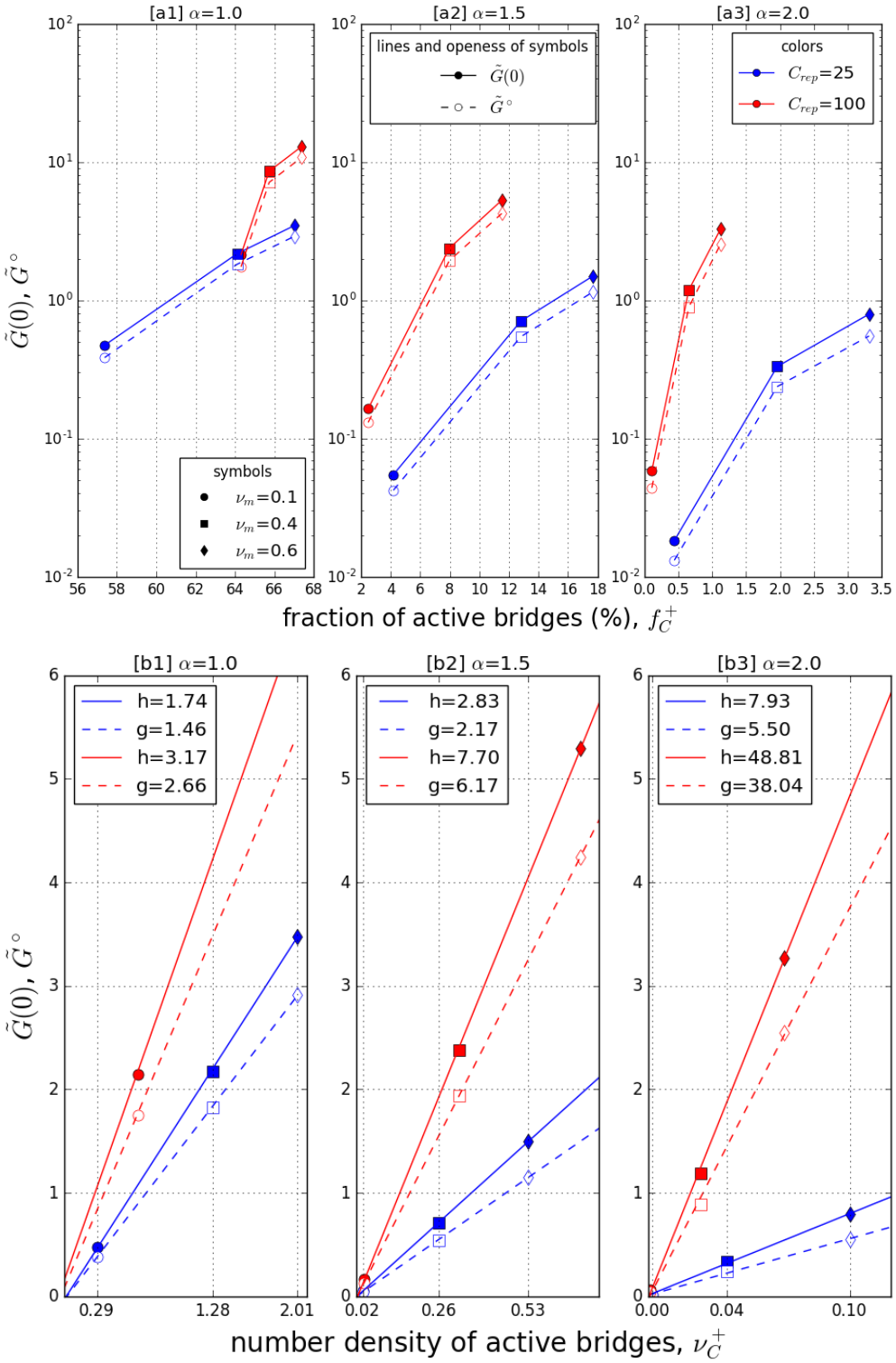

Figure 3.9: Plateau modulus, $\tilde{G}^\circ$, with respect to fraction of elastically active chain, f_C^+ [a∗], and number density of elastically active chain, ν_C^+ [b∗]. α=1, 1.5, and 2 that referes index [∗1], [∗2], and [∗3], respectively. The parameters are the same with figure 3.7.

a bridging chain as Eq. (2.90). Of course, this is not the true when the system forms well-defined network, but level of its dependency is related to network structure. Note that the experimental results show about 2% of chains are elastically active using Green-Tobolsky's theory Suzuki et al. (2012) and Xu et al. (1996). If our simulation system have the same meaning of experimentally reported

In this poorly connected system, the relaxation time is somehow the balance between τ_{BC} and τ_R. Because $\tau_D \gg \tau_{BC} \approx \tau_R$, the relaxation mainly comes with repulsive and elastic parts where the contribution from dissociation is a minor role. From the time ratio factor, R_t, we have

$$\frac{\tau_{BC}}{\tau_R} = \frac{C_{rep}}{12\alpha^2}, \tag{3.8}$$

where α=1.44 shows that two time scales are identical.

For reference purpose, the α=1 with p=6 and α=1.5 and p=10 are compared in 3.10. The only $\tau_D = \tau_R$ case is closer to the single relaxation time and the measured time scale is about half of τ_D. The structure of system for p=6 is already reported in figures 3.4[b] and 3.5 that represent the well percolated system. It is significant that the relaxation time is controlled by the loop-dissociation time, τ_D, where the values of τ_D are arbitrary selected. In the case of a poorly connected system, however, the relaxation time is in between τ_R and τ_D and higher τ_D is not change for the dominant relaxation time. The tails, however, exist when $\tau_D = 250\tau_R$ which suggest that the topological relaxation is minor compared with repulsive dynamics of the system.

Figure 3.10 [b] and [c] are the selected case that has been tested in previous figures. It is noteworthy that all the system are well distributed in spatially, i.e., non-aggregating system. For comparison between time scale, the $\tilde{\nu}_m$=0.6 is used, and the α=1.5 and 2 has been compared. The effect of τ_D is in α=1.5 but not in the case for α=2. Note that the base unit for time is τ_R where $\tau_B = C_{rep}\tau_R$ that suggest the longest time scales between p=10 and 20 cases with α=1.5 are around τ_D.

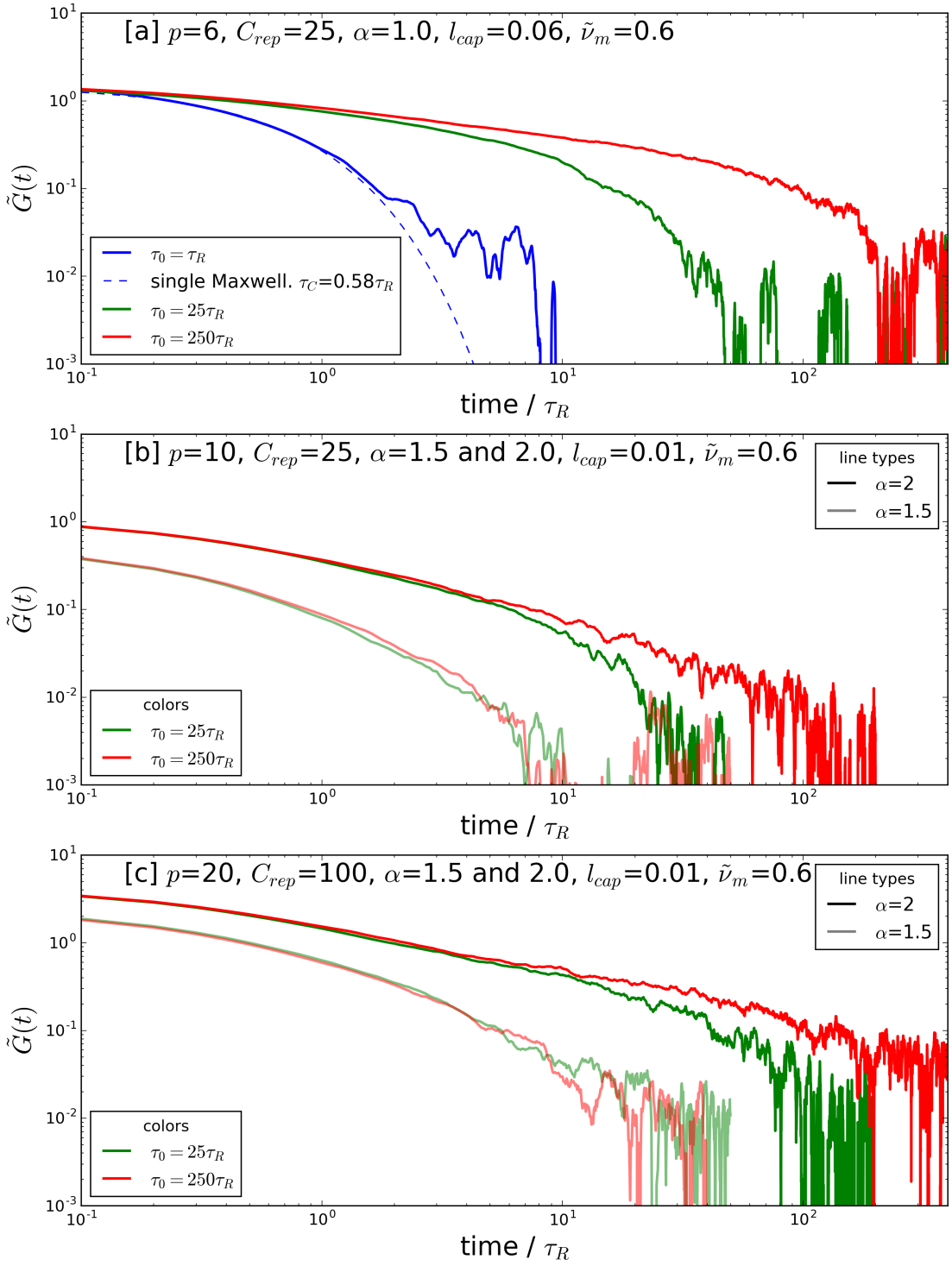

Figure 3.10: Changes of relaxation modulus with changes of τ_D. More network-like structure α=1 and p=6 (top) and sparsely connected case α=1.5 and p=10 (bottom).

3.5.2 Repulsive and Elastic Contributions to the Relaxation Modulus

The components-wise relaxation modulus follows the definition in Eqs. (2.82) and (2.83) where the shape of elastic contribution is similar with single-Maxwell model while its shape of repulsive part depends on the system. Figure 3.13 is results of specially selected parameter to show the single-Maxwell type for each of components where τ_D is set with τ_R. It leads the overall relaxation modulus is given by two-element Maxwell model. With this special case, the complex viscosity is analytically expressed as dashed line. The direct Fourier version for $G^*(\omega)$ is quite scattered but well fitted with two-components Maxwell model. In the case of steady-state viscosity in simple shear, the viscosity level in linear regime is almost same with its expectated value of $\eta^{(el)}$, $\eta^{(rep)}$, and components-wise $\eta^*(\omega)$. This indicate that the non-equilibrium simulation well fitted with the suggested decoupling scheme in Eq. (2.84). The onset of shear-thinning, one of our main objective, is slightly different between $\eta^*(\omega)$ and $\eta(\dot{\gamma})$, but minor in this pilot test.

Unfortunately, the system, in general, is not following component-wise single Maxwell element, because of the way of interactions are coupled to each other that makes a complicated signal in minor contributions. It makes the real difficulty in predicting the components-wise contribution to the η_0 because of the integration domain for viscosity function is related to $tG(t)$ where the increment of time is given by $\log t$. The small deviation of minor components in a long time makes much sensitivity to measure zero-shear viscosity, η_0, and the relatively stable way to select the integration domain through Eq. (2.70): will be discussed in later sections.

$$\eta_0 = \int_0^\infty G(t)dt = \int_{-\infty}^\infty tG(t)d\log t. \tag{3.9}$$

The spectrum have advantage to measure $\tilde{\eta}_0$ where the effect of noise into the $\tilde{\eta}_0$ is easily visualized that suggest the effective range of time to integrate. This negative contribution globally observed when the dynamics are controlled by elastically active chains even if α=2. This is mainly due to the effective association is larger than effective repulsion as described in section 3.2.3. Because of $\tau_D \gg \tau_R$, the bridges are almost permanent for

the time scale about τ_R. In this range, once a pair of micelles is connected by a chain, the distance gradually decreases after time being, that shows a higher probability for repulsion. If we observe virial stress, such a case closer between two interaction sets for k-th particle, $\mathscr{C}_k$ and $\mathscr{P}_k$:

$$\sum_{i\in\mathscr{C}_k} \mathbf{r}_{ik}\mathbf{F}_{ik}^{(el)} + \sum_{i\in\mathscr{P}_k} \mathbf{r}_{ik}\mathbf{F}_{ik}^{(rep)} \approx \sum_{i\in\mathscr{C}_k(\approx\mathscr{P}_k)} \mathbf{r}_{ik}\left(\mathbf{F}_{ik}^{(el)} + \mathbf{F}_{ik}^{(rep)}\right). \tag{3.10}$$

Since the sign between repulsion and elastic is opposite and elastic potential is dominant in the system, the repulsion have mainly opposite sign. This is generally not the case since $\mathscr{C}_k \neq \mathscr{P}_k$. In this sense, the forms for virial stress must keep individual stress forms and the each force contributions have the different role. One of the simplest example is when $\tau_D = \tau_R$, so the relaxation dynamic is controlled by dissociation. In this sense, the correlation between repulsion and elastic potentials becomes smaller. Note that if the exerted force is isotropic and there are no strong correlation with other force contribution, the response is positive. This is already reported in the figure 3.11. In this context, the profound negative $\eta_0^{(rep)}$ is believed the results of the strong correlation between elastic and repulsive contributions where the repulsion is in minor contribution.

3.6 Zero-Shear Viscosity

Measuring zero-shear viscosity from equilibrium simulation should overcome the noise especially the $\tilde{\nu}_C^+$ is in lower values. Figure 3.12 is reference system to show the zero-shear viscosity on the number density of chain, $\tilde{\nu}_C$ where the α is set with 1.5 (top) and 1.2 (bottom). The measured exponents, m, is from 2 to 3 and gradual exponent change is observed in the reported area, that consist with the experimental observations described in section 1.4.1. The test conditions are α=1.5 with l_{cap}=0.06 and α=2 with l_{cap}=0 and 0.06. The p will change from 10 to 20 gradually, but the internal change is not clear. What one can understand is that with increasing of $\tilde{\nu}_c$, some of the chains will increase p while others will affect $\tilde{\nu}_m$. It means the real exponent in higher $\tilde{\nu}_c$ can be reduced when we account this aspect.

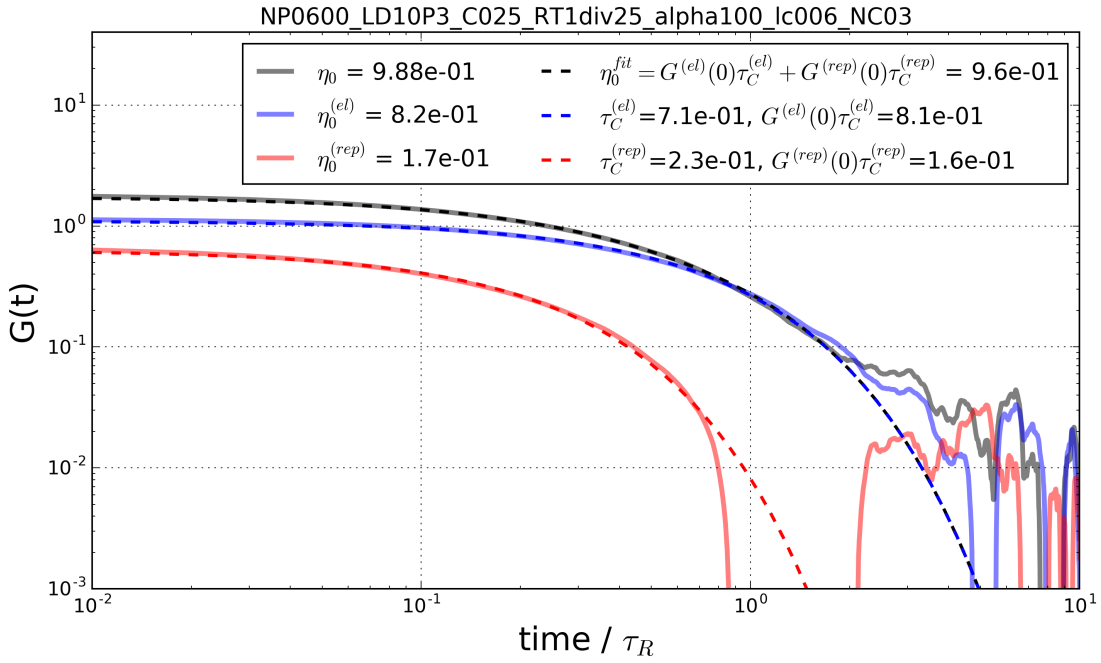

Figure 3.11: Examples for measured relaxation modulus in equilibrium simulation The test condition is here: ν_m=0.6, p=6, C_{rep}=25, α=1, l_{cap}=0.06, and R_t=0.04.

In the case for component-wise contributions to the $\tilde{\eta}_0$, the repulsive one is minor in all the test conditions. The main reason is that the effective association range is larger than that of repulsion, so the repulsive contribution acted as a response to elastic potential introduced by bridges. The positive repulsive contribution happens in the lowest concentration and lowest chain dimension, α=2. In this regime, the repulsive one individually acts, and the viscosity level is comparable with that of elastic contribution. With increasing concentration, elasticity plays an important role in the system, that makes the change of sign about repulsive contribution.

3.7 End-Group Length

For the given detachment frequency, the end-group length is a key parameter to dissociate the stretched chains. In this simulation, l_{cap} mainly selected as 0.01 while the theoretical expectation is about 0.02 in the dimensionless unit. The changes of l_{cap} due to other parameters, especially for p, are ignored with the background knowledge reported in section 1.3. It is noteworthy that change of l_{cap} also affects the energy barrier, W in Eq. (1.25), which, however, ignored throughout the study. The main reason is that change of β_0 will automatically account for τ_D, but the dynamics of the system do not sensitively depend on τ_D when the system is non-percolating. In consequence, the increasing l_{cap} with the same R_t value always increasing the dissociation probability in this simulation.

3.8 Effect of Dissociation Time

The natural time scales of this simulation are τ_D and τ_B with $\tau_D \geq \tau_B$. Because of repulsive and chain connector dynamics, we have additional time scales τ_R and τ_{DB}. With simple shear, the steady-state stress will response with the given shear rate in the regime based on those two time scales, which briefly to make three different sections that shows $\dot{\gamma} < \tau_D^{-1}$, $\tau_D^{-1} < \dot{\gamma} < \tau_R^{-1}$, and $\dot{\gamma} > \tau_R^{-1}$. Before going further, we can start with the case $\tau_D = \tau_R$ even though such a system is physically irrelevant, but only

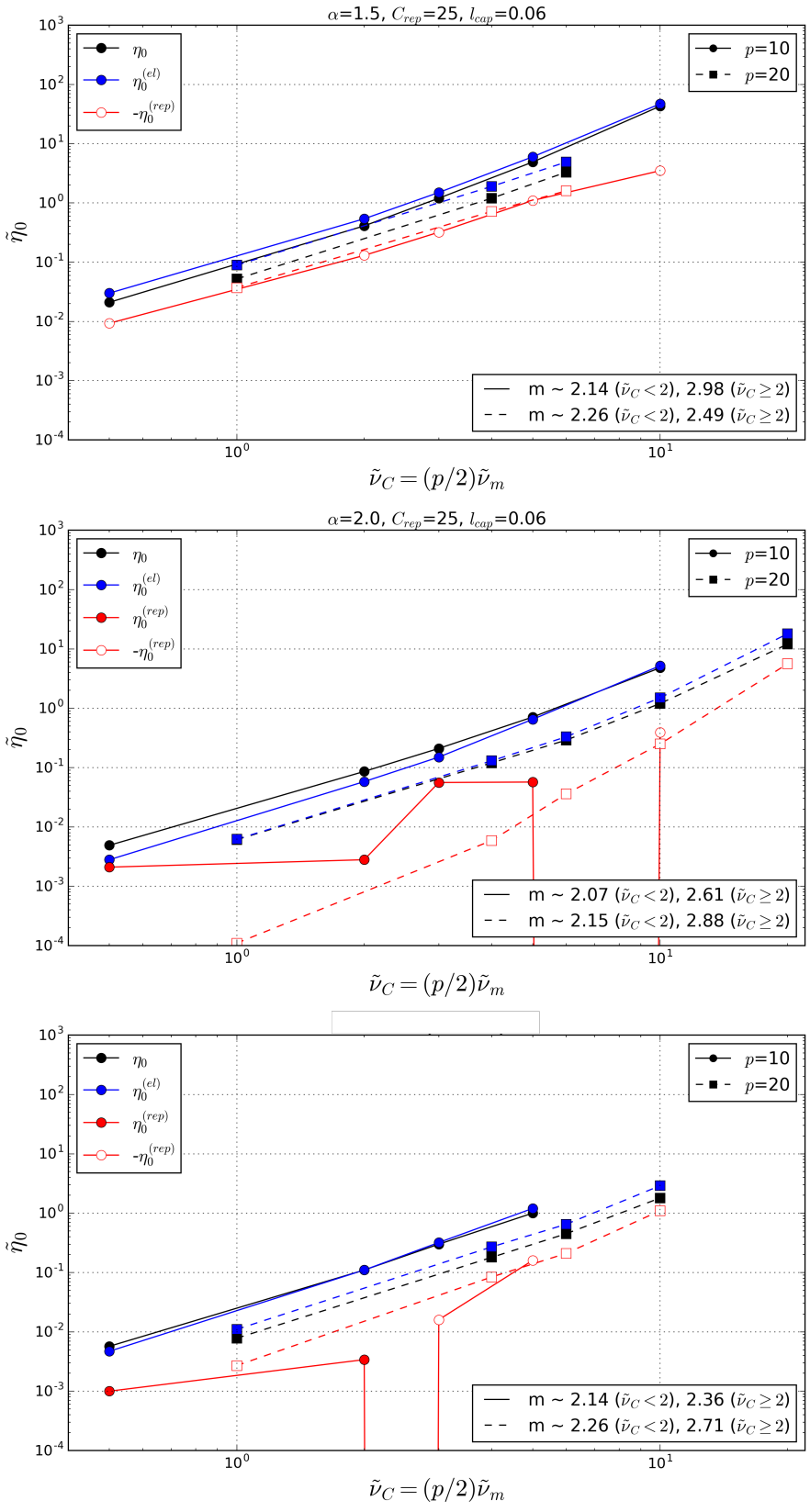

Figure 3.12: Measured zero-shear viscosity in equilibrium simulation. The test conditions are set with C_{rep}=25, $\tau_D = 25\tau_R$, p=10 and 20, and α=1.5 with l_{cap}=0.06 (top), α=2.0 with l_{cap}=0.06 (center), and α=2.0 with l_{cap}=0 (bottom).

two distinguishable regimes for non-equilibrium simulation. FENE is applied for the reference system, but the effect of FENE will be addressed in the other sections.

3.8.1 Dynamic Viscosity

Concerning complex viscosity from equilibrium simulation, as we already discuss the noise about FFT method for $\tilde{G}(t)$ with noise, the results will be scattered in the low Wi_R range because the noise is amplified at longer time scales in figure 3.11. In this specialize example can be decoupled two-elements Maxwell model where the each element relate to the elastic and repulsive contributions. Therefore, the complex viscosity can be shown with analytical form, that is shown as dashed line in figure 3.13 compared with FFT method as scattered green spots. The component-wise FFT is severely scattered to visualize, so it is not plotted. The overall contribution is well fitted between two different methods.

In the case for steady-state viscosity in the simple shear, each component is linear up to Wi_R becomes unity because of $\tau_D = \tau_R$ in this case. Then, the shear thinning is observed around $Wi_R = 1$ that is similar to the equilibrium results. Because of the computational performance, the $Wi_R > 10^1$ is used the same time step, so the unstable peak is observed, which is artificial due to the time step effects. Compare with complex viscosity, the system slightly deviates from Cox-Merz rule, but almost identical. We are not addressing this pilot test system for main objectives since the given parameters are physically irrelevant, but useful to identify different regimes as single time scale is applied.

The effect for time scale is significant for those two systems. As described in section 3.5.2, the components-wise contribution to the $\tilde{\eta}_0$ is negative when $\tau_D = 25\tau_R$. The detailed mechanism is already described, and it is confirmed by the $\tilde{\eta}(\dot{\gamma})$ that shows the negative contribution where the viscosity level is about 1.7 times different. This is due to the measured $\tilde{\eta}_0^{(rep)}$ is not accurate because of it is the minor contribution and largely suffers from system noise. Once $\tau_D \neq \tau_R$, the Wi_R regime can be identified as (i) $\dot{\gamma} < \tau_D^{-1} (< \tau_R^{-1})$, (ii) $\tau_D^{-1} < \dot{\gamma} < \tau_R^{-1}$, and (iii) $(\tau_D^{-1} <) \tau_R^{-1} < \dot{\gamma}$. The components-wise

contribution is highly sensitive for the regimes. Both of elastic and repulsive contributions are linear in the regime (i), the start to shear thinning for the elastic contribution in the regime (ii). Note that the repulsive contribution changes due to the response of the decreasing elastic contribution which leads the increasing (towards positive sign) for the elastic contribution. In the beginning of regime (iii), the shear thinning for repulsive contribution is observed after maximum peak as positiveness. It seems to be repulsive contribution is minor role such a system, but this is because of the chains in the reference system largely active to forms bridges. Therefore, $\eta^{(el)}$ becomes higher.

3.8.2 First Normal Stress Difference Coefficient

These distinguishable regimes also effect to the first normal difference coefficient (middle), $\tilde{\Psi}_1$, in the limited range for the Wi_R because the noise on $\tilde{\Psi}_1$ is higher than that of $\tilde{\eta}_1$. The amplified noise due to the fact of denominator since $\tilde{\Psi}_1$ is given by Eq. (1.43). The regimes are also captured in the same way, but it is importance to aware that the value of $\tilde{\Psi}_{1,0} = \lim_{\dot{\gamma}\to 0} \tilde{\Psi}_1(\dot{\gamma})$ becomes higher in $\tau_D = 25\tau_R$ case that suggests system hash higher anisotropy with implemented shear flow. It is easily understood as already described by Green and Tobolsky (1946) that the reforming of bridges is the way of isotropic. When a rate of dissociation/association is sufficiently fast, the chains will reform as the isotropic way, which is captured in the $\tilde{\Psi}_1$ for $\tau_D = \tau_R$ case. The two different time scale shows the changes for $\tilde{\Psi}_{1,0}$ is about 2 decade although the exact values on here are not clear. The bridge length distribution (bottom) shows the significantly shows such a tendency where the yellow is the $Wi_R = 1$ that is $Wi_0 = 1$ for $\tau_D = \tau_R$ case and $Wi_0 = 25$ for $\tau_D = 25\tau_R$ case.

3.9 Conclusions

In chapter 3, the sample conditions are selected to understand the role of the individual parameters, in particular for the equilibrium simulation. Because of the huge parameter space, we try to reduce the parameter space in a doable range (around 4000

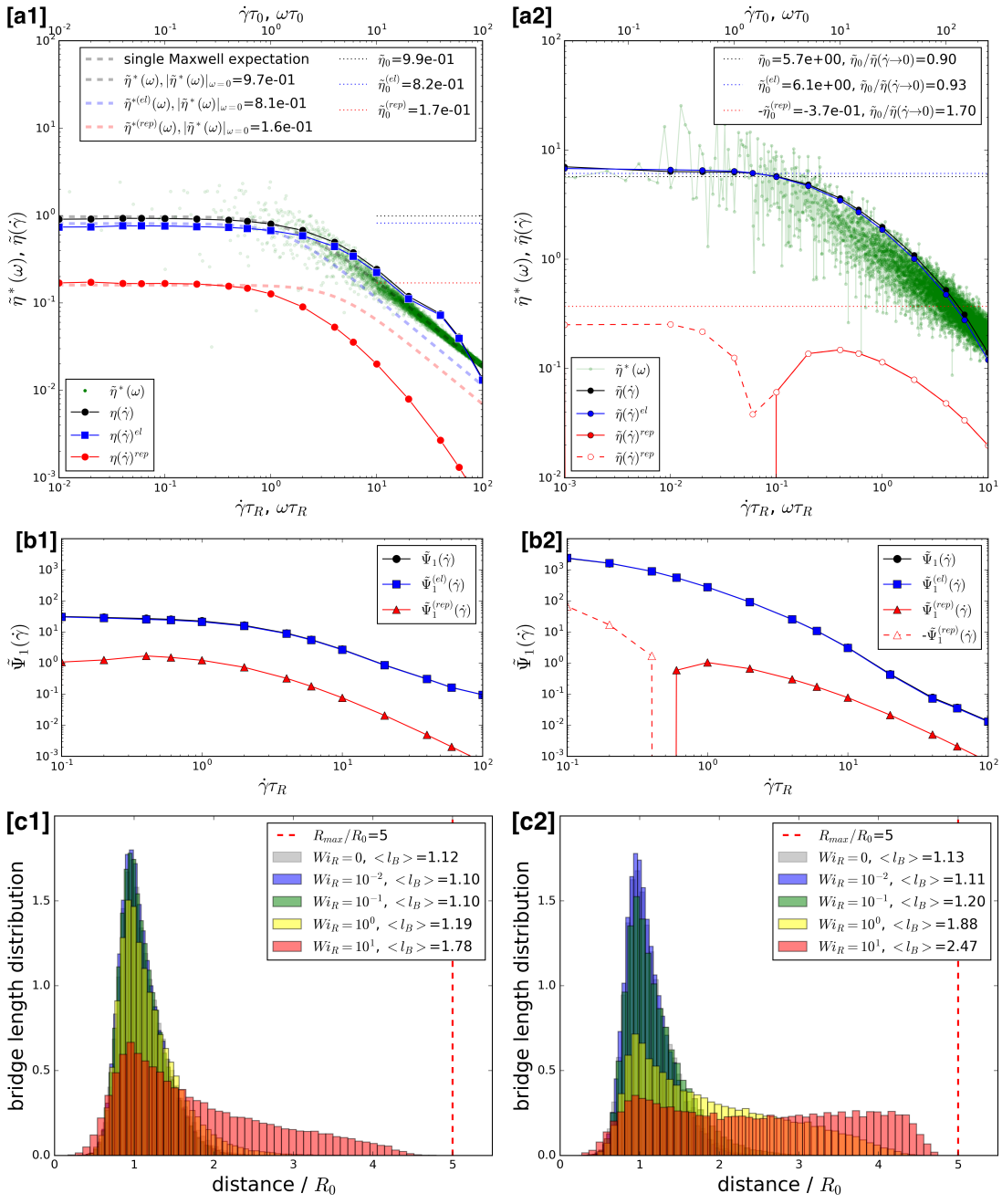

Figure 3.13: Comparison between dynamic viscosity from simple shear and complex viscosity [a∗], first normal stress difference coefficient, $\tilde{\Psi}_1(\dot{\gamma})$ [b∗], and bridge length distribution with respect to Wi_R [c∗]. The τ_D are given by τ_R [∗1] and $25\tau_R$ [∗2]. The rest of test conditions are ν_m=0.6, p=6, C_{rep}=25, α=1, and l_{cap}=0.06.

samples) in the equilibrium. For the given size ratio parameter, $\alpha = R_0/R_c$, the network-structure of the system can range from poorly connected, sparsely percolated, densely percolated, and aggregated cases, figure 3.4. It is noteworthy that the network connectivity for the given number density of micelle can be controlled by aggregation number, figure 3.3. The relaxation modulus, $\tilde{G}(t)$, is changed due to the network connectivity. The scaling exponents for $\tilde{G}(0)$ is an increasing function on α, where the transition of the scaling exponents due to the concentration is also observed as Uneyama et al. (2012), figure 3.8. Relaxation modulus is insensitive to the number density of micelle when the system is poorly connected, while the sensitivity changes due to connectivity, figure 4.5. The effect of topological time scale also depends on the network structure where the insensitivity of τ_D is observed in poorly connected case, which is not the case for the well-connected system, figure 3.10. The scaling exponents for zero-shear viscosity are in the range between 2 and 3, that is consistent with the experimental data (Uneyama et al. 2012), but the details of the scaling exponents depend on initial relaxation modulus and average relaxation time where both of the observables depend on the connectivity.

Chapter 4

Simulation Results of Selected Samples

4.1 Equilibrium Structures in the Selected Samples

4.1.1 Test Conditions

Parameters

In this chapter, we select few sample systems to understand our main reasearch objectives: (i) strain-hardening in shear startup, (ii) break-down of Cox-Merz rule, and (iii) shear thickening. Briefly, we performs more than 4000 equilibrium simulations tuning the parameters that summarized in table 4.1. From this result, we select representative samples to show reasonable scaling exponent in LVE: α=1.5 or 2.0, C_{rep}=25, p=10 or 14 (section 4.1.2), τ_D/τ_B=1. The choice of α is already discussed in conjunction with figure 3.3. The selection of p is suggested by studies on aggregation number in HEUR solutions, section 1.3.2, while C_{rep} is chosen so as to obtain that both repulsive and attractive (bridge) interactions contribute to the overall relaxation modulus. Indeed, if C_{rep} is too large, the repulsive contribution fully controls the dynamics whereas if C_{rep} is too small, micelle aggregation dominates. As regards τ_D, values larger than τ_m slow down relaxation, figure 2.10, thus making the code progressively more costly. The

Table 4.1: Summary of examined (dimensionless) parameters in equilibrium simulations and sample code name.

parameters	test conditions	S1	S2	S3
α	1.0, 1.1, $\cdots$, 1.9, 2.0	1.5	2.0	1.5
C_{rep}	10, 25, 50, 100	25	25	25
p	6, 10, 14, 20	10	10	14
l_{cap}/R_0	0, 0.01, 0.03, 0.06, 0.12	0.01	0.01	0.01
τ_D/τ_B	$1/C_{rep}$, 1, 10	1	1	1
R_{max}/R_0	Gaussian, 4, 3	3	4	3

choice of l_{cap} is dictated by the fact that larger values make shear thinning excessive, thus inducing instabilities that fall beyond the scope of the present paper. Such a selected samples are examined by non-equilibrium simulation in terms of $\tilde{\eta}(\dot{\gamma})$ compare with $\tilde{\eta}^*(\omega)$, then we decide l_{cap}/R_0=0.01. Finally, R_{max}/R_0 is set with half dimension for the PBC box at the highest concentration (section 4.1.1). For simplification, the basic sample conditions are also represented in table 4.2 where the sample codes are defined as S1, S2, and S3.

Maximally Extendable Chain Length and Size of PBC Box

As mentioned in section 2.2.4, cell-list is not applied for non-equilibrium simulation. The box dimension of PBC is restricted by number of micelles in the PBC box because of simulation time. To reach reasonable simulation time, we keep number of micelles in the PBC box no more than 600, which leads the computation time of non-equilibrium simulation within a single day scale. Note that, however, number of micelle in the PBC box smaller than 300 shows statistical poor both of repulsive and bridge interactions. Table 4.2 summerize dimensionless number density of micelles and its box dimension of PBC. In the current simulation code, however, the chain can be stretched no more than half of box dimension for each axis because of definition of minimum distance, Eq.

Table 4.2: The number of particles and box dimension at each number density of micelles. The bridge statistics of S1 at the given number density are reported.

$\tilde{\nu}_m$	N_p	L_D/R_0	f_C^+ (%)	f_{DC}^+ (%)	f
0.1	407	16	3.58	2.56	0.26
0.4	400	10	11.24	8.15	0.82
0.6	600	10	15.92	11.46	1.1
1.0	512	8	24.82	18.03	1.8
1.5	324	6	35.84	26.12	2.6
2.0	432	6	46.14	33.64	3.4
3.0	375	5	-	-	-

(2.64). If we perform non-equilibrium simulation in high shear rate, the bridges are extremly stretched, which introduce additional difficulties to simulate Gaussian chain or FENE chain with higher R_{max} values. Therefore, R_{max} is strictly bounded by the box dimension. For this reason, the effects of R_{max} has been examined in relatively lower concentrations. In these tests, no significant changes are observed between Gaussian, FENE with $R_{max} = 6R_0$, and FENE with $R_{max} = 3R_0$ in terms of stress or viscosity. Note that, f_C^+ is decreasing with decreasing R_{max}, but the stress level becomes similar range. In this context, we used R_{max} based on the half-box dimension of all concentration, which is $3R_0$ ($4.5R_c$ when $\alpha = 1.5$).

4.1.2 Distribution of Micelles and Bridge Statistics

For the sample with α=1.5 and p=10, $g(r)$ is already reported in figure 2.9 ($\tilde{\nu}_m = 1$ in the case of ATP). The first peak experience minor changes due to concentrations (no data shown). Figure 4.1[a] shows $g(r)$ and bridge length distribution of α=2 due to $\tilde{\nu}_m$. In the case of $\tilde{\nu}_m = 0.1$, no first peak is observed in $g(r)$, but smoothly reaches unity. It is noteworthy that $g(r)$ of RBD shows the significant first peak, figure 2.9. This first peak appears when $\tilde{\nu}_m$ is larger because it introduce additional bridges. Obviously, the

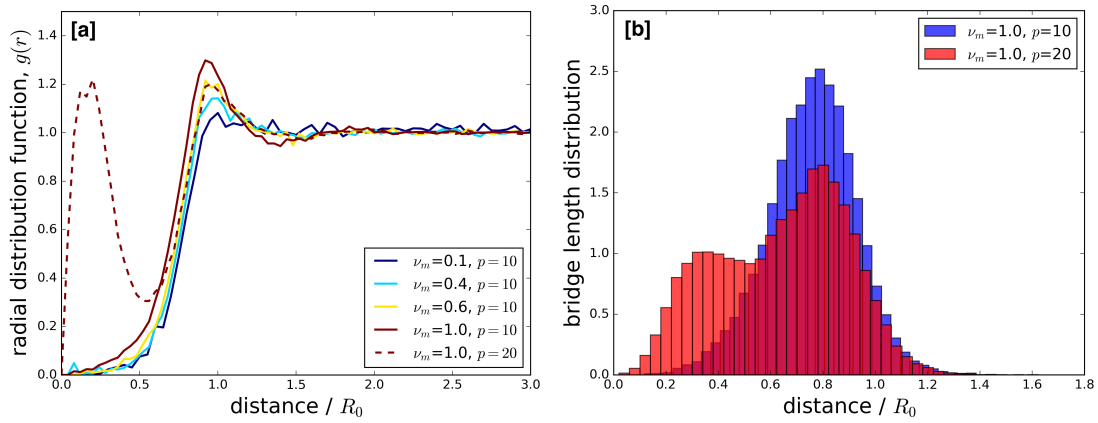

Figure 4.1: Radial distribution function for micelles [a] and bridge length distribution [b] where parameters are given by α=2, C_{rep}=25, p=10 (solid lines) and 20 (dashed lines), $l_{cap}/R_0 = 0$, $\tau_D = \tau_B$, and Gaussian chains. In panel [a], $\tilde{\nu}_m$=0.1, 0.4, 0.6, and 1.0. In panel [b], the only $\tilde{\nu}_m = 1$ case for p=10 and 20 are reported

dynamics of α=2 case are highly influenced by repulsive interaction compare with α=1.5 because of fraction of elastically active chains in the system, figure 3.3. Distributions of micelles for p=10 are homogeneous both of α=1.5 and α=2, but when p is increased, the situation is changed. In figure 4.1[a], p=20 case show two-peaks in the beginning unlike other conditions, which is also confirmed in 4.1[b] where p=10 (blue spectrum) is a single peak while p=20 (red spectrum) is two distingushable peaks in terms of bridge length distribution. Even if statistics are difference, PBC box itself is quite homogeneity by looking it directly, figure 4.2. For this reason, we choose p as 10 or 14 avoiding the initial peak in short-distance range before the major first peak in $g(r)$.

4.1.3 Network Connectivity and Relaxation Time

Network connectivity of sample systems are already reported in figure 3.3. The effect of micelle concentration on the relaxation modulus is reported in figure 4.3. In order to reduce noise, the procedure described in section 2.3.4 is applied with 5 realizations. The initial value $G(0)$ of the modulus scales with $\tilde{\nu}_m^2$, in reasonable agreement with experimental data (Uneyama et al. 2012). Figure 4.3 also shows that relaxation slow

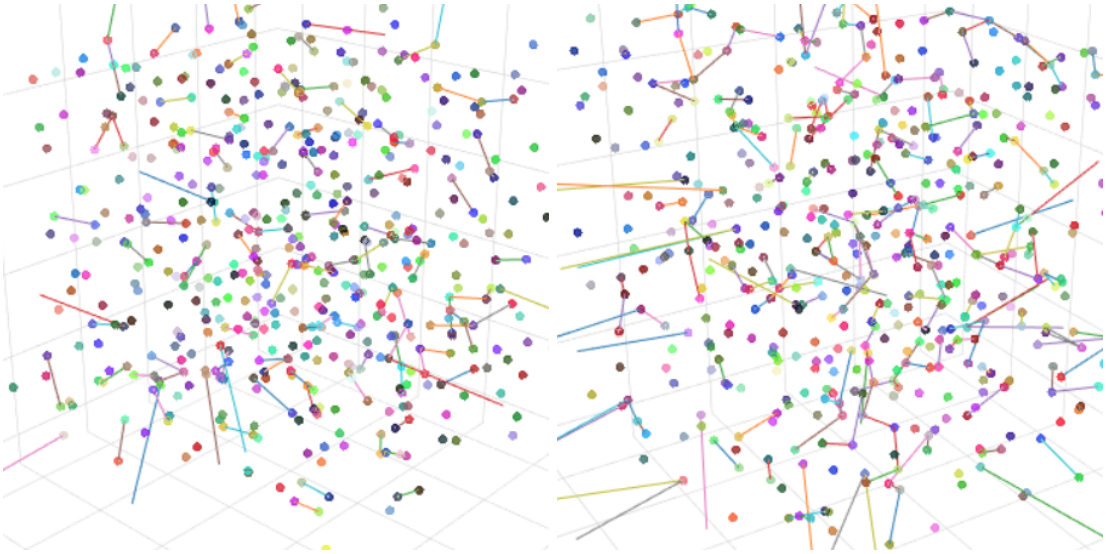

Figure 4.2: Direct visualization of PBC box for $p = 10$ (left) and $p = 20$ (right). The micelle distributions and bridge length distributions are reported in figure 4.1.

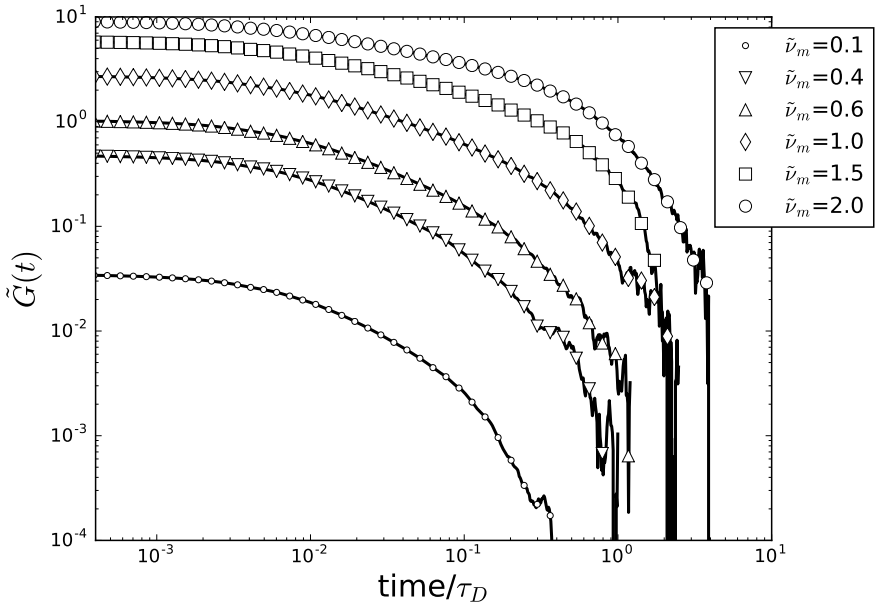

Figure 4.3: Relaxation modulus with different $\tilde{\nu}_m$ of S1. $\tilde{\nu}_m$ are given by 0.1, 0.4, 0.6, 1.0, 1.5, and 2.0 from bottom to top with different symbols described in legend.

down with increasing concentration. This is quantitatively confirmed in figure 4.4 where we report the mean relaxation time,

$$\bar{\tau} = \eta_0^{-1} \int_0^\infty tG(t)dt, \tag{4.1}$$

and the longest relaxation time τ_l, i.e., the reciprocal ultimate slope in a linear-log plot of $G(t)$. Figure 4.4[a] shows those relaxation times both for $p = 10$ and $p = 14$. Note that it should obviously be $\tau_l \geq \bar{\tau}$. At high concentrations, both $\bar{\tau}$ and τ_l scale with $\tilde{\nu}_m$ with an exponent ranging between 0.8 and 0.9, which is somewhat larger than the value 0.68 reported by Uneyama et al. (2012). It is noteworthy that this scaling exponents is sensitive α. By increasing α the number of bridges reduce as already reported in figure 3.3, and relaxation eventually becomes insensitive to $\tilde{\nu}_m$, the system losing its network-like properties.

Since the system does not follows single-mode relaxation, figure 2.12, $\tilde{\eta}_0$ should be measure through cutoff time scheme for viscosity function, Eq. (2.70) (see section 2.3.4). In this context, figure 4.4[b] shows $\tilde{\eta}_0$ with $\tilde{\nu}_m$ where the initial scaling exponent is started with 2 because of $\tilde{G}(0) \propto \tilde{\nu}_m^2$; then, the scaling exponents is changed to 3 that is consistent with the experimental data, figure 1.5. Uneyama et al. (2012) reports scaling exponents as $G^\circ \propto \nu_c^{2.3}$ and $t_0 \propto \nu_c^{0.68}$ in shear thickening regimes. As reported in figure 1.5, the reproduced scaling exponents of η_0 is about 3, which is closer to $G^\circ t_0 \propto \nu_c^{2.98}$ (experimental data is only minor differences when frequency is higher than cross-over frequency). Even if the simulation results cannot be described single relaxation time, we already observed $\tilde{G}^\circ \propto \tilde{G}(0)$ in figure 3.6. In this sense, it is worth to remark the results of scaling exponents of $\tilde{G}(0)$ with respect to $\tilde{\nu}_m$ in figure 3.8.

Before going further, it is useful to see relaxation modulus when $\alpha = 2$ where the number of elastically active chains are dramatically changed compare with $\alpha = 1.5$. Figure 4.5 reports normalized relaxation modulus with $\tilde{\nu}_m$ where no significant changes on relaxation time is observed, which is similar with RBD. The main reason of this additional selection to show results of non-equilibrium simulation is that such a condition sensitively capture the changes of micelle distribution to the dynamics because of its

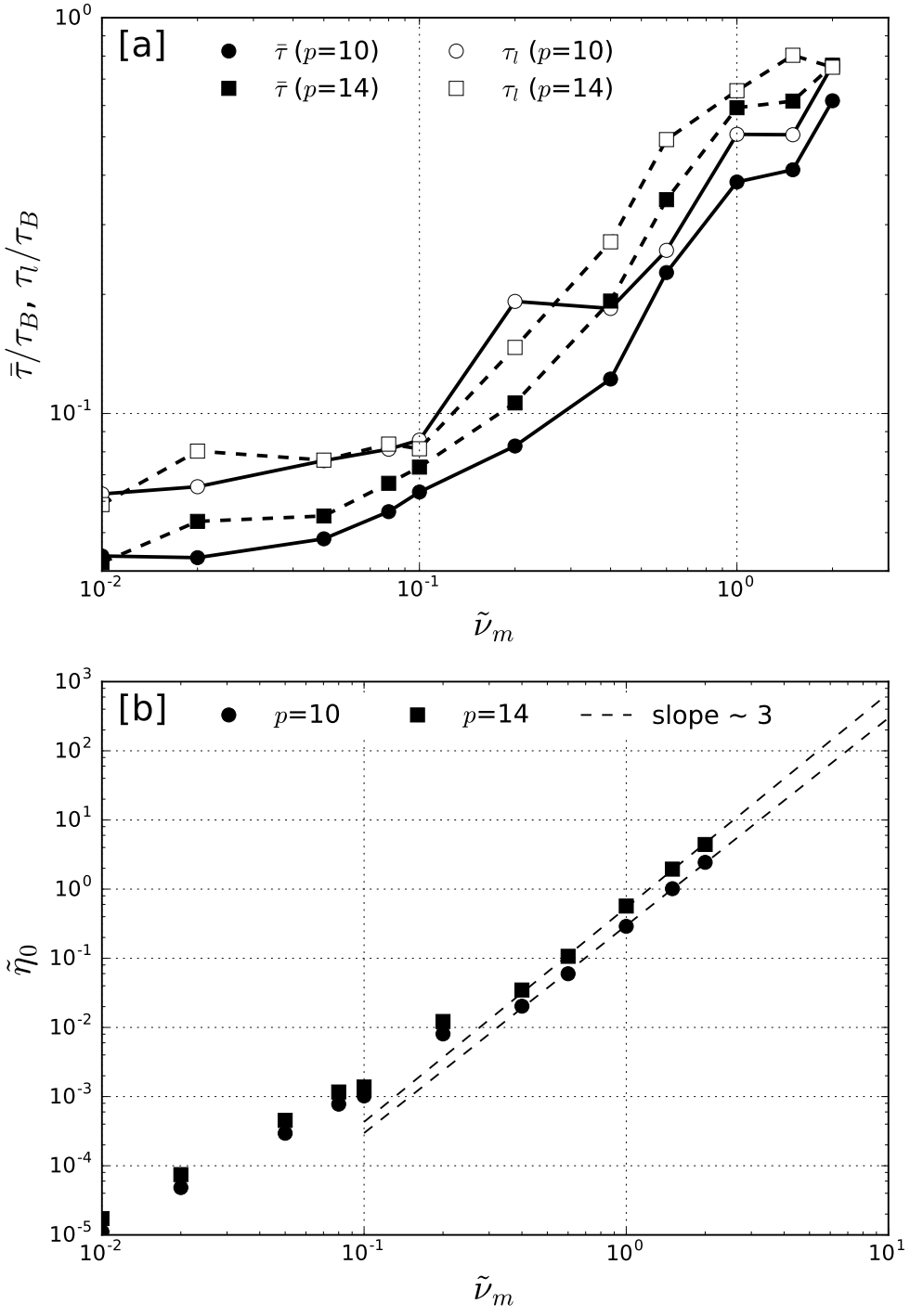

Figure 4.4: Mean and longest relaxation time [a] and zero-shear viscosity [b] obtained from $G(t)$ in figure 4.3. Symbols refer to different values of p, and lines are to guide the eyes.

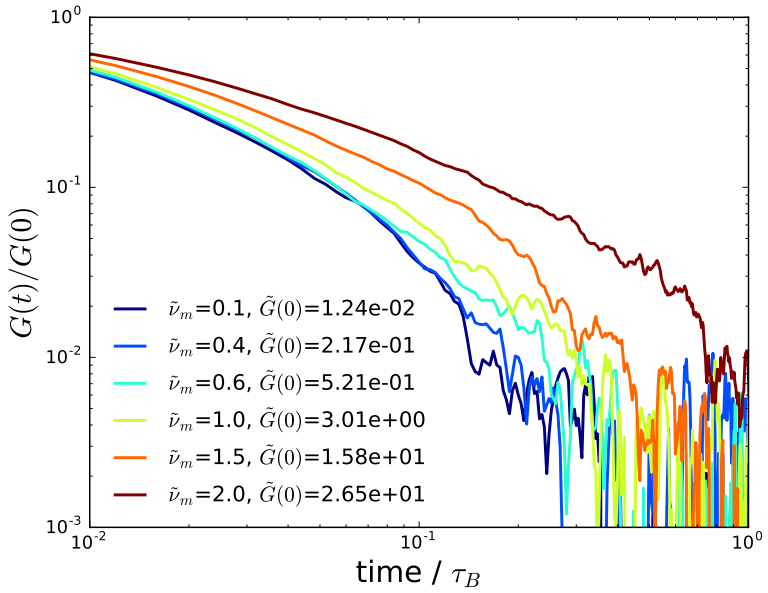

Figure 4.5: Normalized relaxation modulus with different $\tilde{\nu}_m$ of S2. $\tilde{\nu}_m$ are given by 0.1, 0.4, 0.6, 1.0, 1.5, and 2.0 from bottom to top with different colors described in legend.

relatively low contributions from bridge interactions.

Figure 4.5 report normalized relaxation modulus for $\alpha = 2$ that is insensitive with respect to concentration. It means the zero shear viscosity, η_0, is fully controlled by $G(0, \tilde{\nu}_m)$ where its scaling order is about 2.

4.2 Transient Response in Simple Shear

As described in the model section, we apply simple shear using Lees-Edwards sliding brick boundary conditions. During shear startup the most relevant observable is the shear stress growth function, Eq. (1.44). Because of large noise at small $\dot{\gamma}$ values, we take averages over 100 different realizations, starting from differential initial equilibrium boxes. Figure 4.6[a] reports results for $\tilde{\nu}_m = 1$ and for the standard set of parameter values. The dashed line represents the LVE envelope calculated by the viscosity function in Eq. (2.70). The small deviations at short times are due to poor statistics of $\tilde{\eta}^+(t;\dot{\gamma})$. When $Wi_B \geq 1$, the LVE envelope and $\tilde{\eta}^+(t;\dot{\gamma})$ essentially overlap. Conversely, when

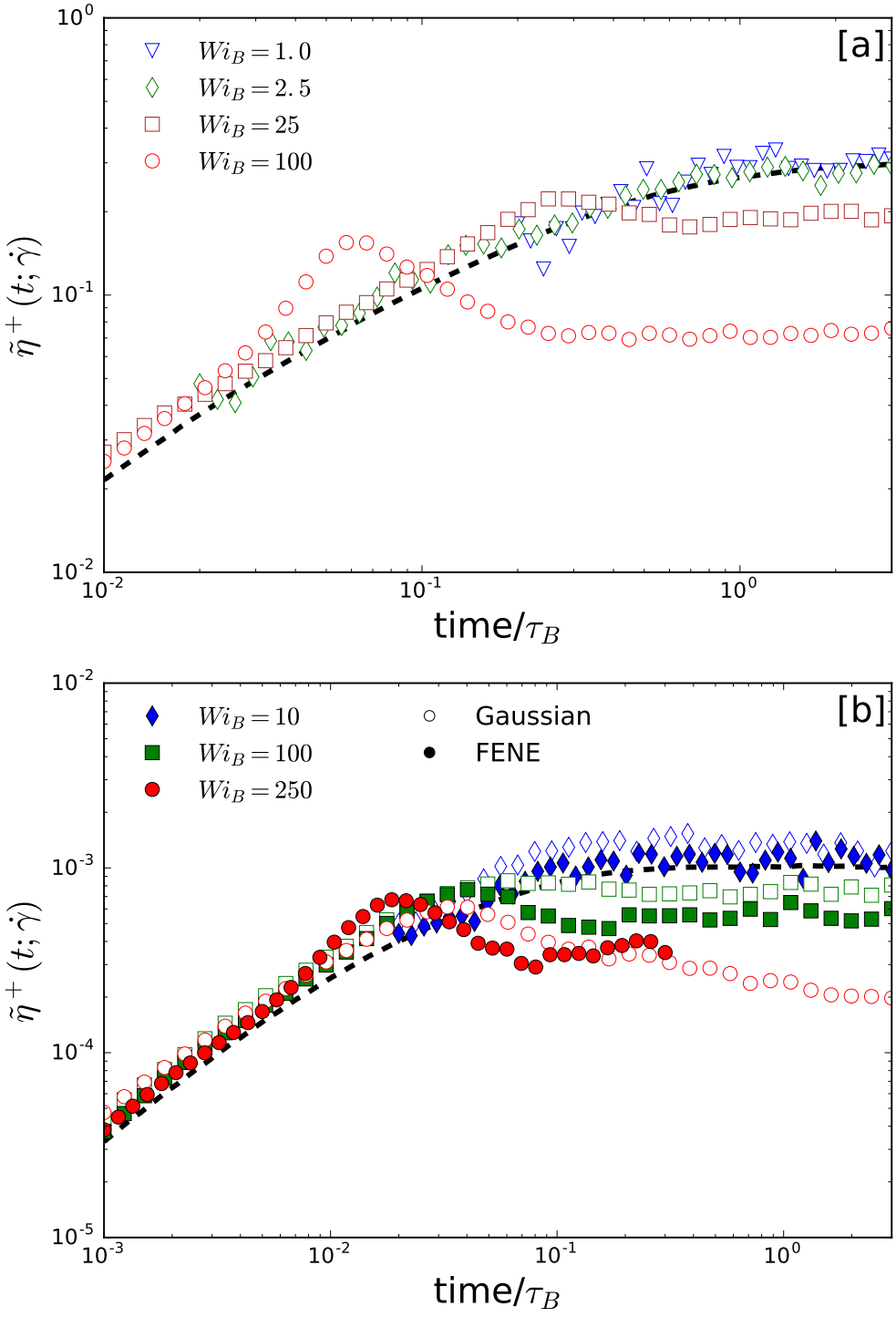

Figure 4.6: Stress growth function during shear startup of ATP with FENE chains at $\tilde{\nu}_m = 1$ [a] and comparison between Gaussian and FENE chains at $\tilde{\nu}_m = 0.1$ [b] for S1.

$Wi_B \gg 1$, the $\tilde{\eta}^+(t;\dot{\gamma})$ curves exhibit strain hardening, before declining and approaching a steady-state value (lower than η_0), thus resembling the experimental data of Suzuki et al. (2012). To better understand the origin of the strain-hardening behavior, figure 4.6[b] shows $\tilde{\eta}^+(t;\dot{\gamma})$ with both Gaussian and FENE chains at the smaller concentration $\tilde{\nu}_m = 0.1$. Indeed, at lower concentrations, the same number of micelles (enough for good statistics) is accommodated in a larger box, wherE Also Gaussian chains can be dealt with. In view of the lower number of elastically active chains, noise is larger than for $\tilde{\nu}_m$=1, but accuracy improves for $Wi_B > 10$. Such a comparison in figure 4.6[b] shows that strain hardening only occurs for FENE chains while Gaussian ones go to steady state without any hardening behavior.

4.3 Steady State in Simple Shear

4.3.1 Cox-Merz Rule

The steady-state viscosity $\tilde{\eta}(\dot{\gamma})$ for the systems examined in figure 4.6 is reported in figure 4.7[a] together with other results referring to systems at different micelle concentrations. In slow flows, the viscosity exhibits the classical Newtonian plateau corresponding to the zero-shear viscosity. With increasing values of the shear rate, the viscosity starts thinning, and the onset of the shear thinning phenomenon shifts to lower shear rates with increasing $\tilde{\nu}_m$. This is consistent with the fact that the mean relaxation time increases with increasing concentration, figure 4.4. Figure 4.7[a] reports the first normal stress difference coefficient, $\tilde{\Psi}_1(\dot{\gamma})$, that shows a thinning behavior similar to $\tilde{\eta}(\dot{\gamma})$, though the onset of the $\tilde{\Psi}_1(\dot{\gamma})$ thinning occurs at lower values of Wi_B. Comparison between panels [a] and [b] also shows there is a minor shear thickening in $\tilde{\eta}(\dot{\gamma})$ at the largest concentration ($\tilde{\nu}_m$=2), which is not revealed by $\tilde{\Psi}_1(\dot{\gamma})$. It should be noted that in all the $\tilde{\nu}_m$ range explored in figure 4.7, the elastic contributions $\tilde{\eta}^{(el)}(\dot{\gamma})$ and $\tilde{\Psi}_1^{(el)}(\dot{\gamma})$ to $\tilde{\eta}(\dot{\gamma})$ and $\tilde{\Psi}_1(\dot{\gamma})$ in fact coincide especially after onset of shear thinning, thus implying that the repulsive contribution is negligible. In figure 4.7[a], we also report the complex viscosity, $\tilde{\eta}^*(\omega)$, in order to check the possible validity of the Cox-Merz rule through the way of section

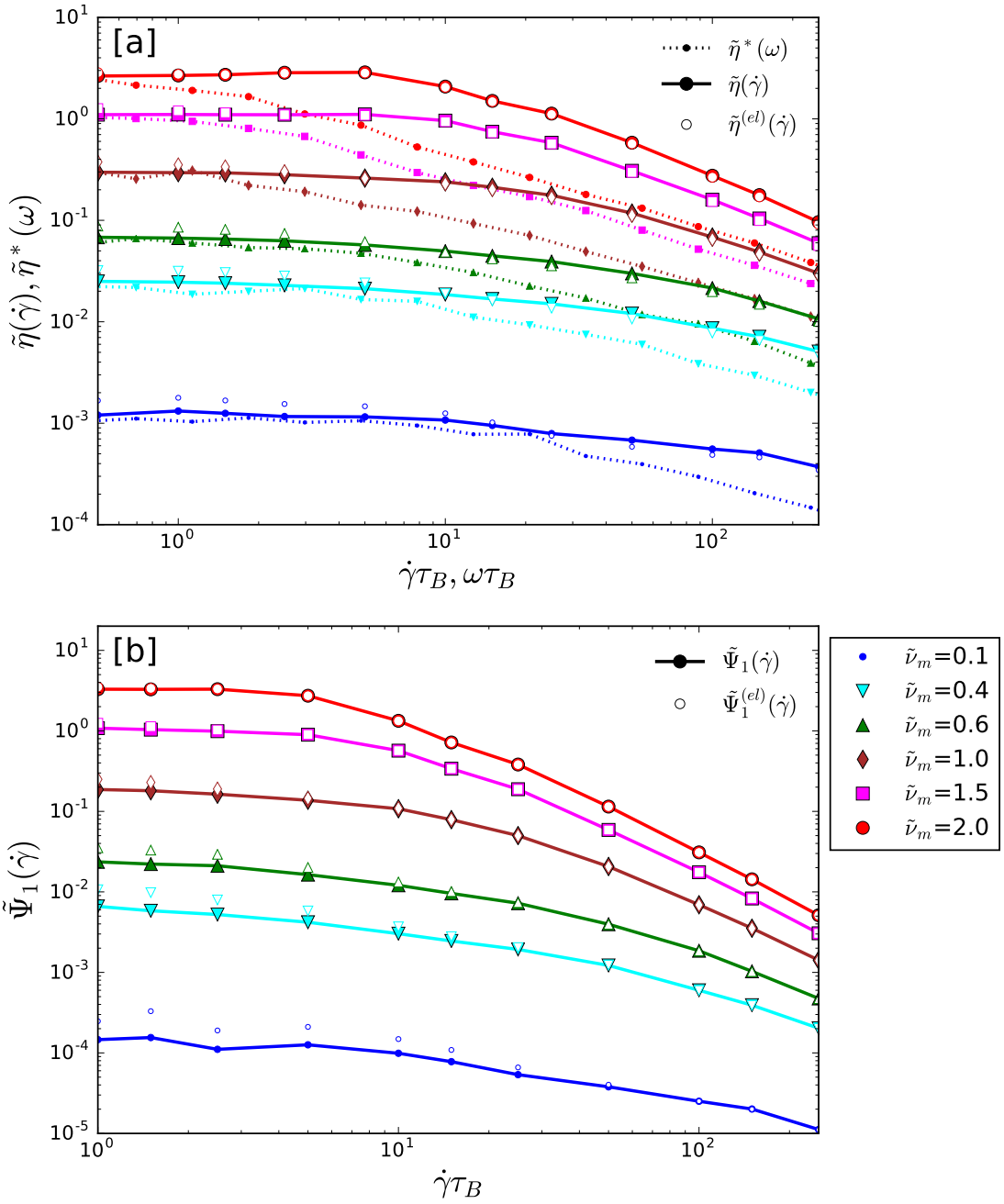

Figure 4.7: Steady-state shear viscosity $\eta(\dot{\gamma})$, and complex viscosity $\eta^*(\omega)$ from LVE [a], and first normal stress difference coefficient $\Psi_1(\dot{\gamma})$ [b] for S1.

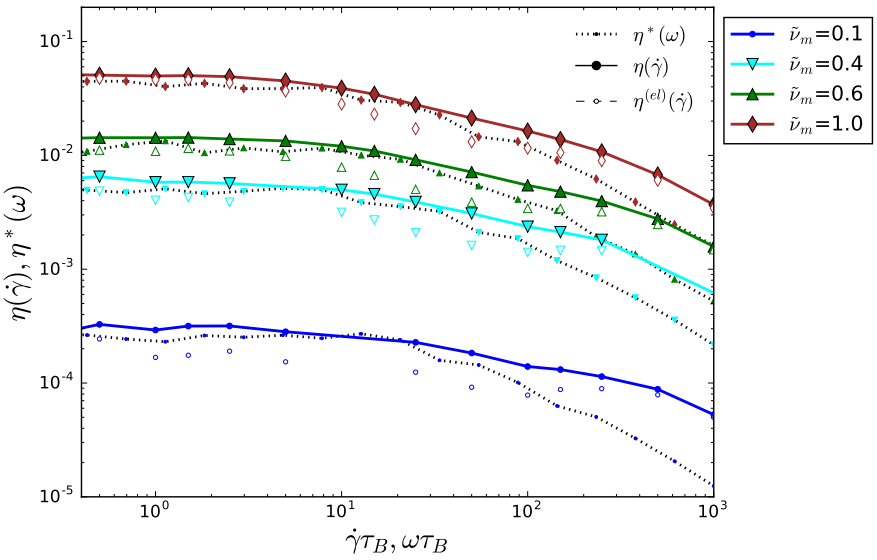

Figure 4.8: Steady-state shear viscosity $\eta(\dot\gamma)$, and complex viscosity $\eta^*(\omega)$ from LVE [a], and first normal stress difference coefficient $\Psi_1(\dot\gamma)$ [b] for S2.

9.1.4. Figure 4.7[a] clearly reveals that the Cox-Merz rule is not obeyed since $\tilde\eta(\dot\gamma)$ shear thins significantly beyond $\tilde\eta^*(\omega)$.

In the case of $\alpha = 2$, figure 4.8 shows broad but spontaneously changes of $\tilde\eta(\dot\gamma)$ before reaching a certain power-law. In this range, $\tilde\eta(\dot\gamma)$ and $\tilde\eta^*(\omega)$ are similar to each other; then, deviation is occurred around the kink. Again, the Cox-Merz rule is not obeyed, but the shape of the viscosities are different compare with figure 4.7.

4.3.2 Elastically Active Bridges

Figure 4.9[a], showing the effect of flow on the f_C^+ and f_{DC}^+ of S1, reveals that shear thinning is due to flow-induced loss of bridges. However, such a loss occurs at shear rates higher than the reciprocal relaxation time of LVE, thus explaining breakdown of the Cox-Merz rule. Notice that f_C^+ systematically decreases with increasing shear rates, at all concentrations, while, remarkably, the f_{DC}^+ shows a shear thickening phenomenon. It is noteworthy that f_{DC}^+ directly connected with functionality f of the system with

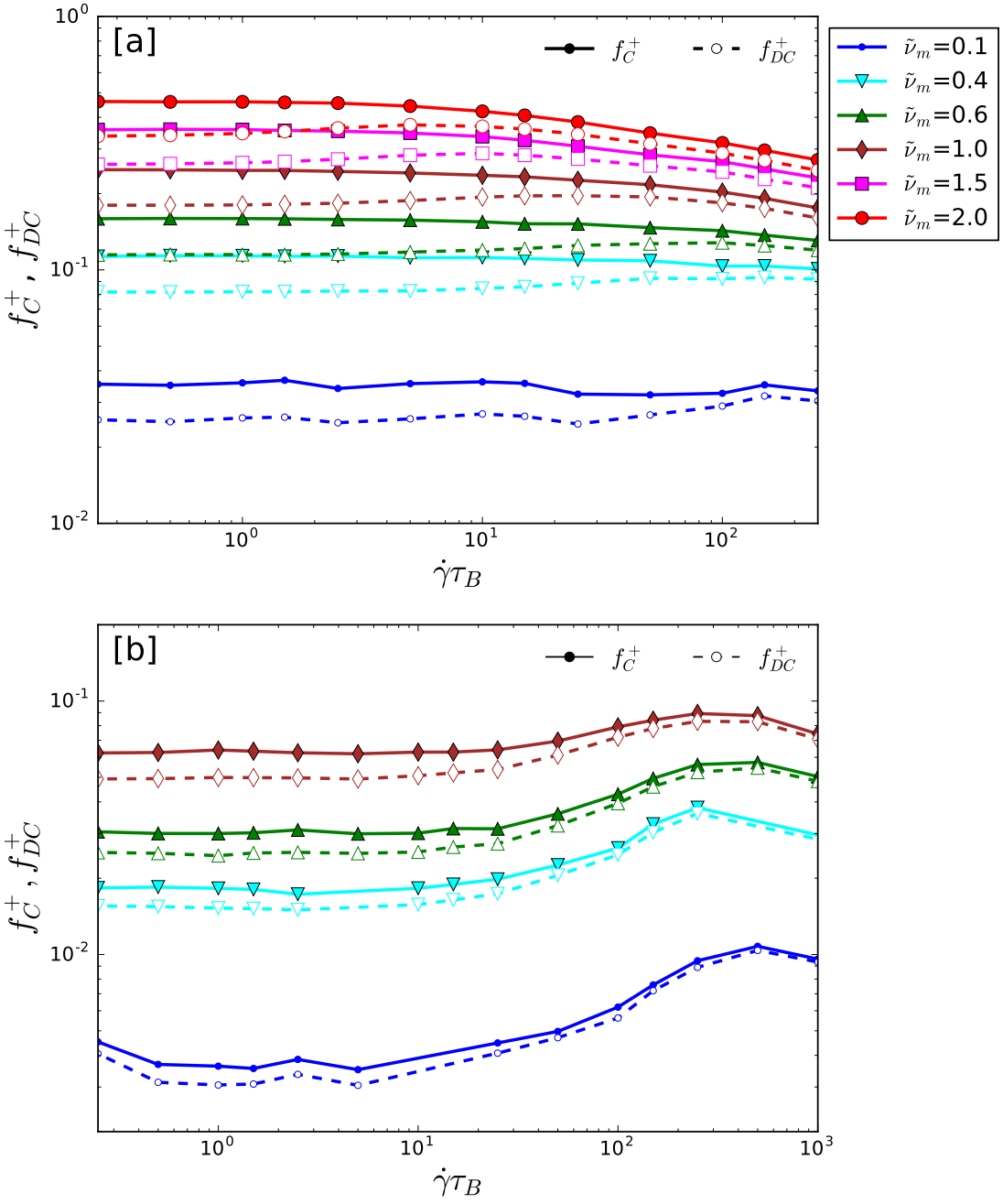

Figure 4.9: Fraction of elastically active chain f_C^+, and of distingushable chains f_{DC}^+, as a function of shear rate of S1 [a] and S2 [b].

f_{DC}^{+} and aggregation number, p, through

$$f = pf_{DC}^{+}. \tag{4.2}$$

In the case of figure 4.9[b], however, we observe increasing of f_C^+ that similar to the shear-induced bridge formation reported in Tam et al. (1998). The reason to increase f_C^+ will be checked in the later studies using micelle distribution.

4.3.3 Pair Correlation Function in Simple Shear

Pair Correlation Function on xy-Plane

In the simple shear flow, the PCF projected into xy-plane, $g(x, y)$, shows anisotropic distribution of micelles when $\dot{\gamma}$ is sufficiently larger, where the laterial direction z remains isotropy. It is noteworthy that Foss and Brady (2000) reports about hard-sphere in with with projected pair-correlation and observe anisotropy for $g(x, y)$ but isotropic $g(x, z)$ and $g(y, z)$ in fast flows. As reported in the following figures 4.11 and 4.10, the blue sphere represent sparse distribution due to the repulsion where its size is directly given by the micelle diameter, R_0. The resolution of $g(x, y)$ depends on time average (and size of box) where the statistics are relatively small in lower number density, $\tilde{\nu}_m$=0.1, so the sparsness of particles decreases the average value. In the higher concentration in lower shear rate, the blue circle is clearly observed which suggest isotropic distribution on xy-plane.

With bridge interaction, the blue circles are started to distorted *slightly* when the shear rate is faster than the reciprocal loop-dissociation time, which is the slowest dynamics. This small anisotropy is related with $Wi_R = 0.4$ case along all the figures, but relatively clear in higher concentration regime, $\tilde{\nu}_m = 1.0$ in figure 4.11. It is obvious that the effect is strong when the shear rate is higher than reciprocal repulsive time, τ_R^{-1}. All the data shows clear anisotropy due to the shear through the distorted blue circle. As regarding S2, the sample relatively insensitive due to the shear rate because of lower f_C^+. In this case, the anisotropy is becomes visible when the shear rate is about τ_R^{-1} rather than τ_D^{-1}.

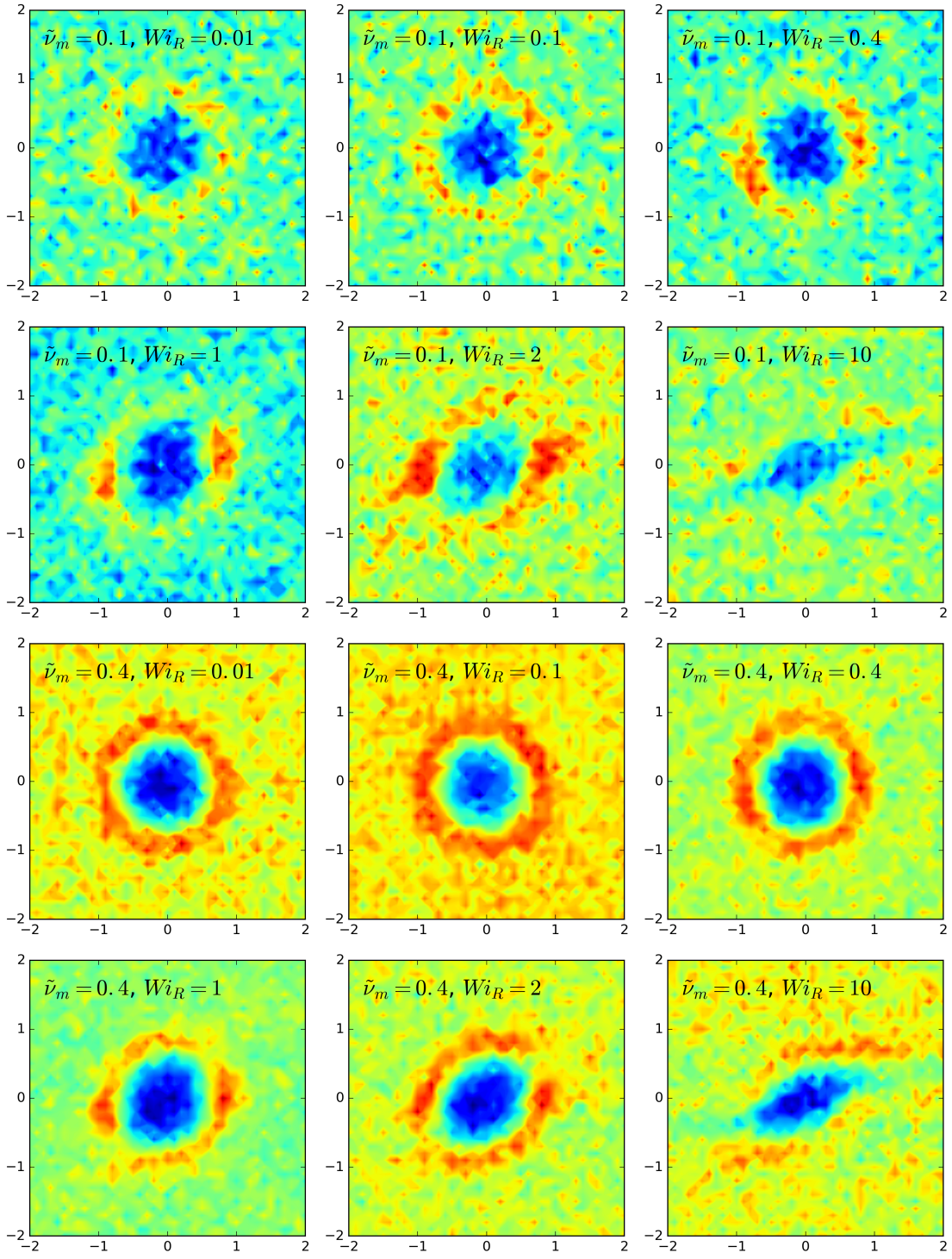

Figure 4.10: Pair correlation function in xy projected plane where the condition is the same with $\tilde{\nu}_m$=0.1 and α=1.5 for S1.

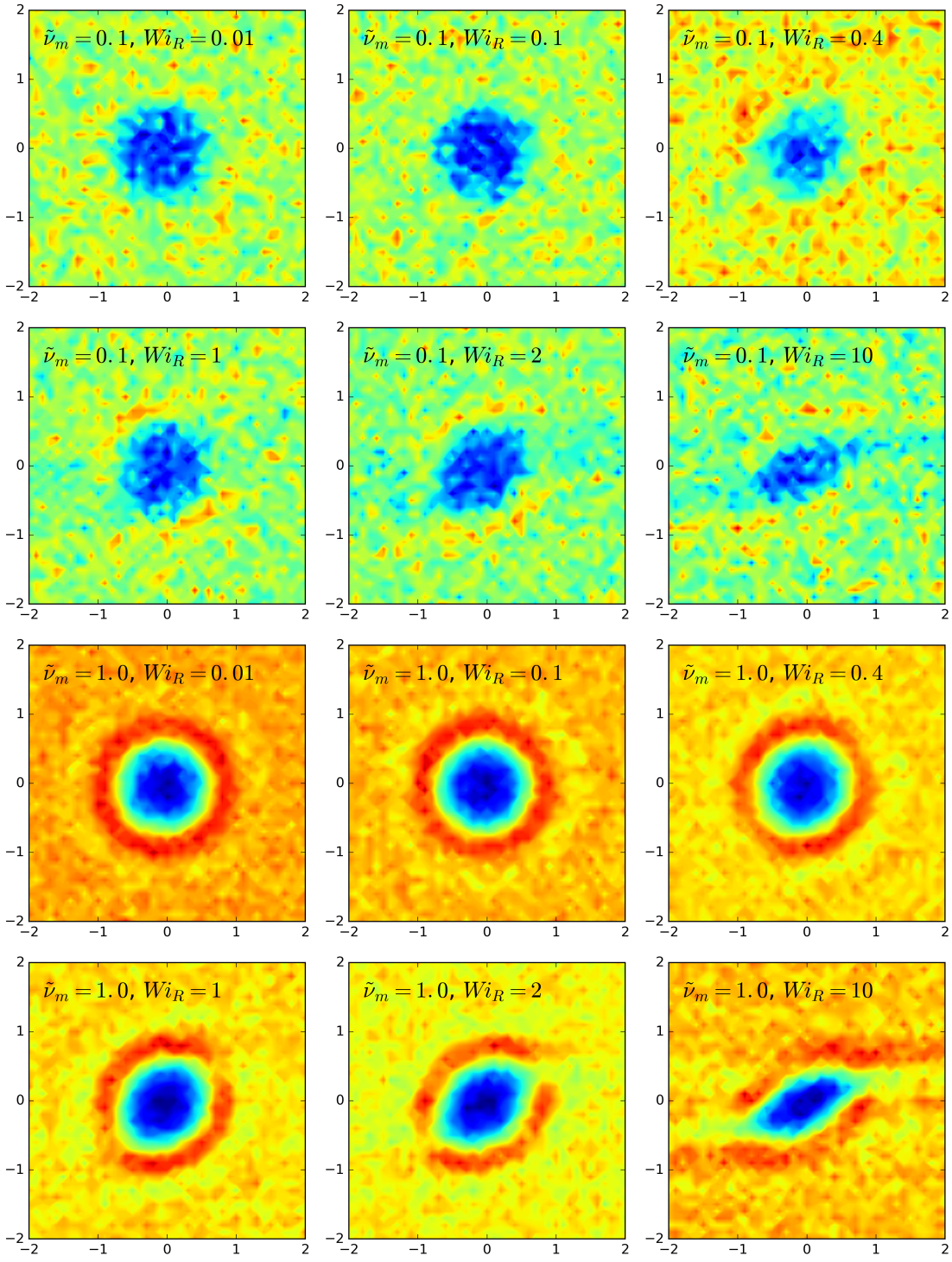

Figure 4.11: Pair correlation function in xy projected plane where the condition is the same with $\tilde{\nu}_m$=0.1 (up) and $\tilde{\nu}_m$=1.0 (down) for S2.

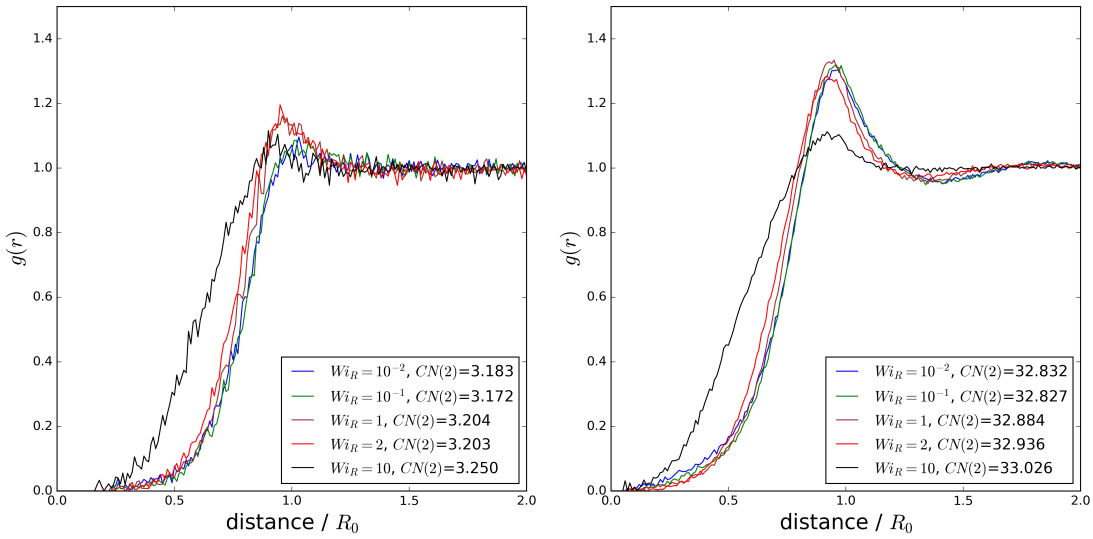

Figure 4.12: Pair correlation function, $g(r)$, under the shear with the number density of micelle, $\tilde{\nu}_m$, as 0.1 (left) and 1.0 (right) in α=2 for S2.

Average Over Angles: Radial Distribution Function

The changes of elastically active bridges are related to the micelle distribution in spatially since the association map is the only function of distance, Eq. (2.40). Because of its spherical indifference, $g(r)$ is useful to understand the suggestion probability of the system for kinetics, figure 4.1. Increasing $\dot{\gamma}$ makes smaller maximum peak distance, and also peak intensity is increased in $\tilde{\nu}_m$=0.1 while the peak intesnity is not distinguishable in the $\tilde{\nu}_m$=1.0. This affect the association map through Eq. (2.40) where the lower distance and higher peak intensity indicate the higher probability of forming bridges. Note that the normalization factor for the Boltzmann distribution is chosen as the cumulation of all the possible bridge formation, Eq. (2.43).

The suggestion probability is proportional to the number at the given distance, which can be measured through the cumulation of $g(r)$ called coordination number, Eq. (9.30). Figure 4.13 reports coordination number measured up to $2R_0$ normalized by its number density of micelle, $\tilde{\nu}_m$, so we can compare the reduced $CN(2R_0)$ in the same range of scales. The changes of normalized CN due to $\tilde{\nu}_m$ shows that sensitivity of expected num-

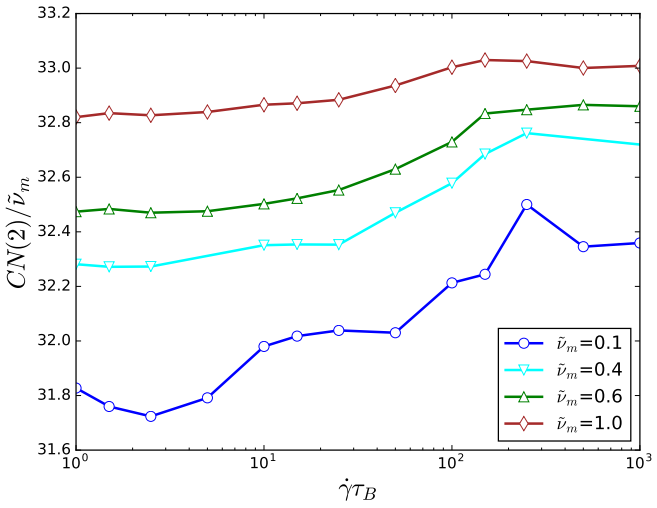

Figure 4.13: Normalized coordination number up to the dimensionless distance $r = 2R_0$ as a function of shear rate for different micelle number densities. Parameters are the same with figure 4.12.

ber within $2R_0$ is decreasing with increasing concentrations. Note that the $CN(2R_0)/\tilde{\nu}_m$ with $\tilde{\nu}_m$ will be the same when the system does not have any itneractions. Here $2R_0$ is twice higher than the maximum distance for repulsive contribution, so the compensation of repulsion in the $g(r)$ is already addressed. In this context, the changes between $CN(2R_0, \tilde{\nu}_m = 1.0)/\tilde{\nu}_m$ and $CN(2R_0, \tilde{\nu}_m = 0.1)/\tilde{\nu}_m$ are due to the changes of bridge interactions.

Note that the coordination number itself without normalization, the value indicate the expected number of particles within the given distance, $2R_0$ in this case. Therefore, the shear effects significant in the blue line ($\tilde{\nu}_m$=0.1) while it becomes minor in the red line ($\tilde{\nu}_m$=1.0). Concerning the decision step to the association, Eq. (2.43), higher suggestion number indicate reducing the loop-forming probability. Note again that distance at the maximum peak intensity is also decreasing with Wi_B, which indicate even the same coordination number, the probability of loop-forming in the decision step is reduced. Combining these two effects, we can expect f_C^+ in figure 4.9 against dissociation of bridges due to shear. In consequence of the sensitivity dependency with the number

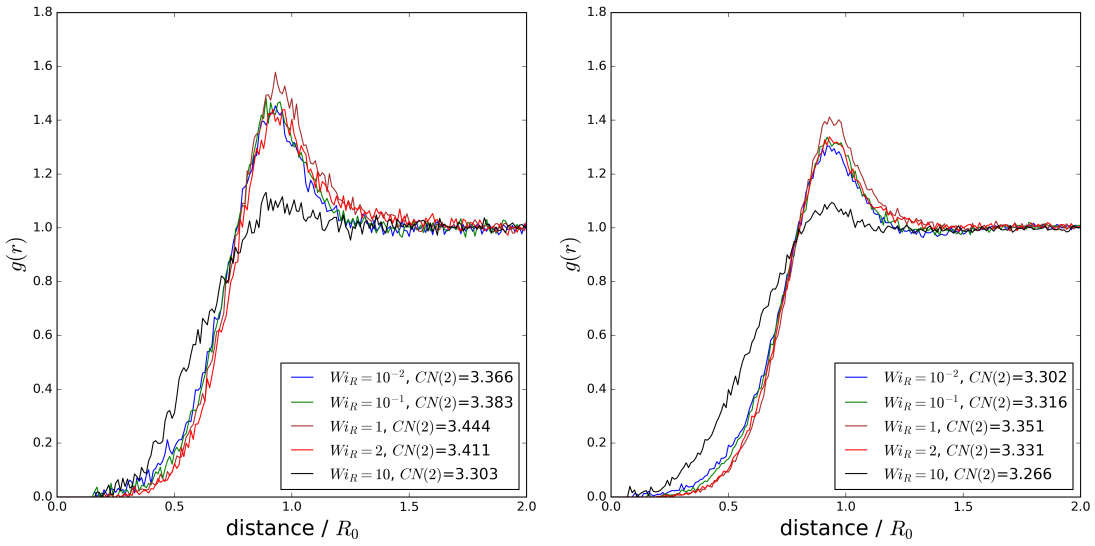

Figure 4.14: Pair correlation function, $g(r)$, under the shear with the number density of micelle, $\tilde{\nu}_m$, as 0.1 (left) and 0.4 (right) in α=1.5 for S1.

density of micelle, the deviation on Cox-Merz rule stronger in lower concentration while it becomes weaker in the higher concentration, section .

4.3.4 Bridge Length Distribution

So far, the only the number of elastically active chains are addressed. The bridge length distribution $\{l_b\}$ is also important to the stress level. Figure 4.15 reports average bridge length $\bar{l}_b$ for S1 [a] and S2 [b] cases where its standard deviations are also reported on the figure as vertical bar for lowest and highest concentrations. There are no significant changes on S2 since the system has much lower connectivity for all the range of concentrations. In the sample S1, however, the rate of chain stretching is gradually increasing with $\tilde{\nu}_m$, which is believed by the force balance on the subjected junctions. In higher concentrations, we have more connectivity where the connections are aligned in shear directions. Imagine a chain stretching as figure 4.16, the retraction becomes efficient when there are no other connectivity. If network connectivity becomes larger, the retraction is unfavorable due to the force balance with each connected bridges, which

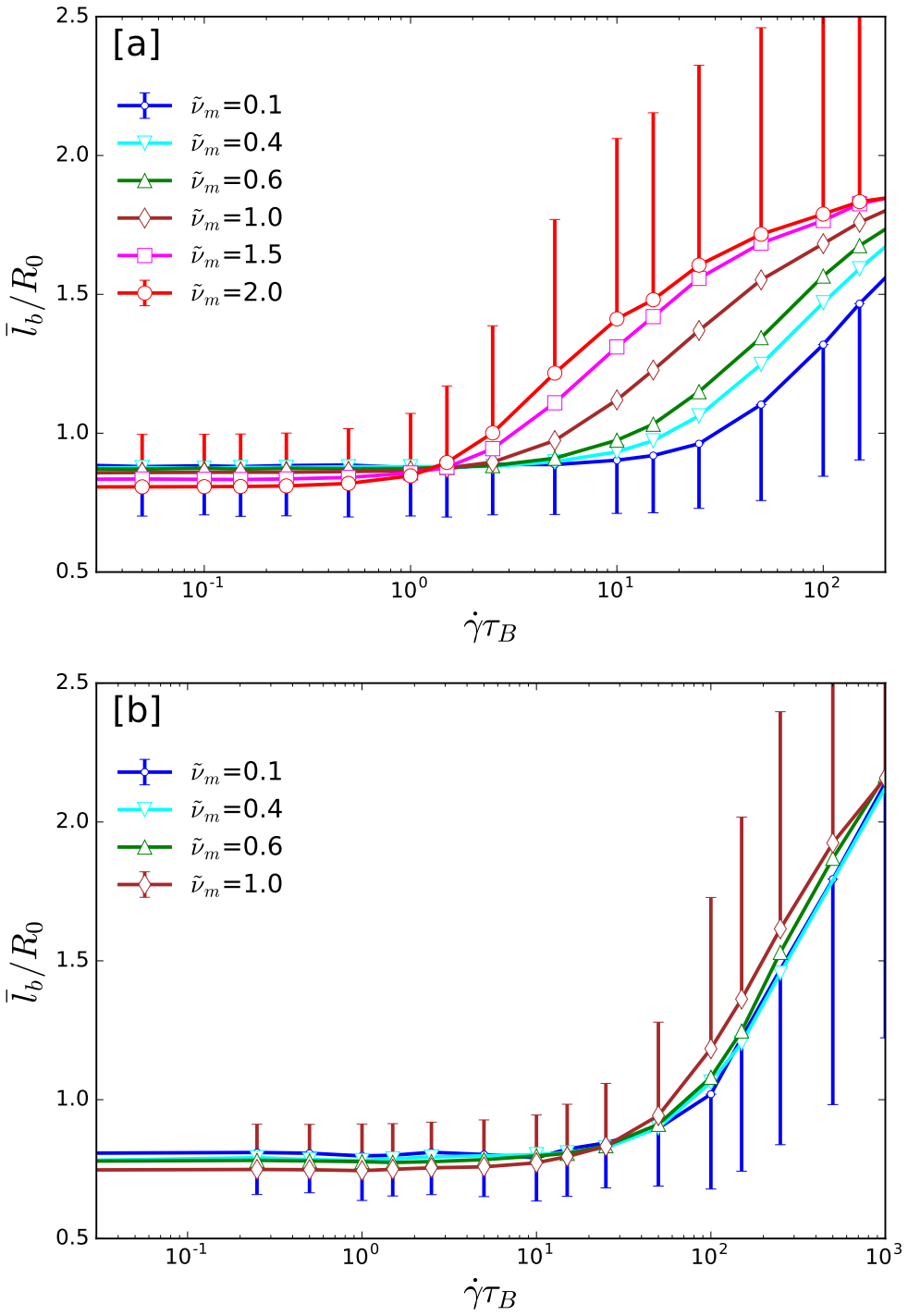

Figure 4.15: Average bridge chain length $\bar{l}_b/R_0$ with its standard deviation (vertical bars) of the bridge length distribution (for the lowest and highest concentrations) for S1 [a] and S2 [b].

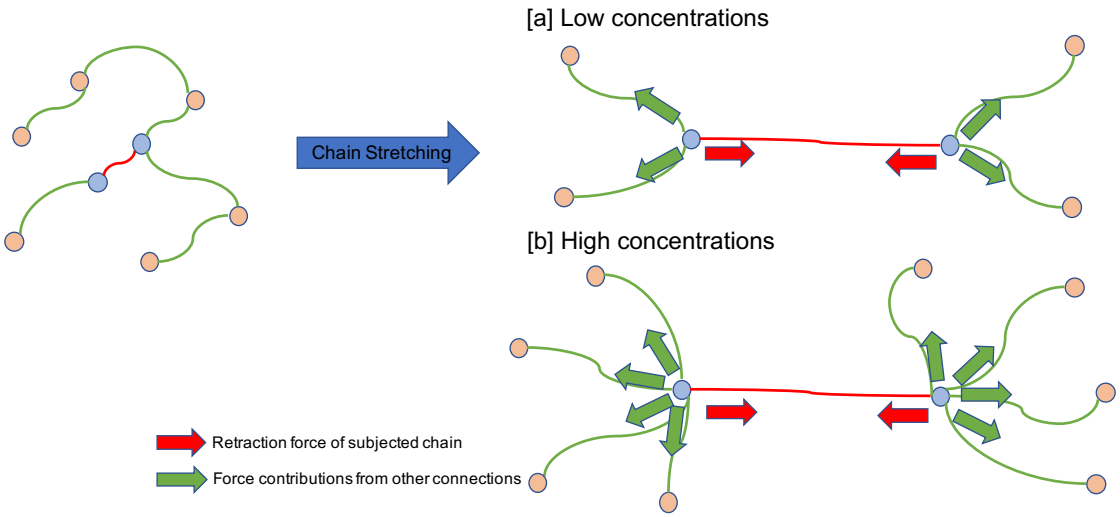

Figure 4.16: Schematic diagram of retraction force contribution in the way of force balance of subjected junctions. For the same level of stretched chains, higher connectivity makes difficulty to retract the given chain, which suggest the change of the rate of chain stretching in S1.

makes difficult to relax for short bridge lengths.

In this context, without dissociation, the chain stretching is more effective in higher concentration (or highly connected networks). Concerning about dissociation, such a stretched chains are dissociated faster thorugh Eq. (2.34), but the effect is relatively minor as reported in figure 4.7. Recall figure 1.6, the $\tilde{\nu}_m = 2$ case can be even lower than the lowest concentration regime (10 g/L case). This interpretation suggest to travel parameter space further in the way that increasing aggregation number p so we have more connectivity at the same $\tilde{\nu}_m$.

4.4 Shear Thickening

We noted above that one of the shear viscosity curves in figure 4.7[a], specifically that at $\tilde{\nu}_m$=2, appeared to exhibit a mild shear thickening. Here we show that a minor change in one of the parameters amplifies the shear thickening effect. We move the

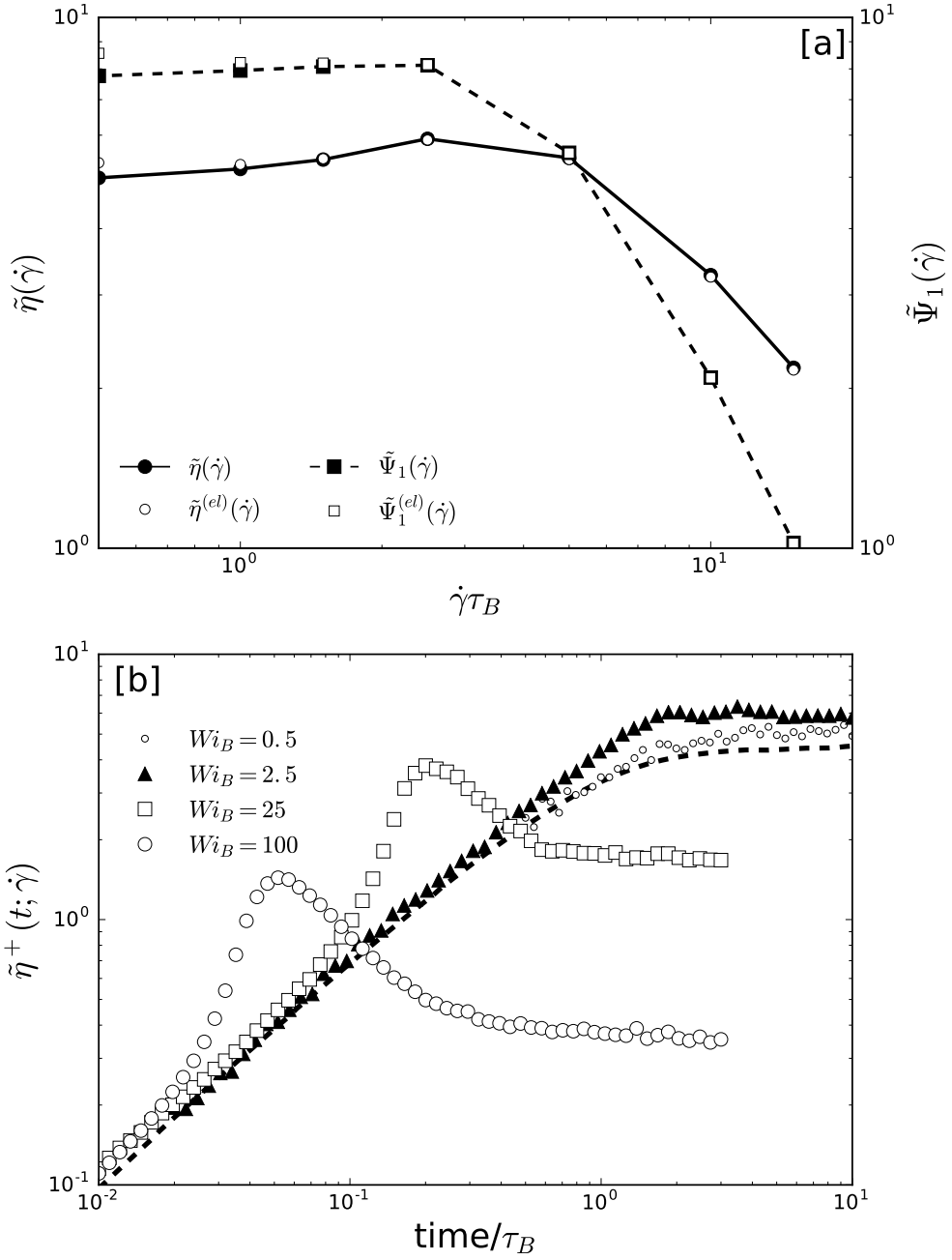

Figure 4.17: Steady-state viscosity and first normal stress different coefficient vs. shear rate [a] and shear stress growth function during startup [b] at $\tilde{\nu}_m = 2$ of S3.

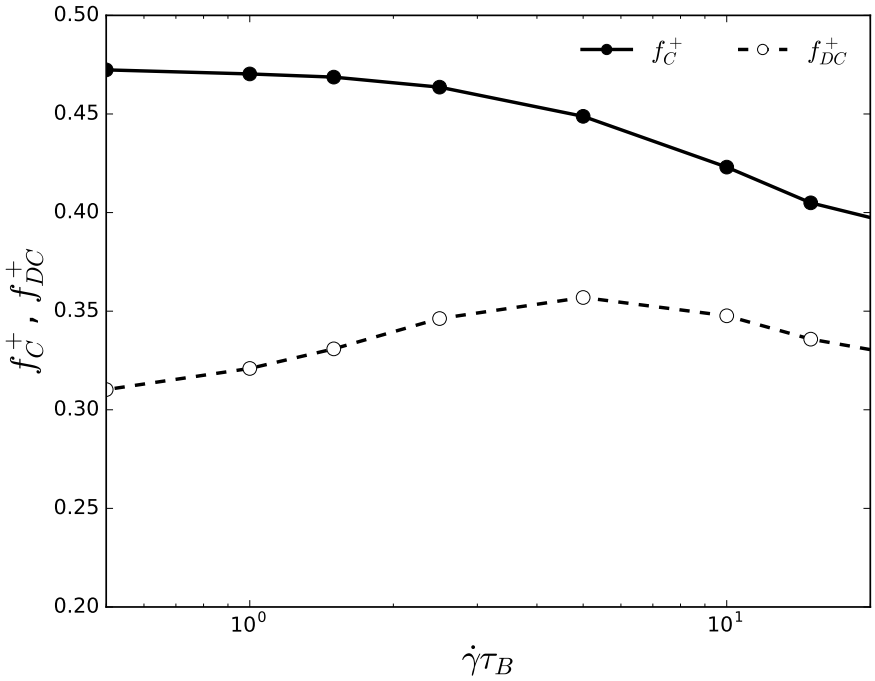

Figure 4.18: Fraction of elastically active chains, indistinguishable f_C^+ and distinguishable f_{DC}^+, with shear rate in shear thickening sample, S3.

average number of chains per micelle from p=10 to p=14, and obtain the results shown in figure 4.17.

Figure 4.17[a] reports for $\tilde{\nu}_m$=2 both $\tilde{\eta}(\dot{\gamma})$ and $\Psi_1(\dot{\gamma})$, clearly showing a shear rate region of viscosity shear thickening, in fact virtually absent in $\Psi_1(\dot{\gamma})$, in qualitative agreement with the experimental data of Suzuki et al. (2013). Quantitatively, we find a ratio $\max[\eta(\dot{\gamma})]/\eta_0$ of about 1.2, to be compared with the value of 1.4 found by Suzuki et al. (2013) at the lowest concentration. We expect that larger shear thickening effects could be obtained by further reducing the parameter l of the hydrophobic chain ends because larger values of the elastic force are required to detach bridge chains, but we do not show results for such a case. Figure 4.17[b] shows shear startup curves for several shear rates, confirming the significance of the shear thickening phenomenon at low rates, and the appearance of strain hardening at high ones.

Similar to section 4.3.2, figure 4.18 shows the decreasing of bridge chains while in-

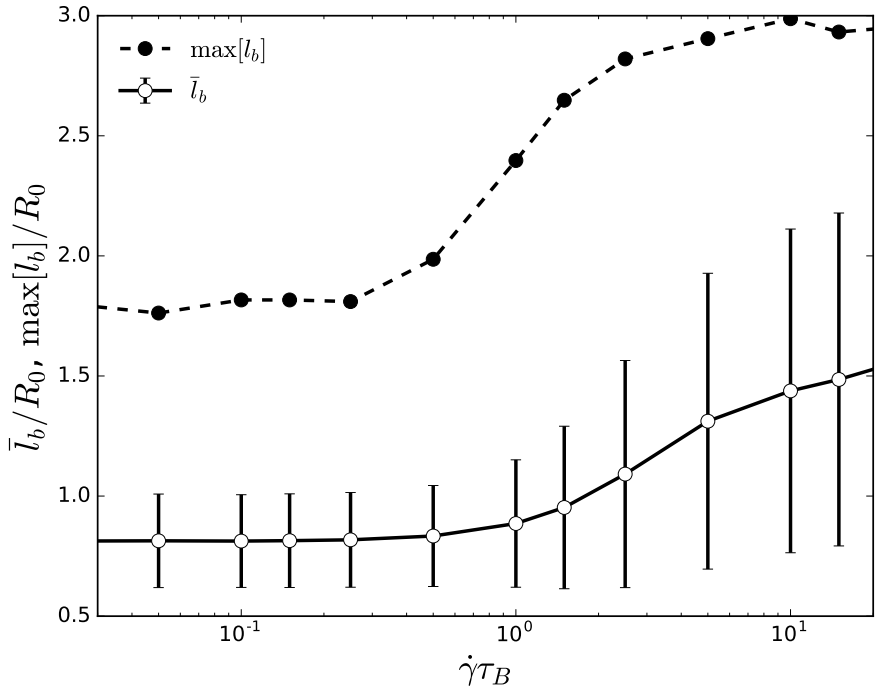

Figure 4.19: Average bridge chain length $\bar{l}_b/R_0$ with its standard deviation (vertical bars) of the bridge length distribution (for the lowest and highest concentrations) and maximum length of bridge chains max[l_b] for S3.

creasing of functionality (linear f_C^+ and f_{DC}^+ vs log $\dot{\gamma}\tau_B$). The mechanism is already described in section 4.3.2, but here we emphasize that about 15% of f_{DC}^+ (or f) is increased at highest $\tilde{\eta}(\dot{\gamma})$ conditions.

Figure 4.19 shows chain stretching of S3 with $\dot{\gamma}$ with its maximum bridge length max[l_b]. No significant changes are observed compared with figure 4.15, so the efficiency of chain retracting scheme is still in hold as figure 4.16.

From this study, further investment or higher concentrations is necessary in order to verify concentration effect to the shear thickening. In the tested concentration regime, table 4.2, only the highest concentrations show shear thickening that suggest the samples S1 and S3 are at $\tilde{\nu}_m$=2 case is one of most dilute concentration in the experimental data (Suzuki et al. 2013). Further increasing the p to 10, shear thickening is again obtained

with values of $\max[\eta(\dot{\gamma})]/\eta_0 \approx$1.2, 1.4, and 1.3, for $\tilde{\nu}_m$ =1.0, 1.5, and 2.0, respectively, probably indicating that the effect eventually disappears with increasing concentration, as shown by data Suzuki et al. (2013).

4.5 Conclusions

Based on the physical insight from chapter 3, chapter 4 studies details about the selected samples, table 4.1, where S1 exhibits more network-like conditions while S2 exhibits poorly connected system, so the repulsive Brownian dynamics is dominant. In the comparison between complex viscosity, $\tilde{\eta}^*(\omega)$, and steady-state viscosity, $\tilde{\eta}(\dot{\gamma})$, the break-down of Cox-Merz rule is globally observed when l_{cap} value is sufficiently small (about 0.01), figures 4.7 and 4.8. One possible reason for the break down of Cox-Merz rule can be the existence of highly stretched chain, figures 4.15, because of the lower l_{cap} values. In sample S2, the deviation between linear and non-linear viscosities is decreasing with increasing the number density of micelle, figure 4.8, which is consistent with the experimental observations (Suzuki et al. 2013; Xu et al. 1996). In the poorly connected system, S2, the increases of elastically active chains is observed, figure 4.9[b], especially at the lowest concentration. In the case of well-defined network-like structure, S1, such a shear-induced bridge formation is not observed. Increasing functionality with a certain shear rate (the steady-state viscosity becomes power-law with shear rate) is observed in both S1 and S2. We also observed anisotropically distributed micelle in the shear flow in pair correlation function in xy-projected plane, figures 4.11 and 4.10, where its angular average (radial distribution function) shows that the first peak shifts to the lower distance and also changes of its intensity, figure 4.12. The coordination number normalized by number density of micelle suggests that the change of coordination number is more sensitive to the lower number density of micelle than that of higher density case. For the transient response, the overshoot before relaxing to steady-state is observed for FENE chains while Gaussian chains follow LVE envelope before approaching steady-state, figure 4.6. By increasing the average number of chains per micelle, a shear

thickening phenomenon is observed, more pronounced in the shear viscosity than in the first normal stress difference (figure 4.17) consistently with the recent data of Watanabe and coworkers (Suzuki et al. 2012, 2013).

Finally, it is fair to say something about the assumption of the simulation. The repulsive coefficient, C_{rep} is given by its pre-averaged value in the box, which means C_{rep} does not change due to the aggregation profile of individual micelle. The aggregation number, p, is given by 10 and 20 as lower and higher working samples that make comparable in the experimental range, figure 1.2. However, the effect of p into the size of the micelle is ignored because of its minor role to the hydrodynamic radius of the micelle, Eq. (1.31). The hydrodynamic interaction (HI) is ignored throughout the study since the research objective is to understand rheological behavior due to the network properties, but it is worth to implement HI effect to see the dynamical changes especially for the poorly connected system.

Modeling of Linear Polymers in Fast Flows

Chapter 5

Non-Equilibrium Molecular Dynamics of Oligomeric Chains

5.1 Introduction

Polymeric liquids exhibit a very complex rheological behavior, especially in fast flows as those encountered in processing applications. Traditional rheological models based on macroscopic, continuum-level approaches are giving the way to molecular models, i.e., to the so-called molecular rheology. In this context, molecular dynamics simulations are progressively becoming a very useful tool to investigate the dynamics of polymeric liquids, thanks to the increasing computational power of available computers. However, in order to deal with the long time scales relevant for polymer rheology, most simulations have been performed by introducing some level of coarse graining, i.e., by "lumping" groups of atoms into beads endowed with force fields determined in such a way to match properties of the more detailed simulations. The lowest level of coarse-graining is achieved in the so-called united-atom simulations where hydrogen atoms are "merged" with larger atoms like carbon or oxygen (Frenkel and Smit 2001). At the opposite extreme, it is worth mentioning simulations where the polymer is replaced by a single bead, as in the so-called RAPID approach developed by Briels and cowork-

ers (Santos de Oliveira et al. 2014). Most molecular dynamics simulations have been performed under equilibrium conditions, but in recent times there has been an increasing interest for non-equilibrium molecular dynamics (NEMD) simulations with the aim of studying the effect of flow on polymer dynamics (Baig and Harmandaris 2010; Ianniruberto et al. 2012). Here, in particular, we briefly summarize our recent research activity based on NEMD simulations aiming at investigating possible flow effects on the monomeric friction coefficient, ζ. Indeed, all existing molecular theories for polymer rheology are based on the assumption that, since ζ is a local monomeric property, flows of practical interest in rheology are not fast enough to modify it. In polymers, however, the thermal relaxation rate of the molecule can be sufficiently slow that flows can induce conformation changes. In particular, when flows (or deformations) start stretching the molecules by inducing some orientational anisotropy of the monomers, there is no reason to assume that the friction coefficient remains unperturbed. This is particularly true in the case of monodisperse polymer melts where all molecules behave in the same way. In those systems, any chain is surrounded by similarly stretched chains, and this anisotropic environment may "act" on the test chain in a way that can be different from equilibrium. In particular it is highly tempting to assume that flow-induced molecular alignment determines a reduction in the monomeric friction coefficient. Since friction is a local property, the effect of flow on it can be sensitive to the chemical structure of the polymer. For this reason we decided to resort to detailed, united-atom molecular dynamics simulations. The chemistry of choice was polystyrene (PS). This was motivated by recent data on monodisperse PS melts in fast extensional flows (Huang et al. 2013b) revealing only moderate chain-stretch-induced strain hardening effects. This unexpectedly "soft" behavior of PS melts is fully compatible with the assumption that friction becomes less and less important because of flow-induced monomeric alignment. In order to gain computing time, and since monomeric friction is a local property, the simulations were limited to short polymers, i.e., to oligomers, the aim being that of proving the existence of possible flow-induced friction-reduction effects. Furthermore, we have limited so far our NEMD simulations to shear flows, which can easily be run indefinitely

in time, thus allowing to determine flow effects on the molecular mobility in steady-state conditions, as described in the next section.

5.2 Methods

The most natural way of measuring the friction coefficient of the oligomer consists in performing the (numerical) experiment of pulling a single oligomer by applying an external force, F, to its center of mass (as schematically depicted in figure 5.1), and by then measuring the resulting drift velocity, v(Ianniruberto et al. 2012). The friction coefficient, ζ, of the oligomer is then given by the ratio, F/v, provided that the force is small enough not to perturb both the pulled and the surrounding molecules. In other words, care must be taken to ensure that the experiment be performed in the Stokes limit where v is directly proportional to F (implying F-independent ζ values). Under equilibrium conditions, the value of the friction coefficient must also be consistent with the Einstein relationship $D = k_BT/\zeta$, where D is the diffusion coefficient of the molecule and k_BT is the thermal energy. Under flow conditions, the Einstein relationship breaks down, and both the friction and the diffusion coefficient become tensors. This implies that in order to determine the whole friction (or mobility) tensor, the pulling experiments should be independently performed along the x, y, and z directions. Needless to say, the velocity v of the pulled molecule must be deprived of convective contributions in the case of NEMD simulations.

5.3 Simulation Details

Molecular dynamics deals with the motion of material points (beads) due to forces derived from potentials (Allen and Tildesley 1989). The equation of motion of the beads is the following:

$$m_i \frac{d^2\mathbf{r}_i}{dt^2} = \frac{\partial U}{\partial \mathbf{r}_i} \tag{5.1}$$

in which $\mathbf{r}_i$ is the spatial coordinates of the i-th beads, while U represents the sum of all the interaction potentials among the beads. In the most detailed description, the beads

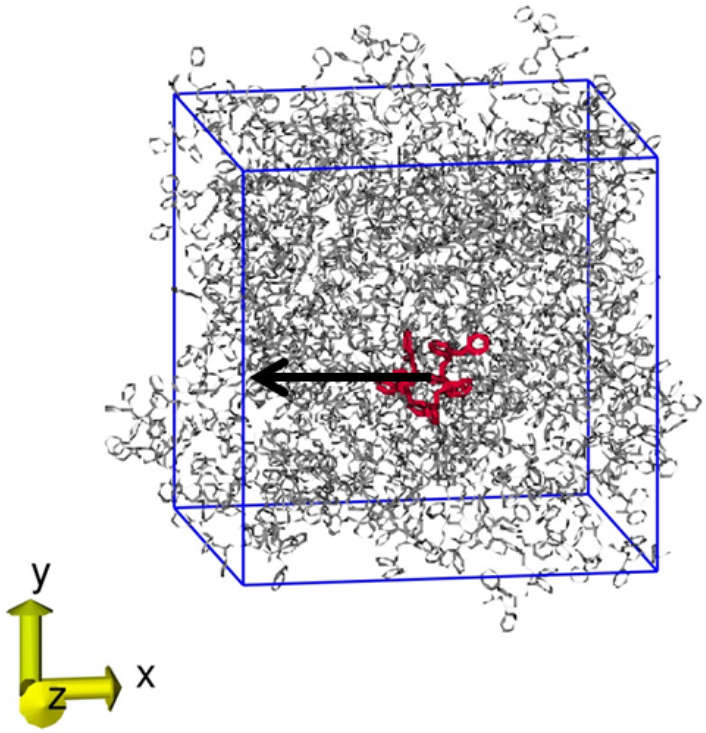

Figure 5.1: Snapshot of the simulation box. The arrow represents the force pulling the red molecule.

represent single atoms while in coarser descriptions a single bead can stand for a specific group of atoms. As mentioned above, in our case we adopted the so-called united atoms description. This is a common choice since it is a good compromise between the required level of detail and the computational efforts needed to obtain the desired information. Despite the level of description, the mass of a bead is given by the sum of the masses of the atoms accounted for by the bead itself. The potential U, here adopted for simulations of polystyrene melts, has the following form:

$$U = U_{bonded} + U_{unbonded} = \sum_{bonds} \frac{k_{ij}^b}{2} \left(d_{ij} - d_{ij}^{eq}\right)^2 + \sum_{angles} \frac{k_{ijk}^\theta}{2} \left(\theta_{ijk} - \theta_{ijk}^{eq}\right)^2 + \quad (5.2)$$

$$= \sum_{dihedrals} k_{ijkl} \left[1 + \cos\left(n\phi_{ijkl} - \phi_{ijkl}^{eq}\right)\right] + \sum_{i>j} 4\varepsilon_{ij} \left[\left(\frac{\sigma_{ij}}{d_{ij}}\right)^{12} - \left(\frac{\sigma_{ij}}{d_{ij}}\right)^{6}\right] \quad (5.3)$$

The first two terms on the right-hand side of equation (2) are harmonic type potentials for bonds between two consecutive beads and for angles between two consecutive bonds, respectively. The third term represents dihedral potentials accounting for torsions, while the last term is the sum of the Lennard-Jones potentials related to the non-bonded interactions. In all the simulations, we adopted the TraPPE united atoms force field (Harmandaris et al. 2006). In order to perform simulations of NVT ensembles, Berendsen thermostat with time constant of $0.1ps$ is then introduced. Periodic boundary conditions with a cut-off range of $1nm$ are imposed. Simulations are carried out using a leap-frog algorithm via GROMACS software package (Van Der Spoel et al. 2005) with a time step of $0.001ps$. Boxes of about 100 styrene oligomers made up of ten monomers (decamers) are initially minimized and then equilibrated through a NPT simulation at $T = 463K$ and $P = 1atm$ run for a time much longer than the oligomer relaxation time. For such purpose a Berendsen barostat with time constant of $2ps$ is adopted. Compressibility is fixed at $9.5 \times 10^{-5} bar^{-1}$. Computation time on 27 processors working in parallel is 30 min/ns. This means that each simulation, typically lasting $100ns$, was performed in about 2 days.

5.4 Results

Figure 5.2 shows the typical trajectory under equilibrium conditions of a pulled molecule in terms of its coordinates x, y, and z as a function of time. The force F has been applied in negative x direction, and its magnitude has been chosen with the following criterion. As mentioned above, the force should be small enough not to perturb the conformation of the pulled molecule. This is expected to occur if the characteristic time, τ_c, of the convective effect induced by F is much longer then the thermal (diffusive) relaxation time, τ_d, of the molecule. The convection time is the time required for the molecule to move over a distance equal to its size R, i.e., $\tau_c = R/v$ (where we recall that v is the drift velocity), while the diffusion time is $\tau_d = R^2/D$. Now, since $v = F/\zeta$ and $D = k_BT/\zeta$, the condition $\tau_c \gg \tau_d$ is equivalent to $F \ll k_BT/R$. As expected, figure 5.2 shows that the force induces a systematic drift along x, while thermal fluctuations dominate the y and z components. The average slope of the function $x(t)$ determines the drift velocity v, and hence the friction coefficient ζ through the ratio $\zeta = F/v$.

Figure 5.3 shows the effect of the external force F on the friction coefficient, always under equilibrium conditions. The horizontal line in the same figure represents the value of the diffusion coefficient measured from the mean square displacement of the unpulled molecules. The diffusion coefficient extracted from pulling experiments is fully consistent with the Einstein relationship, $D = k_BT/\zeta$, at low values of the force. Significant deviations are observed with increasing values of the applied force. Figures 5.2 and 5.3 also reveal that fluctuations, and hence error bars, can be comparable to the measured quantities, and even longer simulations would be required to reduce the statistical uncertainty. Needless to say, we could reduce error bars in the friction coefficient values by also performing (independent) pulling experiments on different molecules.

We now examine the effect of flow on the friction coefficient by performing non-equilibrium molecular dynamics simulations. As mentioned above, with the software GROMACS we can apply a continuous shear deformation to the simulation box, thus easily reaching a non-equilibrium steady state in which we can measure several observ-

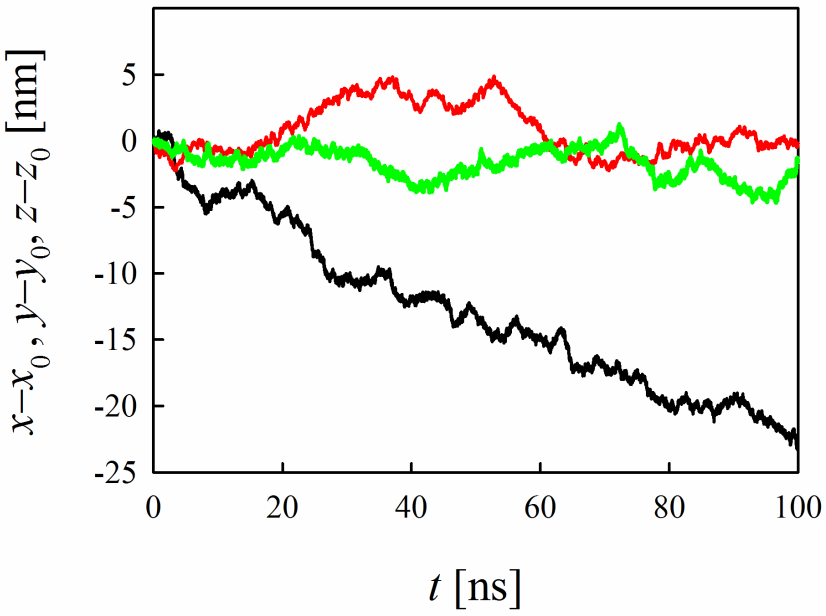

Figure 5.2: Trajectory of a pulled molecule along the pulling direction x (black line), and along the orthogonal directions y and z (red and green lines, respectively).

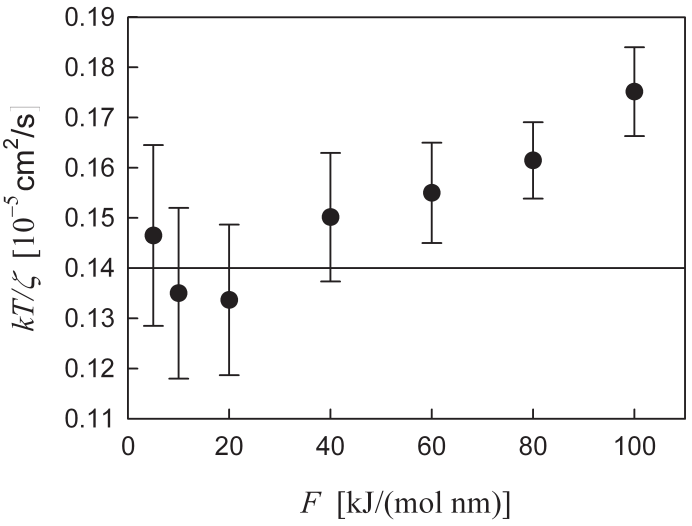

Figure 5.3: Effect of the pulling force F on the friction at equilibrium, the hrizontal line is the center of mass diffusion coefficient, D.

ables, including friction coefficients. In other words, GROMACS allows for simultaneously shearing the box and pulling molecules through external forces, as schematically depicted in figure 5.4. The rate of shear deformation $\dot{\gamma}$, often referred to as shear rate, should be high enough to induce some orientational anisotropy in the oligomers. In other words, $\dot{\gamma}$ should be significantly larger than the thermal relaxation rate whose order of magnitude is, as mentioned above, $1/\tau_d = D/R^2$. Figure 5.5 reports the typical trajectory of a pulled molecule under non-equilibrium conditions at a non-dimensional shear rate $Wi = \dot{\gamma}\tau_d$, where Wi is the so-called Weissenberg number. Figure 5.5 clearly shows that, differently from the equilibrium case in Figure 5.2, the molecule also drifts, though slightly, along the y direction. In other words, in the non-equilibrium case, friction becomes a tensor with non-zero off-diagonal components.

The other (and perhaps most important) message of figure 5.5 emerges when comparing the trajectory along the x direction with the analogous trajectory in figure 5.2. The comparison clearly shows than under flow the pulled molecule has a significantly

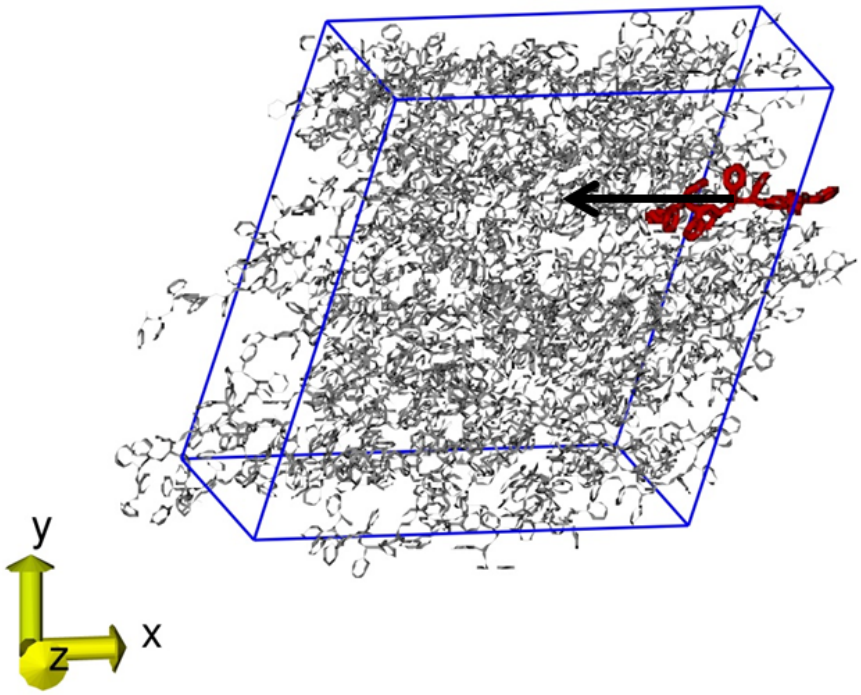

Figure 5.4: Snapshot of the simulation box under shear. The arrow represents the force pulling the red molecule.

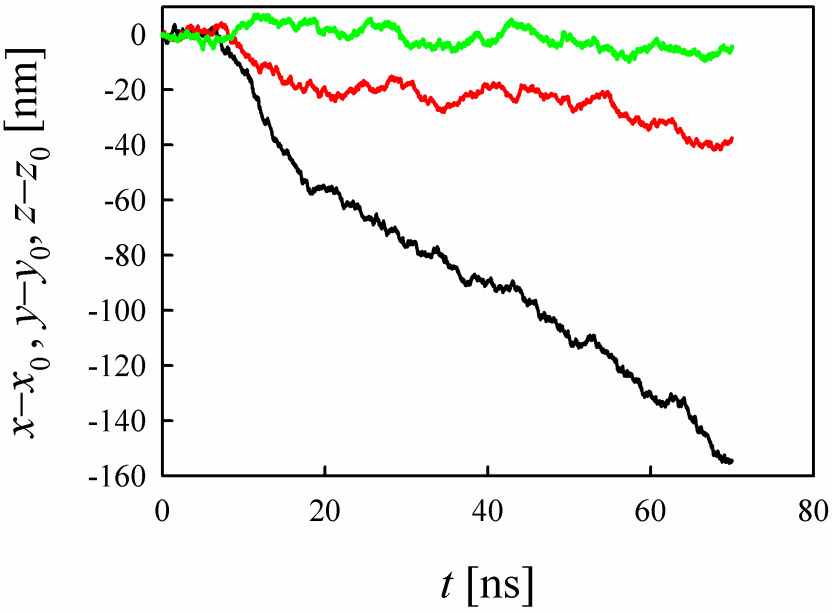

Figure 5.5: Trajectory of a molecule pulled along the x direction with force $F = -10kJ/(mol \cdot nm)$ under a shear flow with $Wi = 100$. Black line is the x coordinate; red and green lines are y and z coordinates, respectively.

larger drift along x, thus revealing that, when pulling along the shear direction x, the mobility along that same direction, equal to the reciprocal of the xx component, ζ_{xx}, of the friction tensor, significantly increases with respect to the equilibrium case. In other words, ζ_{xx} becomes significantly smaller than its equilibrium value ζ_{eq}. It should be recalled that the trajectories in figure 5.5 were deprived from any direct convective contribution. It should also be mentioned that convection is in the positive x direction, while the pulling experiments was performed in the negative x direction. Hence the friction reduction effect is not due to convection *per se*, but it is due to some indirect flow effect, as discussed below.

The upper panel of figure 5.6 reports ζ_{xx} values as a function of dimensionless shear rate Wi, as obtained from pulling experiments analogous to those reported in figure 5.5 for the case $Wi = 100$. In slow flows ($Wi \ll 1$), the function $\zeta_{xx}(Wi)$ approaches a shear rate independent plateau value, equal to ζ_{eq}, as expected. With increasing shear rate, ζ_{xx} significantly decreases, seemingly approaching a second lower plateau, though no definite conclusion can be drawn in very fast flows because of the statistical uncertainty. The lower panel of figure 5.6 reports the so-called monomeric order parameter S, measuring the degree of alignment along the shear direction x of the monomers of the styrene decamer. More specifically S measures the order of the unit vectors specifying the direction connecting alternate carbon atoms along the decamer backbone. Starting from its equilibrium value, $S_{eq} = 0$, S first steeply increases with increasing values of the shear rate, to then approach a quasi-plateau at intermediate rates, before seemingly increasing again. From inspection of figure 5.6, it is highly tempting to link the friction reduction effect to flow-induced monomer co-alignment in shear direction. In fast flows, oligomers are strongly aligned along the shear direction (see Figure 5.4), and it is "easier" to pull each of them through the "maze" of the surrounding ones. In other words, the increase in the molecular mobility is due to flow-induced nematic-like effects. In order to confirm our interpretation we decided to perform pulling experiments on the decamer in different matrices, made by either smaller or larger molecules. More specifically we made simulations of a single decamer in a matrix of dimers, as well as in a matrix of icosamers

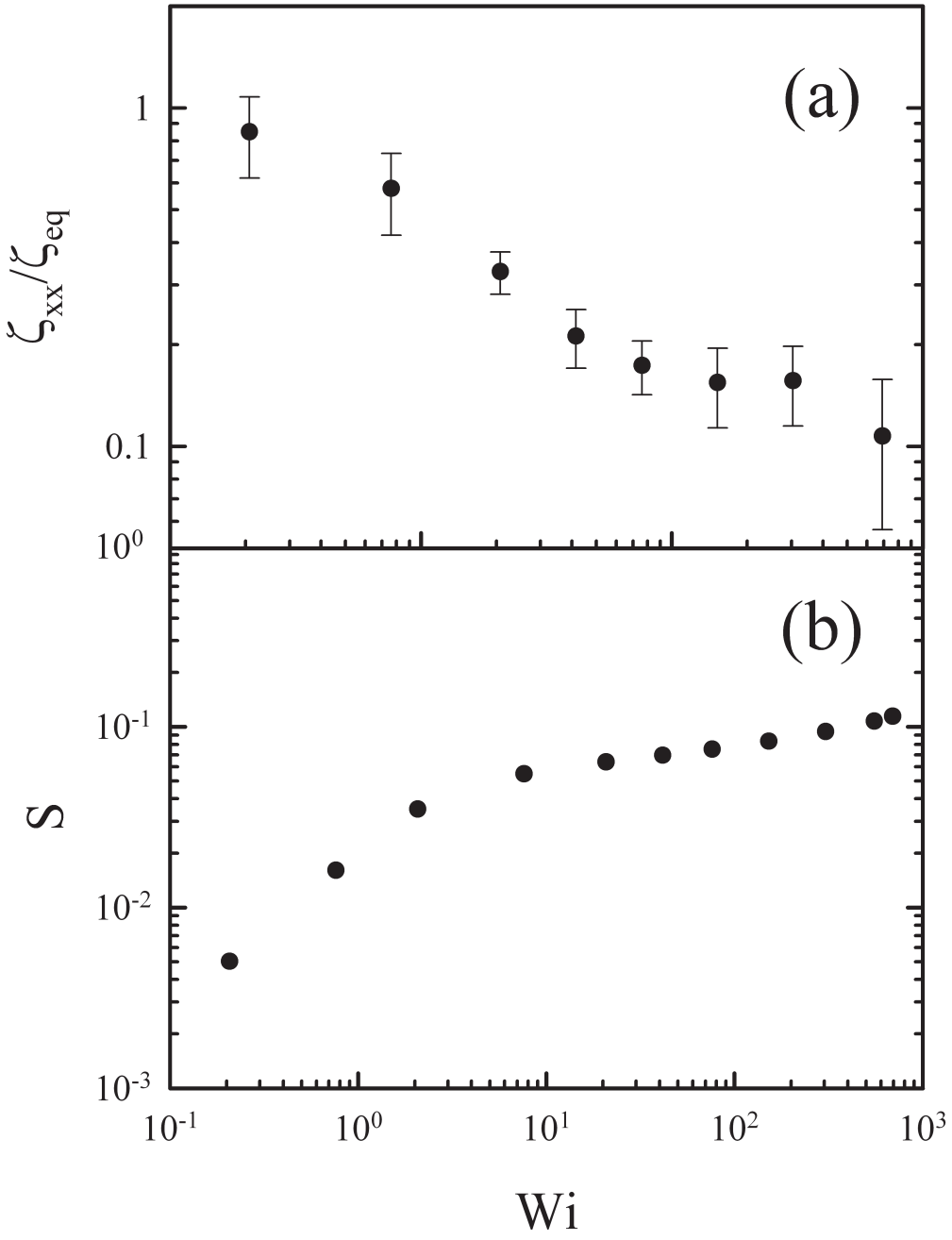

Figure 5.6: Effect of shear flow on the xx component of the friction tensor (a) and on the monomeric order parameter (b).

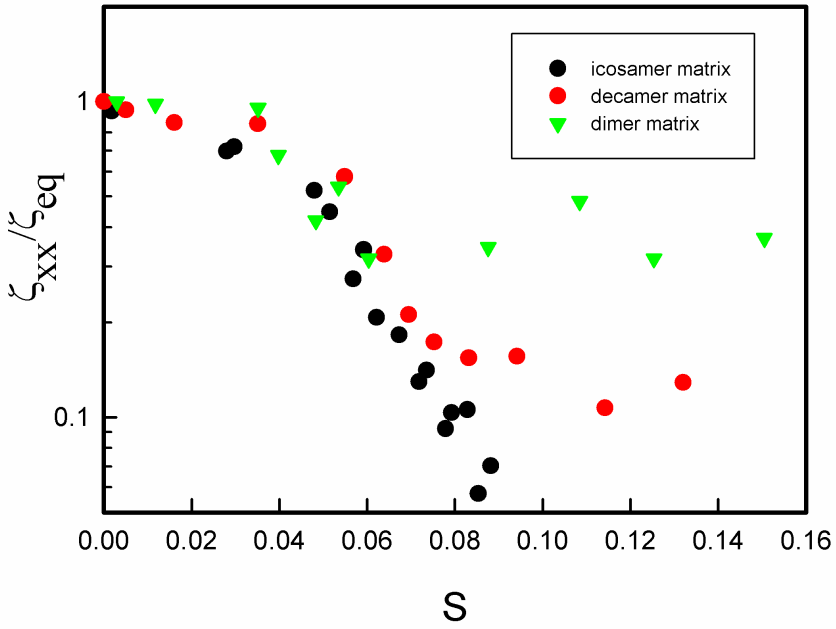

Figure 5.7: Influence of the order parameter, S, of the probe decamer on the xx component of the friction tensor in several matrices. Error bars are omitted for clarity.

(oligomers with 20 monomers). Typical results are reported in figure 5.7, in terms of ζ_{xx}/ζ_{eq} as a function of probe decamer order parameter. When the decamer is pulled in a melt of dimers, no significant friction reduction effect is observed in spite of the fact that the decamer is aligning along the shear direction. This is because the matrix is now made by fast relaxing molecules that are in fact not affected by the background flow. In other words, in order to observe significant friction reduction effects both the matrix and the probe molecule should become anisotropic.

This interpretation is confirmed by the pulling experiments performed in the matrix of icosamers, also reported in figure 5.7. The results clearly show that, when the matrix is made by longer molecules, flow has a more pronounced effect on decamer mobility with respect to pure decamer case. This is due to the fact that, since the icosamer obviously

has a thermal relaxation time longer than the decamer, the icosamer matrix gets more oriented by the flow than the decamer matrix, thus allowing for a larger mobility of the probe molecule.

5.5 Conclusions and perspectives

In this chapter we have briefly reviewed our research activity based on the molecular dynamics simulations performed in recent times by using the GRID computing infrastructure at the Federico II University. Thanks to the computational and storage power made available to us, we were able to perform molecular dynamics simulations that we would not have been able to run by using our own local machines. The simulations have helped us to prove (for the first time) that in fast flows of monodisperse polymer melts the molecular mobility can be significantly enhanced because of flow-induced monomeric alignment. This phenomenon, here quantitatively measured in the case of styrene oligomers, can help understanding the unusual rheological behavior of polystyrene melts recently observed in fast uniaxial extensional flows. Those flows are often encountered in many processing applications, and hence the results here reviewed can have a significant impact in several industrial processes. The flow-induced friction reduction effect is expected to be very sensitive to molecular architecture, polymer chemistry, as well as polymer concentration. Rheological experiments reveal that PS melts behave differently from PS solutions, or from melts with other chemistries (methyl methacrylate, butyl acrylate, etc.). These evidences motivate further simulations, and we are currently working on polymethylmethacrylate (PMMA) melts (though still focusing on oligomers) seemingly showing even stronger friction reduction effects (Huang et al. 2013b). Due to partial charges embedded in the molecule, however, PMMA simulations are computationally more demanding, but we rely on the further increasing computational power of the GRID infrastructure. For that reason, we hope to report results on PMMA in the near future.

Chapter 6

Flow-induced nematic interaction and friction reduction succcessfully describe PS melt and solution data in extension startup and relaxation

6.1 Introduction

In the literature, there is wide consensus on interpreting the complex rheological behaviour of entangled polymer liquids by using the tube model of Doi and Edwards (Doi and Edwards 1988). The linear viscoelastic (LVE) behavior of monodisperse linear polymers can be quantitatively predicted by combining the well-known molecular mechanism of reptation with additional relaxation mechanisms like tube-length fluctuations and constraint release (Likhtman and McLeish 2002; Ruymbeke et al. 2010). The key molecular parameter affecting the LVE behavior of monodisperse linear polymers is the number Z of entanglements per chain: solutions and melts with the same Z exhibit the

same (nondimensional) LVE reponse, even if with a different chemistry (Costanzo et al. 2016; Huang et al. 2015, 2013b; Likhtman and McLeish 2002).

In the nonlinear viscoelastic range, the picture becomes more complicated, and most works focused on the polystyrene (PS) chemistry. In particular, it has recently been shown that PS systems with the same Z behave in the same way in shear flows (Costanzo et al. 2016), while significant differences emerge in extensional flows (Costanzo et al. 2016; Huang et al. 2015, 2013b; Likhtman and McLeish 2002). More specifically, solutions are more prone than melts to extension thickening. When plotting uniaxial extension viscosity data as function of stretch rate, both PS solutions and melts first exhibit a thinning behavior with increasing rate. However, at rates comparable to the reciprocal Rouse time of the chains, solutions show a viscosity upturn while melts go on thinning (Huang et al. 2015).

The absence of any viscosity upturn in PS melts is not compatible with the classical Doi-Edwards theory that predicts a stretch-induced viscosity increase at Rouse-time-based Weissenberg numbers of order unity for both solutions and melts in the same way (McLeish 2002; Watanabe 1999). The first attempt to solve this apparante failure of the Doi-Edwards model in describing PS melt data invoked a flow-induced tube-squeezing phenomenon (not present in the original Doi-Edwards theory where a constant tube diameter was assumed), and a resulting pressure-induced relaxation effect (Marrucci and Ianniruberto 2004). Though seemingly successful for melts, the physics behind the interchain tube-pressure concept again cannot distinguish between melts and solutions, and hence tube pressure, though phenomenologically appealing (Wagner 2015; Wagner et al. 2005), appears not to be the relevant molecular mechanism.

A more physically-sounded molecular mechanism successfully used to explain the above observed discrepancies is absed on the concept of friction reduction effects triggered by flow-induced monomer co-alignment (Ianniruberto et al. 2011). In fast flows of monodisperse PS melts, all monomers align in the flow direction, and it is highly tempting to assume that the monomeric friction gets reduced with respect to its equilibrium value, as indeed confirmed by recent nonequilibrium molecular dynamics simulations

(Ianniruberto et al. 2012). As a consequence of the reduced friction, flow looses grip on the molecule, and is less effective in stretching them. In PS solutions (at least those with ordinary small-molecule solvents) the molecular picture obviously changes since the solvent molecules do not feel the orientation action of the flow, and remain isotropic. Hence, the friction coefficient may well remain close to its equilibrium value, the more so the more dilute is the solution.

The gradual loss of flow-induced friction reduction effects with decreasing polymer concentration was confirmed by recent data of Huang et al. (2015), who compared the nonlinear extensional rheology of a series of PS solutions in a wide concentration range(from the 100% melt case to the most dilute 10% solution), all having the same Z (hence the same LVE nondimensional response). Such data, exhibiting a gradual change with concentration of the steady-state extensional viscosity, from the stretch-rate thinning of the melt to the stretch-rate thickening (or viscosity upturn) of the more dilute solutions, were successfully compared with predictions of a tube-based model accounting for friction reduction effects (Ianniruberto 2015a).

The solvent used in the PS solutions of Huang et al. (2015) was an oligo-styrene molecule with molar mass $M_w = 4k$ (i.e., a few Kuhn segment long). In order to quantitatively describe extensional data in such a long oligomeric solvent, Ianniruberto (2015a) had to account for solvent/polymer nematic interactions, originally suggested in a previous paper of (Huang et al. 2013a) who compared extensional data of three entangled PS solutions only differing for the size of the oligomeric solvent (4k, 2k, and 1k, respectively). Those three solutions, obviously having the same Z (and hence the same LVE), behaved very differently in fast extensional flows, the 1k solution being stretch-rate thickening while the 4k one stretch rate-thinning, and the 2k solution somewhere in between. Huang et al. (2013a) interpreted this difference as due to nematic effects, consisting in the solvent molecules not being isotropic (in spite of their very small relaxation times) because of a nematic interaction with the oriented polymer molecules, the more effective the longer the oligomer. We here explicitly take up their suggestion, and interpret their data by invoking flow induced friction reduction, inclusive of nematic

interaction effects, in the way previously suggested by Iannirubertо (2015a). We will here show that the reason why the 1k solution is stretch-rate thickening while the 4k one is stretch rate-thinning is because friction reduction effects are less significant in the 1k oligomer in view of the reduced importance (or even absence) of nematic interactions.

In order to further confirm the role of flow-induced friction reduction effects, we here also examine the very recent data of Huang and Rasmussen (2016), who performed relaxation experiments following startup of uniaxial extensional flows on several PS systems, including the 1k solution and the melt with the same Z, previously examined by Huang et al. (2013a). The role of flow-induced friction reduction effect in previously published relaxation experiments (Nielsen et al. 2006) was already emphasized by Yaoita et al. (2012). However, we here attempt a quantitative comparison with the new data of Huang and Rasmussen (2016).

6.2 Model

The model is analogous to that recently suggested by Iannirubertо (2015a), the main difference being that, similar to what done by Costanzo et al. (2016), the stretch dynamics is described through a dumbbell-like approach, i.e., by concentrating friction at the chain ends, rather than distributing it along the chain. However, differently from dumbbell models for unentangled polymers, we have to account for the fact that in entangled systems the stress-carrying are the subchains between consecutive entanglements, rather than the chains as a whole. As a consequence, the relevant stretch measure is the average subchain stretch λ, defined as the ratio between the current subchain length and its equilibrium value. We write for the stretch λ the following classical evolution equation Costanzo et al. (2016):

$$\frac{d\lambda}{dt} = \boldsymbol{\kappa} : \bar{\mathbf{S}}\lambda - \frac{f\lambda - f_0}{\tau_R(t)}, \tag{6.1}$$

where the first term on the right-hand side (RHS) gives the affine rate of change of λ, with $\boldsymbol{\kappa}$ the velocity gradient tensor, and $\bar{\mathbf{S}}$ the average subchain orientation tensor (see below). The second term on the RHS of Eq. (6.1) gives the stretch relaxation

rate, with a characteristic time equal to the Rouse time τ_R of the chain (possibly time-dependent because of flow-induced friction reduction effects). The driving force for stretch relaxation is the non-dimensional tension difference $f\lambda - f_0$, with f the non-Gaussian correction factor (and f_0 its, nearly unity, equilibrium value) calculated as:

$$f(\lambda) = \frac{\mathscr{L}^{-1}(\lambda/\lambda_{max})}{3\lambda/\lambda_{max}}. \tag{6.2}$$

In Eq. (6.2), $\mathscr{L}^{-1}$ is the inverse Langevin function, and $\lambda_{max} = a/b$ is the maximum λ value corresponding to the fully extended state of the entangled subchain, a and b being equilibrium subchain and Kuhn lengths, respectively. While there is consensus on the value of b ($b = 1.8nm$ in the PS systems considered here (Rubinstein and Colby 2003)), the value of a (or equivalently the value of the average molar mass M_e of the entangled subchain) is somehow controversial. Rubinstein and Colby (2003) indicate for PS melts the value $a = 8.5nm$ based on the Ferry definition of M_e ($M_{e,Ferry} = 17k$ in PS melts). Within the Doi and Edwards theory Doi and Edwards (1988), M_e is predicted to be smaller than $M_{e,Ferry}$ by a 3/5 or 4/5 factor arising from the independent alignment approximation (IAA) or no-IAA orientation tensor, $\mathbf{Q}$, respectively (Likhtman and McLeish 2002). In the literature, however, $\mathbf{Q}$ tensors other than the Doi-Edwards tensor have been proposed, based on force-balance requirements at the entanglement nodes (Marrucci et al. 2000a,b). They belong to the category of the so-called Seth-type orientation tensors, and have the following form

$$\mathbf{Q} = \frac{\mathbf{B}^q}{tr\mathbf{B}^q}, \tag{6.3}$$

where $\mathbf{B} = \mathbf{F}^T \cdot \mathbf{F}$ is the Finger tensor of the given deformation gradient tensor, $\mathbf{F}$. The exponent q is a parameter, and the choice $q = 1/3$ is strongly encourged by an excellent aggrement with data in a wide range of situation (step strain, and startup of shear and uniaxial extensional flows) (Ianniruberto 2015b). The corresponding a values for PS melts is $a_{melt} \approx 5nm$ (Ianniruberto 2015b). Values of a smaller than those reported by Rubinstein and Colby (2003) are also suggested by multi-chain Brownian simulation of entangled polymer (Masubuchi et al. 2013), naturally accounting for the force balance

condition at the entanglements, as well as for their 3D fluctuations. In any event, it is to be emphasized that in the present model the value of a only affects the non-Gaussian correction factor f of Eq. (6.2). In the case of PS solutions in theta solvents (like the styrene oligomers used by Huang et al. (2013b) and Huang and Rasmussen (2016), we computed a by using the dilution law $a = a_{melt}\phi^{-1/2}$, with ϕ the polymer volume fraction.

While the single-mode approximation in the stretch dynamics does not deteriorate agreement with data (Costanzo et al. 2016), the same approximation cannot be adopted for the orientation dynamics, exhibiting a broad multi-mode spectrum already in the LVE limit. By following the same approach adopted in previous papers (Costanzo et al. 2016; Ianniruberto 2015a,b; Wagner et al. 2005), we extract the equilibrium orientation spectrum $\{G_i, \tau_{i0}\}$ from the LVE response by performing a multi-mode Maxwell fit of the G', G'' data, and then move on to the nonlinear situation by writing the following integral equation over past deformation history for the orientation tensor, $\mathbf{S}_i$, of each mode:

$$\mathbf{S}_i(t) = \int_{-\infty}^{t} \frac{dt'}{\tau_i(t')} \exp\left[-\int_{t'}^{t} \frac{dt''}{\tau_i(t'')}\right] \mathbf{Q}\left[\mathbf{F}(t,t')\right]. \tag{6.4}$$

Here, similarly to Eq. (6.1), the i-th mode relaxation time, τ_i, is taken to be time dependent because of flow-induced friction reduction effects, as well as because of convective constraint release (CCR). The latter mechanism is not significant in startup of uniaxial extensional flows (Costanzo et al. 2016; Ianniruberto 2015a), while is important during relaxation, as already emphasized by Ianniruberto (2015b), and confirmed in the following. We here account for CCR by simply adding a convective contribution to the i-th mode thermal orientational relaxation rate (indicated as $1/\tau_{i,T}(t)$):

$$\frac{1}{\tau_i(t)} = \frac{1}{\tau_{i,T}(t)} + \beta\left(\boldsymbol{\kappa} : \bar{\mathbf{S}} - \frac{1}{\lambda}\frac{d\lambda}{dt}\right). \tag{6.5}$$

At equilibrium the thermal orientational relaxation time, $\tau_{i,T}(t)$ reduces to τ_{i0}, while out of equilibrium, $\tau_{i,T}(t)$, can become smaller than τ_{i0} because of flow-induced friction reduction effects (see later). On the RHS of Eq. (6.5), the convective orientational relaxation rate is proportional to the relative velocity between the entangled chain and

its confining tube (Ianniruberto and Marrucci 1996), through a (unknown) numerical coefficient, β, of order unity, determining the CCR effectiveness. The average tube segment orientation, $\bar{\mathbf{S}}$, is taken to obey an equation similar to Eq. (6.4), where τ_i is replaced by an average orientational (or disengagement) relaxation time τ_d:

$$\tau_d(t) = \frac{\sum_i G_i \tau_i^2(t)}{\sum_i G_i \tau_i(t)}. \tag{6.6}$$

For what concerns the effect of flow-induced monomer co-alignment on the monomeric friction coefficient, ζ, which was directly proved by the non-equilibrium molecular dynamics simulations performed by Ianniruberto et al. (2012) and Masubuchi et al. (2013), we here adopt the same simple recipe of previous papers (Costanzo et al. 2016; Ianniruberto 2015a)

$$\frac{\zeta}{\zeta_0} = \begin{cases} 1 & \text{for } S \leq S_c \\ \left(\frac{S}{S_c}\right)^{\alpha} & \text{for } S > S_c \end{cases}, \tag{6.7}$$

where ζ_0 is the equilibrium value of the monomeric friction coefficients, S is the average monomeric order parameter (not to be confused with tensors $\mathbf{S}_i$ and $\bar{\mathbf{S}}$ referring to subchain orientation), S_c is the critical value of S above which friction reduction effects become important. The order parameter, S, is a weighted average between the order parameter of the polymer and that of the solvent, S_P and S_S, respectively, i.e., $S = \phi S_P + (1-\phi) S_S$. In the absence of nematic interactions between polymer and solvent, it is $S_S = 0$ because the orientation of solvent molecules is unaffected by flow. When nematic interactions are relevant, the order parameter of the solvent is assumed to be proportional to that of the polymer, i.e., $S_S = \varepsilon S_P$, with ε a nematic interaction parameter (Ianniruberto 2015a). Hence, the equation for S becomes

$$S = [\phi + (1-\phi)\varepsilon]\, S_P, \tag{6.8}$$

including the absence of nematic interactions when $\varepsilon = 0$.

The average monomeric order parameter of the polymer is determined by (i) the average tube segment orientation and (ii) the chain stretch. In the uniaxial extensional flows here considered, S_P, is calculated from (Yaoita et al. 2012):

$$S_P(t) = \frac{\lambda^2}{\lambda_{max}^2} \left(\bar{S}_{zz} - \bar{S}_{rr}\right), \tag{6.9}$$

where z is the stretching direction and r is orthogonal to it. The flow-induced change of the monomeric friction affects all relaxation times. In other words, as mentioned above, out of equilibrium, the thermal orientational relaxation times, τ_{i0}, must be replaced by $\tau_{i,T} = (\zeta/\zeta_0)\tau_{i0}$. Similarly, the Rouse time, τ_R, is calculated as $\tau_R = (\zeta/\zeta_0)\tau_{R0}$, where τ_{R0} is the Rouse time based on the equilibrium friction, ζ_0.

Finally, we need to specify the stress expression. In line with the (classical) decoupling approximation between stretch and orientation adopted so far, we write (Costanzo et al. 2016)

$$\boldsymbol{\sigma}(t) = \lambda^2(t)\frac{f(\lambda)}{f_0}C_Q\sum_i G_i\mathbf{S}_i, \tag{6.10}$$

where the $\mathbf{Q}$-dependent numerical coefficient C_Q (equal to $3/q$ for the unit-trace Seth-type tensors used here) guarantees that Eq. (6.10) properly reduces to the multi-mode Maxwell equation in the LVE limit. (In such a limit, it is $\lambda = 1$, and the tangential component of $\mathbf{Q}$ in shear reduces to γ/C_Q, where γ is the shear deformation.)

The model described above contains several parameters, and it is appropriate to distinguish those relevant in the LVE limit (i.e., the set $\{G_i, \tau_{i0}\}$), from those playing a role in the nonlinear range. The latter are: (i) the equilibrium value τ_{R0} of the Rouse time in Eq. (6.1), (ii) the maximum subchain stretch ratio, λ_{max}, in Eqs. (6.2) (6.3), (iii) the exponent q of the orientation tensor, $\mathbf{Q}$, in Eq. (6.3), (iv) the CCR parameter β in Eq. (6.5), and (v) the friction reduction parameters α, S_C, ε in Eqs. (6.7) (6.8). For all PS systems examined in the next section, four of the above parameters are held fixed at values equal to those used previously (Ianniruberto 2015a), namely: $q = 1/3$, $\beta = 0.2$, $\alpha = 1.25$, and $S_C = 0.14$. The other three parameters (τ_{R0}, λ_{max}, and ε) are system-dependent, and are detailed in the next section.

6.3 Results

We start buy analyzing the data of Huang et al. (2013a) referring to several entangled PS solutions, only differing for the molar mass M_w (1k, 2k, and 4k) of the oligomeric styrene solvents. The polymer is a nearly monodisperse (polydispersity index 1.12) PS

Table 6.1: Nonlinear parameters of the PS samples (τ_{R0} is at $130°C$)

Sample name	τ_{R0} $[s]$	λ_{max}	ε
PS285K	200	2.7	-
PS545k/4k-52	93	3.8	0.5
PS545k/2k-58	38	3.6	0.3
PS545k/1k-52	0.5-0.8	3.8	0
PS285k/2k-44	2.4	4.1	0.3
PS285k/2k-72	17.5	3.2	0.3

with $M_w = 545k$, and its volume fraction ϕ is equal to 52% in the case of the 1k and 4k solvents, while it is $\phi = 58\%$ fot the 2k oligo-styrene solvent. The three solutions are referred to as PS545/1k-52, PS545/2k-58, PS545/4k-52, respectively (Huang et al. 2013a).

The LVE moduli of the three solutions come out in fact indistinguishable (in spite of the just mentioned minor PS concentration difference) if plotted in the nondimensional form G'/G_N°, G'/G_N° vs. $\omega\tau_{e0}$ (Huang et al. 2013a). Here G_N° is the plateau modulus and τ_{e0} is the high-frequency time parameter of the Baumgaertel-Schausberger-Winter (BSW) fitting model of LVE, roughly corresponding to the equilibrium Rouse time of the subchain between consecutive entanglement (Bach et al. 2003). The nondimensional form automatically accounts for the different glass transition temperatures due to the different solvent (Huang et al. 2013a). The LVE behavior of the three solutions is also superimposable to that of the PS melt with $M_w = 285k$ (referred to as PS285k) examined by Huang et al. (2013b). The reason is that all four systems have nearly the same number Z of entanglements per chain, i.e., the same value of the product $M_w\phi$. As a consequence, for all four systems we can use the same nondimensional discrete relaxation spectrum $\{G_i/G_N^\circ, \tau_{i0}/\tau_{e0}\}$, reported in table 2 of Ianniruberto (2015a) who already examined the PS285k melt and the PS545k/4k-52 solution, but with a slightly different, more detailed model than that adopted here. We, therefore, start with those

two systems (before considering the PS545k/1k-53 and PS545k/2k-58 solutions) in order to verify that the simplified model adopted here behaves equally well.

Figure 6.1 reports the model predictions obtained by using the same parameter values alrady used by Iannirubertо (2015a), also reported here in table 6.1. The prediction in figure 6.1 are indistinguishable from those previously obtained by distributing the friction along the chain (cf. full lines in figures 1(a) and 2(a) of Iannirubertо (2015a)), thus confirming that the simpler dumbbell-like stretch equation, Eq. (6.1), can reasonably replace the partial differential equation adopted by Iannirubertо (2015a) (see his Eq. 4). In view of what follows, it is of important to note that the results reported in figure 6.1, referring to the PS545/4k-52 solution, are obtained by choosing for the nematic interaction parameter the value $\varepsilon = 0.5$ (see table 6.1).

Next we move on to the other two solutions, not previously examined by Iannirubertо (2015a). In figure 6.2, we report the comparison of the model predictions with the data on the PS545k/2k-58 and PS545k/1k-52 solutions in lower molar mass solvents. A comparison with PS solution data in a 2k solvent was already made by Costanzo et al. (2016), where however the polymer had a lower M_w (285k instead of 545k). Since the nematic effects are expected not to be dependent on the polymer molar mass (while they do depend on the oligomer size), we here adopt for all the systems in a 2k solvent the same ε value already used by Costanzo et al. (2016), i.e., $\varepsilon = 0.3$. Figure 6.2(a), referring to PS545k/2k-58, reports predictions obtained with the equilibrium Rouse time $\tau_{R0} = 38s$. Such a value is very close to that indicated by Huang et al. (2013a), and derived by them on the basis of the τ_{e0} value of the BSW fit and of the Doi-Edwards number of entanglements Z, as $\tau_{R0} = \tau_{e0}Z^2$. It is however worth remarking that such a Rouse time prediction from LVE data is correct only in the order of magnitude, i.e., only to within a numerical factor of order unity.

Figure 6.2(b) shows the comparison with the PS545k/1k-52 solution data. Predictions were obtained by setting $\varepsilon = 0$ (i.e., by assuming no nematic interactions) for two values of τ_{R0}. The first of them, $\tau_{R0} = 0.8s$, gives the best fit in figure 6.2(b). The other one, $\tau_{R0} = 0.5s$, is instead suggested by the relaxation data. Both values are again of

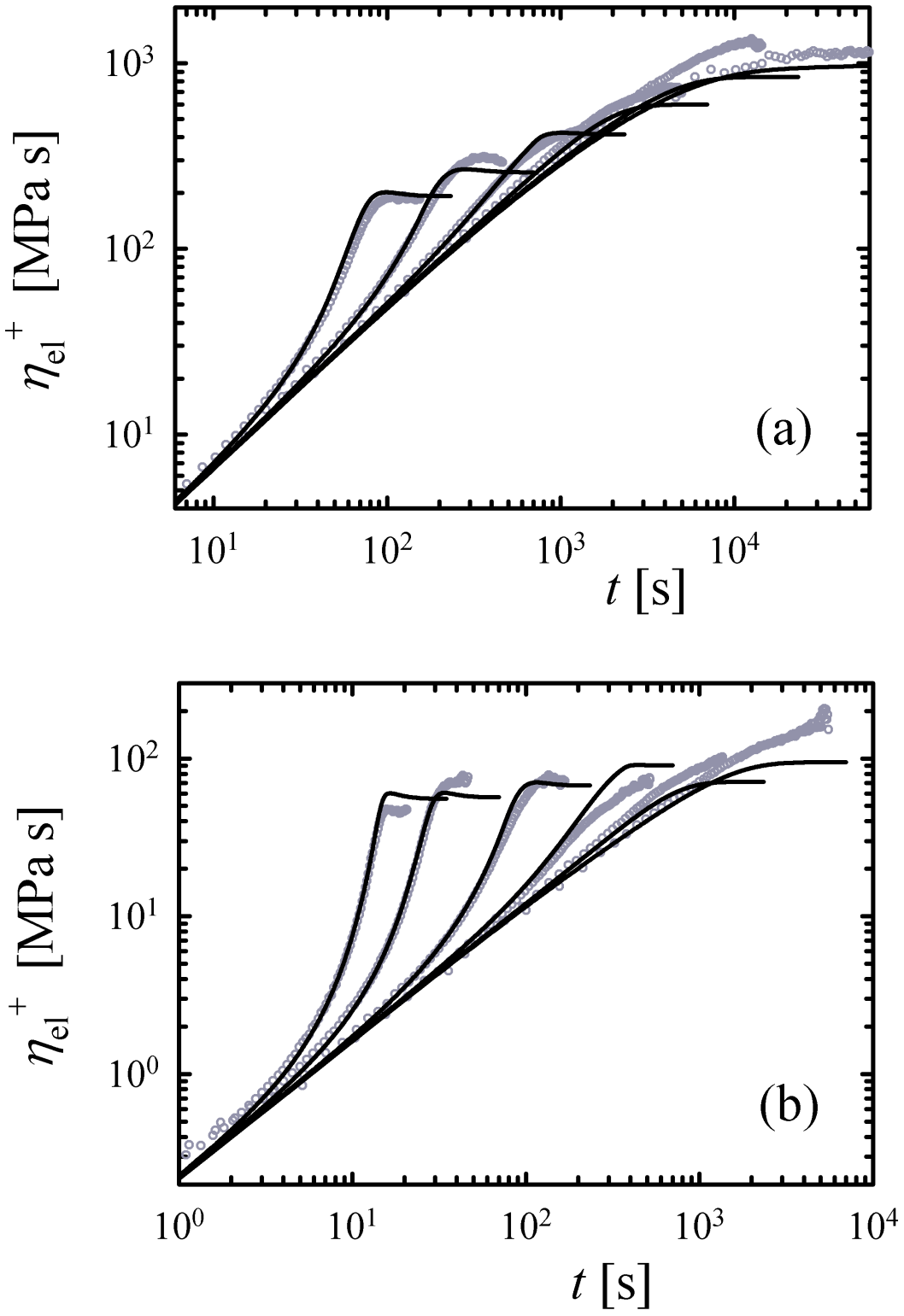

Figure 6.1: Extensional stress growth coefficient vs. time for several stretch rates: comparison of predictions (black lines) to data (gray symbols) for (a) PS285k melt and (b) PS545k/4k-52 solution. Stretch rates [s^{-1}] are, from left to right: (a) 0.03, 0.01, $3{\cdot}10^{-3}$, 10^{-3}, $3{\cdot}10^{-4}$, $3{\cdot}10^{-5}$; (b) 0.1, 0.03, 0.01, $3{\cdot}10^{-3}$, 10^{-3}.

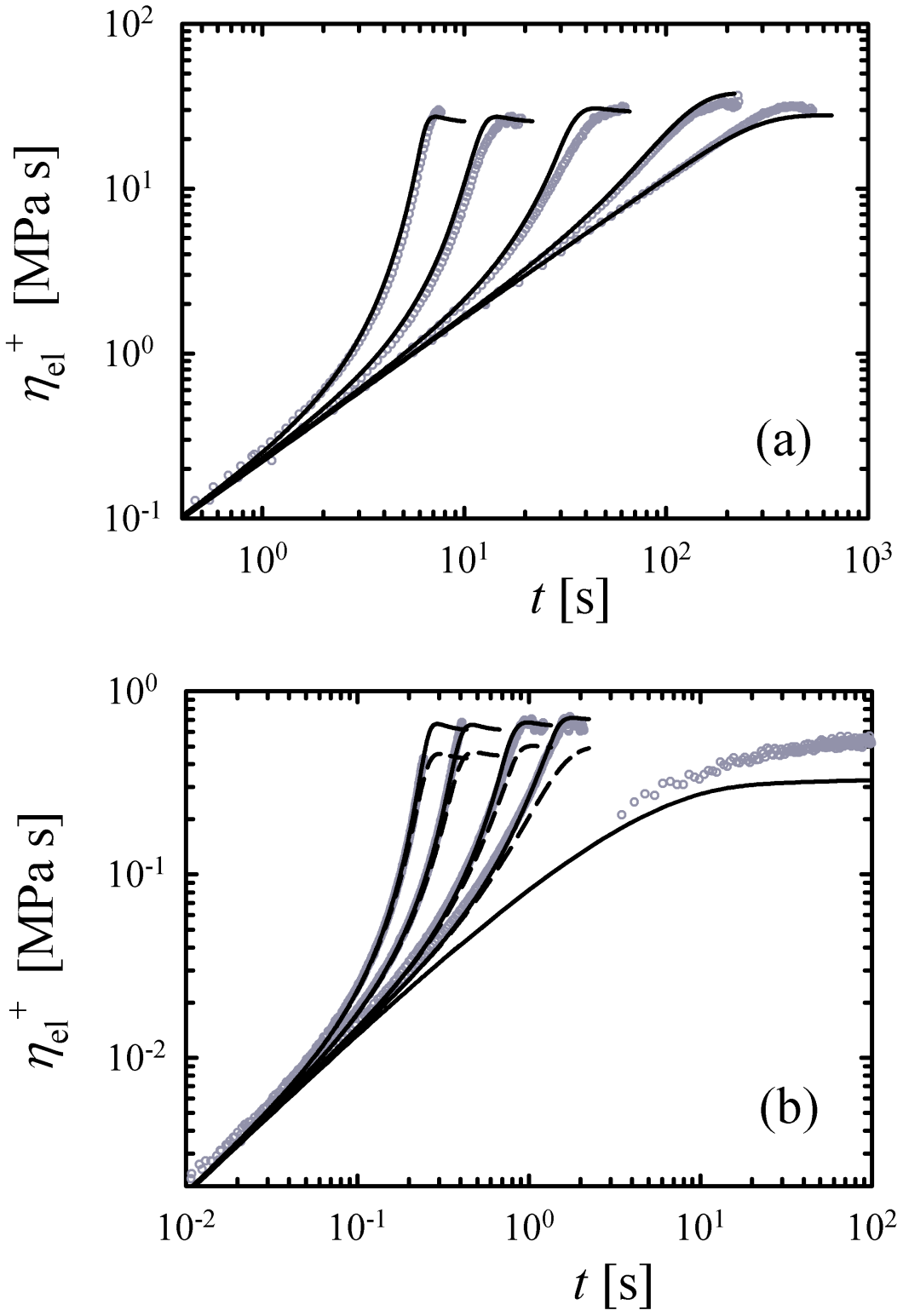

Figure 6.2: Extensional stress growth coefficient vs. time for several stretch rates: comparison of predictions (black lines) to data (gray symbols) for (a) PS545k/2k-58 and (b) PS545k/1k-52. Stretch rates $[s^{-1}]$ are, from left to right: (a) 0.45, 0.23, 0.076, 0.023, $7.6{\cdot}10^{-3}$; (b) 11.5, 7.4, 3.7, 2.2, 0.011. In (b), solid and dashed lines are obtained with $\tau_{R0} = 0.8s$ and $\tau_{R0} = 0.5s$, respectively.

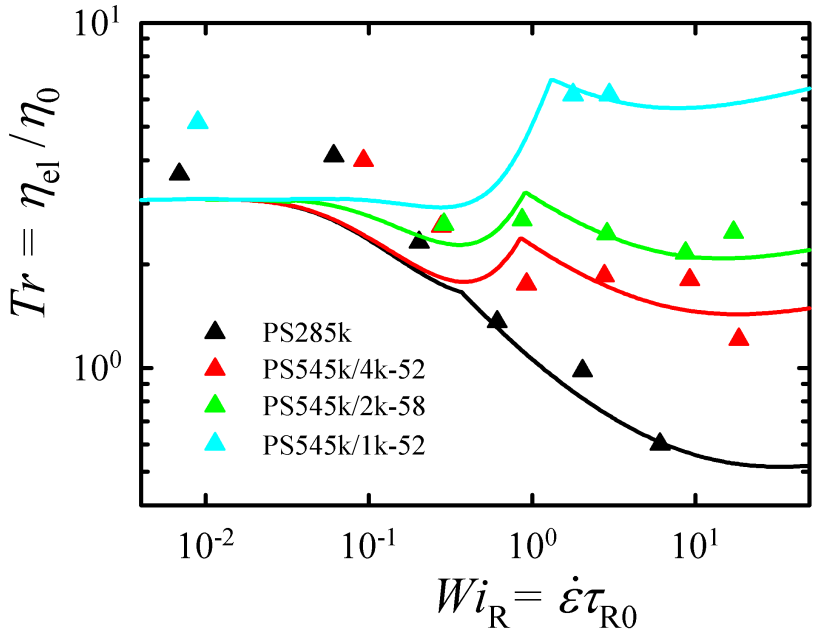

Figure 6.3: Trouton ratio vs. Rouse-time based Weissenberg number for the first four samples of table 6.1. (For PS545/1k-52 we here use $\tau_{R0} = 0.8s$). Symbols are data from figure 3 of Huang et al. (2013b). Lines are model predictions, and the cusps are due to the abrupt onset of friction reduction effects (see Eq. (6.7)).

the same order of magnitude of the value suggested by figure Huang et al. (2013a).

The suggestion that nematic effects are absent in the short 1k oligomer, while certainly present in longer ones, is indeed confirmed by looking at the steady-state extensional viscosity. Figure 6.3 shows the comparison between model predictions and data at steady state from Huang et al. (2013a) for all four systems so far considered. In slow flows, all data appear to approach the expected value of the Trouton ratio, $Tr = 3$, with the notable exception of the PS545k/1k-52 solution. In this regards, it is appropriate to mention that Huang et al. (2013a) denounce a symmetry breaking of the filament of that solution in startup experiments at low stretch rates. More importantly, figure 6.3 confirms in quantitative terms the key role of flow-induced nematic ineteraction effects on the monomer-solvent friction coefficient in the nonlinear rheology of polymer solu-

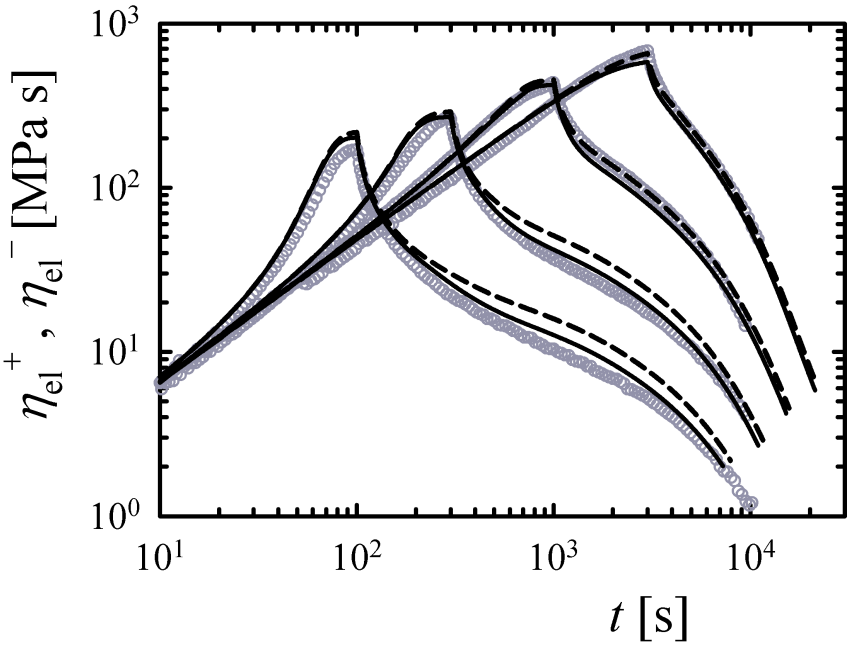

Figure 6.4: Comparison between predictions (lines) and PS285k melt data (symbols) from Huang and Rasmussen (2016) in extension startup followed by relaxation upon flow cessation. Stretch rates are 0.03, 0.01, $3{\cdot}10^{-3}$, $10^{-}3$ s^{-2}, from left to right. Solid and dashed lines are with and without CCR, $\beta = 0.2$ and $\beta = 0$, respectively.

tions. Moving from the solution with the longest 4k oligomer to that with the smallest 1k oligomer, the Trouton ratio progressively increases by as much as a factor of nearly 3 at high Weissenberg numbers, in spite of the fact that the linear rheology is the same for all solutions (in nondimensional units). Figure 6.3 also confirms the concentration effect previously discussed (Huang et al. 2015; Ianniruberto 2015a) since the melt curve runs well below all solution curves, in spite of the fact that (we repeat) the PS285k melt has the same (nondimensional) LVE response of the three solutions.

We then proceed by examining the relaxation data of Huang and Rasmussen (2016), starting from the PS285k melt in figure 6.4. The comparison between the solid and the dashed lines, obtained by setting $\beta = 0.2$ and $\beta = 0$ (i.e., with and without CCR), shows that while CCR plays no significant role in extension startup, it is certainly more

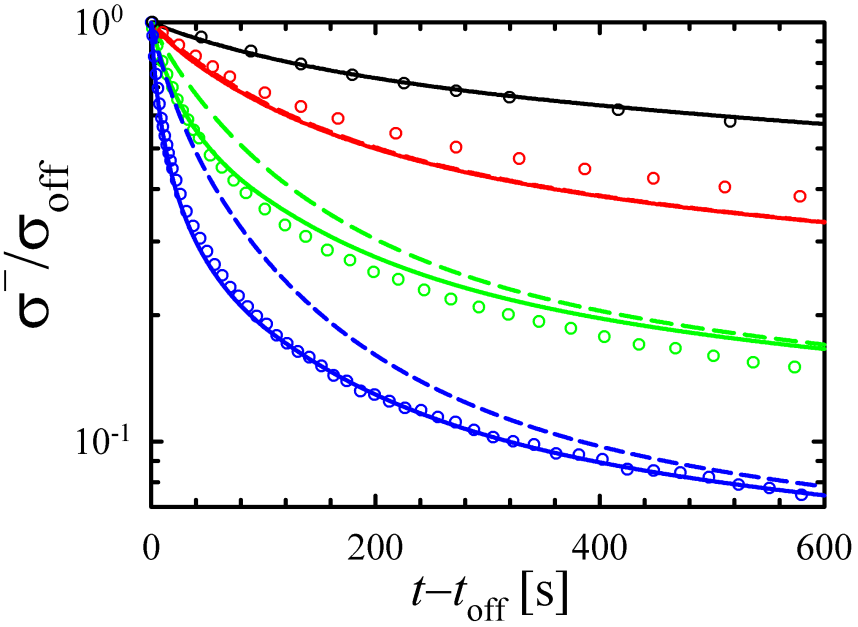

Figure 6.5: Normalized plot of the relaxation data reported in figure 6.4. Stretch rates increase from top to bottom. Solid lines correspond to the solid lines in figure 6.4. Dashed lines are here obtained by setting all relaxation times at their equilibrium value for $t \geq t_{off}$.

important during the relaxation following fast flows. We here recall that within the tube model CCR arises from the flow-induced relative motion between the test chain and its surrounding tube, Eq. (6.5). When a fast flow ($Wi_R > 1$) is switched off after a sufficiently large deformation, chain retraction activates a constraint release process, thus accelerating relaxation, as indeed shown by the predictions in figure 6.4, and confirmed by the better comparison with data. A similar "beneficial" role of CCR typically emerges in the relaxation experiments following a large step strain (Ianniruberto 2015b).

Relaxation experiments are also useful to highlight the importance of the friction reduction effects induced by the preceding flow, as already emphasized by Yaoita et al. (2012). This is confirmed in figure6.5 where the PS285k relaxation data (and predictions) are plotted in terms of the ratio between the stress σ at time t during the relaxation

process and the stress σ_{off} attained at the time t_{off} when the flow is switched off. In such a normalized plot, all data obviously start from unity at $t = t_{off}$, but then initially decay with an increasing rate by increasing the value of the stretch rate $\dot{\varepsilon}$ of the preceding flow, eventually approaching the same slope at long times. The acceleration of the relaxation process with increasing $\dot{\varepsilon}$ values is quantitatively captured by the model only if accounting for friction reduction effects. To confirm this conclusion, in figure 6.5 we also report predictions obtained by artificially setting all relaxation times at their equilibrium values from $t = t_{off}$ onwards. At short times, relaxation is accelerated also in this case because of stretch and CCR effects, but data do suggest a more significant acceleration, the latter being attributed to flow-induced friction reduction effects. At long times, friction reduction does not play any role because monomer isotropy is essentially recovered, and all relaxation times go back to their equilibrium values.

We next consider the startup and relaxation data of the PS545k/1k-52 solution reported in figure 4 of Huang and Rasmussen (2016), measured at $89°C$ (rather than at $130°C$). To work out predictions for these data, all relaxation times have been therefore shifted from $130°C$ to $89°C$ by using the shift factor, $\alpha_T = 440$, reported in table II of Huang and Rasmussen (2016). Consequently, τ_{R0} becomes either 352s or 220s, depending on whether τ_{R0} at $130°C$ is taken equal to 0.8s or 0.5s, respectively, table 6.1. Figure 6.6 shows that the agreement between model predictions and data can be deemed extremely satisfactory if $\tau_{R0} = 220s$ is used (solid lines in figure 6.6), whereas $\tau_{R0} = 352$ gives too slow a relaxation (dashed lines). Notice also that, suprisingly, at long times data do not show the change of curvature typical of the transition from stretch to orientational relaxation (clearly visible in figure 6.4 for the melt) even after a thousand seconds, in spite of the fact that (at $89°C$) the Rouse time τ_{R0} is a few hundreds Seconds. We cannot exclude experimental artifcats, possibly related to the loss of symmetry of the samples due to a too low viscosity, as mentioned by Huang et al. (2013a).

We finally focus on the last two samples examined by Huang and Rasmussen (2016) having a different number of entanglements with respect to the four samples so far considered. Those samples are two solutions of PS285k in a 2k oligomer, with a polymer

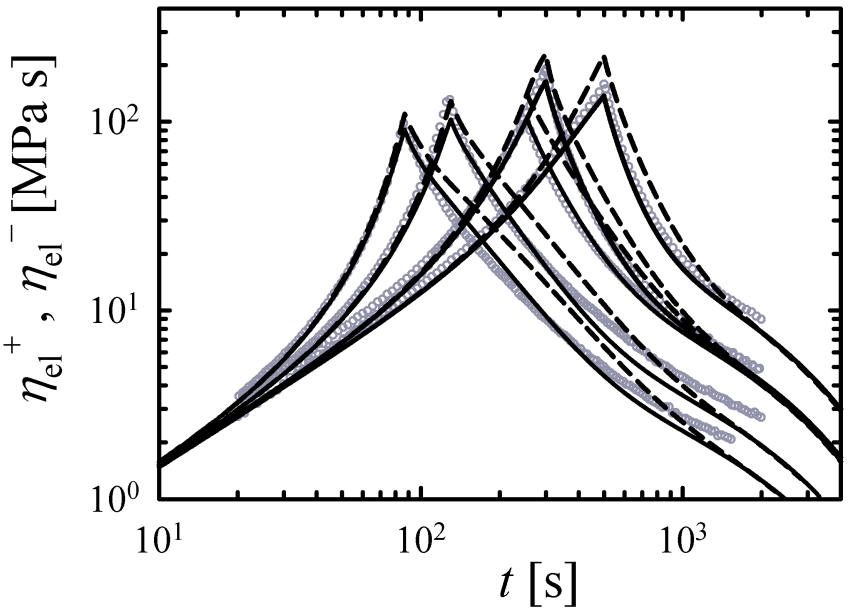

Figure 6.6: Comparison between predictions (lines) and PS545k/1k-52 solution data at $89°C$(symbols) from Huang and Rasmussen (2016) in extension startup followed by relaxation. Solid and dashed lines are obtained with $\tau_{R0} = 220s$ and $\tau_{R0} = 352$, respectively. Stretch rates are 0.03, 0.02, 0.01, $6{\cdot}10^{-3}$ s^{-1}, from left to right. At $\dot{\varepsilon} = 0.01s^{-1}$, the two sets of data are obtained by stopping the flow at two different times.

Table 6.2: Relaxation spectra of PS285k/2k-44 and PS285k/2k-75 at 130°C.

PS285k/2k-44		PS285k/2k-72	
G_i [M Pa]	tau_{i0} [s]	G_i [M Pa]	τ_{i0} [s]
3.3	1.1×10^{-4}	3.1	1.2×10^{-3}
8.4×10^{-2}	2.5×10^{-3}	1.3×10^{-1}	2.1×10^{-2}
3.2×10^{-2}	1.3×10^{-2}	5.3×10^{-2}	1.0×10^{-1}
1.6×10^{-2}	6.1×10^{-2}	2.7×10^{-2}	4.7×10^{-1}
1.0×10^{-2}	2.9×10^{-1}	2.3×10^{-2}	2.4
9.4×10^{-3}	1.3	2.5×10^{-2}	1.2×10^{1}
9.4×10^{-3}	5.5	3.0×10^{-2}	2.3×10^{2}
7.6×10^{-3}	1.8×10^{1}	3.0×10^{-2}	2.3×10^{2}
4.8×10^{-5}	1.6×10^{2}	6.3×10^{-3}	1.4×10^{3}

volume fraction equal to 0.44 and 0.72 (named PS285k/2k-44 and PS285k/2k-72, respectively). Table 6.2 reports the discrete relaxation spectrum at 130°C of those two solutions, obtained by fitting their LVE response reported in figure 3 of Huang et al. (2013b). The system-dependent nonlinear parameters are reported in table 6.1. For both solutions we have adopted the Rouse time indicated by Huang et al. (2013b), as well as the value $\varepsilon = 0.3$ already used for 2k solvents.

Startup and relaxation experiments on these two samples were performed ad different temperature, 110°C and 120°C for PS285k/2k-44 and PS285k/2k-72, respectively. Predictions were therefore obtained by shifting all relaxation times in tables 6.1 and 6.2 by using the temperature shift factors $a_T = 56$ and $a_T = 8$, respectively, reported in table II of Huang and Rasmussen (2016).

Figure 6.7 shows the results obtained for PS285k/2k-44. For some of the startup runs, relaxation was not monitored. As already emerged in the previous figures, the largest discrepancies between predictions and data are observed in the startup experiments at low stretch rates. In this regards, it is appropriate to mention that the lowest stretch

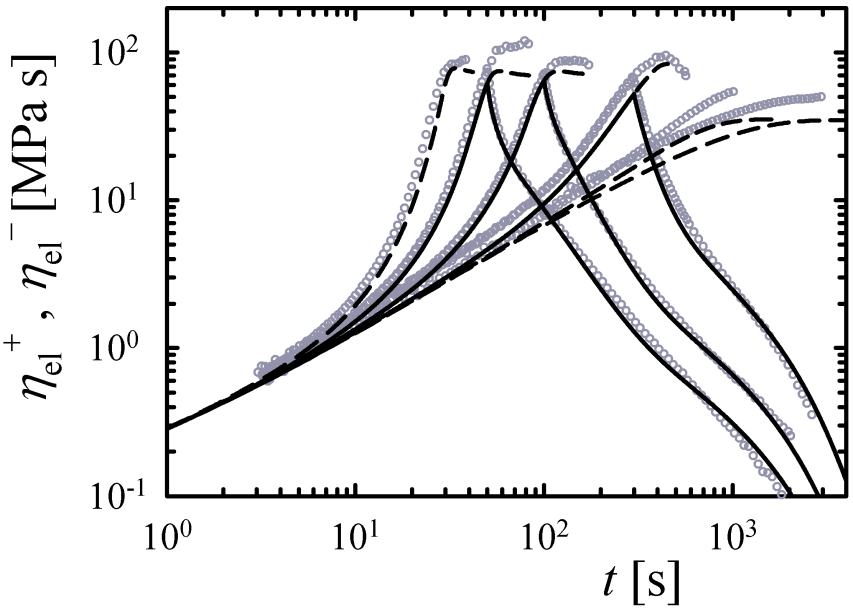

Figure 6.7: Comparison between predictions (lines) and data (symboles) for PS285k/2k-44 solution at $110°C$ from Huang and Rasmussen (2016) in extension startup followed by relaxation upon flow cessation. Stretch rates are 0.1, 0.06, 0.03, 0.01, 3×10^{-3}, 1×10^{-3} s^{-1}, from left to right. Relaxations were monitored only at 0.06, 0.03, 0.01 s^{-1}, and the corresponding predictions are solid lines, while mere startup predictions are dashed lines.

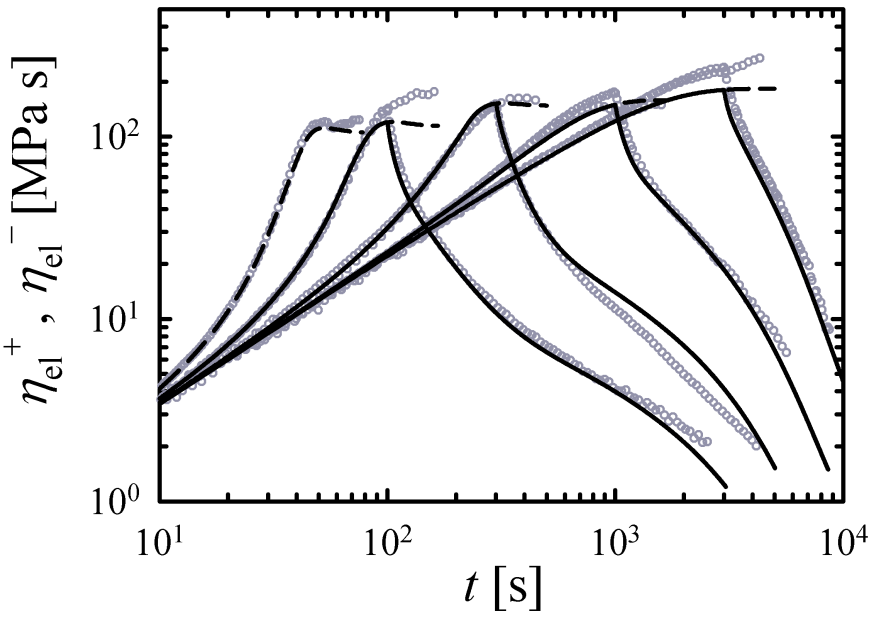

Figure 6.8: Comparison between predictions (lines) and data (symboles) for PS285k/2k-72 solution at 120°C from Huang and Rasmussen (2016) in extension startup followed by relaxation upon flow cessation. Stretch rates are 0.06, 0.03, 0.01, 3×10^{-3}, 1×10^{-3} s^{-1}, from left to right. Solid and dashed lines as in figure 6.7.

rate cooresponds to a Weissenberg number (based on the average disengagement time, τ_{d0}) of order unity. Therefore, discrepancies at the onset of the nonlinear response can perhaps be attributed to some sample polydispersity (PI=1.09) (Huang et al. 2013b), which is ignored in the model that adopts a single value for the Rouse time.

Figure 6.8 shows similar results obtained for the PS285k/2k-72 solution at $120°C$, where again in some cases startup runs are not followed by relaxation data. The overall agreement of predictions with data in both figure 6.7 and 6.8 can certainly be deemed satisfactory.

6.4 Conclusions and Remarks

We have here shown that the recent uniaxial extensional data of Huang et al. (2013a) and Huang and Rasmussen (2016) on several entangled PS systems (five solutions and one melt) can be quantitatively interpreted within the Doi-Edwards theory by accounting for flow-induced friction reduction effects. In particular, we here quantitatively confirm the suggestion advanced by Huang et al. (2013a) that, in solutions based on oligomeric styrene solvents, nematic interactions between the polymer and the solvent become increasingly important with increasing the size of the oligomers. Those interactions, absent in the linear viscoelastic range where isotropy prevails, only emerge in fast extensional flows where the flow-induced polymer alignment nematically "propagates" to the neighboring solvent molecules (all having a relaxation time much smaller than the flow time scale). The solvent-polymer co-alignment effectively contributes to a reduction in the monomeric friction, Eqs. (6.7) and (6.8), macroscopically visible in terms of a reduction of the stress levels (compare in figure 6.3 red data and predictions for the 4k oligomer with the green and cyan ones for the 2k and 1k solvents, respectively).

Although figure 6.3 closely resembles the TOC figures of Ianniruberto (2015a), an important difference should be emphasized. In the previous work (Ianniruberto 2015a), data on polymers with the same number of entanglements but different concentrations were examined to show that "*... the gradual change with concentration of the steady-*

state extensional viscosity, from the strain-rate thinning of the melt to the strain-rate thickening of the more dilute solutions, is due to the gradual loss of friction-coefficient reduction with decreasing polymer concentration". In this paper, conversely, we have considered data on solutions with the same polymer concentration but different size of the oligomeric solvent in order to quantitatively confirm the key role of nematic interactions.

We have also shown that flow-induced friction reduction effects also help in explaining the relaxation data following uniaxial extensional flows recently reported by Huang and Rasmussen (2016). This is best seen in figure 6.5 where predictions with and without friction reduction are compared with the relaxation data on the PS285k melt. Friction reduction induced by the preceding flow induces a clear acceleration of the relaxation process, as originally suggested by Yaoita et al. (2012), and here confirmed by performing a quantitative comparison with several data on PS melts and solutions.

The relaxation experiments flowing fast extensional flows also reveal that CCR effects induced by chain retraction play an important role, insofar as they also contribute the acceleration of the relaxation process, figure 6.4. This conclusion is in line with a previous analysis of relaxation data following large step strains.

It is finally fair to note that the model is not hundred percent successful. Indeed, the analysis of the startup and relaxation experiments on the PS545/1k-52 solution revealed that the best fit of the startup data is obtained with a value of the Rouse time somewhat different from that needed for the relaxation data (cf. figure 6.2(b) and figure 6.6). For such a reason in table 6.1 we have reported a range of Rouse time values for that solution (0.5-0.8s). Further data on solutions with the same solvent and the same polymer concentration but different polymer molar mass, M_w, may help understanding the origin of this uncertainty in view of the fact that the Rouse time must come out proportional to M_w^2.

Summary and Conclusions

In part 1, we have explored a new coarse-grained simulation scheme for telechelic associating polymers at concentrations higher than the critical micellar concentration, hence forming flower-like micelles. The model ignores the individual chain friction, so that pendant chains instantly reattach to a micellar core, forming either bridge or loop chains. Ignoring individual chain friction also implies that micelles remain spherical objects during flow. Friction of the whole micelle is accounted for, however, influencing both micelle free self-diffusion, and micelle dynamics (repulsion) during micelle overlap. Micelles are dispersed in a periodic simulation box, and with increasing concentration, chain detaching from the core of a micelle can bridge to a neighboring one, thus eventually forming a 3D network-like system. One of the difficulties of these simulations is that the parameter space is particularly wide, and here by necessity we spanned a limited range of that space, mostly in order to explore the qualitative consistency of the model predictions with observations.

In the chapter 3, the role of each parameters described in table 3.1 is examined. The morphogical changes induced by changing the size ratio between chain and micelle dimensions are addressed in terms of aggregation (section 3.2.3), network connectivity (section 3.2.4), and micelle distributions (section 3.3). In the case of dynamical observables in equilibrium simulations, the apparently linear relation between plateau modulus and initial relaxation modulus (section 3.4.1), scaling exponents of initial relaxation modulus (section 3.4.2), and zero-shear viscosity (section 3.6) are examined. The effect of end-group length scale (section 3.7) and loop-dissociation time (section 3.8) are

reported.

In the chapter 4, the detailed studies in both equilibrium and non-equilibrium simulations are performed for selected samples (table 4.1). The effect of concentration on the linear rheology is emphasized (section 4.1) showing in particular that the zero-shear viscosity becomes more sensitive to concentration when bridge chains progressively increase in number, consistently with data (Suzuki et al. 2013; Tripathi et al. 2006; Xu et al. 1996). The typical predictions on nonlinear rheological properties in shear flows is tested (section 4.2). We emphasize the role of FENE effects on the strain hardening behavior in startup flows. The violation of the Cox-Merz rule is believed to be due to persistence of bridge that means the dissociation of chain ends relatively insensitive to implemented shear flow (section 4.3). The shear thinning in steady shear is due to flow-induced bridge destruction, but bridge stretch moderates and somehow "delays" this thinning, hence keeping the steady shear viscosity well above the complex viscosity. Deviation between the steady-shear viscosity and the complex viscosity appear to decrease with increasing polymer concentration in less dense networks, i.e., in networks with a lower fraction of bridge chains. This is due to the fact that in those systems flow induces a bridge formation phenomenon (opposing shear thinning), and this is more pronounced in less concentrated systems (section 4.3.2). We attribute this shear-induced increased association to the anisotropy of the micelle pair correlation function, creating a smaller micellar distance in the upstream direction (section 4.3.3). Association is also favored by a minor micelle clustering induced by flow, the latter being revealed by the micelle coordination number. In section 4.4, analysis of shear thickening is addressed. The shear thickening is more pronounced in the shear viscosity than in the first normal stress difference, which is consistent with experimental data (Suzuki et al. 2012, 2013).

In conclusion of part 1, we found that, for suitable values of the parameters, the simulations reproduce qualitatively (or even quantitatively) the behavior observed experimentally in both the scaling laws of linear properties, and the nonlinear behavior of shear thickening and strain hardening. It should be mentioned however that, differently from many experiments, we never found a single-mode Maxwell-like response in

the linear viscoelasticity, probably because we could not explore large values of the loop dissociation time τ_D for computational limitations.

In part 2, the concepts of monomeric friction reduction and possible nematic interactions between different length of oligomers are described (see chapter 5), and then applied to recently published extensional data Huang et al. (2013a) and Huang and Rasmussen (2016) in chapter 6.

In chapter 5, the methdological approach to measure friction tensor using molecular dynamics simulation is represented in sections 5.2 and 5.3. The preliminary results of such a method are reported in section 5.4 in terms of components for friction tensor with respect to shear rate. Especially the xx components of the friction tensor *vs.* order parameter on the different matrix molecules (figure 5.7) is of important to further studies in chapter 6.

In chapter 6, the recent uniaxial extensional data of Huang et al. (2013a) and Huang and Rasmussen (2016) on several entangled PS systems (five solutions and one melt) can be quantitatively interpreted within the Doi-Edwards theory by accounting for flow-induced friction reduction effects. In particular, we here quantitatively confirm the suggestion advanced by Huang et al. (2013a) that, in solutions based on oligomeric styrene solvents, nematic interactions between the polymer and the solvent become increasingly important with increasing the size of the oligomers. Those interactions, absent in the linear viscoelastic range where isotropy prevails, only emerge in fast extensional flows where the flow-induced polymer alignment nematically "propagates" to the neighboring solvent molecules (all having a relaxation time much smaller than the flow time scale). The solvent-polymer co-alignment effectively contributes to a reduction in the monomeric friction, macroscopically visible in terms of a reduction of the stress levels.

This page has been intentionally left blank

Appendix

Chapter 7

Additional Theoretical Backgrounds for Models

7.1 Stress-Strain Relations for Ideal Networks

7.1.1 Connections of mechanical power and stress power

For the given work done by the applied force, $\mathscr{W}$, the mechanical power, P, can be defined the material time derivation of $\mathscr{W}$:

$$P = \frac{d\mathscr{W}}{dt} = \int_V \mathbf{b} \cdot \mathbf{v} \rho \, dV + \int_\Omega \mathbf{t} \cdot \mathbf{v} \, dS, \tag{7.1}$$

where $\frac{d}{dt}$ is the material time derivation, $\mathbf{b}$ is body force per unit mass, $\mathbf{v}$ is velocity field, and $\mathbf{t}$ is traction vector is given by

$$\mathbf{t} = \mathbf{T} \cdot \mathbf{n}, \tag{7.2}$$

where $\mathbf{T}$ is Cauchy stress tensor and $\mathbf{n}$ is surface normal vector. Applying Gauss diversions theorem, we have

$$P = \int_V \frac{1}{2} \rho \frac{d}{dt} \left(\mathbf{v} \cdot \mathbf{v} \right) dV + \int_V \nabla \mathbf{v} : \mathbf{T} dV, \tag{7.3}$$

where $\nabla \mathbf{v}$ is transposed velocity gradient tensor, $\mathbf{L}$. Note that the first term of RHS in Eq. (7.3) is being related with the contribution of internal kinetics energy, $\frac{1}{2}\mathbf{v} \cdot \mathbf{v}$, and

the integrand of the second part is called stress power: $w = \mathbf{T} : \mathbf{L}$. With Reynold's transport theory, the meaning of two contributions are significant:

$$P = \frac{d}{dt}K + \int_V w dV, \tag{7.4}$$

where K is kinetic energy of the system.

7.1.2 Measure of Strains

It is not unique how to describe strains. The common way in continuum mechanics is based on the deformation gradient tensor, $\mathbf{F}$, where it is described by the material coordinate system and spatial coordinate system. With the fundamental assumption of continuum mechanics, $\mathbf{F}$ is a non-singular tensor, which allows using polar decomposition:

$$\mathbf{F} = \mathbf{R} \cdot \mathbf{U} = \mathbf{V} \cdot \mathbf{R}, \tag{7.5}$$

where $\mathbf{R}$ is an orthogonal tensor, and $\mathbf{U}$ and $\mathbf{V}$ are called right and left stretching tensors. Note that $\mathbf{U}$ and $\mathbf{V}$ are symmetric and positive definite. Since the orthogonal tensor, $\mathbf{R}$, controls rotation of the system the real deformation can be described without rotational one through

$$\mathbf{B} = \mathbf{F} \cdot \mathbf{F}^T = \mathbf{V} \cdot \mathbf{R} \cdot \mathbf{R}^T \cdot \mathbf{V}^T = \mathbf{V} \cdot \mathbf{V} \tag{7.6}$$

$$\mathbf{C} = \mathbf{F}^T \cdot \mathbf{F} = \mathbf{U}^T \cdot \mathbf{R}^T \cdot \mathbf{R} \cdot \mathbf{U} = \mathbf{U} \cdot \mathbf{U}, \tag{7.7}$$

which are called left and right Cauchy-Green tensors, respectively. There are many ways to define a measure of strains, which are outside of the focus of the thesis.

7.1.3 Construction of strain energy function

Relation between velocity gradient tensor and deformation gradient tensor is described by

$$\mathbf{L} = \frac{d\mathbf{F}}{dt} \cdot \mathbf{F}^{-1}, \tag{7.8}$$

which implies

$$w = \mathbf{T} : \mathbf{L} = tr\left(\mathbf{T} \cdot \mathbf{L}\right) \tag{7.9}$$

$$= tr\left(\mathbf{T} \cdot \frac{d\mathbf{V}}{dt} \cdot \mathbf{V}^{-1}\right) + tr\left(\mathbf{T} \cdot \frac{d\mathbf{R}}{dt} \cdot \mathbf{R}^{T}\right) \tag{7.10}$$

$$= tr\left(\mathbf{T} \cdot \frac{d\mathbf{V}}{dt} \cdot \mathbf{V}^{-1}\right) \tag{7.11}$$

$$= tr\left(\mathbf{V}^{-1} \cdot \mathbf{T} \cdot \frac{d\mathbf{V}}{dt}\right) \qquad (\because \text{ trace is invariance under cyclic permutation}). \tag{7.12}$$

Let define strain energy function, W:

$$w = \frac{d}{dt}W(\mathbf{V}) \quad \text{or} \quad w = \frac{d}{dt}W(\mathbf{U}), \tag{7.13}$$

we have

$$w = tr\left(\mathbf{V}^{-1} \cdot \mathbf{T} \cdot \frac{d\mathbf{V}}{dt}\right) = \frac{d}{dt}W(\mathbf{V}) = tr\left(\frac{\partial W(\mathbf{V})}{\partial \mathbf{V}} \cdot \frac{d\mathbf{V}}{dt}\right) \tag{7.14}$$

$$\Rightarrow tr\left(\left(\mathbf{V}^{-1} \cdot \mathbf{T} - \frac{\partial W(\mathbf{V})}{\partial \mathbf{V}}\right) \cdot \frac{d\mathbf{V}}{dt}\right) = 0, \tag{7.15}$$

which must be hold with arbitrary deformation, $\mathbf{V}$. With pull-back notation from $\mathbf{V}$ to $\mathbf{B}$, we can express

$$\mathbf{V}^{-1} \cdot \mathbf{T} = 2\mathbf{V} \cdot \frac{\partial W(\mathbf{B})}{\partial \mathbf{B}}, \tag{7.16}$$

which implies general constitutive equation for hyperelastic body

$$\mathbf{T} = 2\mathbf{B} \cdot \frac{\partial W(\mathbf{B})}{\partial \mathbf{B}}. \tag{7.17}$$

7.1.4 Constitutive equation

With incompressible isotropic assumptions, we have

$$tr\mathbf{T} = p\mathbf{I}, \tag{7.18}$$

where p is called hydrostatic pressure and determined by boundary conditions, and $\mathbf{I}$ is identity tensor. For constitutive equation, stress is frequently defined only for its deviatoric part as

$$\tilde{\mathbf{T}} = \mathbf{T} - tr\mathbf{T} = 2\mathbf{B} \cdot \frac{\partial W(\mathbf{B})}{\partial \mathbf{B}} - p\mathbf{I}. \tag{7.19}$$

Let assumed that the principal directions for stress and strains are the same as isotropic material, and let $\{\lambda_1, \lambda_2, \lambda_3\}$ and $\{t_1, t_2, t_3\}$ are set of principal strains and stress, respectively. From Eq. (7.19), we have

$$t_k = \lambda_k \frac{\partial W}{\partial \lambda_k} - p. \tag{7.20}$$

For simplification, let the first principal axis is the main deformation axis while the third one is stress-free, we have principal stress-strain relations:

$$t_1 = \lambda_1 \frac{\partial W}{\partial \lambda_1} - \lambda_3 \frac{\partial W}{\partial \lambda_3}. \tag{7.21}$$

7.2 Hydrodynamic Interactions

From the generalized Langevin equation, Eq. (2.7), we can easily implement hydrodynamic interactions (HI) and one of the simplest way is through the Oseen tensor, Eq. (7.22).

$$\mathbf{D}_{ij} = D_{ij}(r_{ij}) \left(\mathbf{I} + \hat{\mathbf{r}}_{ij}\hat{\mathbf{r}}_{ij}\right) \quad i \neq j. \tag{7.22}$$

Then we need to decompose $\mathbf{D}_{ij}$ into the fluctuation terms for Wiener process: $\mathbf{C}$. The procedure can be done through the Cholesky decomposition or iterative method with orthogonal polynomial (Fixman 1986).

7.2.1 Simplified Single Connector

With the molecular picture like a dumbbell. This imagination is very valid especially when the system has a lower fraction of active bridges, $f_C^+ \approx 2\%$, once micelle has connector, it typically contains only single connector, and opponents attached micelle is the same. For simplification, let assumed that only connector force exerted (ignore repulsive parts). In this visualization, the HI part easily measurable through

$$\sum_j \mathbf{D}_{ij} \cdot \mathbf{F}_j = \mathbf{D}_{11} \cdot \mathbf{F}_1^{(nh)} + \mathbf{D}_{12} \cdot \mathbf{F}_2^{(nh)} \tag{7.23}$$

$$= D_0 \mathbf{F}_{12} + D_{12} \left(-\mathbf{F}_{21} - \mathbf{F}_{21}\right) \tag{7.24}$$

$$= \left(D_0 - 2D_{12}\right) \mathbf{F}_{12}. \tag{7.25}$$

In Oseen tensor, the diffusion coefficient are approximately given by

$$D_0 = \frac{k_B T}{\zeta} = \frac{k_B T}{6\pi\eta(R_0/2)} \tag{7.26}$$

$$D_{12} = \frac{k_B T}{\zeta_{12}} = \frac{k_B T}{8\pi\eta r_{12}}, \tag{7.27}$$

which indicate

$$\frac{1}{k_B T}\left(D_0 - 2D_{12}\right) = \frac{1}{\zeta}\left(1 - \frac{2\zeta}{\zeta_{12}}\right) = \frac{1}{\zeta}\left(1 - \frac{3R_0}{4r_{12}}\right). \tag{7.28}$$

In average value for r_{12} depends on α and dissociation rule, but the range is approximately from 0.5 to 2.0 in dimensionless space. When it is equal to the micelle diameter, R_0, the friction is 0.25 times lower than self-diffusion friction.

7.2.2 Hydrodynamics for Simplified Repulsion

Because repulsive force has opposite direction to the relative vector, $\mathbf{r}_{12}$, the HI effect becomes zero as the following sequence:

$$\mathbf{D}_{12} \cdot \mathbf{F}_{21}^{(rep)} = D_{12}(r_{12})\left(\mathbf{I} + \hat{\mathbf{r}}_{12}\hat{\mathbf{r}}_{12}\right) \cdot \left|\mathbf{F}_{21}^{(rep)}\right| (-\hat{\mathbf{r}}_{21}) \tag{7.29}$$

$$= D_{12}(r_{12})\left(\mathbf{F}_{21}^{(rep)} - \mathbf{F}_{21}^{(rep)}\right) = \mathbf{0}. \tag{7.30}$$

Figure 7.1 reports about the non-dimensional diffusion coefficient, $\tilde{D} = D/D_0$, with and without HI in the *simplified* single connector case. The dimensionless forces are given by $\tilde{F} = \frac{R_0}{k_B T}\mathbf{F}$ that will report in the secion of . In this *simplified* example, the hydrodynamic interaction really affect to the relaxation time for connector since the effective diffusivity reduced about factor of 4.

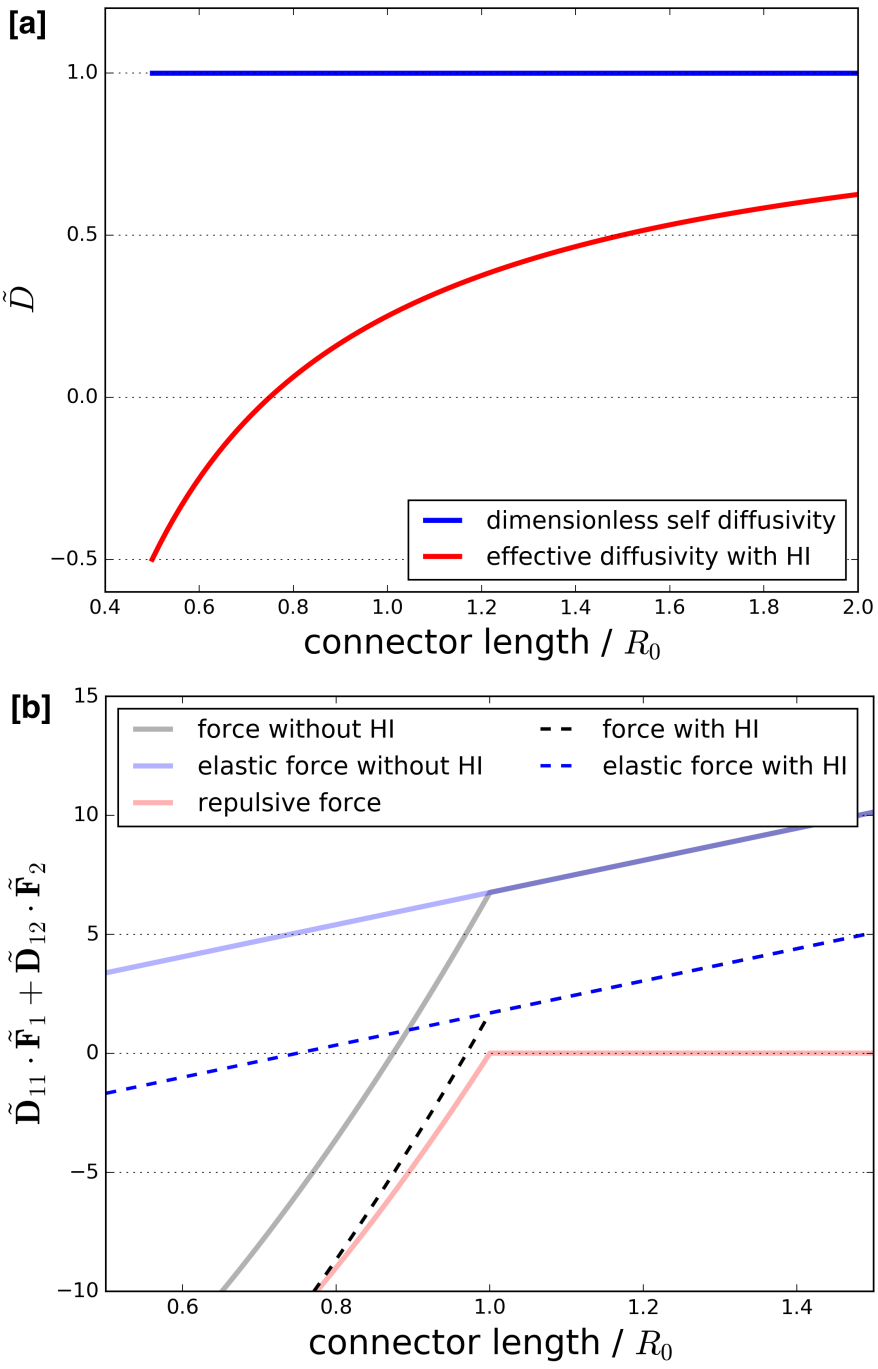

Figure 7.1: Comparison between the diffusivity with and without hydrodynamic interaction [a] and its effect too the time evolution [b].

Chapter 8

Development of Code

8.1 Data Structure

8.1.1 Mapping between One and Multi-Dimensional Arrays

For compatibility and convenience, the multi-dimensional arrays are expressed by one-dimensional array by index mapping function. To be specific, the given N by M 2-dimensional array may have the form of table 8.1, which is possibly mapped to table 8.2. The advantage for this expression can be thought as two parts: coding interface can be united and we can use several compression techniques such as lower occupation for a symmetric matrix. There are various numerical packages have been used this way: BLAS, LAPACK, GSL, and so on.

Table 8.1: Example for typical 2-dimensional array

index	0	1	2	$\cdots$	M
0	val(0,0)	val(0,1)	val(0,2)		val(0, M)
1	val(1,0)	val(1,1)	val(1,2)		val(1, M)
		$\vdots$		$\ddots$	
N	val(N,0)	val(N,1)	val(N,2)		val(N,M)

Table 8.2: Example for mapping to 1-dimensional array from 2-dimensional array.

index	0	1	⋯	M	M+1	⋯	NM
coord.	(0,0)	(0,1)	⋯	(0,M)	(1,0)	⋯	(N,M)
val.	val(0,0)	val(0,1)	⋯	val(0,M)	val(1,M)	⋯	val(N,M)

8.1.2 Adjacency Matrix and List

Consider the given association information, we can express the information using adjacency matrix:

$$\mathbf{C}_m = [\mathscr{C}_{ij}]\,, \tag{8.1}$$

where $\mathscr{C}_{ij}$ is number of associations for the pair of i- and j-th particles. The expression is quite simple, and it contains all the existing information. However, the adjacency matrix is expensive both of time and space complex because adjacency matrix explicitly denotes zeros inside the array, which needed more time for zero identification during processing. Hence, the adjacency list has been used:

$$\mathbf{C}_l = [\mathscr{I}_i(j)]\,, \tag{8.2}$$

where i denote the index of the subject particle, j denote index of columns, and $\mathscr{I}_i(j)$ is the index that is j-th connection to the i-th particle. For instance, consider the given network has the form of figure 8.1, then the adjacency matrix becomes table 8.3 and the adjacency list is expressed in table 8.4. Note that the weight for the bridge should be stored in separated array for adjacency list.

8.2 Implementation of Periodic Boundary Condition

8.2.1 Minimum Image Convention

At the moment, only the rectangular PBC is under the consideration. When we are computing some potential or distance, we have to account all image of particles

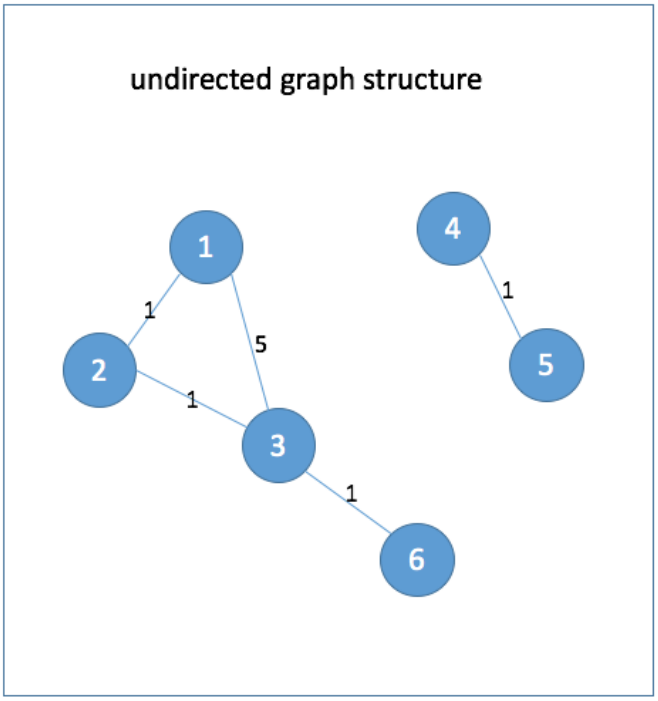

Figure 8.1: Example for association maps. It can be regarded as undirected graph since there is no directional information for the association (edge as CS notation) between particles (vortex as CS notation).

with different cells. Without loss of generality on a spatial dimension, the minimum is determined by following codes.

```
1       double UTIL_ARR::get_minimum_image_k_from_x(double x, double k,
            double dimension)
2       {
3         double kd[3] = {k-dimension - x, k - x, k+dimension - x};
4         double re= kd[get_index_minimum_abs(kd, 3)] + x;
5         return re;
6       }
7
8       MKL_LONG GEOMETRY::get_minimum_distance_pos_vector(TRAJECTORY& TRAJ,
             MKL_LONG index_t, MKL_LONG given_index, MKL_LONG target_index,
            MATRIX& given_vec)
9       {
```

Table 8.3: Example of adjacency matrix for figure 8.1.

	1	2	3	4	5	6
1	N_1	1	5	0	0	0
2	1	N_2	1	0	0	0
3	5	1	N_3	0	0	1
4	0	0	0	N_4	1	0
5	0	0	0	1	N_5	0
6	0	0	1	0	0	N_6

Table 8.4: Example of adjacency list for figure 8.1.

bead	0	1	2
1	2	3	0
2	1	3	0
3	1	2	6
4	5	0	0
5	4	0	0
6	3	0	0

```
10          for(MKL_LONG k=0; k<TRAJ.dimension; k++)
11          {
12            given_vec(k) = UTIL_ARR::get_minimum_image_k_from_x(TRAJ(index_t
                  , given_index, k), TRAJ(index_t, target_index, k), TRAJ.
                  box_dimension[k]);
13          }
14          return 0;
15        }
```

8.2.2 Component-wise Minimum Distance

```
1 double get_minimum_image_k_from_x(double x, double k, double dimension)
```

```
{
    double kd[3] = {k-dimension - x, k - x, k + dimension - x};
    double re = [get_index_minimum_abs(kd, 3)] + x;
    return re;
}
```

8.2.3 Applying Periodic Boundary Condition for Trajectory

The application of PBC on the trajectory is doable using the absolute value of coordinate. The sourcecode is using 0 as origin, and all the box dimension is set as a positive value from the origin. Therefore, it is needed to transit to make center as origin, taking modulo operator, then transit to original coordinate. The approach is described by the following codes.

```
MKL_LONG GEOMETRY::minimum_image_convention(TRAJECTORY& TRAJ,
    MKL_LONG target_t)
{
  for (MKL_LONG i=0; i<TRAJ.Np; i++)
  {
    for (MKL_LONG k=0; k<TRAJ.dimension; k++)
    {
      double diff = TRAJ(target_t, i, k) - 0.5*TRAJ.box_dimension[k
          ];
      double sign = diff/fabs(diff);
      if (fabs(diff) > 0.5*TRAJ.box_dimension[k])
      {
        TRAJ(target_t, i, k) -= sign*TRAJ.box_dimension[k];
      }
    }
  }
  return 0;
}
```

8.2.4 Trajectory Conversion

Because of minimum image convention, we need to recover from PBC image to real beads trajectory to measure MSD. This conversion is doable with an appropriate condition for the identity for trajectory. Here, the identity of boundary jumping is through the half of box dimension is changed from the previous output step, the trajectory is identified as jump and post-processing code will recover it. Note that the trajectory output frequency is lower than the all time steps, if this conversion is needed, we have to reduce the overall time steps. The core parts of the code are listing as below.

```
1     def sign(x):
2     if x < 0.:
3     return -1.
4     return 1.
5
6     def inv_PBC(x_now, x_next, LB):
7     dX = x_next - x_now
8     if abs(dX) > 0.5*LB:
9     return inv_PBC(x_now, x_next - sign(dX)*LB, LB)
10    return x_next
11
12    for i in range(NP):
13    for k in range(ND):
14    index_Rik = 2*ND*i + 1 + k
15    for t in range(1, Nt):
16    dat[t, index_Rik] = inv_PBC(dat[t-1, index_Rik], dat[t, index_Rik], LB
          )
```

Note that the inverse mapping function, inv_PBC, is using recursive call, that is because the main process override the opened dat array for effienciency issue, that sometimes amplified the existing gap during correction. Therefore, it is of importance to check the range is valid for inverse mapping using recursive call. From this conversion, we can expect the trajectory from figure 8.2. Note that the judgment is based on the half of box dimension.

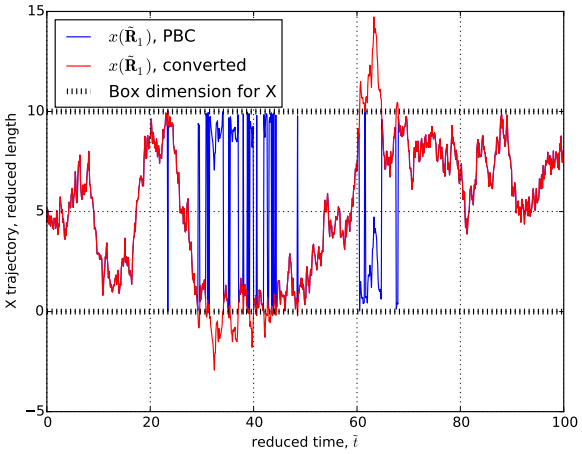

Figure 8.2: Test results for trajectory conversion. Blue color represent the trajectory using periodic boundary condition (PBC) and the red color represent the converted data. The test is done using pure Brownian motion with 100 reduced time step, and trajectory is involved only for x-coordinate of the first beads among 100 beads on the system.

8.3 Parallel Computing

Up to now, the only shared memory parallelization is supported via OpenMP package. In order to support GRID computing with multiple nodes. As described in section 8.4.4, OpenMP is enough to satisfy the simulation size. It is noteworthy that OpenMP on the C++ has some importance issue to make private variable. Since class instant is used for our convenience that described in above, the private class instance for OpenMP always calls "default constructor". Because default constructor of MATRIX library is suffers from overhead, it must be used in firstprivate rather than private. The option "firstprivate" is taking copy-constructor rather than default constructor.

8.3.1 Random Streams

The random number generation of this code is through GSL support (as MKL backend), which is NOT thread-safe. If we are using the same stream with the different thread, the generated random number will violate the statistics. On this regards, the

pre-allocated stream-line for the random number is used, and the number of stream-line is the same with the number of threads. Therefore, we can avoid the violate random streaming. Near future, random generation by MKL will be implemented that is thread-safety. Therefore, the multiple streaming is applied (appendix 8.4.4.

8.3.2 Brownian Update

For detail, see part of Euler Integrator in lib_evolution.cpp file.

```
1     #pragma omp parallel for default(none) shared(TRAJ, POTs, CONNECT,
          index_t_now, index_t_next, R_minimum_vec_boost,
          R_minimum_distance_boost, vec_boost_Nd_parallel, force_spring,
          force_repulsion, force_random, r_boost_arr, N_THREADS_BD,
          given_condition) num_threads(N_THREADS_BD) if(N_THREADS_BD > 1)
2       for (MKL_LONG i=0; i<TRAJ.Np; i++)
3         {
4           MKL_LONG it = omp_get_thread_num(); // get thread number for
                shared array objects
5
6           force_spring[i].set_value(0);
7           force_repulsion[i].set_value(0);
8           force_random[i].set_value(0);
9
10          if(given_condition("Step")!="EQUILIBRATION")
11            INTEGRATOR::EULER_ASSOCIATION::cal_connector_force_boost(TRAJ,
                  POTs, CONNECT, force_spring[i], index_t_now, i,
                R_minimum_vec_boost, R_minimum_distance_boost);
12          INTEGRATOR::EULER::cal_repulsion_force_boost(TRAJ, POTs,
                force_repulsion[i], index_t_now, i, R_minimum_vec_boost,
                R_minimum_distance_boost);
13          INTEGRATOR::EULER::cal_random_force_boost(TRAJ, POTs,
                force_random[i], index_t_now, r_boost_arr[it]);
14          for (MKL_LONG k=0; k<TRAJ.dimension; k++)
15            {
16              TRAJ(index_t_next, i, k) = TRAJ(index_t_now, i, k) + TRAJ.dt
                    *((1./POTs.force_variables[0])*force_spring[i](k) +
```

```
                    force_repulsion[i](k)) + sqrt(TRAJ.dt)*force_random[i](k
                    );
17              }
18          }
```

Because of overhead for copy constructor in the MATRIX class, all the internal variables are avoided the overloaded operators. The reference pass through pre-allocated objects are very fast in C++, but to reduce the readability of the code. The way to implement copy constructor inside of operator overload without overhead will be considered in future.

8.3.3 Parallelization of Topological Rearrangement

LOCKING Bead

The parallelization for Brownian update is very simple as depicted in above. In the case of topological update, however, it is quite tricky because of parallelization potentially violate the statistics of randing picking - dissociation - association chains. On this regards, LOCKING mechanism is introduced that means whenever the beads are an invisited state; the bead is locked until the processing on the bead is done. The main parts of locking are described in the below code. The check is through the OpenMP critical directive, which means the only one process allowed to enter following bracket. However, this scheme makes strong overhead to reduce the efficiency of parallelization. For instance, the computation time for topological update is 2.5 when we use 6 processors.

```
1 #pragma omp critical(LOCKING)  // LOCKING is the name for this critical
      blocks
2               {
3                 // CHECKING
4                 for(MKL_LONG I_BEADS = 0; I_BEADS < 3 && N_THREADS_SS > 1;
                        I_BEADS++)
5                   {
6                     if(LOCKER(IDX_ARR[it].beads[I_BEADS]))
7                       {
```

```
8                       IDENTIFIER_ACTION = IDX_ARR[it].CANCEL;
9                       IDENTIFIER_LOCKING = TRUE;
10                      break;
11                    }
12                }
13              // this is LOCKING procedure
14              if(!IDENTIFIER_LOCKING)
15                {
16                  cnt++;  // preventing LOCKING affect to the
                        IDENTIFICATION of stochastic balance
17                  for(MKL_LONG I_BEADS = 0; I_BEADS < 3 && N_THREADS_SS
                        > 1; I_BEADS++)
18                    {
19                      LOCKER(IDX_ARR[it].beads[I_BEADS]) = TRUE;
20                    }
21                }
22              else
23                {
24                  cnt_lock ++;
25                }
26            }
```

8.3.4 Interfacial Design for Cell-List

Cell List in Equilibrium Simulation

Since the implementation of the cut-off scheme through cell-list is on queue, it is much efficiency compared with the suggested LOCKING procedure. The cell-list composed of a different block of cells inside the box and the cell dimension is higher than a cut-off radius. On this scheme, to pick beads inside the different cell does not violate the statistics. The implementation will be done in future.

Modified Cell List: Dynamic Offset

It is of importance to aware the change of PBC boundary condition also affect to search neighbour-list through cell list. Dobson et al. (2016) summarized two difference way to overcome this problem: dynamic size and dynamic offset methods. By these names, we can adjust the size of subjected cell or searching mechanism using offset. For instance, GROMACS allows multiple cut-off schemes for short-range interactions, which is the sign that they also identify different cell list scheme from the original one. Before applying multiple cell list scheme, the dynamic offset will be applied first as it is easy to implement.

First of all, we have to think the PBC condition reported in the previous section: modulo. The modulo is applied after mechanical perturbation, which means the subjected PBC box keep bricks-shape as it was. In consequence, there are no changes for cells inside PBC box with all of the neighbor cells are inside PBC box.

For the case of cells in boundary which means it must travel beyond the boundary to count all the neighbor cells, recall the equation (2.61) which keeps the coordination on the up-center box with time evolution into the up-center box with periodic truncation, modulo. The thing is index function for modulo is still the same. The index for new coordinate is easyly computed by

$$\mathscr{I}_C^{eq} = \mathbf{r}' \mod L_C, \tag{8.3}$$

where $\mathbf{r}'$ is perturbed position.

8.4 Overview of Code

The main simulation codes are fully developed by C++ with supporting of scientific packages. The package is controlled by bash scripts and version control, git, is used to keep individual stable and developing branches to test different methodology. The test conditions are described accordingly the personally define the input file format. Through the parsing of the given input file, the code has great flexibility to test in various condition

and handling. The post-processing codes are mainly builded up Python with supporting of numpy, scipy, and matplotlib. The core library has three layers that (i) the basic infrastructure, (ii) handling various functionality, and (iii) to assemble the supported functionality into working code as a simulator. The library for (i) and (ii) are in lib directory while the simulators are in 'src' directory. There is several division in the code interface that will be explained in later sections.

8.4.1 Scientific Packages

In the back-end, the Math Kernel Library (MKL) from Intel is used to handle several numerical packages and variable types. The main mathematical functions are supported by GNU's Scientific Library (GSL) especially for the random noise, sorting algorithm, and interface with CBlas. Blas interface is somehow importance to achieve the performance. The interface of LaPack is through the MKL, but which is not critical in this simulation code.

Intra-node parallelism is applied using OpenMP, and it is enough for the simulation purpose. The reasons will be described in later in the technical details, but briefly related with the performance analysis. The methodology is composed of two individual time evolutions where the Langevin equation highly parallelizable because of the all the information is given by the previous history through the simplified Euler integrator combined with cell-list. In the case of topological renewal, however, this stochastic simulation have some sequential information that makes difficult to make parallelization.

8.4.2 Computation Flow Chart

Before entering the deeper side of the simulation, it will be helpful to see the sequence of simulation flows corresponding the methodology developed in section 2. Figure 8.3 report its simplified point of view with time analysis that without cell-list (because of non-equilibrium simulation) in 8 processor case. The details of the parts will be covered in the following sections.

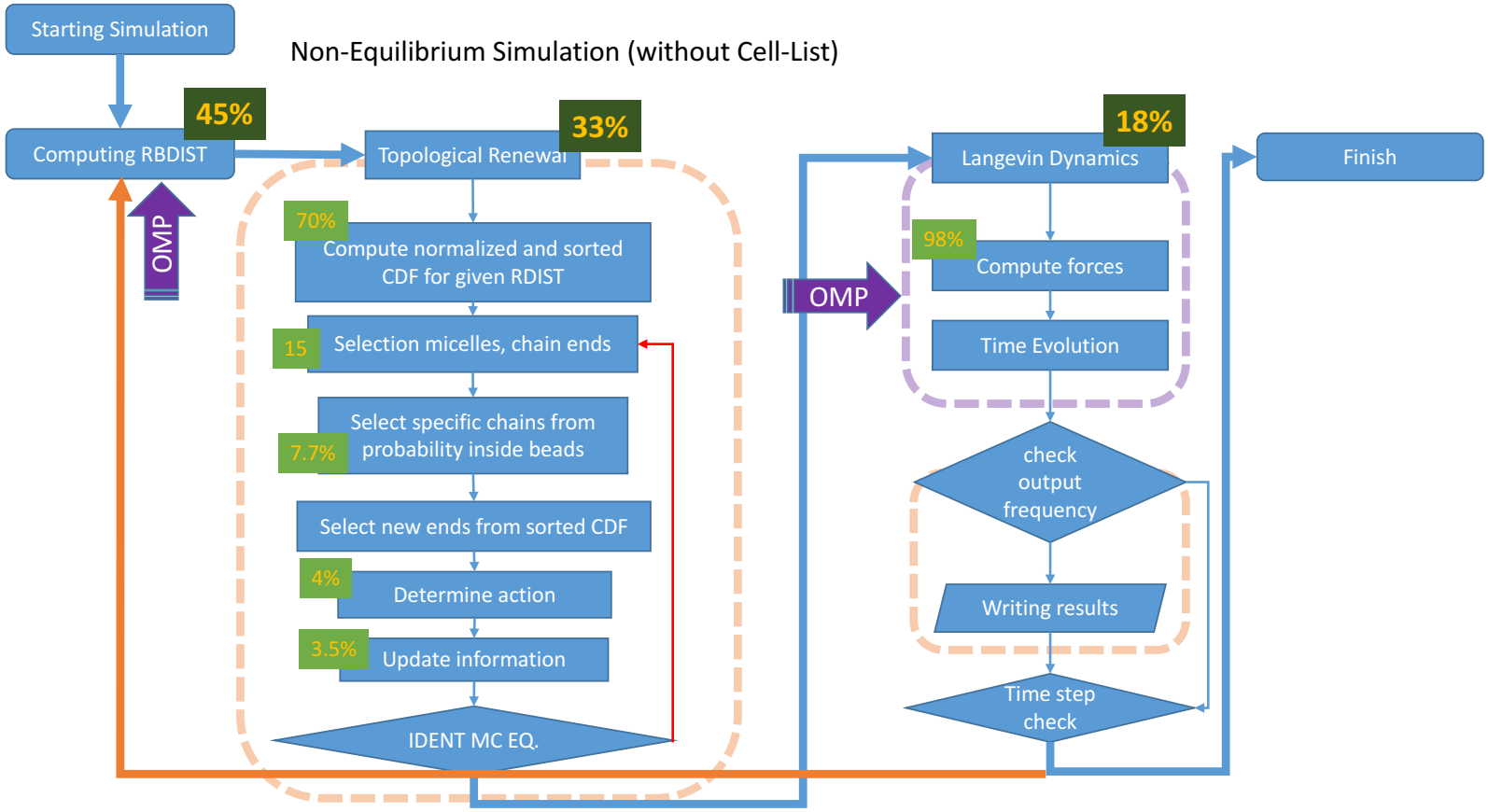

Figure 8.3: Overall flow charts for the simulation. The computational cost is represent as % in the three main blocks: (i) getting distance distribution (without cell-list since the chart shows non-equilibrium simulation, (ii) topological renwal, and (iii) Langevin update. The minor contributions are ignored to reports such as minimum image convention.

8.4.3 Version Control System

git is used to handle individual versions for many purposes. To make new simulation usually involved with many developing branches where the branches are not fully stabilized. In this aspect, version control system suggests having stable branch where only verified tests through memory leakage and regression test are fetched while individual developing branches still live and support the ability to merge in a selective way. Figure 8.4 shows the activities for code development in the statistics of git and part of change, merge, and branching about stable and developing branch in 30 commits out of 687 commits.

8.4.4 Layer 1: Building Blocks

Brief introduction for codes are revised in here. The main message is to keep the interfacial design without loss of performance, so the development branches can have its structures that replaced by the other branches. The building block layer composed of 5 individual libraries that handle the details of individual tricks and core of the simulation while those layers are free from the specific system dependency or sequence of simulation like the computational flow chart reported in figure 8.3. The libraries in the building block layer are designed for general purpose, although minor system dependency is there, there are many interfacial functions to bridge between powerful numerical packages and design of our libraries.

Matrix Interface: matrix.h

This library mainly related to the interfacial function between scientific package and personally defined matrix class. The matric operation are overloaded as following manner.

```
C = A*B + C;
```

```
1 double& MATRIX::operator()(MKL_LONG i, MKL_LONG j);
2 double& MATRIX::operator()(MKL_LONG i);
```

Project name:
.git
Generated:
2017-02-20 23:01:21 (in 74 seconds)
Generator:
GitStats (version 55c5c28), git version 2.10.1 (Apple Git-78), gnuplot 5.0 patchlevel 5
Report Period:
2015-07-14 13:27:40 to 2017-02-19 03:46:36
Age:
587 days, 240 active days (40.89%)
Total Files:
11319
Total Lines of Code:
1819262 (4431736 added, 2612474 removed)
Total Commits:
687 (average 2.9 commits per active day, 1.2 per all days)
Authors:
2 (average 343.5 commits per author)

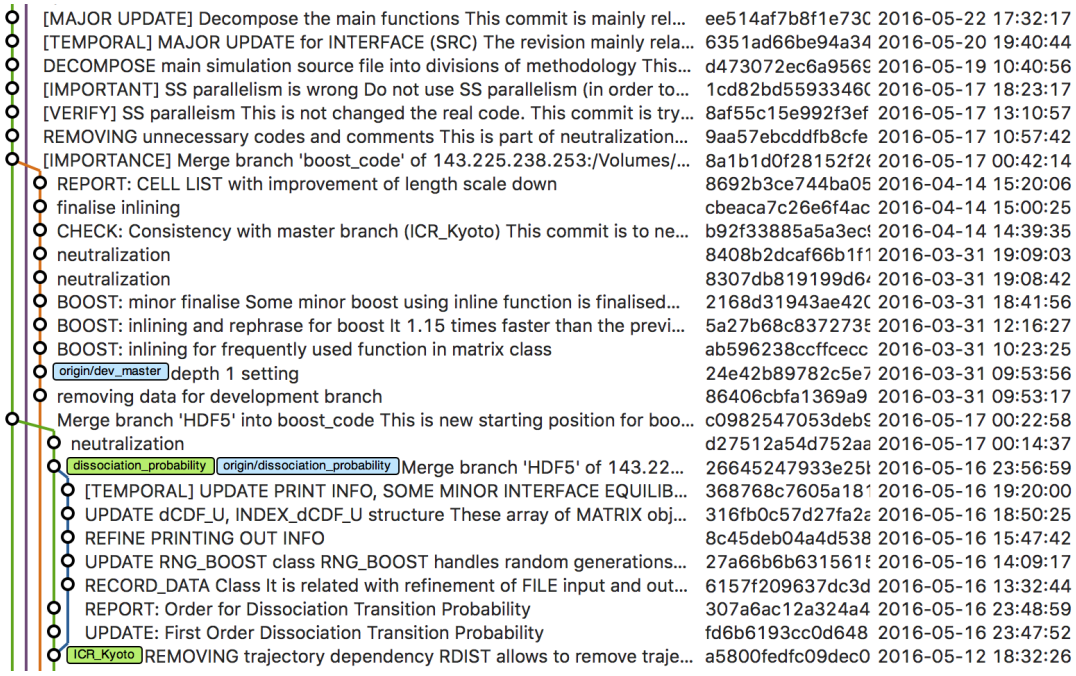

Figure 8.4: Activity log of code development (top) and part of git commit history to show how to keep stable branch and developing branches and selective merge.

```
3     MATRIX& MATRIX::operator=(const MATRIX &Mat);
4     MATRIX& MATRIX::operator+=(const MATRIX &Mat);
5
6     // MATRIX Addition : C = A+B
7     MATRIX operator+(const MATRIX &A, const MATRIX &B);
8     MATRIX operator-(const MATRIX &A, const MATRIX &B);
9     // Scalar Multiplification : C = a*A
10    MATRIX operator*(const double a, const MATRIX &A);
11    // MATRIX Multiplification : C = A*B
12    MATRIX operator*(const MATRIX &A, const MATRIX &B);
13
14    // Unary operator
15    MATRIX operator-(const MATRIX &A);
```

Note that these overloaded operator are used when in development branch while the fully tested codes are replaced by the operators in scientific packages because of performance.

Parsing Test Condition: file_IO.h

For general purpose program, the personally developed format for input file is used. The COND class contains basic information of given condition file and handling of it in to several ways. Here is a working test condition with all the given variables.

```
1  ## METHOD
2  ## METHOD::Basic Methodological input
3  ## METHOD::Method: BROWNIAN, DUMBBELL, REPULSIVE_BROWNIAN,
       NAPLE_ASSOCIATION
4  ## METHOD::Step: EQUILIBRIATION, NO_EQUILIBRIATION
5  ## METHOD::Stochastic Integrator: Only 'Euler' is applied at this moment
6
7  Method=NAPLE_ASSOCIATION
8  Step=NO_EQUILIBRATION
9  Integrator=Euler
10
11 ## DIMENSION
12 N_dimension=3
```

```
box_dimension=10.0

## TIME::Time scales and data resolutions
dt/tauR=0.01
Nt=1000000
reset_initial_time=TRUE
## TIME::TOPOLOGY
N_steps_block=1
Rt=1
## TIME::DATA_RESOLUTION
N_skip_ener=10
N_skip_file=1000
record_RDIST=TRUE
N_skip_rdist=1000

## THREADS
## THREADS::LANGEVIN
N_THREADS_BD=4
## THREADS::TOPOLOGY
N_THREADS_SS=1


## PARTICLE
Np=400
## PARTICLE::friction: DEFAULT or DISSOCIATION_TIME
friction_junction=LOOP_DISSOCIATION_TIME
## PARTICLE::REPULSION
repulsion_coefficient=25
effective_distance=1.0

## CHAIN
N_chains_per_particle=5
## CHAIN: it allows to track all the index of individual chain ends
tracking_individual_chain=TRUE

## CHAIN::KINETICS
```

```
49 ## CHAIN::KINETICS::check transition probability
50 ### transition_probability can be DISSOCIATION, CUTOFF_DISSOCIATION, or
       MINIMUM_R0_DISSOCIATION
51 transition_probability=MINIMUM_R0_DISSOCIATION
52 ### association_probability can be DEFAULT, EQUAL_CUTOFF_RANGE, or
       minimum_R0_Boltzmann
53 association_probability=minimum_R0_Boltzmann
54 ## CHAIN::KINETICS::probability to select the specific chain (end)
55 chain_selection=UNIFORM
56 ## CHAIN::KINETICS::number of allowed fluctuation for chain ends per
       micelle
57 tolerance_allowing_connections=3
58 ## CHAIN::KINETICS::stochastic cut-off for bridge forming
59 cutoff_connection=2.0
60 ## CHAIN::KINETICS::length scale related with physical aggregation in
       hydrophobic chain ends
61 l_cap=0.12
62
63 ## CHAIN::ELASTICITY
64 ## CHAIN::ELASTICITY::chain properties: Gaussian, Modified_Gaussian, FENE
65 connector=Modified_Gaussian
66 ## CHAIN::ELASTICITY::MODIFIED_GAUSSIAN::related with re-scaling factor,
       alpha:= R0/rms(R_chain)
67 scale_factor_chain=1.5
68
69 ## UTILITY: some other features
70 allowing_multiple_connections=TRUE
71 MC_renewal=FALSE
72 cell_list=TRUE
73
74 ## NE::Non-Equilibrium Simulation
75 ## NE::related with mechanical perturbation: FALSE, SIMPLE_SHEAR,
       STEP_SHEAR
76 MECHANICAL_PERTURBATION=FALSE
77 ## NE::axis (0, 1, 2) = (x, y, z)
78
```

```
79 ## NE::SHEAR
80 shear_axis=0
81 shear_grad_axis=1
82 ## NE::SHEAR::SIMPLE_SHEAR
83 #### NE::SIMPLE_SHEAR::tau_C depends on the definition of the system
84 #### NE::SIMPLE_SHEAR::note that this definition will be chainged in the
       future
85 Wi_tau_C=0.5
86 ### NE::SHEAR::STEP_SHEAR
87 gamma_0=0.5
88
89 ## SEEDS
90 ## random seeds: it is related with the random sampling and average over
       it
91 ### in the case for SCoPE grid server, the automatic submission will be
       varied depends on the
92 basic_random_seed=100
93 ### random seeds for stochastic evolution
94 basic_random_seed_SS=150
95
96 ## file information
97 output_path=short_test
98 filename_base=NP0400_LD10P3_C025
99
100 ## note that CONTINUATION_STEP should be -1 as default
101 ## otherwise, it will inherit with the given number of steps
102 CONTINUATION_TRAJ=TRUE
103 CONTINUATION_STEP=-1
104 CONTINUATION_TRAJ_FN=LD10P3/EQ3D_NP0400_LD10P3.traj
105
106 CONTINUATION_CONNECTION=FALSE
107 CONTINUATION_HASH_FN=FALSE
108 CONTINUATION_WEIGHT_FN=FALSE
109
110 CONTINUATION_CHAIN=FALSE
111 CONTINUATION_CHAIN_FN=FALSE
```

```
112
113 ## the following will be used for debugging or analysis of each instance
        of stochastic step
114 ## it will record all the stochastic decision including rolling
        probability
115 MC_LOG=FALSE
116 MC_ASSOCIATION_MAP=FALSE
117
118 # unncessary options at this moment
119 # tolerance_association=0.001
120 # ratio_RM_R0=11
```

Note that the operator overloading is useful to handling the conditions. For instance, if we need the value for "condition", we simply use COND("condition") that return the value as string class. If we need C-style string, just use c.str() method. In any case, checking conditional phrase is doable by following way.

```
1   if (given_condition("Integrator") == "Euler")
2   {
3     N_basic = 2;
4   }
```

Interfacial Functions for Random Signal: random.h

Since the randomness is of importance for Brownian motion, and the multiple generating random numbers are of importance for parallelization. In principle, there are two ways to generate the random sequence in a parallel computation where the first one is using the single random seed to allocate individual blocks of random sequences, then used each block in each thread. The second one is using the different random seed where the seeds are distinguishably defined for each thread that makes independence between difference random sequence in different threads. There are pros and cons for each of the way, but here the codes are designed to follow the second method because of easier to handle random seed especially when we perform multiple samples in the GRID server.

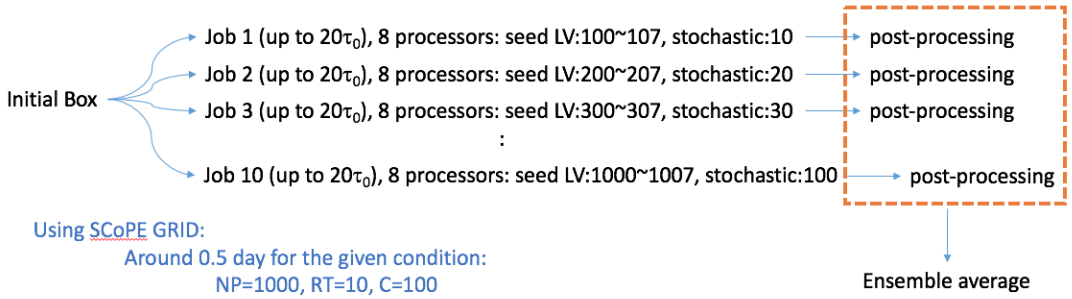

Figure 8.5: Sequence of random sampling allocation in the GRID server

Figure 8.5 shows how the random seeds are allocated when we use multiple sampling for the same condition. Using this individuality, we have great flexibility to handle the processor in efficiency manner. The random.h is composed of RNG_BOOST class and the following functions where the function is given by individually rather than member function in order to keep the similarity between interface.

Trajectory of Particles: trajectory.h

No matter what type of simulation will be performed, Brownian, repulsive Brownian, dumbbell, and associating telechelic polymers, the positions of the particles must be tracked. As already described in section 8.1, the 1-dimensional array is used for each of time step, where only two steps are necessary to tracking in the case of Euler integrator, Eq. (2.23). In this sense, TRAJECTORY class inherits from MATRIX class and its index function to connect between 1-dimensional and 2-dimensional arrays.

Cell-List: cell_list.h

The basic idea of cell-list is already described in section and also the parallelization scheme is reported in. It contains plenty of information related to PBC box that makes possible boosting up the code in any sense. It is noteworthy that the CLIST class is forced to use even without cell-list option to keep the function interface while this makes a single cell as PBC box and boundary check is replaced by its initial minimum image

convention. The index functions, index_vec2sca and index_sca2vec, is working to map between index array in 1-dimensional and 2-dimensional similar to the data structure of TRAJECTORY. In order to remove overhead, however, the function is only called when the constructor for CLIST is called.

Supporting Network Connectivity: connectivity.h

This is building block for handling index of the connectivity, while its application form is defined in the layer 2 where the classes inherit CONNECTIVITY and CHAIN_NODE classes defined in connectivity.h. The main reason to decouple the index handling in hierarchy manner is different level on the purpose and the complexity of its handling. It is a pair to note that this handling is the core of the simulation code since the core library for Langevin dynamics executable through well-known open sources such as LAMMPS and GROMACS. The handling connectivity for such a libraries are enough for the permanent network system, while our focus is mainly on the transient system which needs to track all the details of connectivity with each chain ends effectively. The CONNECTIVITY class support the basic class using adjacent list, section 8.1.2, that reduce time and space complexity for the simulation. In the case of CHAIN_NODE class, it support node of individual chains keep the attached point as index of micelles, but the change of degeneracy chains (chain connected with the same pair of micelle) are randomly selected to take an action. Note that CHAIN_NODE is distinguishable class that can be turn-on or off due to our needs.

8.4.5 Layer 2: Utility

In this layer, the 8 individual libraries are builded up to support the utility of basic properties. Notice that the libraries in this layer typically involved with the specific dependency that will be defined in the application layer later.

Allocation Potentials and Kinetics: potential.h

The design of potential.h is to support various pre-determined potential that can be replaced by the input file, section 8.4.4. The main idea is to keep the flexibility through the input file while the potentials and association/dissociation kinetics are given by pointer-function, so the initial constructing simulation time (only the beginning of simulation) that allocate the pointer function with the given pre-determined potentials. It is noteworthy that the define potentials are in the way of inline function, so the overhead for multiple calling of a small function is reduced. The class declaration for POTENTIAL_SET is described in below.

```
1  class POTENTIAL_SET
2  {
3   public:
4    double *force_variables;
5    double (*zeta_particle)(MKL_LONG N_connectors, double* given_variables);
6    double (*f_connector)(double distance, double* given_variables);
7    double (*e_connector)(double distance, double* given_variables);
8    double (*PDF_connector)(double distance, double* given_variables);
9    double (*f_repulsion)(double distance, double* given_variables);
10   double (*e_repulsion)(double distance, double* given_variables);
11   double (*scale_random)(MATRIX& basic_random_var_unity, double*
         given_variables);
12   double (*w_function)(double distance, double (*force)(double, double*),
         double* given_varialbes);
13   double (*transition)(double distance, double (*force)(double, double*),
         double* given_varialbes);
14   POTENTIAL_SET();
15   virtual ~POTENTIAL_SET();
16 };
```

Distance and Position Maps: geometry.h

The geometry.h contains plenty of functions that mainly related with PBC box and the relative distance between micelle with minimum distance in an optimized way. One of the main class in geometry.h is RDIST where its information keeps the distance distribution between micelles in the given effective cut-off distance (or PBC box when cut-off is turned off).

```
1 class RDIST : public CLIST
2 {
3 public:
4   MATRIX** Rvec; // Rvec[i][j] will be the relative vector between i- and
        j-th particles
5   MATRIX* Rsca; // Rsca[i](j) will be the relative distance between i- and
         j-th particles. The form is differ from the original.
6
7   RDIST();
8   RDIST(COND& given_condition);
9   virtual ~RDIST();
10 }
```

Individually, the namespace UTIL_ARR and GEOMETRY are designed to suggest utility functions that (i) easy implementation in the application layer when handling the RDIST related information such as potentials and association/dissociation kinetics, and (ii) to optimize the computation time with the inheritance of the effective cells.

Handling Association Index: association.h

The class ASSOCIATION inherit the CONNECTIVITY in appendix 8.4.4 with additional functionality to implement the association and dissociation kinetics in adjacency list, appendix 8.1.2. In this regards, ASSOCIATION class has details about probability for kinetics especially for the cumulating the association probability, Eq. 2.43, as member function. ASSOCIATION class is very lengthy and contains tidies functions, so here even the basic structure are omitted, but three important aspects are reported in here:

(i) the association map is sorted to suggest the highest performance for selection steps of topological index in backtrace way, (ii) TOKEN for individual micelles are computed to keep to know how many distinguishable particles are associated to the subjected micelle, and (iii) the dissociation procedure is mainly obtained in the way of opposite chain end since the selection probability for the chain ends belong the same chain are identical. The reason of (iii) is related to the efficiency for cell-list because the association map is based on the distance from the subjected micelle rather than opposite chain end.

In the case of individual chain ends, the additional layer for CHAIN_NODE is defined: CHAIN_INFORMATION. Since CHAIN_NODE suggest the individual node similar to linked-list (note that the real structure is not given by linked-list, but some pointer map has similar feature to have optimized performance). In this class, the individual chain ends are tagged with the micelle that breaks degeneracy of bridges in the random selection manner.

Utilizing Association Index: handle_association.h

This library is the highest level to handle network index where the class INDEX_MC support additional layer handling object of ASSOCIATION class. This utilized class support the interface with parallelization, especially for OpenMP. With INDEX_MC class, the function in application layer handles the index in different threads without difficulty. In addition, the library support additional layer for chain end tags, CHAIN_HANDLE, so the inheritance map is given by CHAIN_HANDLE::CHAIN_INFORMATION. With this class, all the chain ends support user-friendly interfacial function that will be used in the application layer.

Computing the Components-Wise Contribution for Integrator: time_evolution.h

The library is originally designed for supporing time evolution in the different integrator, but now the integrator is moved in the application layer (i.e., simulator) and only computation of component-wise contribution is accounted. The parallel computation is supported through OpenMP package, and the computation of virial stress (without scale

factor) is involved individual functions. Note that the virial stress is collected variable for the given PBC box, Eq. (2.67), computing virial stress in post-processing is a time-consuming task, which is the reason that virial stress is recorded in simulation time.

Locking Parallelization for Topological Renewal: parallel.h

The parallel.h is designed to support parallel computation for topological renewal, appendix 8.3.3, which, however, is stopped to use because of overhead during thread locking procedure. This point will be revised in future work. The strategy can be found in appendix 8.3.3.

8.4.6 Layer 3: Application

This is frequently called simulator layer in previous sections. The main reason is that the codes in this division support individual simulators such as Brownian, repulsive Brownian, dumbbell, and association telechelic polymers. It is understood that those simulators have common features similar to the inheritance class objects. For instance, the Brownian motion will be used for all the package, that suggest a basic feature for Brownian motion is defined in the namespace of BROWNIAN and with the structure of BROWNIAN_VARIABLE. Then, the repulsive Brownian motion will be changed the characteristic time from τ_B to τ_R, so this changes with a computation of repulsive contribution are involved in inheritance manner, which is also the same with the simulator for associating telechelic polymer as following.

```
1  struct REPULSIVE_BROWNIAN::
2  TEMPORAL_VARIABLE
3  : BROWNIAN::BROWNIAN_VARIABLE
4  {
5    statements;
6  };
7
8  struct
9  HEUR::
10 TEMPORAL_VARIABLE_HEUR
```

```
11    : REPULSIVE_BROWNIAN::TEMPORAL_VARIABLE
12    {
13      statements;
14    };
```

Note that dumbbell simulator only inherits the Brownian simulator because no repulsion is accounted and only CONNECTIVITY class is necessary rather than ASSOCIATION::CONNECTIVITY. The details on the application layer are omitted since it is too lengthy compare with its meaning, but the simulators are made up of the functions given by layer 1 and 2.

This page has been intentionally left blank

Chapter 9

Analysis of Simulation Results

9.1 Relaxation Modulus in Equilibrium Simulation

9.1.1 Calculation Cross-Correlation using Fast-Fourier Transform

In principle, the stress autocorrelation in Eq. (2.68) can be calculated by cross-correlation directly. The time complexity, however, the cross-correlation takes $\mathscr{O}(N_t^{*2})$ where N_t^* means the given number of time steps. Note that $N_t^* \neq N_t$ in general in order to reduce space complexity of data output, which is not problem when we measure rheological observable, such as η_0, when relaxation time is sufficiently large. To be specific, the time step is given by $10^{-2}\tau_R$ but the data recording for stress components is 1 per 10 time steps; then, the recorded stress components becomes 10^3. In this context, the computational time for direct cross-correlation reaches similar range of simulation time itself. Hence, Fast-Fourier transform (FFT) algorithm is applied based on the following relations (Borsellino and Poggio 1973)

$$\mathscr{F}\left[Corr[f,g]\right] = \bar{\mathscr{F}}[f]\mathscr{F}[g], \tag{9.1}$$

where $\mathscr{F}$ is Fourier operator and bar denote complex conjugate, which is not important since we consider real valued function for f and g. Because the computation time for FFT is $\mathscr{O}(N)$, it dramatically reduces the computation time.

9.1.2 Average Over Directional Contributions

As described above, $G(t)$ from Green-Kubo relation is suffers from its noise where the noise reduction typically involved in increasing box dimension and decreasing time step, and the both of the suggestion are not preferable because of simulation time. Daivis and Evans (1994) suggest the way of improving statistics in the way of average over the directional average for isotropic fluid:

$$10G(t) = \frac{V}{k_B T}\langle \boldsymbol{\tau}'(t) : \boldsymbol{\tau}'(0)\rangle_t = \frac{V}{k_B T}\langle \tau'_{ij}(t)\tau'_{ji}\rangle_t, \tag{9.2}$$

where $\boldsymbol{\tau}'$ is deviatoric part of $\boldsymbol{\tau}$ and summation convention is used.

$$10G(t)\frac{k_B T}{V} = 2\sum_{i,j>i}\langle \tau_{ij}(t)\tau_{ij}(0)\rangle + \sum_i \left\langle \left(\tau_{ii} - \frac{1}{3}tr\boldsymbol{\tau}\right)(t)\left(\tau_{ii} - \frac{1}{3}tr\boldsymbol{\tau}\right)(0)\right\rangle. \tag{9.3}$$

Because of the symmetric of stress, the off-diagonal parts easily derived into summation form, which means it is average over shear directions. The second parts of RHS in Eq. (9.3), let say $(*)$ for this section, is much complicate form with diagonal components of stress tensor. For simplification, let define the normal stress different between i and j axis as $N_{ij} = \tau_{ii} - \tau_{jj}$ and let omit the domain notation, (t) or (0), then the expansion the symbol becomes simpler but the product must be non-commutative, $N_{ij}N_{pq} \neq N_{pq}N_{ij}$, and anti-symmetric, $N_{ij} = -N_{ji}$. Obviously, it has property

$$N_{ij}N_{ik} - N_{ij}N_{jk} = N_{ij}N_{ij} \quad \text{and} \quad N_{ik}N_{ij} - N_{jk}N_{ij} = N_{ij}N_{ij}, \tag{9.4}$$

which make the expansion form easiler since

$$\left(\tau_{11} - \frac{1}{3}tr\boldsymbol{\tau}\right)(t)\left(\tau_{11} - \frac{1}{3}tr\boldsymbol{\tau}\right)(0) = \frac{1}{3}(N_{12} + N_{13})(N_{12} + N_{13}). \tag{9.5}$$

Applying these conventions into the second part of RHS in Eq. (9.3), we have

$$(*) = \frac{1}{9}\left[(N_{12} + N_{13})(N_{12} + N_{13}) + (N_{21} + N_{23})(N_{21} + N_{23}) + (N_{31} + N_{32})(N_{31} + N_{32})\right] \tag{9.6}$$

$$= N_{12}N_{12} + N_{12}N_{13} - N_{12}N_{23} + \cdots + N_{23}N_{23} \tag{9.7}$$

$$= \frac{1}{3}\left(N_{12}N_{12} + N_{13}N_{13} + N_{23}N_{23}\right). \tag{9.8}$$

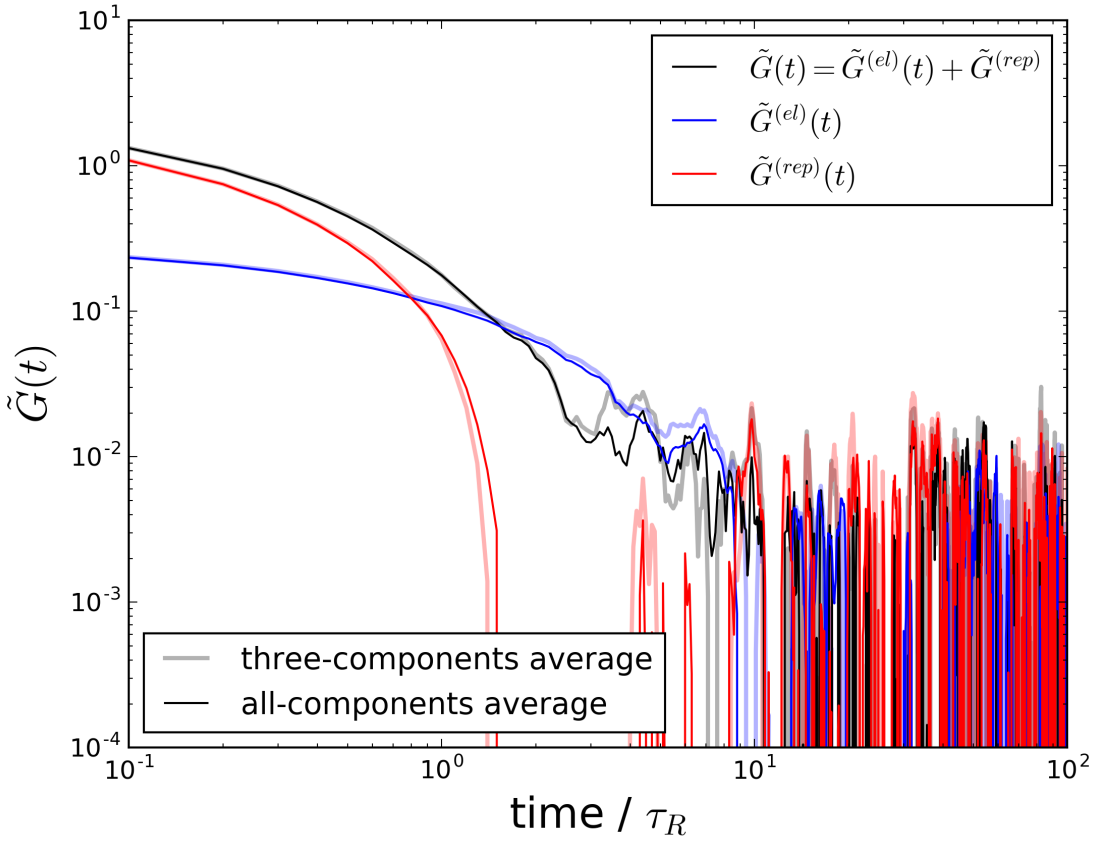

Figure 9.1: Comparison for the different average scheme.

Therefore, the final form of relaxation modulus becomes

$$G(t) = \frac{V}{5k_BT}\sum_{i,j>i}\langle\tau_{ij}(t)\tau_{ij}(0)\rangle + \frac{V}{30k_BT}\sum_{i,j>i}\langle N_{ij}(t)N_{ij}(0)\rangle, \tag{9.9}$$

which is the exactly same form with Ramirez et al. (2010).

9.1.3 Time Average and Sample for Relaxation Modulus

Despite the directional average, the figure 9.1 is not significantly changed. Underline ergodicity, we can apply time average for the relaxation modulus. In principle, the time gap between each blocks should be uncorrelated which means we must perform very long computation for the given condition. If we allows very minor correlation level, the efficiency to take time average becomes larger. One of the efficient way to average

over different time blocks are dividing time series into half block. Let assumed that system has N of time series then the half block obviously have $N/2$ time steps. Let assumed that N_{div} is number of division that shows the sufficient small correlation value at $t(N/(2N_{div}))$. Then, we can divide N_{div} blocks for the first half block and each block produce $G(t)$ with $t \in [t_i, t_i + N/2]$ where t_i is initial time for the subject block.

Since the SCoPE supercomputer is used for simulation, submit multiple samples is also useful. For equilibrium simulation, we compute relatively long time scale, so we do not have to change initial box condtion. Besides, we have to set different random seeds.

The relaxation modulus reports in figure 4.3 is the combination of average over 10 time blocks and 5 different samples (so, taking 50 sampling average) which shows at least one additional decade of $G(t)$ is readable compare with the case without these treatment. This additional resolution is of important to measure rheological observable.

9.1.4 Effective Cut-off Time of Relaxation Modulus

Since we cannot fully avoid noisy in relaxation modulus, we have to decide an effective cut-off time of relaxation modulus in order to measure zero-shear viscosity through Eq. (2.70) or other rheological observables from $G(t)$. Using change of variables, the spectrum can be shown in the way of figure 9.2 where the plot is $tG(t)$ vs. $log(t)$. In this way, we can identify the effective cut-off time when spectrum reaches zero before noisy is amplified.

9.2 Pair Correlation Function

9.2.1 Definition

The pair correlation distribution, $\rho(\mathbf{r}_1, \mathbf{r}_2)$, is one of commonly used function to show the spatial distribution of micelles (or particles). For given canonical ensemble (N, V, T), let Z be configurational integral, partition function:

$$Z = \int d\mathbf{\Gamma}_1^N \exp\left(-\beta U(\mathbf{\Gamma}_1^N)\right), \tag{9.10}$$

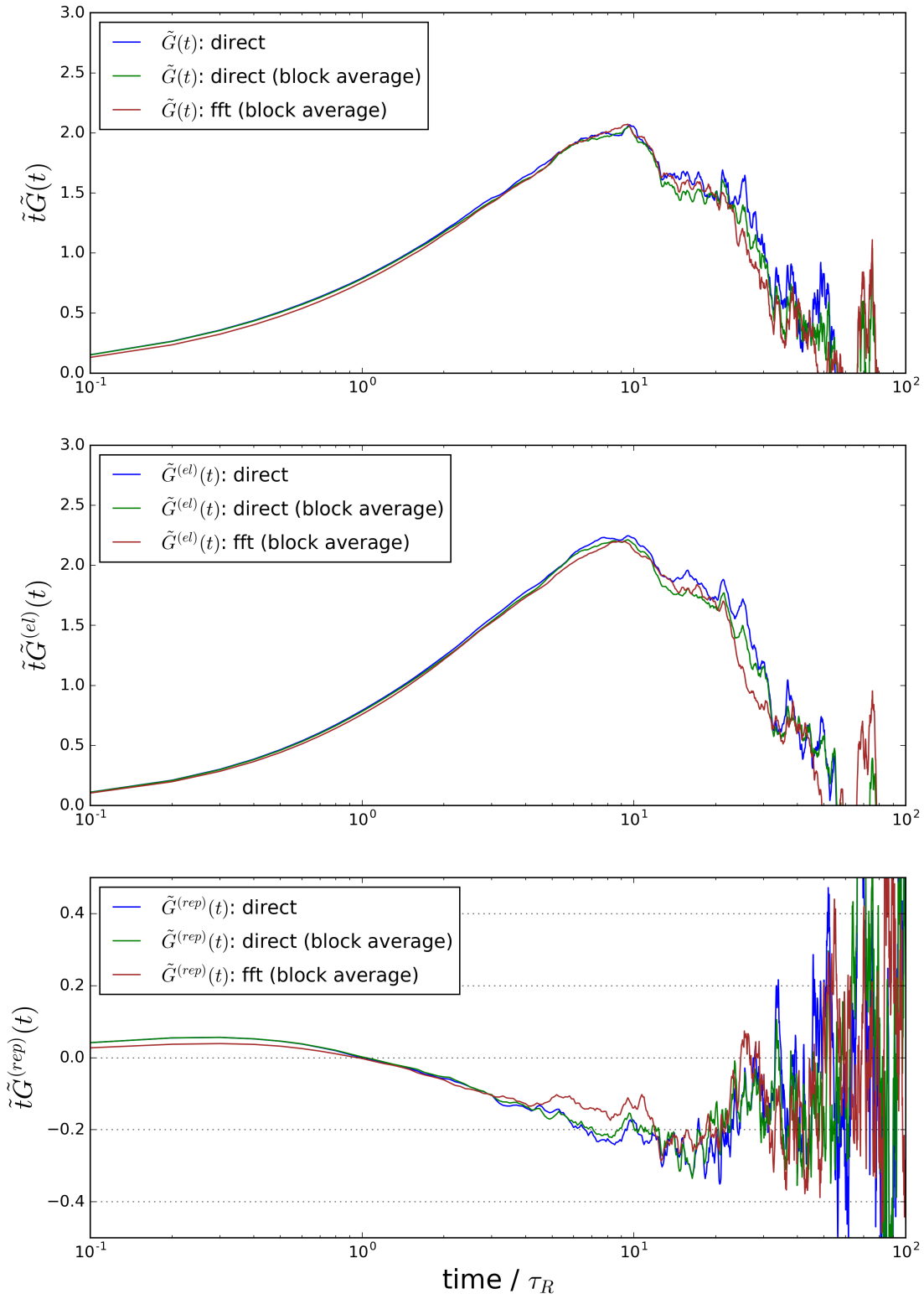

Figure 9.2: Component-wise comparison between correlation method.

where β be Boltzmann factor, $\mathbf{\Gamma}_1^N = \{\mathbf{r}_1, \cdots, \mathbf{r}_N\}$ and $d\mathbf{\Gamma}_1^N = d\mathbf{r}_1 \cdots d\mathbf{r}_N$. Then, the probability of an elementary configuration is expressed by

$$P(\mathbf{\Gamma}_1^N)d\mathbf{\Gamma}_1^N = \frac{\exp\left(-\beta U(\mathbf{\Gamma}_1^N)\right)}{Z} d\mathbf{\Gamma}_1^N, \tag{9.11}$$

where $d\mathbf{\Gamma}_1^N = d\mathbf{r}_1 \cdots d\mathbf{r}_N$. Let $P(\mathbf{\Gamma}_1^N)$ be configurational distribution over set of N-number of state variables, $\mathbf{\Gamma}_1^N = \{\mathbf{r}_1, \cdots, \mathbf{r}_N\}$. Since the configurational distribution $P(\mathbf{\Gamma}_1^N)$, is function of potential energy, $U(\mathbf{\Gamma}_1^N)$, it cannot account only for single particle. Hence, we can eliminating dependency of other particles using integrate over configurational space:

$$P(\mathbf{\Gamma}_1^n) = \int d\mathbf{\Gamma}_{n+1}^N P(\mathbf{\Gamma}_1^N), \tag{9.12}$$

which is joint PDF for finding particle $\{1, 2, \cdots, n\}$ at $\{\mathbf{r}_1, \mathbf{r}_2, \cdots, \mathbf{r}_n\}$, respectively. It is called *specific* PDF because of the index of particles are fixed. Let $\mathbf{\Omega}_1^n = \{\mathbf{r}_1, \cdots, \mathbf{r}_n\}$ be the set of particles which is arbitrarily chosen. If the particles are identical (indistinguishable system), we can express *generic* PDF when we allow choosing particles, arbitrarily:

$$\rho(\mathbf{\Omega}_1^n) = \frac{N!}{(N-n)!} P(\mathbf{\Gamma}_1^n) \tag{9.13}$$

For simplification, consider the given material is isotropic. Then the first order generic PDF becomes its density: $\rho(\mathbf{r}_1) = \rho = N/V$. When the particles independent to each other, the joint probability becomes

$$P_{id}(\mathbf{\Gamma}_1^N) = \prod_{k=1}^{N} P(\mathbf{r}_k) = \rho^N. \tag{9.14}$$

Therefore, the generic PDF for independent particle becomes

$$\rho_{id}(\mathbf{\Omega}_1^n) = \frac{N!}{(N-n)!} P(\mathbf{\Gamma}_1^n) = \frac{N!}{(N-n)!} \rho^n. \tag{9.15}$$

The correlation function g is given by the fraction of generic PDF of the system to the independent case:

$$g(\mathbf{\Omega}_1^n) \equiv \frac{\rho(\mathbf{\Omega}_1^n)}{\rho_{id}(\mathbf{\Omega}_1^n)} = \frac{P(\mathbf{\Gamma}_1^n)}{P_{id}(\mathbf{\Gamma}_1^n)} = \frac{1}{\rho^n} P(\mathbf{\Gamma}_1^n). \tag{9.16}$$

For convenience, $h(\mathbf{\Omega}) = g(\mathbf{\Omega}) - 1$ is frequently used as correlation function. Inversely, we have *specific* PDF:

$$P(\mathbf{\Gamma}_1^n) = \rho^n g(\mathbf{\Omega}_1^n). \tag{9.17}$$

When order is 2, the correlation functions is called pair correlation function:

$$g(\mathbf{r}_1, \mathbf{r}_2) = \frac{1}{\rho^2} P(\mathbf{r}_1, \mathbf{r}_2) = \frac{1}{\rho^2} \int d\mathbf{\Gamma}_3^N P(\mathbf{r}_1, \mathbf{r}_2) \tag{9.18}$$

$$= \frac{1}{\rho^2} \int d\mathbf{\Gamma}_3^N \frac{\exp(-\beta U(\mathbf{\Gamma}_1^N))}{Z}. \tag{9.19}$$

For spherically symmetric system, the probability between $\mathbf{r}_i$ and $\mathbf{r}_j$ becomes

$$P(\mathbf{r}_i, \mathbf{r}_j) = P(\mathbf{r}_i - \mathbf{r}_j). \tag{9.20}$$

For further details, see Chandler (1987).

9.2.2 Isotropic Radial Distribution Function

Let $\langle n_i(r, \Delta r; t)\rangle_t$ be the average number in the shell at distance between r and $r+\Delta r$ at time t:

$$\langle n_i(r, \Delta r; t)\rangle_t = \frac{1}{T} \sum_{j=1}^{T} n_i(r; t_j). \tag{9.21}$$

Note that $\langle n_i(r)\rangle$ is independent on i, then we can define ensemble average of number of particles as

$$\langle n(r, \Delta r; t)\rangle \equiv \frac{1}{N} \sum_{i=1}^{N} \frac{1}{T} \sum_{j=1}^{T} n_i(r, \Delta r; t_j). \tag{9.22}$$

Let assumed the particles are uncorrelated, the same assumption of independent probability between particles in equation (9.14), then we averaged number in the shell at distance r:

$$\langle n(r, \Delta r)\rangle_{unc} = \rho V(r, \Delta r)(N-1)/N, \tag{9.23}$$

where $V(r, \Delta r)$ is Volume of shell between r and $r+\Delta r$, and ρ is density. The alternative form of the radial distribution function is the ratio between averaged number of particles

on a shell with distance r and the uncorrelated number:

$$g(r) = \frac{\langle n(r, \Delta r; t) \rangle}{\langle n(r, \Delta r) \rangle_{unc}} \tag{9.24}$$

$$= \frac{1}{\rho V(r, \Delta r)(N-1)T} \sum_{i=1}^{N} \sum_{j=1}^{T} n_i(r, \Delta r; t_j). \tag{9.25}$$

If the given material is liquid-like and is not highly ordered case, the averaged number at long distance becomes un-correlated averaged number:

$$\lim_{r \to \infty} g(r) = \frac{\lim_{r \to \infty} \langle n(r, \Delta r; t) \rangle}{\langle n(r, \Delta r) \rangle_{unc}} = \frac{\langle n(r, \Delta r) \rangle_{unc}}{\langle n(r, \Delta r) \rangle_{unc}} = 1. \tag{9.26}$$

Because of system size, the density ρ should be replaced by local density, i.e., the counted number for all the particles divided by total area that is considered:

$$\rho_D = \frac{1}{T(N-1)V_D} \sum_{k=1}^{N-1} \langle n(r, \Delta r; t) \rangle \equiv \frac{n_D}{T(N-1)V_D}, \tag{9.27}$$

where subscript D denote domain of computation. For simplification, let $\rho(r)$ be the averaged density between r and $r + \Delta r$:

$$\rho(r) = \frac{\langle n(r, \Delta r; t) \rangle}{V(r, \Delta r)}. \tag{9.28}$$

Note that $\rho(r)$ is not affected by Δr since the counted number for histogram directly proportional to the volume: $\langle n(r, \Delta r; t) \rangle \propto V(r, \Delta r)$. The equation (9.25) becomes

$$g(r) = \frac{\rho(r, \Delta r)}{\rho_D} = \frac{V_D}{n_D} \frac{\langle n(r, \Delta r; t) \rangle}{V(r, \Delta r)}. \tag{9.29}$$

The coordination number with the given distance, R, is defined as

$$CN(R) = 4\pi\rho \int_0^R g(r) r^2 dr, \tag{9.30}$$

where this number indicate the expected number of particles within the distance, R. Note that this is cumulating pair correlation function, where the cumulated number directly related with the finding probability for kinetics models.

```
1 def get_ddf(traj, ts, Np, N_dimension, box_dimension, cut_ratio):
2     ddf = []
```

```
3     for t in ts:
4         for i in range(Np-1):
5             for j in range(i+1, Np):
6                 d = lin.norm(get_rel_vec(traj, t, i, j, N_dimension,
                      box_dimension))
7                 if d<cut_ratio*box_dimension:
8                     ddf.append(d)
9     return ddf
10
11 def get_rdf_ref(traj, ts, dr, Np, N_dimension, box_dimension, cut_ratio):
12     Nr = int(cut_ratio*box_dimension/dr)
13     rdf = zeros([Nr, 3])
14     rdf[:,0] = arange(0, cut_ratio*box_dimension, dr)
15     ddf = get_ddf(traj, ts, Np, N_dimension, box_dimension, cut_ratio)
16     N_tot = size(ddf)
17     Nt = size(ts)
18     for r in ddf:
19         rdf[int(r/dr), 1] += 1
20     if (N_dimension == 3):
21         Vr = (4./3.)*pi*((rdf[:,0]+dr)**3.0 - rdf[:,0]**3.0)
22         Vrmax = (4./3.)*pi*(cut_ratio*box_dimension)**3.0
23         rho_local = N_tot/(Nt*0.5*(Np-1)*Vrmax)
24     elif (N_dimension == 2):
25         Vr = pi*((rdf[:,0]+dr)**2.0 - rdf[:,0]**2.0)
26         Vrmax = pi*(cut_ratio*box_dimension)**2.0
27         rho_local = N_tot/(Nt*0.5*(Np-1)*Vrmax)
28     print 'rho_local = ', rho_local
29     rdf[:,2] = rdf[:,1]/(Vr*0.5*(Np-1)*Nt*rho_local)
30     rdf[0, 2] = 0.
31     return rdf
```

9.2.3 Anisotropic Radial Distribution Function

When shear is introduced, the micelle distribution is no more isotropic. In this sense, it is better to introduce angle, θ, defined by the angle from the x axis in the xy plane.

Note that here we used x axis as shear direction and y axis as shear gradient direction. In this sense, we have anisotropic number measure

$$\langle n(r, \Delta r, \Delta\theta; t)\rangle \equiv \frac{1}{NT}\sum_{i=1}^{N}\sum_{j=1}^{T} n_i(r, \Delta r, \Delta\theta; t_j), \tag{9.31}$$

where its isotropic form is the same with Eq. (9.22). It leads

$$g(r, \theta) = \frac{1}{\rho V(r, \Delta r, \Delta\theta)(N-1)T}\sum_{i=1}^{N}\sum_{j=1}^{N} n_i(r, \Delta r, \Delta\theta; t_j), \tag{9.32}$$

with

$$V(r, \Delta r, \Delta\theta) = \frac{2\pi}{3}\left((r+\Delta r)^3 - r^3\right)\left(\cos\theta - \cos(\theta+\Delta\theta)\right), \tag{9.33}$$

where $\cos(\theta_{ij}) = \hat{\mathbf{r}}_{ij}\cdot\hat{\mathbf{x}}$.

9.2.4 Pair Correlation in Projected XY Plane

When simple shear is implemented along the x direction and with its gradient direction y. The micelle distribution will be changed due to the given mechanical perturbation. In this sense, to measure pair correlation function in projected xy plane is useful. The main definition is the same with Eq. (9.18) that suggesting integrate over z direction when there are no flow effect along the z-direction. In this sense, the PCF becomes

$$g(x, y) = \frac{V_D}{n_D}\frac{\langle n(x, y; \Delta x, \Delta y; t)\rangle}{V_{dx\,dy\,L_z}} \tag{9.34}$$

9.3 Graph Algorithms to Analysis Network Connectivity

9.3.1 Graph

Mathematically, a graph is an ordered pair $G = (V, E)$ where a set V of vertices and a set E of edges. For instance, we have vertices and edges for figure 9.3 as

$$V = \{0, 1, 2, 3, 4, 5\} \tag{9.35}$$

$$E = \{(0,1), (0,3), (1,2), (2,4), (2,5), (3,4), (4,5)\}, \tag{9.36}$$

which in consequence V is set of all the index for particles and E is set of all pairs of index for bridges. It is of importance that the identification of percolation is not necessary to count weight on the bridge, i.e., number of connections for the same bridge, so we do not need count all the weight array on this graph analysis. In addition, the given graph is undirected since all the element for E is symmetric under the pair index: $(i, j) = (j, i)$.

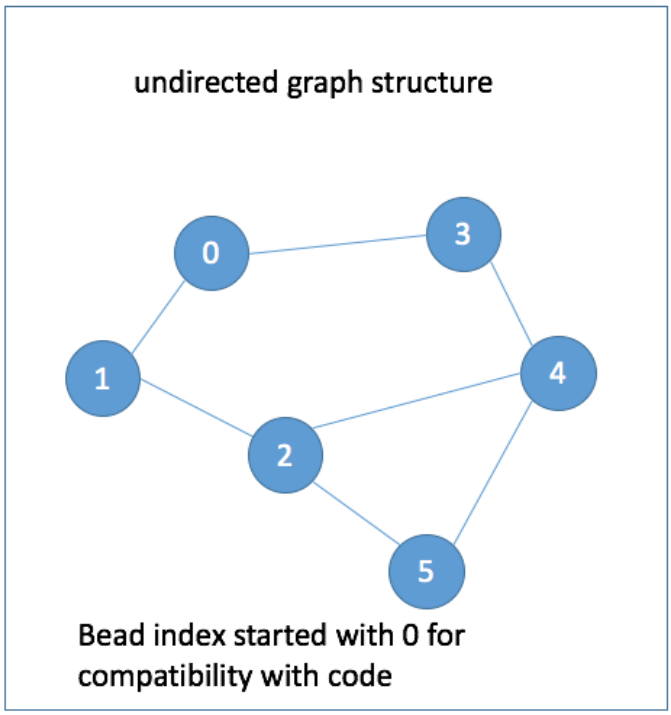

Figure 9.3: Example for association maps. This example will be used DFS testing and the starting index changed to 0 from 1 for compatibility with the code infrastructure. Therefore, index zero indicate the zero-th particle and -1 indicate there is no association.

9.3.2 Tree and Spanning Tree

The tree is a linearized graph, which means graph without any circle of bridges. For given network structure is not a tree because of association can happen to make a loop. To understand tree structure, however, is of importance since the algorithms to travel

graph is based on the tree. The graph cannot be merged to the tree structure, but if we ignore loop bridges, we can span tree structure from given graph which is called *spanning tree*. In consequence of linearization, the spanning tree is not unique that depends on the algorithms to travel.

To be specific, for graph depicted in figure 9.3, if we apply DFS algorithm, the spanning tree has the form of figure 9.4 (left). Here, the 0-th particle is selected as root, and the rank of a child is represented by depth from the root. If we use BFS algorithm, the spanning tree changed to figure 9.4 (right). The travel sequence for DFS becomes $0 \to 1 \to 2 \to 4 \to 3 \to 5$ while BFS becomes $0 \to 1 \to 3 \to 2 \to 4 \to 5$. Since DFS is used as default, this article only contains details about DFS. The adjacency list for the given graph is described in table 9.1.

Table 9.1: Adjacency list for the given graph, figure 9.3

	1	2	3
0	1	3	-1
1	0	2	-1
2	1	4	5
3	0	4	-1
4	2	3	5
5	2	4	-1

9.3.3 Travel Algorithm

Travel for Vertex: Measuring Cluster Size Distribution

Let say cluster as the group of particles that is connected. The size of a cluster is defined by a number of particles on the subjected cluster; then we can measure cluster size distribution of given system.

The given associated network has the same structure with the undirected graph that is composed of vertexes (particles in this case) and edges (association in this case).

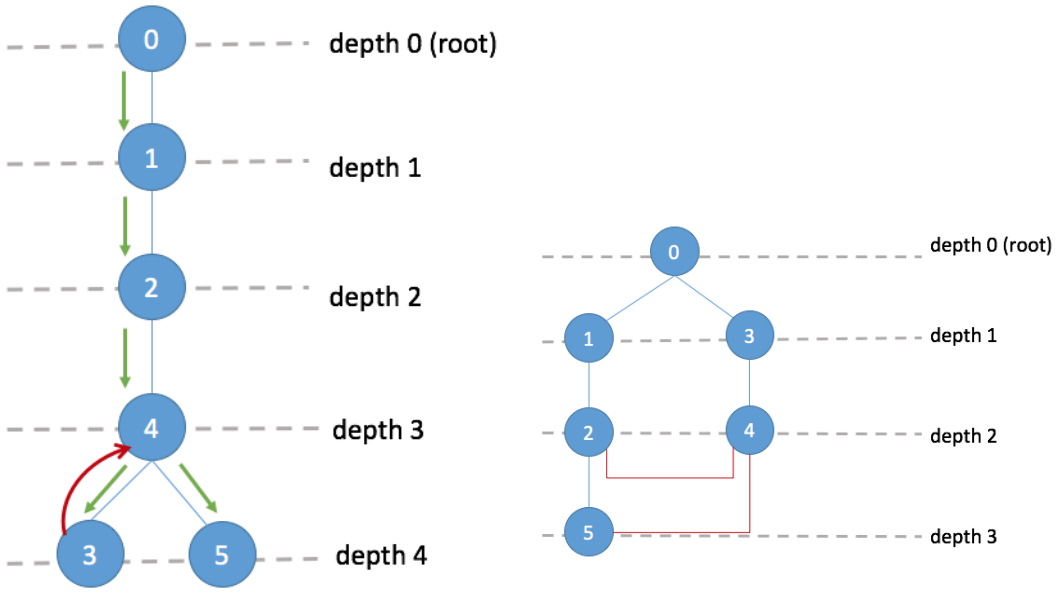

Figure 9.4: DFS spanning tree for graph depicted in figure 9.3 (left) and BFS spanning tree for graph depicted in figure 9.3 (right)

Undirected means that bridge chain is symmetric under the index of pair of particles, $\mathbf{r}_{ij} = \mathbf{r}_{ji}$. Extracting information of association topology is done through traveling the network, and the data is given by adjacency list. In general, depth-first search (DFS) and breadth-first search (BFS) are good for this aspect with different spanning tree. The details of the data structure and algorithm are described in appendix 8.1.

Travels for Edges: Identify Travels Beyond PBC Box

Travel for vertex means we visit all the particles that connected with the given root particle, but it does not guarantee that visiting all the edges (bridges). The percolation identification depends on the bridges, not about particles itself, which means we need to modify travel algorithm. There is various way to travel edges rather than vertex, but we need only information of edge not about real travels. Hence, the algorithm is slightly modified to record the identifier for shift factor for all the possible travel path - but do not act the travel when the target particle is already in-visited status.

Travels inside PBC Box

As already mentioned in above, the travel is only allowed inside the box, and whenever travel is experienced beyond the box, travel is canceled and it will be recorded for percolation identification. To be specific, consider the networks in figure 9.5 shows that different percolation scheme. However, the percolation through x-axis in the (b) of figure 9.5 cannot be captured by given scheme since the percolation line through the boundary of subjected box. For relatively large 3-dimensional box, the situation is not so common, which is the reason to use introduced identification procedure.

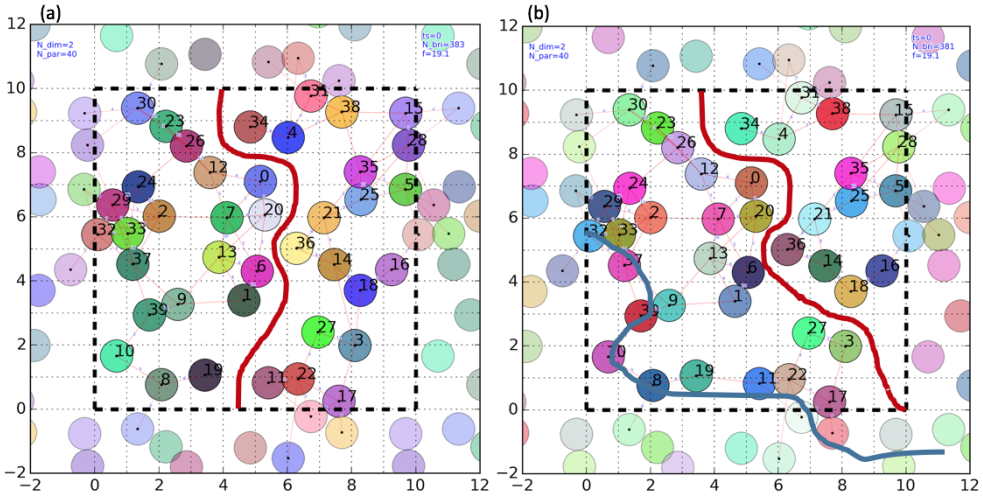

Figure 9.5: Two dinsintuishable 2-dimensional cluster system. Left figure (a) represent percolation happens along y axis while no percolation along x axis. Right figure (b) represent the percolation happens both of x and y axis, but x percolation line beyond the subjected box. The thick red line represent isolation while the thick blue line represent percolation line along x axis.

It also works well for 3-dimensional case. The given association information depicted in 9.6. By eyes, it is not easy to judge there exist percolation cluster or not. From this algorithm, it reveals that the root index 0 is composed of 191 pairs of association that percolated along all the axis: x, y, and z. If we measure cluster size distribution and identify the given cluster is percolated with specified axis or not, the figure 9.7 is useful

to understand the problem. There are 60 distinguishable clusters and 2122 total number of particles in 60 clusters. Since the number of distinguishable association is 6022, 3900 particles are isolated or attached to the wall. For detail distribution, the travel should be allowed for directed image (which will be implemented later) then the distribution will be more accurate.

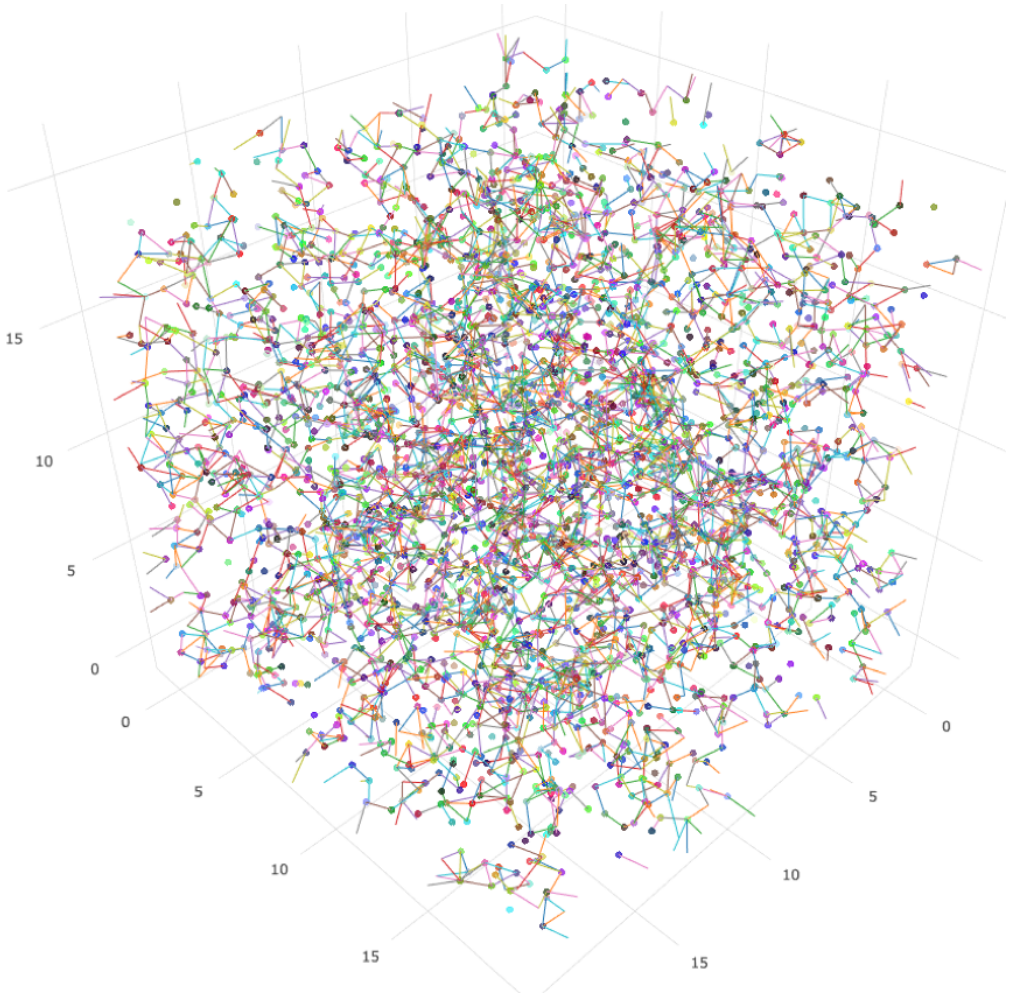

Figure 9.6: Equilibrium topology with the given condition: 3200Np, 20^3 dimensionless volume, 25 chains per each particle. Re-scaling factor is used 2.0.

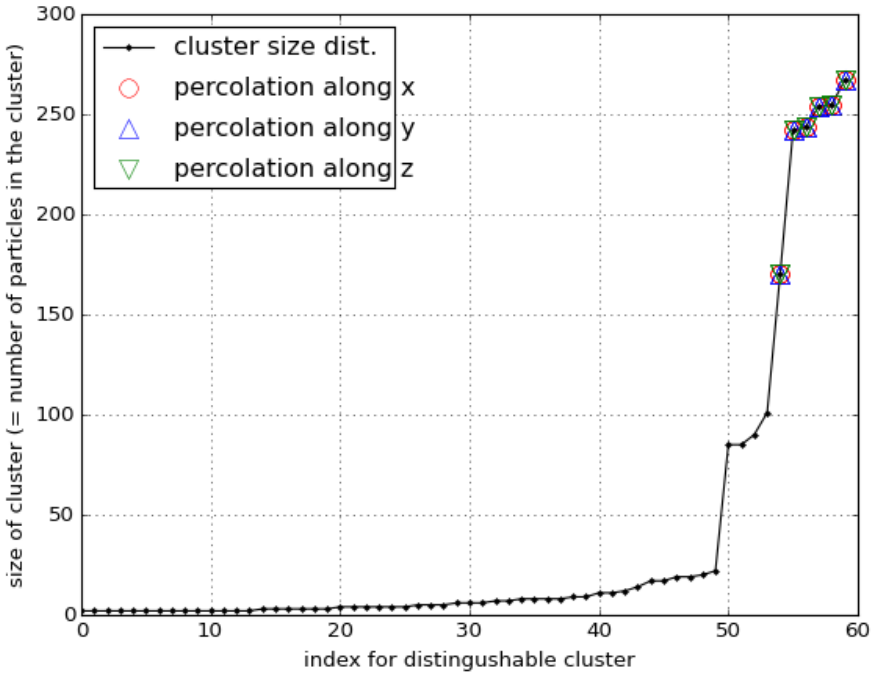

Figure 9.7: Cluster size distribution and identification for percolation with each independent axis.

Allowing Travel Beyond Boundary of Box

It might be a more general way to allow travel beyond the boundary of the box. At this moment, there are several difficulties to allow such a travels. The most importance question is *how to identify percolation*. Allowing one more image of the subjected box is a key to identify percolation. During travels, we have to record all the parity of the travel identifier since it is a key of the image. Sum of all travel identifier for a given axis, say image identifier, should not lower than -1 and higher than +1, which means the only direct image of subjected box will be accounted. It is of importance to distinguish between particles in the different box even if they have the same index number, which

can be achieved using image identifier:

$$I^k = \sum_{i=1}^{N_{tb}} s_i^k, \tag{9.37}$$

where N_{tb} is number of travel beyond boundary, k denote k-th spatial dimension and $s_i^k \in \mathscr{S}$. It is quite simple that the image identifier, I^k can be any value of $\mathscr{S} = \{-1, 0, +1\}$, which direct the current travel happen in the left, center, or right side of the box, respectively. Therefore, *recorded shift factor is not the instance shift factor but sum of all instance shift factors.* Note that the travel to image particle is allowed even if its original particle in current PBC box is visited status. Once the travel is finished, all the particles in its direct image have been visited status, and we have to make sure the all the edges are accounted for identification of travel.

The identifier for this case is the same with travel identifier inside the box: one cluster for k-th axis shows both of left and right imaginary shift factor, this is percolated. We do not need to travel further from the direct visualization of PBC box. For simplification, the index vector is introduced:

$$\mathbf{I} = [i_1, i_2, i_3]^T, \tag{9.38}$$

where i_1, i_2, i_3 are the index for each axis. If the subjected particle is in current PBC box, the components are $i_1 = i_2 = i_3 = i$ where i is the original index for the particle. If it is in directed image of PBC box, we can use shifted index:

$$i_k = i + S_k N_p, \tag{9.39}$$

where S_k is the shift factor for the given axis and N_p is a number of particles. For instance, if the system has 10 particles inside PBC box, then the i_k value becomes -10 to 20: -10 to -1 for the left image of k-th axis, 0 to 10 for the current box, and 11 for 20 for the right image of k-th axis. The mapping function from image of box to current box is easily given by i_k modulo N_p: $i_k \% N_p$. This benefit to recording and tracking the stack memory of the iterative DFS algorithm.

9.3.4 Python Code for Measuring Cluster Size and Percolation Identification

There is various way to develop DFS algorithm for tree structure in a general way. It is quite simple to use recursive form since DFS is using call stack. With given size of a cluster, however, the recursive call is limited by the system for safety reason, and have potential overhead because of calling functions typically taking time. On this regards, the code is developed by the iterative manner with some set of if-phrase to identify edge travels. The root index will be given by the argument index (default is zero). When we need to travel all the sub-graph of given graph (existing several clusters), we can iterate root index from zero to a number of particles; then we can extract distinguishable clusters, which is the way to measure cluster size distribution.

9.3.5 DFS for identification of percolation

```
1  def check_travel_beyond_box(pos, index, target, Ld):
2      Nd = shape(pos)[1]
3      for k in range(Nd):
4          if (ident_minimum_distance_k_from_x(pos[index, k], pos[target, k
               ], Ld) != 0):
5              return 1
6      return 0
7
8  def ident_minimum_distance_k_from_x(x, k, box_dimension):
9      kd = asarray([k-box_dimension - x, k-x, k+box_dimension-x])
10     return argmin(abs(kd)) - 1 # will return [-1, 0, +1]
11
12 def ident_over(hash, index, order_count):
13     N_cols = shape(hash)[1]
14     if order_count >= N_cols:
15         return 1
16     if int(hash[index, order_count]) is -1:
17         return 1
18     return 0
```

```
19
20 def cluster_edge_DFS_travel_restricted_box_iter(hash, pos, Ld,
       record_component, index=0, order_count=1, cnt=0, IDPC=[], IDPI=[],
       stack=[], stack_order=[]):
21     cnt = 0; const_new_order_count = 1 # initialisation variables
22     N_cols = shape(hash)[1] # limitation for the hash tables
23     stack.append(int(index)); stack_order.append(order_count) # initial
           stacking
24     while(size(stack) > 0): # will false when size(stack) is 0 if it is
           not initial step
25         cnt += 1 # temporal counting
26         ident_over_cols = ident_over(hash, index, order_count)
27         if ident_over_cols: # in the case that the hash[index,
               order_count] reaching end (-1 or order_count is over)
28             stack = stack[:-1]; stack_order = stack_order[:-1]
29             if (size(stack) > 0):
30                 index = stack[-1]; order_count = stack_order[-1] + 1
31         else: # in the case that the hash[index, order_count] is properly
                defined
32             target = hash[index, order_count]
33             travel_beyond_box = check_travel_beyond_box(pos, index,
                   target, Ld)
34             if (target in record_component) or travel_beyond_box: # when
                   target is in stack stack or travel beyond box boundary
35                 if travel_beyond_box:
36                     for id in range(shape(pos[index, :])[0]):
37                         ident_IDP = ident_minimum_distance_k_from_x(pos[
                               index, id], pos[target, id], Ld)
38                         if (int(ident_IDP) is not 0) and ([index, target]
                               not in IDPI):
39                             IDPC.append([id, ident_IDP])
40                             IDPI.append([index, target])
41                 # when particle is duplicated or travel_beyond_box
42                 index = index; order_count = order_count + 1;
43
```

```
44                  # this means it inherit the exist index for bead but
                        increase order_count
45                  # note that the target for next step is given by hash[
                        index, order_count]
46              else: # when the target will stack
47                  record_component.append(int(target))
48                  stack.append(int(target)); stack_order.append(order_count
                        ) # record element and its order for stack
49                  index = target; order_count = const_new_order_count; #
                        depth first search
50          return size(stack)
```

Bibliography

Alami, E., M. Almgren, W. Brown, and J. François (1996). "Aggregation of hydrophobically end-capped poly (ethylene oxide) in aqueous solutions. Fluorescence and light-scattering studies". *Macromolecules* 29.6, pp. 2229–2243.

Allen, P. and D. Tildesley (1989). *Computer Simulation of Liquids*. Oxford Science Publ. Clarendon Press.

Annable, T., R. Buscall, and R. Ettelaie (1993). "The rheology of solutions of associating polymers: Comparison of experimental behavior with transient network theory". *Journal of Rheology* 37.

Anthony, R. L., R. H. Caston, and E. Guth (1942). "Equations of state for natural and synthetic rubber-like materials. I. Unaccelerated natural soft rubber". *Journal of Physical Chemistry* 46.8, pp. 826–840.

Bach, A., K. Almdal, H. K. Rasmussen, and O. Hassager (2003). "Elongational Viscosity of Narrow Molar Mass Distribution Polystyrene". *Macromolecules* 36.14, pp. 5174–5179.

Baig, C. and V. A. Harmandaris (2010). "Quantitative analysis on the validity of a coarse-grained model for nonequilibrium polymeric liquids under flow". *Macromolecules* 43, pp. 3156–3160.

Bell, G. (1978). "Models for the specific adhesion of cells to cells". *Science* 200.4342, pp. 618–627.

Bird, R., C. Curtiss, R. Armstrong, and O. Hassager (1987). *Dynamics of Polymer Liquids Vol. 2 Kinetic Theory*. Wiley.

Borsellino, A. and T. Poggio (1973). "Convolution and correlation algebras". *Kybernetik* 13.2, pp. 113–122.

Chandler, D. (1987). *Introduction to Modern Statistical Mechanics*. Oxford University Press.

Cho, K. S. and G. W. Park (2013). "Fixed-point iteration for relaxation spectrum from dynamic mechanical data". *Journal of Rheology* 57.2, p. 647.

Costanzo, S., Q. Huang, G. Ianniruberto, G. Marrucci, O. Hassager, and D. Vlassopoulos (2016). "Shear and Extensional Rheology of Polystyrene Melts and Solutions with the Same Number of Entanglements". *Macromolecules* 49.10, pp. 3925–3935.

Cox, W. P. and E. H. Merz (1958). "Correlation of dynamic and steady flow viscosities". *Journal of Polymer Science Part A: Polymer Chemistry* 28.118, pp. 619–622.

Daivis, P. J. and D. J. Evans (1994). "Comparison of constant pressure and constant volume nonequilibrium simulations of sheared model decane". *The Journal of chemical physics* 100.1, pp. 541–8.

Dobson, M., I. Fox, and A. Saracino (2016). "Cell list algorithms for nonequilibrium molecular dynamics". *Journal of Computational Physics* 315.C, pp. 211–220.

Doi, M. and S. Edwards (1988). *The Theory of Polymer Dynamics*. International series of monographs on physics. Clarendon Press.

Elliott, P. T., L.-l. Xing, W. H. Wetzel, and J. E. Glass (2003). "Influence of Terminal Hydrophobe Branching on the Aqueous Solution Behavior of Model Hydrophobically Modified Ethoxylated Urethane Associative Thickeners". *Macromolecules* 36.22, pp. 8449–8460.

Ermak, D. L. and J. A. McCammon (1978). "Brownian dynamics with hydrodynamic interactions". *The Journal of chemical physics* 69.4, p. 1352.

Evans, D. and G. Morriss (2008). *Statistical Mechanics of Nonequilibrium Liquids*. Cambridge University Press.

Evans, E. and K. Ritchie (1997). "Dynamic strength of molecular adhesion bonds." *Biophysical journal* 72.4, pp. 1541–1555.

Fixman, M. (1986). "Construction of Langevin forces in the simulation of hydrodynamic interaction". *Macromolecular* 19, pp. 1204–1207.

Foss, D. R. and J. F. Brady (2000). "Structure, diffusion and rheology of Brownian suspensions by Stokesian Dynamics simulation". *Journal of Fluid Mechanics* 407, pp. 167–200.

François, J., S. Maitre, M. Rawiso, and D. Sarazin (1996). "Neutron and X-ray scattering studies of model hydrophobically end-capped poly (ethylene oxide) aqueous solutions at rest and under shear". *Colloids and Surfaces A: ...*

Frenkel, D. and B. Smit (2001). *Understanding Molecular Simulation: From Algorithms to Applications*. Computational science series. Elsevier Science.

Graessley, W. W. (1980). "Polymer chain dimensions and the dependence of viscoelastic properties on concentration, molecular weight and solvent power". *Polymer* 21.3, pp. 258–262.

Green, M. S. and A. V. Tobolsky (1946). "A New Approach to the Theory of Relaxing Polymeric Media". *The Journal of chemical physics* 14.2, p. 80.

Greiner, A., W. Strittmatter, and J. Honerkamp (1988). "Numerical integration of stochastic differential equations". *Journal of Statistical Physics*.

Harmandaris, V. A., N. P. Adhikari, N. F. A. van der Vegt, and K. Kremer (2006). "Hierarchical Modeling of Polystyrene: From Atomistic to Coarse-Grained Simulations". *Macromolecules* 39.19, pp. 6708–6719.

Hernández Cifre, J. G., T. M. A. O. M. Barenbrug, J. D. Schieber, and B. H. A. A. van den Brule (2003). "Brownian dynamics simulation of reversible polymer networks under shear using a non-interacting dumbbell model". *Journal of non-newtonian fluid mechanics* 113.2-3, pp. 73–96.

Hernández Cifre, J. G., R. Pamies, A. L. Kjøniksen, K. D. Knudsen, B. Nyström, and J. García de la Torre (2007). "Brownian dynamics simulation of reversible polymer networks using a non-interacting bead-and-spring chain model". *Journal of non-newtonian fluid mechanics* 146.1-3, pp. 3–10.

Huang, Q., N. J. Alvarez, Y. Matsumiya, H. K. Rasmussen, H. Watanabe, and O. Hassager (2013a). "Extensional Rheology of Entangled Polystyrene Solutions Suggests Importance of Nematic Interactions". *ACS Macro Letters* 2.8, pp. 741–744.

Huang, Q., L. Hengeller, N. J. Alvarez, and O. Hassager (2015). "Bridging the Gap between Polymer Melts and Solutions in Extensional Rheology". *Macromolecules* 48.12, pp. 4158–4163.

Huang, Q., O. Mednova, H. K. Rasmussen, N. J. Alvarez, A. L. Skov, K. Almdal, and O. Hassager (2013b). "Concentrated Polymer Solutions are Different from Melts: Role of Entanglement Molecular Weight". *Macromolecules* 46.12, pp. 5026–5035.

Huang, Q. and H. K. Rasmussen (2016). "Stress relaxation following uniaxial extension of polystyrene melt and oligomer dilutions". *Journal of Rheology* 60.3, pp. 465–471.

Ianniruberto, G. (2015a). "Extensional Flows of Solutions of Entangled Polymers Confirm Reduction of Friction Coefficient". *Macromolecules* 48.17, pp. 6306–6312.

Ianniruberto, G. (2015b). "Quantitative appraisal of a new CCR model for entangled linear polymers". *Journal of Rheology* 59.1, pp. 211–235.

Ianniruberto, G., A. Brasiello, and G. Marrucci (2011). "Friction coefficient does not stay constant in nonlinear viscoelasticity". *Proceedings of the 7th Annual ...*

Ianniruberto, G., A. Brasiello, and G. Marrucci (2012). "Simulations of Fast Shear Flows of PS Oligomers Confirm Monomeric Friction Reduction in Fast Elongational Flows of Monodisperse PS Melts As Indicated by Rheooptical Data". *Macromolecules* 45.19, pp. 8058–8066.

Ianniruberto, G. and G. Marrucci (1996). "On compatibility of the Cox-Merz rule with the model of Doi and Edwards". *Journal of non-newtonian fluid mechanics* 65.2-3, pp. 241–246.

Ianniruberto, G. and G. Marrucci (2015). "New Interpretation of Shear Thickening in Telechelic Associating Polymers". *Macromolecules* 48.15, pp. 5439–5449.

Koga, T. and F. Tanaka (2005). "Molecular origin of shear thickening in transient polymer networks: A molecular dynamics study". *The European Physical Journal E* 17.2, pp. 115–118.

Larson, R. G. (1999). *The structure and rheology of complex fluids*.

Li, H. and T. A. Witten (1994). "Polymers Grafted to Convex Surfaces - a Variational Approach". *Macromolecules* 27.2, pp. 449–457.

Likhtman, A. E. and T. C. B. McLeish (2002). "Quantitative Theory for Linear Dynamics of Linear Entangled Polymers". *Macromolecules* 35.16, pp. 6332–6343.

Marrucci, G., S. Bhargava, and S. L. Cooper (1993). "Models of shear-thickening behavior in physically crosslinked networks". *Macromolecules* 26.24, pp. 6483–6488.

Marrucci, G., F. Greco, and G. Ianniruberto (2000a). "Possible role of force balance on entanglements". *Macromolecular Symposia* 158, pp. 57–64.

Marrucci, G., F. Greco, and G. Ianniruberto (2000b). "Simple strain measure for entangled polymers". *Journal of Rheology* 44.4, pp. 845–854.

Marrucci, G. and G. Ianniruberto (2004). "Interchain Pressure Effect in Extensional Flows of Entangled Polymer Melts". *Macromolecules* 37.10, pp. 3934–3942.

Masubuchi, Y., T. Yaoita, Y. Matsumiya, H. Watanabe, G. Ianniruberto, and G. Marrucci (2013). "Stretch/orientation Induced Acceleration in Stress Relaxation in Coarse-grained Molecular Dynamics Simulations". *Nihon Reoroji Gakkaishi* 41.1, pp. 35–37.

McLeish, T. C. B. (2002). "Tube theory of entangled polymer dynamics". *Advances in Physics* 51.6, pp. 1379–1527.

Meng, X.-X. and W. B. Russel (2005). "Structure and Size of Spherical Micelles of Telechelic Polymers". *Macromolecules* 38.2, pp. 593–600.

Nielsen, J. K., H. K. Rasmussen, O. Hassager, and G. McKinley (2006). "Elongational viscosity of monodisperse and bidisperse polystyrene melts". *Journal of Rheology* 50.4, pp. 453–476.

Oesterhelt, F., M. Rief, and H. E. Gaub (1999). "Single molecule force spectroscopy by AFM indicates helical structure of poly(ethylene-glycol) in water". *New Journal of Physics* 1.1, pp. 6–6.

Öttinger, H. (1996). *Stochastic Processes in Polymeric Fluids: Tools and Examples for Developing Simulation Algorithms*. Stochastic Processes in Polymeric Fluids: Tools and Examples for Developing Simulation Algorithms. Springer.

Persson, K., S. Abrahmsen, P. Stilbs, F. K. Hansen, and H. Walderhaug (1992). "The association of urethane-polyethyleneoxide (HEUR) thickeners, as studied by NMR self-diffusion measurements". *Colloid and Polymer Science* 270.5, pp. 465–469.

Ramirez, J., S. K. Sukumaran, B. Vorselaars, and A. E. Likhtman (2010). "Efficient on the fly calculation of time correlation functions in computer simulations". *The Journal of chemical physics* 133.15, pp. 154103–12.

Rubinstein, M. and R. H. Colby (2003). *Polymer Physics*. OUP Oxford.

Ruymbeke, E. van, D. Vlassopoulos, M. Kapnistos, C. Y. Liu, and C. Bailly (2010). "Proposal to Solve the Time-Stress Discrepancy of Tube Models". *Macromolecules* 43.1, pp. 525–531.

Santos de Oliveira, I. S., B. W. Fitzgerald, W. K. den Otter, and W. J. Briels (2014). "Mesoscale modeling of shear-thinning polymer solutions". *Journal of Chemical Physics* 140.10, pp. 104903–12.

Semenov, A. N., J. F. Joanny, and A. R. Khokhlov (1995). "Associating polymers: equilibrium and linear viscoelasticity". *Macromolecules* 28.4, pp. 1066–1075.

Sprakel, J., E. Spruijt, J. van der Gucht, J. T. Padding, and W. J. Briels (2009). "Failure-mode transition in transient polymer networks with particle-based simulations". *Soft Matter* 5.23, pp. 4748–9.

Suzuki, S., T. Uneyama, T. Inoue, and H. Watanabe (2012). "Nonlinear Rheology of Telechelic Associative Polymer Networks: Shear Thickening and Thinning Behavior of Hydrophobically Modified Ethoxylated Urethane (HEUR) in Aqueous Solution". *Macromolecules* 45.2, pp. 888–898.

Suzuki, S., T. Uneyama, and H. Watanabe (2013). "Concentration Dependence of Nonlinear Rheological Properties of Hydrophobically Modified Ethoxylated Urethane Aqueous Solutions". *Macromolecules* 46.9, pp. 3497–3504.

Tam, K. C., R. D. Jenkins, M. A. Winnik, and D. R. Bassett (1998). "A structural model of hydrophobically modified urethane-ethoxylate (HEUR) associative polymers in shear flows". *Macromolecules* 31.13, pp. 4149–4159.

Tanaka, F. and S. F. Edwards (1992a). "Viscoelastic properties of physically crosslinked networks. 1. Transient network theory". *Macromolecules*.

Tanaka, F. and S. F. Edwards (1992b). "Viscoelastic properties of physically crosslinked networks: Part 1. Non-linear stationary viscoelasticity". *Journal of non-newtonian fluid mechanics* 43.2-3, pp. 247–271.

Tanaka, F. and S. F. Edwards (1992c). "Viscoelastic properties of physically crosslinked networks: Part 2. Dynamic mechanical moduli". *Journal of non-newtonian fluid mechanics* 43.2-3, pp. 273–288.

Treloar, L. (1975). *The Physics of Rubber Elasticity*. Monographs on the physics and chemistry of materials. Oxford University Press, USA.

Tripathi, A., K. C. Tam, and G. McKinley (2006). "Rheology and Dynamics of Associative Polymers in Shear and Extension: Theory and Experiments". *Macromolecules* 39.5, pp. 1981–1999.

Uneyama, T., S. Suzuki, and H. Watanabe (2012). "Concentration dependence of rheological properties of telechelic associative polymer solutions". *Physical Review E* 86.031802, pp. 1–15.

Van den Brule, B. and P. J. Hoogerbrugge (1995). "Brownian dynamics simulation of reversible polymeric networks". *Journal of non-newtonian fluid*.

Van Der Spoel, D., E. Lindahl, B. Hess, G. Groenhof, A. E. Mark, and H. J. C. Berendsen (2005). "GROMACS: Fast, flexible, and free". *Journal of Computational Chemistry* 26.16, pp. 1701–1718.

Vlassopoulos, D. and M. Cloitre (2014). "Tunable rheology of dense soft deformable colloids". *Current Opinion in Colloid & Interface Science* 19.6, pp. 561–574.

Wagner, M. H. (2015). "An extended interchain tube pressure model for elongational flow of polystyrene melts and concentrated solutions". *Journal of non-newtonian fluid mechanics* 222.C, pp. 121–131.

Wagner, M. H., S. Kheirandish, and O. Hassager (2005). "Quantitative prediction of transient and steady-state elongational viscosity of nearly monodisperse polystyrene melts". *Journal of Rheology* 49.6, pp. 1317–1327.

Warner Jr, H. R. (1972). *Kinetic theory and rheology of dilute suspensions of finitely extendible dumbbells*. Industrial & Engineering Chemistry Fundamentals.

Watanabe, H. (1999). "Viscoelasticity and dynamics of entangled polymers". *Progress in Polymer Science* 24.9, pp. 1253–1403.

Winnik, M. A. and A. Yekta (1997). "Associative polymers in aqueous solution". *Current Opinion in Colloid & Interface Science* 2.4, pp. 424–436.

Xu, B., A. Yekta, L. Li, Z. Masoumi, and M. A. Winnik (1996). "The functionality of associative polymer networks: The association behavior of hydrophobically modified urethane-ethoxylate (HEUR) associative polymers in aqueous solution". *Colloids and Surfaces a-Physicochemical and Engineering Aspects* 112.2-3, pp. 239–250.

Yaoita, T., T. Isaki, Y. Masubuchi, H. Watanabe, G. Ianniruberto, and G. Marrucci (2012). "Primitive Chain Network Simulation of Elongational Flows of Entangled Linear Chains: Stretch/Orientation-induced Reduction of Monomeric Friction". *Macromolecules* 45.6, pp. 2773–2782.

Yekta, A., B. Xu, J. Duhamel, H. Adiwidjaja, and M. A. Winnik (1995). "Fluorescence Studies of Associating Polymers in Water - Determination of the Chain-End Aggregation Number and a Model for the Association Process". *Macromolecules* 28.4, pp. 956–966.

Zhou, M. (2003). "A new look at the atomic level virial stress: on continuum-molecular system equivalence". *Proceedings of the Royal Society of London, Series A* 459.2037, pp. 2347–2392.